



VNIVERSIDAD
D SALAMANCA
CAMPUS DE EXCELENCIA INTERNACIONAL



Luminescent sensors for emerging contaminants based on Eu^{3+} complexed by clay minerals - amino acids hybrid materials

Denis Talarico de Araujo

UNIVERSIDADE DE FRANCA
UNIVERSIDAD DE SALAMANCA

Franca 2022



VNIVERSIDAD
D SALAMANCA
CAMPUS DE EXCELENCIA INTERNACIONAL



UNIFRAN
Universidade
de Franca

Sensores luminescentes para contaminantes emergentes baseados em Eu³⁺ complexado em materiais híbridos argilominerais - aminoácidos

Sensores luminiscentes para contaminantes emergentes basados en Eu³⁺ complejoado en materiales híbridos minerales arcillosos - aminoácidos

Tese apresentada pelo Licenciado em Química **Denis Talarico de Araujo** para obter o Título de Doutor em Ciências Químicas

Tesis presentada por el Licenciado en Química **Denis Talarico de Araujo** para obtener el título de Doctor en Ciencias Químicas

Franca, 25 de janeiro de 2022

Salamanca, 25 de enero de 2022

Denis Talarico de Araujo



VNIVERSIDAD
D SALAMANCA
CAMPUS DE EXCELENCIA INTERNACIONAL



UNIFRAN
Universidade
de Franca

**O AUTOR OFERECE UM AGRADECIMENTO ESPECIAL PELO
FINANCIAMENTO DESTA TESE PELA FAPESP**

Através de bolsa de doutorado com projeto de nº 2017/01719-0 intitulado
**“Materiais biohíbridos (caulinita-aminoácidos) como sensores
luminescentes de poluentes emergentes”** no período de 01/07/2018 a
18/01/2022

E através de bolsa BEPE – doutorado com projeto de nº 2018/26569-3
intitulado **“Materiais biohíbridos (Caulinita-aminoácidos) como sensores
luminescentes de poluentes emergentes”** no período de 02/09/2019 a
19/03/2020

Com apoio da CAPES e CNPq.

Denis Talarico de Araujo

Emerson Henrique de Faria, Professor de Química da Universidade de Franca, Brasil, e Miguel Ángel Vicente Rodríguez, Catedrático de Química Inorgánica da Universidade de Salamanca, Espanha, como orientadores do trabalho intitulado “Sensores luminescentes para contaminantes emergentes baseados em Eu^{3+} complexado em materiais híbridos argilominerais - aminoácidos”.

AFIRMAM:

Este trabalho foi realizado pelo Licenciado em Química Denis Talarico de Araujo para se candidatar ao Doutorado em Química, dentro dos Programas de Doutorado “Ciências – Universidade de Franca, Brasil” e “Ciência e Tecnologia Químicas – Universidad de Salamanca, Espanha”. Considerando que constitui um trabalho de pesquisa original, está completo e cumpre todos os requisitos exigidos para a defesa pública, autorizando sua apresentação.

Franca, 25 de janeiro de 2022

Salamanca, 25 de enero de 2022



Emerson Henrique de Faria



Miguel Ángel Vicente Rodríguez

Emerson Henrique de Faria, Profesor de Química de la Universidad de Franca, Brasil, y Miguel Ángel Vicente Rodríguez, Catedrático de Química Inorgánica de la Universidad de Salamanca, España, como orientadores del trabajo titulado “Sensores luminiscentes para contaminantes emergentes basados en Eu^{3+} complejoado en materiales híbridos minerales arcillosos - aminoácidos”.

HACEN CONSTAR:

Este trabajo fue realizado por el Licenciado en Química Denis Talarico de Araujo para postularse al Doctorado en Química, dentro de los Programas de Doctorado “Ciencia - Universidad de Franca, Brasil” y “Ciencia y Tecnología Químicas - Universidad de Salamanca, España”. Se trata de un trabajo de investigación original, se encuentra completo y cumple con todos los requisitos para la defensa pública, por lo que autorizamos su presentación.

Franca, 25 de janeiro de 2022

Salamanca, 25 de enero de 2022



Emerson Henrique de Faria



Miguel Ángel Vicente Rodríguez

Agradecimentos

Desde 2008 quando estava terminando o ensino médio já havia me interessado pelo mundo da química devido aos ótimos professores que tive nos últimos anos. De fato, nossa formação é muito influenciada pelas experiências e pelas pessoas que admiramos. Eu sempre quis ser professor de ciências, eu queria ser como os professores que eu admirava, que pareciam saber de tudo, que eram simpáticos com nossas dúvidas e que atiçavam nossas curiosidades. Então em 2008 mesmo, eu decidi ser professor de química, e não somente um professor, mas um professor doutor em química.

Desde quando decidi fazer Licenciatura em Química pelo Instituto Federal Goiano em Rio Verde-GO já era minha intenção fazer mestrado e doutorado. Queria fazer desde 2008 meu doutorado em uma boa Universidade, que me desse espaço para pesquisa, para experimentar, queria estudar fora, conhecer o mundo. Mas sendo bastante sincero, como a maioria dos nossos sonhos, eu não achei que fosse conseguir. Mas aqui estou eu, terminando meu doutorado em Ciências pela Universidade de Franca, no qual pude ter o privilégio de fazer em regime de co-tutela com a Universidade de Salamanca, na Espanha, realizando os meus sonhos profissionais, imaginados lá em 2008, antes de fazer meu vestibular em 2009.

São mais de uma década no mundo da química, então como agradecer todos que passaram pela minha vida, que contribuíram com minha formação e com a realização deste sonho? São tantas pessoas que peço perdão a todos quem eu esquecer de mencionar, porque foram tantas pessoas que contribuíram de alguma forma que não sei se seria capaz de lembrar de todas elas.

Quero agradecer primeiramente a Deus, o meu Deus, Senhor de tudo, que me guiou a cada dia para chegar até aqui. Eu não O conheço apenas de ouvir falar, mas pude experimentar Deus no meu processo de formação como homem, como pai e como químico. Me sinto privilegiado apenas por poder sentir Tua presença em todos os dias, a qual não posso mais viver sem. Quero agradecer aos meus pais que sempre fizeram o possível e o impossível para me ver chegar até aqui. Eu lembro do meu pai emocionado com meu diploma, como seu primeiro filho a se formar, de como me sinto honrado por ter nascido nesta família, tendo o Claudinei e a Claudia como pais, de forma que não posso expressar minha gratidão a Deus por ter me dado este presente.

Quero agradecer ao Prof. Celso Belisário do Instituto Federal Goiano em Rio Verde por ter me inspirado a continuar a estudar e a amar a profissão de professor, e por todos os outros professores do IF que me ajudaram na formação. Quero agradecer os professores da Unifran, em especial o prof. Calefi que me apresentou à pesquisa, que também me incentivou a ser professor, aos professores Lucas Rocha, que me ajudou na qualificação e com sua didática exemplar, me ajudou com muitas dúvidas na área de luminescência, juntamente com o Prof. Eduardo Nassar que foi quase um coorientador, me ajudando em tudo que pedi e precisei sem me negar nada, a Profa. Liziane Marçal,

Prof. Eduardo Molina e Prof. Tiago Silva que foram além de professores, meus amigos e me ajudaram em tudo que precisei.

Quero agradecer à reitora e professora Katia Ciuffi, que me apoiou sempre que pode. Me senti muito privilegiado quando entrou em contato comigo preocupada com a pandemia quando estava na Espanha, que nos poucos momentos que conversamos, sempre me tratou muito bem, de forma que me fez sentir especial. Muito obrigado pelo apoio. Também quero agradecer a todos os professores da Universidade de Salamanca, em especial a Profa Elena que sempre me ajudou com minhas dúvidas com paciência e carinho. Aos meus colegas Misol e Alejandro que foram verdadeiros amigos no tempo que estive lá em Salamanca. A profa. Raquel Trujillano e ao Prof. Vicente Rives que me ajudaram com tudo que precisei e pedi e especialmente ao meu orientador Prof. Miguel Vicente que contribuiu tanto com minha formação antes mesmo de ir à Espanha que não tenho palavras para agradecer todo o apoio, dedicação e paciência com que agiu comigo durante todo este tempo. Se não fosse seu esforço em aprovarmos meu primeiro artigo, não teria conseguido entrar no doutorado, então estou aqui hoje também por causa de você. Gracias profesor.

Quero agradecer ao meu orientador Prof. Emerson H. de Faria que é meu pai científico, esteve comigo desde 2014 na graduação até hoje me orientando. Tenho uma admiração profunda pela sua pessoa, pela forma que vê a química, pela forma que faz as coisas, pela forma que leciona e pela forma que orienta. O sr. sempre foi um orientador rígido, mas não no sentido de um opressor, mas de alguém que tenta extrair o potencial máximo de seus alunos. Não teria realizado meu sonho sem você, não teria chegado até aqui sem você. Com exceção do nosso passeio em Barcelona, acho que nunca te vi fora do ambiente de trabalho ou de atividades profissionais, mas mesmo sem ter este contato, mesmo mantendo um relacionamento profissional, você é meu melhor amigo. Você é o meu padrão de profissional, de químico e de professor. É alguém em quem confio. Do que seria de mim se não fosse por você? Será que teria feito mestrado? Será que teria conhecido um acelerador de partículas? Que teria feito Doutorado? Será que teria ido pra Salamanca? Será que gostaria de química e que veria a profissão da mesma forma? Não sei dizer realmente, mas sei que sou muito grato por todas as oportunidades que me deu e por me ajudar a voar.

Quero agradecer aos meus amigos Bruno, Jesse e Ana Claudia que estiveram comigo desde o ensino fundamental até hoje. Ao meu amiiiiigo Tobias que é um verdadeiro parceiro na minha vida. Acho que nunca vou achar um amigo como você, e nunca vou me perdoar por ter feito você vir para a Espanha na pandemia. Aos meus amigos de laboratório Eduardo, Breno, Vinicius, Gabriel, Lorrana, Jéssica, Suelen e todos os outros que me fizeram companhia e que me ajudaram no laboratório, em especial ao meu amigo Vinilson que me ajudou demais no meu período de doutorado e é um verdadeiro amigo e muito valioso para mim.

Quero agradecer meus irmãos Lenin e Diego que sem perceber me ajudaram na minha caminhada me oferecendo apoio que somente irmãos poderiam dar. E por fim,

agradecer a minha esposa Neiva que entre todas as pessoas, mais viveram comigo os dramas, as preocupações, os estresses e conquistas, que foi meu apoio emocional, que é meu porto seguro, que me sustenta nesta caminhada. Não sei o que seria de mim sem você. No meu agradecimento no mestrado, eu disse que você carregava o Francisco e me deus este presente maravilhoso que é este meu filho muito amado, e agora novamente, agora neste agradecimento no doutorado você carrega meu segundo filho Lucca, em quem espero com ansiedade e que já amo muito, e muito. Vocês são minha vida.

*“Toda a descoberta da ciência pura é potencialmente subversiva;
por vezes a ciência deve ser tratada como um inimigo possível.”*

Aldous Huxley

List of Acronyms and Abbreviations

Kao – Purified kaolinite;

Pro – L-proline;

Phe – L-phenylalanine;

LDH – Lamellar double hydroxide (hydrotalcite);

Sap – Saponite;

Lap – LAPONITE®;

DMSO – Dimethylsulfoxide;

APTES – 3-aminopropyltriethoxysilane;

tta - 2-thenoyltrifluoroacetate;

FTIR – Fourier transform infrared molecular absorption spectroscopy;

SEM – Scanning electron microscopy;

DTA – Differential thermal analysis;

TG – Thermogravimetry;

DTG – Derived thermogravimetry;

BET – Surface analysis using the Brunauer, Emmett and Teller method;

CTC – Cation exchange capacity;

SE – Specific surface area;

XRD – X-ray diffraction;

List of Figures

Figure 1 - Optical properties model of the Eu(III), a) on the Stokes pseudoshift and b) emissions and excitation lifetimes. Adapted from Bodman and Butler (BODMAN; BUTLER, 2021).....	6
Figure 2 - Examples of amino acids with cyclic radicals: (a) Proline, (b) Histidine, (c) Phenylalanine and (d) Tryptophan.....	7
Figure 3 - Luminescence spectra of Tb _{1.828} Eu _{0.172} -MOF demonstrating the suppression of luminescence in a) solvents, b) Pb ²⁺ and c) Fe ³⁺ at different concentrations. (WANG et al., 2016).....	9
Figure 4 - Research data on title, abstract or keywords of publications in the Scopus database, containing the words "Sensor", "Luminescence or Luminescent" together with the words a) MOF or Metal-Organic Framework, b) Polymer, c) Silica and d) clay or clay mineral. The survey was conducted on June 21, 2021.....	11
Figure 5 - Clay minerals of the 1:1 and 2:1 type. Oa, Ob are apical and basal oxygens respectively. Adapted from Brigatti (BRIGATTI; GALAN; THENG, 2006).	12
Figure 6 – Schematic representation of kaolinite functionalization by boric acid catalyzed amidation reaction. (DE ARAÚJO et al., 2021)	16
Figure 7 - Structure of the lamellar double hydroxide with the anion intercalated. Adapted from Crepaldi and Rives (CREPALDI; VALIM, 1998; RIVES; ULIBARRI, 1999).	17
Figure 8 - Schematic representation of amino acid conformation in hydrotalcite. (Font: author)	20
Figure 9 - Schematic representation of the saponite. (Font: author)	21
Figure 10 - a) Schematic representation of LAPONITE® and b) interaction sites. Adapted from (DAS et al., 2019).	22
Figure 11 - Flowchart of experimental procedures for samples with kaolinite.	36
Figure 12 - Flowchart of experimental procedures for samples with hydrotalcite.	41
Figure 13 - Flowchart of experimental procedures for samples with saponite and LAPONITE®.	45
Figure 14 – Examples of Kaolinite network parameters.	139
Figure 15 - X-ray diffractograms of the samples: a) kaolinite purified with main Miller's reflections; b) functionalized materials with 2θ degrees at 5-25; c) 50-65 degrees at 2θ; d) of complexed materials at 5-25 degrees at 2θ and d) 50-65 degrees at 2θ.	141
Figure 16 - Representation of obtaining data for calculating the Hinckley index. Reproduced from ALABA et al. (2015).	142
Figure 17 - Schematic representation of the intercalation process of kaolinite with DMSO. (Reproduced from ZHANG et al., 2018)	144

Figure 18 - Schematic representation of kaolinite with hydroxyl positions. Adapted from TOSONI; DOLL; UGLIENGO, (2006).....	148
Figure 19 - Infrared absorption spectroscopy of purified kaolinite between 4000 to 400 cm^{-1} with break in 3200-1600 cm^{-1}	148
Figure 20 - Infrared absorption spectroscopy of organofunctionalized materials between 4000 to 400 cm^{-1} with breakage of 3200-2000 cm^{-1} (a) and of materials after complexation of europium III ion with breakage of 3200-2000 cm^{-1} (b).....	149
Figure 21 - Infrared spectra of amino acids a) Proline (Between 4000 to 400 cm^{-1}) and phenylalanine between b) 4000 to 1600 cm^{-1} and c) 1600 to 400 cm^{-1}	154
Figure 22 - TG, DTG and DTA curves of purified kaolinite obtained in an oxidizing atmosphere (O_2) with a heating rate of 20°C/min.	160
Figure 23 - Thermal analysis of kaolinite samples being: TG, DTG and DTA before (a, c, and respectively) and (b, d, f respectively) after complexation of the europium ion (III).	162
Figure 24 - Scanning electron microscopy of purified kaolinite and organofunctionalized samples. Images taken with a working distance of approximately 12.5 mm and beam energy of 5.0 kV.	166
Figure 25 - X-ray diffractograms of LDH samples, a) purified LDH and intercalated with amino acids and b) complexed with europium ion (III).....	168
Figure 26 - Proposed schematic representation of the structure of amino acids intercalated in hydrotalcite for a) C-LDHPhe, b) C-LDHPro, c) R-LDHPhe and d) R-LDHPro.....	171
Figure 27 - Infrared spectra (FTIR) of samples with a) hydrotalcite and b) after complexation of Eu(III) ion.....	173
Figure 28 – Thermal analysis of synthetic LDH. With ramp from 25 to 900 °C, at 20 °C per min and in an oxidizing atmosphere.	175
Figure 29 - TG of R-LDHPPro samples before and after complexation with Eu^{3+} ion, with a ramp from 25 to 900 °C, at 20 °C per min and in an oxidizing atmosphere.	176
Figure 30 – Thermal analysis of C-LDHPPro samples before and after complexation with Eu^{3+} ion, with a ramp from 25 to 900 °C, at 20 °C per min and in an oxidizing atmosphere.....	177
Figure 31 - Thermal analysis of R-LDHPhe samples before and after complexation with Eu^{3+} ion, with a ramp from 25 to 900 °C, at 20 °C per min and in an oxidizing atmosphere.....	178
Figure 32 - Thermal analysis of C-LDHPhe samples before and after complexation with Eu^{3+} ion, with a ramp from 25 to 900 °C, at 20 °C per min and in an oxidizing atmosphere.....	179
Figure 33 - SEM images for pure and amino acid intercalated LDH samples.....	183
Figure 34 - X-ray diffractograms of LAPONITE® (a) and saponite (b) samples.....	185

Figure 35 - Infrared vibrational spectra for samples with LAPONITE® (a) and saponite (b) and their main attributions.	188
Figure 36 - Thermal analysis (TG, DTA and DTG) of pure LAPONITE® and intercalated with amino acid complexes. With ramp from 25 to 900 °C in oxidizing atmosphere.	191
Figure 37 - Thermal analysis (TG, DTA and DTG) of pure saponite and intercalated with amino acid complexes. With ramp from 25 to 900 °C in oxidizing atmosphere.	194
Figure 38 - SEM images of pure LAPONITE® and intercalated with Eu(III) complexes.	195
Figure 39 - SEM images of pure saponite intercalated with Eu(III) complexes.	196
Figure 40 - Schematic representation of a common fluorimeter (font = author).	198
Figure 41 - Representation of energy levels in the process of energy transfer from the ligand to the Eu(III) ion. W_{ET} and W_{BT} are energy transfer rates and back energy transfer rates respectively. (font: author)	199
Figure 42 - Representation of the pseudo baseline emission of the Eutta(KaoPro) sample to find the calculated intensities ratio (R_{CJ}), being J = 0 and 2.	203
Figure 43 - Luminescence spectra of europium transitions for the kaolinite materials a) excitation and b) Emission with normalized intensity from the transition ${}^5D_0 \rightarrow {}^7F_1$	205
Figure 44 - Luminescence spectra of kaolinite materials a) excitation and b) Emission with normalized intensity from the transition ${}^5D_0 \rightarrow {}^7F_1$	208
Figure 45 - Emission lifetimes of samples with hydrotalcite. With emission set at 612 nm and excitation set at 365 nm.	210
Figure 46 - Sample emission lifetime decay curves a) Eutta(R-LDHPPro); b) Eutta(R-LDHPhe); c) Eutta(C-LDHPPro) and d) Eutta(C-LDHPhe), varying the photon input and output slits from 2 to 5 nm.	213
Figure 47 - Luminescence spectra of excitation (a and b) and emission (c and d) LAPONITE® and saponite materials. The excitation intensities of samples with saponite were normalized by the ${}^5D_2 \leftarrow {}^7F_0$ transition, and in the emission, all analyzed samples had the intensity normalized by the ${}^5D_0 \rightarrow {}^7F_1$ transition.	216
Figure 48 - Radioactive decay of samples with LAPONITE® with emission fixed at 614 nm and excitation fixed at 362 nm.	219
Figure 49 - Sample emission lifetime decay curves of Eutta(LapPhe), varying the photon input and output slits from 2 to 5 nm.	221
Figure 50 - Calibration curves for a) Cr^{3+} ; b) caffeine and c) estrogen.	224
Figure 51 - Adsorption kinetics where qt is the adsorption capacity of the material at time t , for materials with adsorption of a) Cr^{3+} , b) Caffeine and c) Estrogen.	226

Figure 52 - Adsorption isotherms for kaolinite samples for Cr ³⁺ , caffeine and estrogen contaminants.	243
Figure 53 - Adsorption isotherms for samples with hydrotalcite for Cr ³⁺ , caffeine and estrogen contaminants.	243
Figure 54 - Adsorption isotherms for samples with LAPONITE® for Cr ³⁺ contaminants.	243
Figure 55 - Adsorption isotherms for samples with saponite for Cr ³⁺ , caffeine and estrogen contaminants.	245
Figure 56 - Photoluminescence spectra of samples complexed with Eu ³⁺ ion obtained after adsorption tests with Cr ³⁺ in times from 1 to 120 min.	251
Figure 57 - Photoluminescence spectra of samples complexed with Eu ³⁺ ion obtained after adsorption tests with caffeine in times from 1 to 120 min. .	254
Figure 58 - Photoluminescence spectra of samples complexed with Eu ³⁺ ion obtained after adsorption tests with estrogen in times from 1 to 120 min.	255
Figure 59 – Variation in the relationship between intensities R_2 (${}^5D_0 \rightarrow {}^7F_2 / {}^5D_0 \rightarrow {}^7F_1$) of the samples in relation to the concentration of Cr ³⁺	259
Figure 60 - Variation in the relationship between intensities R_2 (${}^5D_0 \rightarrow {}^7F_2 / {}^5D_0 \rightarrow {}^7F_1$) of the samples in relation to the concentration of caffeine.	260
Figure 61 - Variation in the relationship between intensities R_2 (${}^5D_0 \rightarrow {}^7F_2 / {}^5D_0 \rightarrow {}^7F_1$) of the samples in relation to the concentration of estrogen.	260
Figure 62 - Stern-Volmer plot and modified Stern-Volmer equation (inset) for the detection of Cr ³⁺ for the samples where it was possible to draw a linear line for the detection limits.	266
Figure 63 - Stern-Volmer plot and modified Stern-Volmer equation (inset) for the detection of caffeine for the samples where it was possible to draw a linear line for the detection limits.	268
Figure 64 - Stern-Volmer plot and modified Stern-Volmer equation (inset) for estrogen detection for the Eutta(SapPhe) sample, where it was possible to draw a linear line for the detection limits.	268
Figure 65 - Schematic representation of the energy diagram between ligands, contaminants and europium III ion.	270
Figure 66 - CIE chromaticity coordinates of samples complexed with Eu ³⁺ ion and images before and after the incidence of ultraviolet light (360 nm) on the samples.	277

Table List

Table 1 - Examples of kaolinite-functionalized materials from our research group and their respective applications.	14
Table 2 - Amino acid intercalation in LDH by the reconstruction method where d is the basal spacing and LDH(500 °C) is the hydrotalcite calcined at 500 °C. Adapted from Nakayama (NAKAYAMA; WADA; TSUHAKO, 2004)....	19
Table 3 - Proportion between sample mass and europium(III) chloride volume in samples containing kaolinite.	40
Table 4 - Ratio of sample mass to volume of tta:Na 0.1 M added.	48
Table 5 - Mass ratio used at each time in the kinetic adsorption study.	50
Table 6 - Structural order properties of purified kaolinite.	143
Table 7 - basal spacing (d); basal spacing variation (Δd); intercalation/functionalization ratio (α); particle orientation degree (R) and the ratio of the peak widths of the reflection d_{001} (FWHM) kaolinite samples, kaolinite intercalated with DMSO and organofunctionalized kaolinite samples.	145
Table 8 - Assignment of infrared absorption bands characteristic of kaolinite structure to purified kaolinite (Kao) and organofunctionalized materials.	151
Table 9 - Assignment of infrared absorption bands characteristic of the amino acids proline and phenylalanine to organofunctionalized kaolinite materials.....	156
Table 10 - Relative mol number for kaolinite samples according to proposed structures for the interaction between matrix and organic matter... ..	164
Table 11 - Network and basal space parameters of X-ray diffractograms of samples with hydrotalcite.	169
Table 12 - <i>FWHM</i> index of reflection 003 and the respective crystallite sizes of samples with LDH.	172
Table 13 - Calculated chemical formulas for hydrotalcite samples intercalated with amino acids.	182
Table 14 - Basal space (d) and <i>FWHM</i> index of X-ray diffractograms of samples obtained by LAPONITE® and saponit.....	186
Table 15 - Optical properties of materials complexed with Eu(III) ion. Total radiation (A_{rad}) and non-radiation (A_{nrad}) emission rate; obtained lifetime ratio (τ_{obs}) and lifetime of radiative emission (τ_{rad}); number of water molecules in the first coordination sphere (q) and internal quantum yield of radiative emission (Q_{LnLn}).	206
Table 16 - Ratio between the areas of the bands corresponding to (R_0) and (R_2); ratio between areas corrected of the bands corresponding to (R_{c0}) and (R_{c2}) and Judd-Ofelt parameters Ω_2 and Ω_4	207

Table 17 - Ratio between the areas of the bands corresponding to (R_0) and (R_2) and Judd-Ofelt parameters Ω_2 and Ω_4 .	209
Table 18 - Optical properties of materials complexed with Eu(III) ion. Total radiation (A_{rad}) and non-radiation (A_{nrad}) emission rate; obtained lifetime ratio (τ_{obs}) and lifetime of radiative emission (τ_{rad}); number of water molecules in the first coordination sphere (q) and internal quantum yield of radiative emission ($QLnLn$).	210
Table 19 - Optical properties of materials complexed with Eu(III) ion. Total radiation (A_{rad}) and non-radiation (A_{nrad}) emission rate; obtained lifetime ratio (τ_{obs}) and lifetime of radiative emission (τ_{rad}); number of water molecules in the first coordination sphere (q) and internal quantum yield of radiative emission ($QLnLn$).	217
Table 20 - Ratio between the areas of the bands corresponding to (R_0) and (R_2); ratio between areas corrected of the bands corresponding to (R_{C0}) and (R_{C2}) and Judd-Ofelt parameters Ω_2 and Ω_4 .	222
Table 21 - Adsorption capacity (qt) in the longest time (t) for Cr^{3+} , caffeine and estrogen contaminants.	228
Table 22 - Properties obtained from pseudo first order and pseudo second order kinetic models for Cr^{3+} adsorbents.	231
Table 23 - Properties obtained from pseudo first order and pseudo second order kinetic models for caffeine adsorbents.	232
Table 24 - Properties obtained from pseudo first order and pseudo second order kinetic models for estrogen adsorbents.	233
Table 25 - Parameters obtained by the Langmuir isotherm and its linear regression for Cr^{3+} , caffeine and estrogen contaminants.	239
Table 26 - Parameters obtained by the Freundlich isotherm and its linear regression for Cr^{3+} , caffeine and estrogen contaminants.	240
Table 27 - Parameters obtained by the nonlinear Freundlich isotherm.	247
Table 28 - Linear correlation data between the luminescence intensity of the synthesized hybrid materials and the adsorbed amounts of Cr^{3+} , caffeine and estrogen.	262
Table 29 - Properties of luminescent sensors obtained by the Stern-Volmer equation.	269

Summary

1. Chapter 1 – Introduction and Objectives	1
1.1. Emerging Pollutants	1
1.2. Hybrid materials as optical sensors	4
1.3. Ln³⁺ luminescent sensors	5
1.4. Clay minerals as an inorganic matrix of hybrid materials ...	11
1.4.1. Kaolinite.....	13
1.4.2. Lamellar double hydroxides (LDH)	16
1.4.3. Saponite and LAPONITE®.....	20
1.5. Objectives	23
1.6. Materials and reagents use	26
1.7. References	27
2. Chapter 2 - Experimental	36
2.1. Kaolinite materials	36
2.1.1. Purified kaolinite	37
2.1.2. Intercalation of kaolinite with DMSO.....	37
2.1.3. Functionalization by the displacement method.....	38
2.1.4. Kinetic study of the boric acid catalyzed amidation reaction.	38
2.1.5. Functionalization of kaolinite by boric acid catalyzed amidation reaction	39
2.1.6. Complexation with Eu ³⁺ ion	39
2.1.7. Addition of the secondary ligand sodium tenoyltrifluoroacetate (tta:Na).....	40
2.2. Hydrotalcite (LDH) materials	40
2.2.1. Synthesis of lamellar double hydroxides (LDH).....	41
2.2.2. Addition of amino acids by reconstruction method	42
2.2.3. Addition of amino acids by the co-precipitation method.....	43
2.2.4. Complexation of hydrotalcite samples with Eu ³⁺	43
2.2.5. Addition of the tenoyltrifluoroacetate (tta) ligand in HDL complexes	44
2.3. Saponite and LAPONITE® materials	44
2.3.1. Commercial LAPONITE® RD and Pure Saponite (microwave)	45

2.3.2. Complexation of the amino acids proline and phenylalanine with Eu ³⁺	46
2.3.3. Intercalation of Eu ³⁺ complexes in saponite and LAPONITE®	47
2.3.4. Addition of the tta ligand in the complexes intercalated in saponite and LAPONITE®	47
2.4. Leaching tests	48
2.5. Adsorption tests for Estrogen, Caffeine and Cr³⁺ contaminants	49
2.5.1. Calibration curves	49
2.5.2. Adsorption Kinetics	49
2.5.3. Chemical equilibrium in the adsorption process	50
2.6. Characterization Techniques	51
2.6.1. X-ray diffraction (XRD)	51
2.6.2. Fourier Transform Infrared Molecular Spectroscopy (FTIR)	51
2.6.3. Thermal analysis (TG/DTG/DTA)	51
2.6.4. Specific surface by BET isotherms (Brunauer, Emmett e Teller)	52
2.6.5. Determination of particle size	52
2.6.6. Electron microscopy (SEM/TEM)	52
2.6.7. Absorption spectroscopy in the UV-Visible region	53
2.6.8. Luminescence spectroscopy	53
2.7. References	53
3. Chapter 3 – Results published in journals	58
4. Chapter 4 – Results not published in journals	138
4.1. Discussion and characterization of hybrid materials	138
4.1.1. Materials obtained with kaolinite	138
4.1.2. Hydrotalcite Materials (LDH)	167
4.1.3. Materials obtained from LAPONITE® and saponite (smectites)	184
4.2. Luminescent properties of the materials obtained	197
4.2.1. Optical properties of materials immobilized in kaolinite	204
4.2.2. Optical properties of materials immobilized in LDH	208
4.2.3. Optical properties of materials immobilized on LAPONITE® and saponite	214

4.3. Applications of luminescent materials	223
4.3.1. Adsorption Tests	223
4.3.2. Quenching measurements for luminescent sensors....	247
4.3.3. Application in enhanced latent fingerprint detection ...	272
Conclusions	278
References	280
Final considerations and perspectives.....	291
APPENDIX	301

Resumo

Com o avanço do desenvolvimento social e econômico nas últimas décadas, milhões de compostos químicos são jogados nos efluentes naturais, colocando em risco tanto o bioma quanto à saúde humana. A falta de pesquisa e conhecimento sobre o comportamento destes contaminantes no meio ambiente, assim como o surgimento de novas substâncias oriundas da mistura destes poluentes são um desafio para a química verde. Pensando nisto, foram sintetizados materiais híbridos empregando-se argilominerais e aminoácidos complexados ao íon Eu^{3+} para serem aplicados como sensores luminescentes dos contaminantes Cr^{3+} , cafeína e estrogênio. Os íons lantanídeos possuem propriedades ópticas únicas tais como bandas finas de emissão e longos tempos de vida de emissão, que fornecem ao sensor seletividade e sensibilidade (pré-requisitos necessários principalmente para quantificações em analitos em concentrações reduzidas). Foram utilizados como matrizes para os complexos luminescentes o argilomineral natural caulinita e os argilominerais sintéticos hidrotalcita, LAPONITA® e saponita e os aminoácidos fenilalanina e prolina foram utilizados como ligantes, assim como o ligante secundário tenoiltrifluoroacetona (tta) foi utilizado. Os materiais foram caracterizados por difração de raios X, espectroscopia de absorção molecular na região do infravermelho, análises térmicas, microscopia eletrônica de varredura, espectroscopia UV/Visível e de luminescência. Os materiais com fenilalanina apresentaram melhores propriedades ópticas e maiores rendimentos quânticos de emissão (de 15 a 52%). As amostras de caulinita apresentaram maiores forças de interação com os complexos e tanto as amostras com caulinita quanto com saponita apresentaram boas propriedades como sensor luminescente para os contaminantes Cr^{3+} e cafeína com correlação linear maior que 97%. Os estudos cinéticos de adsorção apresentaram melhor convergência para o modelo de pseudo-segunda ordem, enquanto os estudos de equilíbrio apresentaram maior convergência para a isoterma de Freundlich.

Palavras-chave: caulinita, saponita, LAPONITA®, HDL, materiais híbridos, sensores ópticos, európio (III), prolina, fenilalanina.

Resumen

Con el avance del desarrollo social y económico en las últimas décadas, millones de compuestos químicos se vierten en efluentes naturales, poniendo en riesgo tanto el bioma como la salud humana. La falta de investigación y conocimiento sobre el comportamiento de estos contaminantes en el medio ambiente, así como la aparición de nuevas sustancias a partir de la mezcla de estos contaminantes son un desafío para la química verde. Teniendo esto en cuenta, se sintetizaron materiales híbridos de minerales arcillosos y aminoácidos complejados con el ion Eu^{3+} para aplicarlos como sensores luminiscentes de contaminantes Cr^{3+} , cafeína y estrógeno. Los iones lantánidos tienen propiedades ópticas únicas, tales como bandas de emisión delgadas y un tiempo de vida de emisión prolongada, lo que proporciona al sensor selectividad y sensibilidad (requisitos previos necesarios principalmente para la cuantificación de analitos en concentraciones reducidas). El mineral de arcilla natural caolinita y los minerales de arcilla sintética hidrotalcita, LAPONITA® y saponita se utilizaron como matrices para los complejos luminiscentes y los aminoácidos fenilalanina y prolina como ligandos, así como el ligando secundario tenoiltrifluoroacetona (tta). Los materiales se caracterizaron por difracción de rayos X, espectroscopía de absorción molecular infrarroja, análisis térmico, microscopía electrónica de barrido, espectroscopía UV/Visible y de luminiscencia. Los materiales con fenilalanina mostraron mejores propiedades ópticas y mayores rendimientos de emisión cuántica (del 15 al 52%). Las muestras de caolinita mostraron mayores fuerzas de interacción con los complejos y tanto las muestras de caolinita como de saponita mostraron buenas propiedades como sensor luminiscente para contaminantes de Cr^{3+} y cafeína con correlación lineal superior al 97%. Los estudios de cinética de adsorción mostraron una mejor convergencia para el modelo de pseudo segundo orden, mientras que los estudios de equilibrio mostraron una mayor convergencia para la isoterma de Freundlich.

Palabras clave: caolinita, saponita, LAPONITA®, LDH, materiales híbridos, sensores ópticos, europio (III), prolina, fenilalanina.

Abstract

With the advancement of social and economic development in recent decades, millions of chemical compounds are dumped into natural effluents, putting both the biome and human health at risk. The lack of research and knowledge about the behavior of these contaminants in the environment, as well as the emergence of new substances from the mixture of these pollutants are a challenge for green chemistry. Thus, hybrid materials of clay minerals and amino acids complexed to the Eu^{3+} ion were synthesized to be applied as luminescent sensors of contaminants Cr^{3+} , caffeine and estrogen. Lanthanide ions have unique optical properties such as: they have thin emission bands and long emission lifetimes, which provide the sensor with selectivity and sensitivity (necessary prerequisites mainly for quantification of the analytes at reduced concentrations). The natural clay mineral kaolinite and the synthetic clay minerals hydrotalcite, LAPONITE® and saponite were used as matrices for the luminescent complexes and the amino acids phenylalanine and proline were used as ligands, as well as the secondary ligand tenoyltrifluoroacetone (tta) was used. The materials were characterized by X-ray diffraction, infrared molecular absorption spectroscopy, thermal analysis, scanning electron microscopy, UV/Visible and luminescence spectroscopy. Materials with phenylalanine had better optical properties and higher quantum emission yields (from 15 to 52%). The kaolinite samples showed higher interaction strengths with the complexes and both the kaolinite and saponite samples showed good properties as a luminescent sensor for Cr^{3+} and caffeine contaminants with linear correlation greater than 97%. The adsorption kinetic studies showed better convergence for the pseudo-second order model, while the equilibrium studies showed greater convergence for the Freundlich isotherm.

Keywords: kaolinite, saponite, LAPONITE®, LDH, hybrid materials, optical sensors, europium (III), proline, phenylalanine

1. Chapter 1 – Introduction and Objectives

1.1. Emerging Pollutants

The concept of protected source was initially attributed to the water body that does not receive domestic or industrial effluents. Nonetheless, over time, this concept became more permissive, with those who had contact only with effluents from domestic sewage being considered as protected, which are considered suitable for the production of drinking water (HESPANHOL, 2015). However, with the advancement of economic and social development in recent decades, thousands of synthetic and natural chemical compounds are dumped daily into natural effluents only by domestic sewage, which are not properly identified and removed by sewage treatments (VARGAS-BERRONES et al., 2020).

Considering together with the production of pollutants from industrial activity, there was an advance from 1 million to 400 million tons produced per year of anthropogenic chemical products between 1930 and 2000's. (GAVRILESCU et al., 2015). In the year 2017, approximately 100 million tons were reported as environmentally harmful and nearly 92 million tons were considered hazardous to human health (VARGAS-BERRONES et al., 2020). Within this quantity and variety of contaminants present in natural aquifers, a new class of contaminants called emerging pollutants appears, also called micropollutants (with a concentration between 10^{-9} to 10^{-6} g/L) or emerging contaminants (EC), which are the result of the disposal of chemical products such as surfactants, pharmaceuticals, personal care products, pesticides, among others.

As this is a new class of contaminants, conventional sewage treatments are not able to identify and/or remove these compounds, there is also no specific regulation for monitoring/removal and research for identification and treatment is still scarce, making this a global public health and environmental problem.

Among the problems caused by these pollutants, we can highlight three main ones to justify the research and development of technologies to identify and remove these compounds from the environment. The first is the disruption of endocrine activity, which has been reported for several species of invertebrate animals, fish and amphibians in contact with these contaminants, even at low concentrations, resulting in adverse effects on metabolic development, reproductive processes, embryonic development, in sexual differentiation, growth and the digestive system (FLINT et al., 2012). Second, it is related to the formation of new compounds by mixing these contaminants with unknown effects on the biome and human health (DEBLONDE; COSSU-LEGUILLE; HARTEMANN, 2011) and finally the increase in antimicrobial resistance resulting from the contact between bacteria and antibiotics, potentially toxic metals and disinfectants in effluents, promoting the transfer of resistant genes (HOCQUET; MULLER; BERTRAND, 2016).

Related to Latin America, specifically in Brazil, the amount of information about the influence of emerging pollutants is even smaller, with the first work published only in 2000 by Stumpf et al. (STUMPF et al., 1999), where the concentration of drugs in treated and untreated natural waters in Rio de Janeiro, Brazil was monitored. In a review by Peña-Guzmán et al. (PEÑA-GUZMÁN et al., 2019), of the 51 emerging pollutants found in wastewater in Latin America,

caffeine was the one with the highest concentration (5,597,000 ng/L) followed by ibuprofen and among the endocrine disruptors the hormone estrogen (17 β -estradiol) was the one that presented higher concentration with 11,400 ng/L. The same is true for drinking water with 3,800 ng/L for caffeine and 2,400 ng/L for estrogen and for surface water with 106,000 ng/L for caffeine and 13,450 ng/L for estrogen. However, it is not possible to quantify these concentrations through conventional techniques, such as UV-Vis spectroscopy, making the detection process of these pollutants even more difficult.

Along with emerging pollutants, potentially toxic metals such as chromium, cadmium, zinc, among others, have also generated major disturbances in the ecosystem and human health. The aggravating factor of these contaminants is the ability to reach groundwater and irrigation regions, being easily absorbed by cultivation. Chromium is a metal widely known in the industry in general, especially in the tanning industry, widely present in the city of Franca, Brazil, being classified as a common environmental contaminant (PUSHKAR et al., 2021). Cr(III) and Cr(VI) concentrations above 1.0 mg/mL and 0.2 mg/L consequently can damage DNA and are highly carcinogenic (NOVOTNIK et al., 2016) in addition to contributing to antimicrobial resistance when present in natural aquifers.

Given what has been presented, the need to develop new technologies for detection and removal of these contaminants from the environment is evident, both for human health and for the natural biome. In this work, the development of luminescent sensors for the emerging contaminants caffeine and estrogen (β -estradiol) was proposed due to the high concentration of these contaminants in natural effluents, and for the potentially toxic metal Cr(III) due

to the social-economic context of the region of Franca (Brazil), where the industries related to footwear and leather bring large amounts of residues with high concentrations of this metal.

1.2. Hybrid materials as optical sensors

There are several analytical methods for identifying chemical compounds in the environment. Among the most used are thin layer chromatography (TLC) (BOCHEŃSKA; PYKA, 2013), high performance liquid chromatography (HPLC) (GIRÓN; ALAIZ; VIOQUE, 1992), high performance capillary electrophoresis (WANG et al., 2012), among others. However, the disadvantage of these methods is the need for analysis at relatively high concentrations, complex chemical-physical processes, low thermal resistance and great difficulty in performing these tests in situ. On the other hand, optical sensors are attractive because they can be synthesized at low temperatures using the sol-gel method, they are easy to incorporate contaminants for identification, they can be applied in situ and with detection limits in the quantification process that can vary up to 10^{-9} g/L (ATTIA; DIAB; EL-SHAHAT, 2014).

Both organic and inorganic materials have been proposed as optical contaminant sensors. Inorganic compounds have high thermal stability, can be easily synthesized by different techniques while organic materials have versatility and reactivity, being possible to modulate their structure to increase the selectivity and quality of the sensor (WANG et al., 2013b). However, these isolated materials have restricted characteristics and specific environments that restrict their application in practice. In this context, organic-inorganic hybrid materials stand out for combining the thermal stability and rigidity of inorganic

materials with the malleability and versatility of organic compounds. Unique properties not present in isolated materials can also arise, in addition to significantly increasing the optical properties of the sensor (GAO; KODAIMATI; YAN, 2021).

For hybrid materials used as sensor, generally the inorganic part is used as the protective matrix, while the organic part dispersed in the matrix is responsible for detection (WANG et al., 2013b). However, in recent years there has been a significant advance in the area of sensors where both parts, organic and inorganic, contribute to the quality and selectivity of materials. Several matrices have been used to synthesize hybrid materials such as metal-organic structures (MOFs) (YANG et al., 2021), fibrous nanosilica (CHATTERJEE et al., 2021), silica (CHATTERJEE et al., 2019), graphene (ZHANG et al., 2015a), surfactants (BARJA; ARAMENDÍA, 2008) etc.

1.3. Ln³⁺ luminescent sensors

Lanthanide ions have unique optical properties such as thin, easily identifiable emission bands, large stokes shifts (Figure 1), long excited state lifetimes (Figure 1) and low influence of the chemical environment, which makes these ions attractive for luminescent applications (CHEN; XU; LI, 2020).

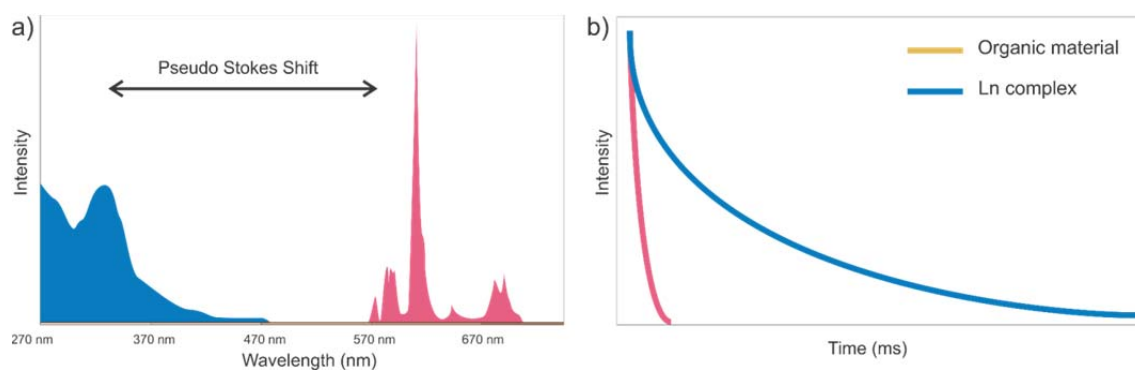


Figure 1 - Optical properties model of the Eu(III), a) on the Stokes pseudoshift and b) emissions and excitation lifetimes. Adapted from Bodman and Butler (BODMAN; BUTLER, 2021).

The thin emission bands result from the electronic configuration $[\text{Xe}] 4f^n$ where the 4f sublevel is shielded by the 5s and 5p orbitals, resulting in low influence of the chemical environment and low molar absorption coefficients ($< 3 \text{ M}^{-1}\text{s}^{-1}$) (BUNZLI; PIGUET, 2005). Under Laporte's selection rule, the only transitions allowed are those accompanied by a parity change ($g \rightarrow u$ or $u \rightarrow g$), therefore, electric-dipole f-f transitions are prohibited while magnetic-dipole transitions are weakly allowed (BÜNZLI, 2016). However, these dipole-electrical transitions are allowed when there is loss of the center of symmetry (i), which occurs by the combination of bonding orbitals, spin-orbit coupling, vibronic coupling and Jahn Teller effect (spontaneous geometry deformations caused by degenerate orbitals to reduce system energy (degeneracy)) (BÜNZLI, 2016; JAHN AND TELLER, 1937). Another parameter that can change the positions of energy levels is the total angular momentum (J), where states with different values of J can combine into a crystalline field (CF), an effect known as "*J-Mixing*" (SOUZA, 2012).

Due to these factors, Ln^{3+} ions need ligands with good molar absorptivity coefficients to transfer the received energy to the central ion, a phenomenon known as "antenna effect" (BELTRÁN-LEIVA et al., 2017; SIGOLI et al., 2001).

Organic ligands with aromatic or highly conjugated rings are very promising for these materials. In the context of this thesis, cyclic amino acids such as L-proline, L-phenylalanine and L-tryptophan (Figure 2) are good candidates for the formation of luminescent hybrid materials, as they are low cost, non-polluting and have high molar absorptivity, increasing the Ln^{3+} ion radioactive emission yield. Amino acids are generally used for biomedical applications because of the chirality that offers distinct functional groups (YOOSEFIAN et al., 2020). Furthermore, these additional functional groups of amino acids increase the accessibility of analytes for more selective detection as a luminescent sensor.

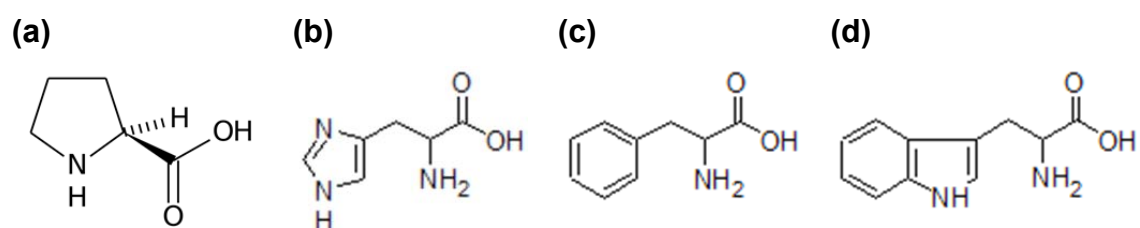
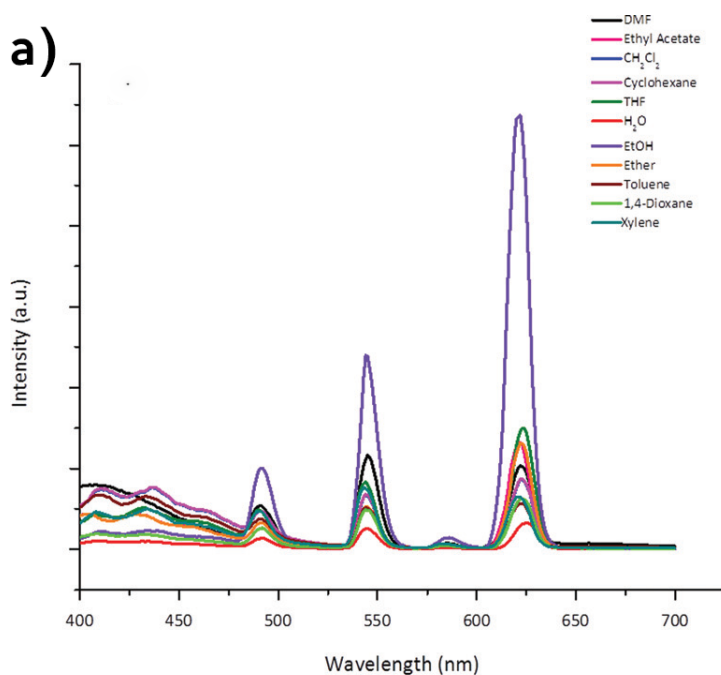


Figure 2 - Examples of amino acids with cyclic radicals: (a) Proline, (b) Histidine, (c) Phenylalanine and (d) Tryptophan.

The trivalent oxidation state is the most stable of these ions and its coordination number varies between 6 to 12 and the radiative emission of lanthanides can vary between phosphorescent emissions (eg Eu^{3+} and Tb^{3+}), fluorescent (eg Ho^{3+} and Yb^{3+}) or be both fluorescent and phosphorescent (such as Pr^{3+} and Nd^{3+}) (BÜNZLI, 2016). For this work, the Eu^{3+} ion was chosen because it is phosphorescent, with long lifetimes, thus increasing the selectivity and quality as a sensor. These properties have attracted researchers in the last decade for the application of luminescent sensors for pH (LIU et al., 2013; MOORE et al., 2012; TUREL et al., 2008), temperature (JIANG et al., 2015;

KOZAK et al., 2014), drugs (ATTIA et al., 2012), metals (KOTOVA; COMBY; GUNNLAUGSSON, 2011; ZHAI et al., 2012; ZHOU et al., 2013), among others.

The sensing occurs when oscillating groups such as water molecules, organic groups (NH₂, COOH, etc.), among others, complexed to the Eu(III) ion in the first or second coordination sphere, disperse the energy by vibronic relaxation resulting in quenching (BÜNZLI, 2015). This phenomenon is used to quantify different molecules adsorbed together with these complexes immobilized on solid matrices. Wang and co-workers (WANG et al., 2016) evaluated different solvents, anions and cations in contributing to the suppression of luminescence and they managed not only to synthesize a chemical sensor of Fe³⁺ and Pb²⁺ but also to quantify the concentration of these ions, as shown in figure 3.



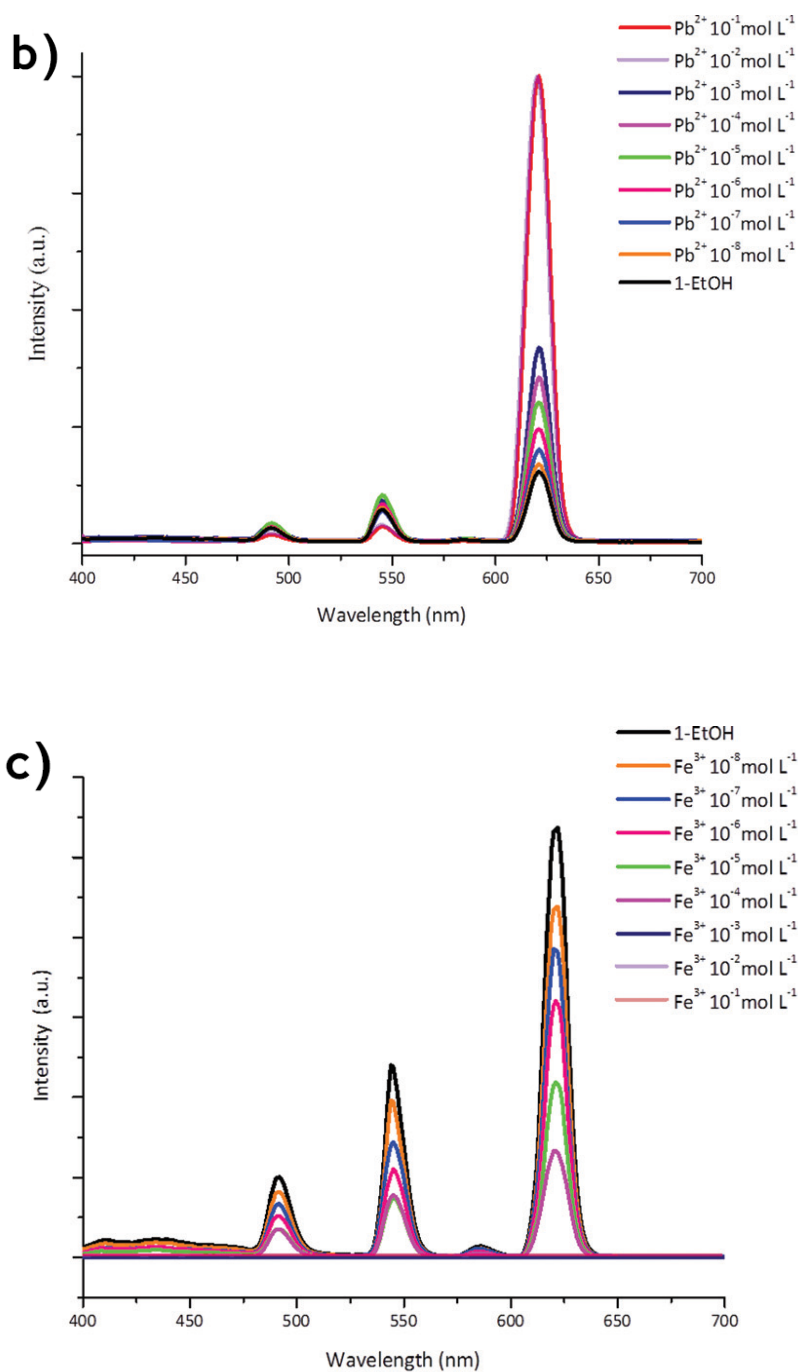
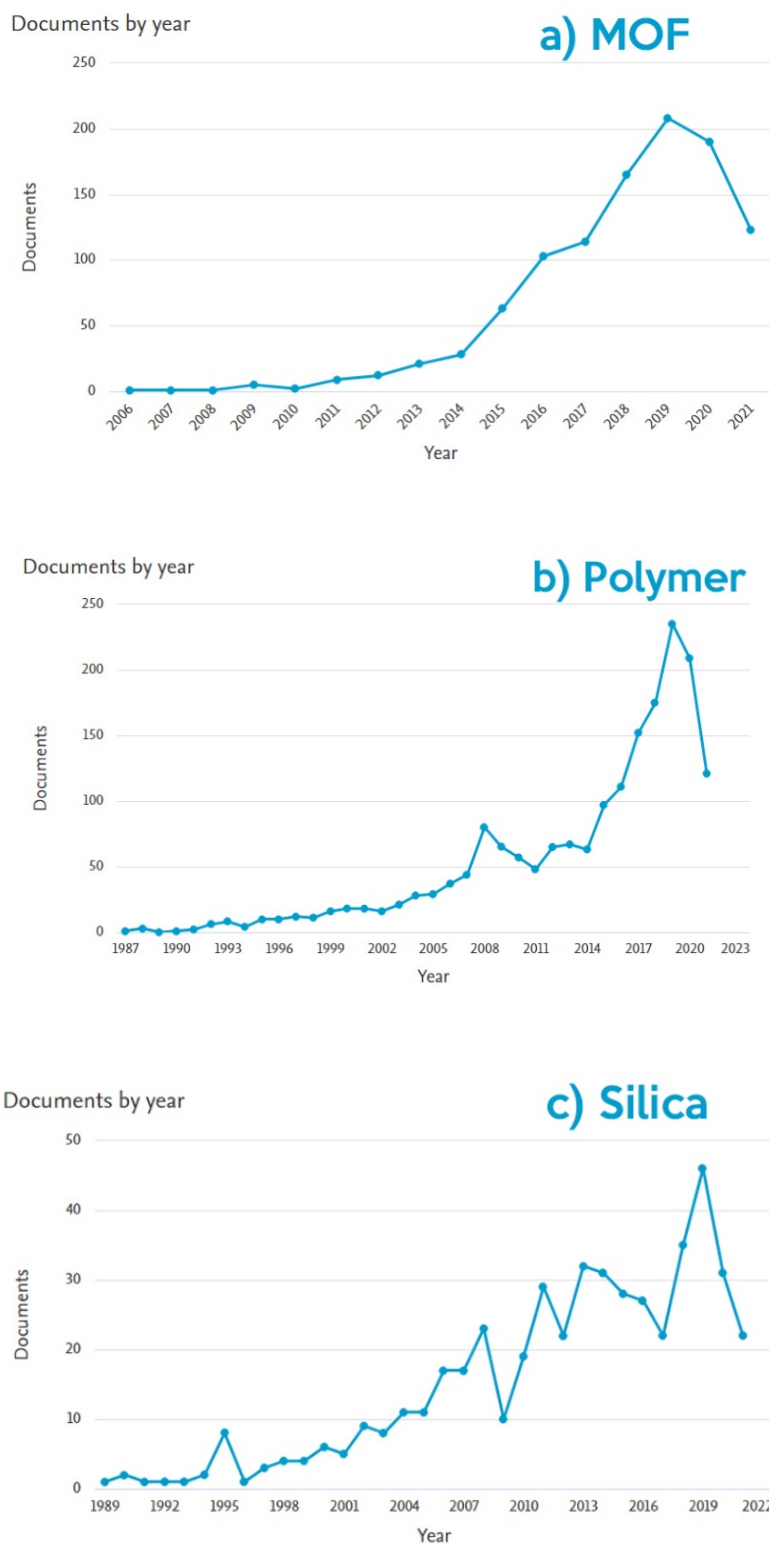


Figure 3 - Luminescence spectra of Tb_{1.828}Eu_{0.172}-MOF demonstrating the suppression of luminescence in a) solvents, b) Pb²⁺ and c) Fe³⁺ at different concentrations. (WANG et al., 2016)

Among the hybrid materials most used as sensors are coordination polymers, more precisely metal-organic structure (MOFs) where metal ions are connected to organic ligands containing noble metals and rare earth elements such as Au, Pt, Ru, Ir, Tb and Eu to provide the optical properties of the sensor

(GAO; KODAIMATI; YAN, 2021; YANG et al., 2021; ZHAN et al., 2019). Figure 4 shows a search in the Scopus database containing the words “Luminescence or luminescent” and “sensor” with different types of matrices.



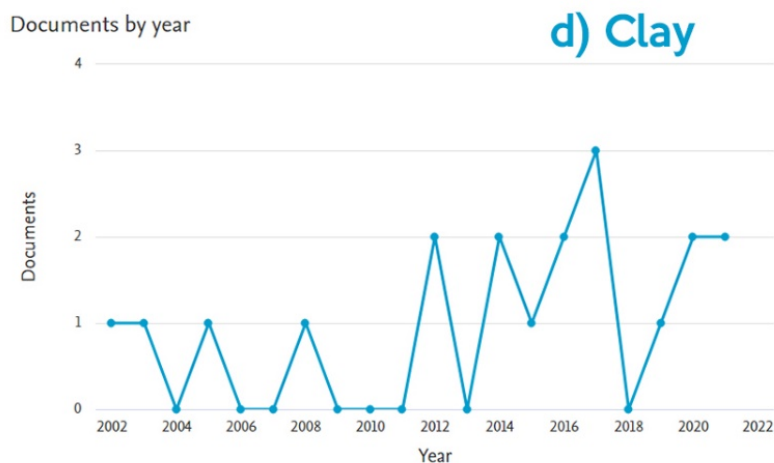


Figure 4 - Research data on title, abstract or keywords of publications in the Scopus database, containing the words "Sensor", "Luminescence or Luminescent" together with the words a) MOF or Metal-Organic Framework, b) Polymer, c) Silica and d) clay or clay mineral. The survey was conducted on June 21, 2021.

As shown in Figure 4, there has been an advance in the research of luminescent sensors in recent years using the most diverse matrices, mainly on polymeric matrices and on metal-organic structures, with more than 200 publications each just last year and analyzing only the database of Scopus. On the other hand, the number of works relating clay minerals as an inorganic matrix in obtaining sensors is practically negligible in this comparison. Lamellar clay minerals are abundant in sites for incorporation of molecules of interest, offer greater thermal resistance and the dispersion necessary for application in sensors and the lack of publications with these matrices justifies the research proposed in this work. In addition, clay minerals have both chemical affinity for cations (smectites) and anions (LDH) offering good selectivity for electrically charged contaminants (RIVES, 2001; WHITTAKER et al., 2019).

1.4. Clay minerals as an inorganic matrix of hybrid materials

Clay minerals are a diverse group of aluminosilicates, with low granulometry (particle size $<2\mu\text{m}$ according to geologists and $<4\mu\text{m}$ for

engineers), develop plasticity when wet, have a large proportion of surface area by volume and constitute the majority of phyllosilicates, which are minerals of arrangement of tetrahedral groups of silica in sheet form (DE FARIA, 2011; HUGGETT, 2015). They are extremely abundant in nature covering much of the Earth's surface and many of these are easily synthesized in the laboratory. Its lamellar structure is organized in the form of layers divided into two groups: Type TO or 1:1 with a tetrahedral sheet of silica (SiO_4) and another octahedral sheet of M_3^{+2} (dioctahedral) or M_2^{+3} (trioctahedral), where M a metallic ion such as Al, Fe, Mg, etc. The second group consists of TOT or 2:1 layers with two tetrahedral silica layers and an octahedral layer (BRIGATTI; GALAN; THENG, 2006) as shown in figure 5.

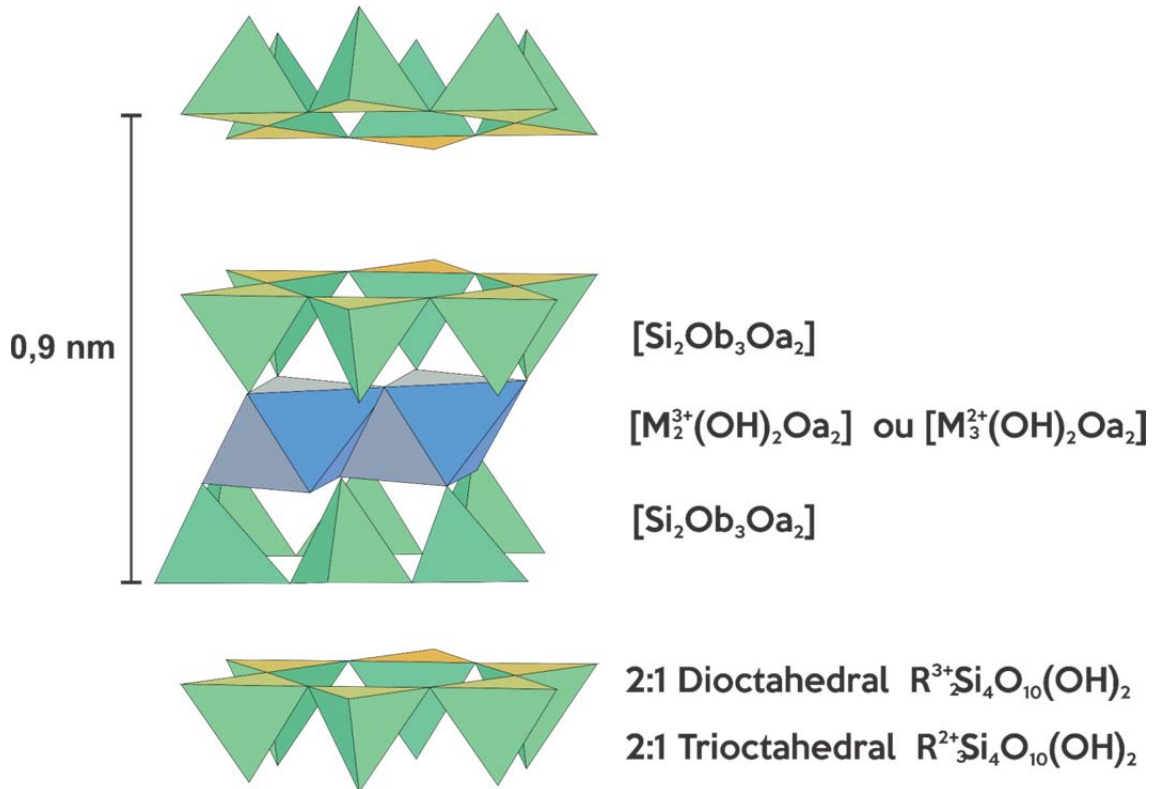


Figure 5 - Clay minerals of the 1:1 and 2:1 type. Oa, Ob are apical and basal oxygens respectively. Adapted from Brigatti (BRIGATTI; GALAN; THENG, 2006).

1.4.1. Kaolinite

Kaolinite has a 1:1 lamellar structure (TO), with a structural formula $\text{Al}_2\text{Si}_2\text{O}_5(\text{OH})_4$ being 10-95% of the kaolin mineral composition (ALABA et al., 2015). Its unit cell is electrically neutral and has between the lamellae a hydroxylic surface from aluminol $[\text{Al}(\text{OH})_3]$, this site being responsible for the interactions. Kaolinite stands out from other clay minerals due to this hydroxylic surface that forms a dense network of hydrogen bonds between the lamellae, resulting in strong cohesion, with a basal spacing of 0.7 nm (DEDZO; DETELLIER, 2016).

Due to this characteristic, this clay mineral was considered for a long time as non-expandable, until Jackson in 1960 studied the intercalation of kaolinite for the qualitative determination of mineral species (JACKSON, 1960). García and Camazano in 1968 demonstrated that it is possible to intercalate kaolinite with highly polar molecules with a low molecular radius, being the first to intercalate kaolinite with dimethylsulfoxide (GONZÁLEZ GARCÍA; SÁNCHEZ CAMAZANO, 1968). After pre-intercalation with DMSO it is possible to intercalate larger molecules for a wide range of applications (HE et al., 2013).

Kaolinite intercalation is the result of weak interactions such as hydrogen bonds and Van der Waals forces between the intercalant and aluminol. Functionalization occurs when there are stronger bonds such as covalent bonding involved in the intercalation process (LETAIEF; DETELLIER, 2011; NGNIE; DEDZO; DETELLIER, 2016; RIBEIRO et al., 2015). Initially, kaolinite is intercalated with small, polar molecules such as dimethylsulfoxide (DMSO), dimethylformamide (DMF), among others, to increase the interlamellar space

for later functionalization with the molecules of interest. The best known method for functionalization is the displacement method, through the displacement of the DMSO from the basal space with the molecule of interest (NGNIE; DEDZO, 2020) (Table 1).

Table 1 - Examples of kaolinite-functionalized materials from our research group and their respective applications.

Functionalized Material	Application	Reference
Eu³⁺ and Tb³⁺ Picolinic acid complexes	Luminescent application	(DE FARIA et al., 2011)
Titanium(IV) isopropoxide	Photodegradation for dyes	(BARBOSA et al., 2015)
Porphyrin	catalyst for oxidation reactions	(BIZAIA et al., 2009)
Fe(III) pyridine-carboxylate complexes	catalyst for oxidation reactions	(DE FARIA et al., 2012)
Me(II)-dipicolinate complexes	degradation of dyes	(ARAÚJO et al., 2014)

However, our research group has been working with a new route for the functionalization of kaolinite through an amidation reaction between amino acids and 3-aminopropyltriethoxysilane alkoxide (APTES) catalyzed by boric acid (DA SILVA et al., 2020; DE ARAÚJO et al., 2020, 2021). The amidation reaction is widely used in the pharmaceutical industry and indispensable for the formation of peptides (BODE, 2015; PATTABIRAMAN; BODE, 2011). This reaction is carried out naturally in living organisms and can be carried out in the laboratory, however, in the synthetic form an activator as a catalyst or high temperatures is necessary, generating many undesirable by-products or contaminating waste. In this context, the boric acid catalyst was chosen because it is low cost, non-

toxic and efficient for the amidation reaction between the amino acid and the alkoxide APTES for the functionalization of kaolinite (DE ARAÚJO et al., 2021).

In previous works, kaolinite was functionalized with APTES and then subjected to an amidation reaction with the amino acid proline (DE ARAÚJO et al., 2020). However, it had low radiative emission yields and large amounts of water molecules in the first coordination sphere, in addition to having low efficiency in modifying the alkoxide with the amino acid. To solve this problem, another route was developed, subjecting APTES and the amino acid to a catalyzed amidation reaction before being functionalized into kaolinite, which raised the optical properties of the material above both the first amidation reaction route and for the synthesis of kaolinite functionalization by the displacement method, offering very promising results for application as a luminescent sensor for contaminants. This is due to the ease of interaction between APTES and the amino acid, without the steric hindrance or competition caused by the presence of kaolinite in the chemical environment. The amidation reaction of the proposed material is shown in Figure 6.

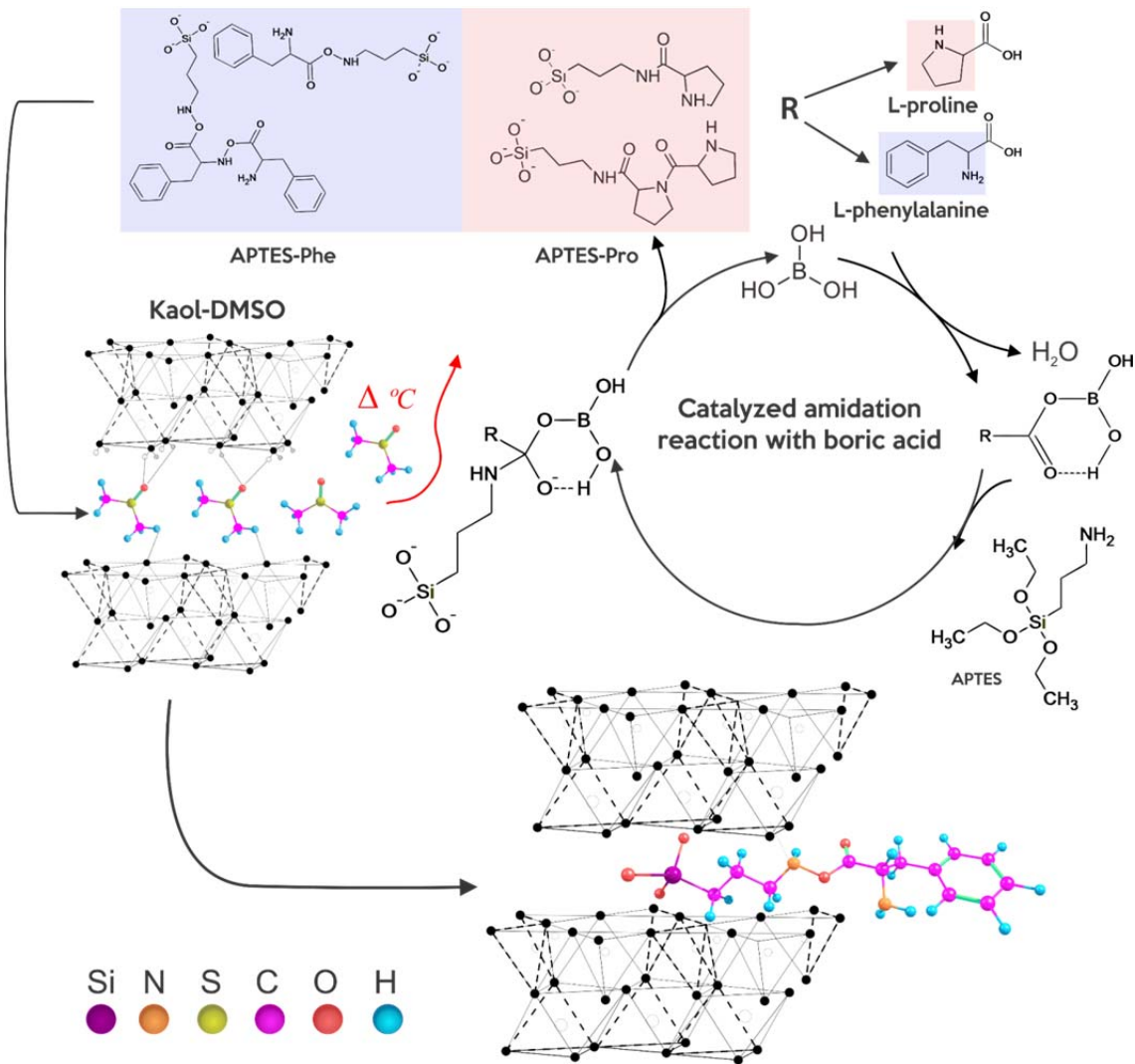


Figure 6 – Schematic representation of kaolinite functionalization by boric acid catalyzed amidation reaction. (DE ARAÚJO et al., 2021)

1.4.2. Lamellar double hydroxides (LDH)

Hydrotalcite is a less abundant anionic clay mineral in nature compared to others, which contains carbonate anions interspersed between layers of double hydroxides of magnesium and aluminum, making them better known as layered double hydroxides (LDH) (CREPALDI; VALIM, 1998). Precisely because they are less abundant in nature and because they are relatively easily synthesized, most HDL works are obtained with the synthetic form of this clay mineral, being represented by the general formula: $[M^{2+}_{1-x}M^{3+}_x(OH)_2 [X^{n-}]_{x/n} \cdot zH_2O]$, where M^{2+} and M^{3+} are bivalent and trivalent metals respectively and X^{n-}

is a anion with charge n^- (RIVES, 2001; SILVA; DUARTE; MEILI, 2021), as shown in figure 7.

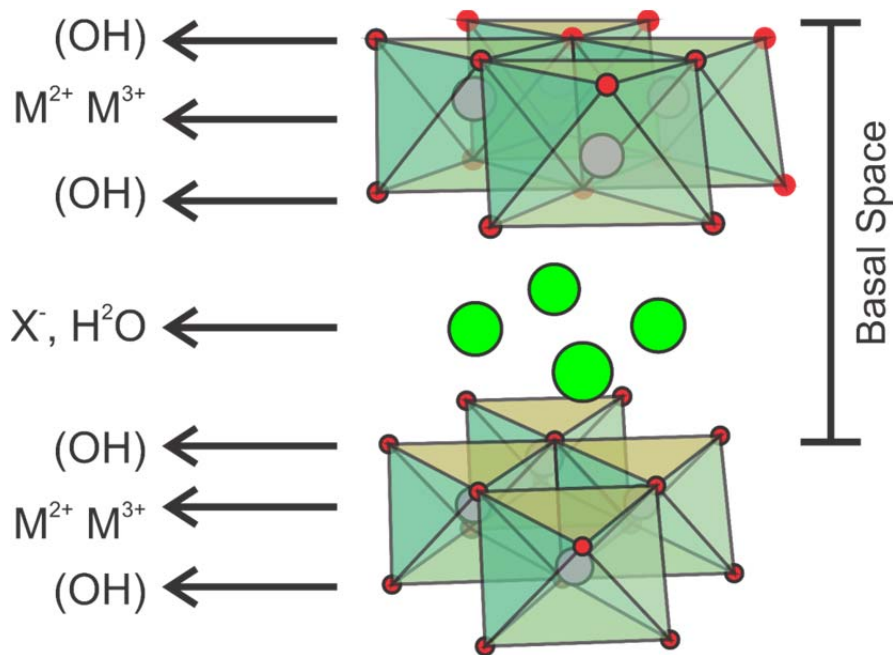


Figure 7 - Structure of the lamellar double hydroxide with the anion intercalated. Adapted from Crepaldi and Rives (CREPALDI; VALIM, 1998; RIVES; ULIBARRI, 1999).

These octahedral layers are neutral and considered to be of the brucite type $[\text{Mg}(\text{OH})_2]$, but when bivalent cations are replaced by trivalent ones, these lamellae become positively charged, requiring interlamellar anions to stabilize the charge. Thus, there are three main methods for intercalation of hydrotalcite: the first is by anion exchange where the interlamellar anions are exchanged by the molecules of interest (OLFS et al., 2009). Another form of intercalation of hydrotalcite is by direct synthesis or co-precipitation where LDH is formed by mixing Mg-Al with a solution of the material to be intercalated (CAMACHO CÓRDOVA et al., 2009; CUNHA et al., 2016; TRAN; LIN; CHAO, 2018). Finally, by the reconstruction method, performed by rehydrating the previously calcined hydrotalcite containing the solution of the molecule to be intercalated (NAKAYAMA; WADA; TSUJIKAWA, 2004; PRAKRUTHI; JAI PRAKASH; BHAT,

2015). The thermal decomposition of LDH species leads to the formation of oxides with specific properties such as the homogeneous distribution at the atomic level of the components, contributing to the so-called "memory effect", where the original structure is recovered after the rehydration of the ex-LDH oxides, as long as the conditions of both heat treatment and rehydration are respected (KOWALIK et al., 2013).

In the context of this work, the intercalation of amino acids in hydrotalcites is hampered by the anion exchange method, because the amino acids remain in the zwitterionic form and are electrically neutral at pH close to 7 (NAKAYAMA; WADA; TSUHAKO, 2004). By the reconstruction method, it is possible to intercalate amino acids under certain conditions. Nakayama and collaborators performed the intercalation of several amino acids to study the ideal intercalation conditions for the reconstruction method (NAKAYAMA; WADA; TSUHAKO, 2004).

They showed that intercalation does not occur when LDH is calcined below 300 °C and phase separation occurs above 700 °C and reconstruction is no longer possible, with the ideal calcination temperature being 500 °C. The reaction is optimized at a temperature of 40 °C and time is relevant in the intercalation process, as very high times promote the subsequent exfoliation and deintercalation of some amino acids, reducing the yield of intercalated material. In this case, the amino acids were classified between the amino acids where dissolution occurs at high reaction times and those that do not have this characteristic as shown in table 2. The first group (Group 1) of amino acids have an ideal intercalation reaction time of 3 hours, these being Gly, Ala, Thr, Pro, Asn, Gln and His. The second group (Group 2), longer times (24 hours) are

more effective for intercalation as there is no dissolution and are constituted by the amino acids Val, Leu, Ile, Phe, Trp, Ser, Cys, Met, Asp and Glu. Intercalation of Lys and Arg amino acids by the reconstruction method were not observed.

Table 2 - Amino acid intercalation in LDH by the reconstruction method where *d* is the basal spacing and LDH(500 °C) is the hydrotalcite calcined at 500 °C. Adapted from Nakayama (NAKAYAMA; WADA; TSUHAKO, 2004).

Amino acids	<i>d</i> (Å)	Yield in mmol per 0.56 g LDH(500 °C)
Grupo 1		
Gly	7,8	2,5
Ala	7,8	2,6
Thr	7,8	2,4
Pro	7,8	2,7
Asn	7,8	1,3
Gln	7,8	0,9
His	17,5	2,6
Grupo 2		
Val	12,2	3,0
Leu	14,6	2,4
Ile	14,0	2,1
Phe	16,0	2,6
Trp	20,0	2,1
Ser	7,8	2,6
Cys	7,8	1,7
Met	15,3	2,6
Asp	7,8	1,3
Glu	7,8	1,3

As shown in table 2, amino acids with a highly hydrophobic R group, the molecular arrangement stabilizes in the form of monolayers, while for the other amino acids the structure is stabilized in parallel with the layers of hydrotalcite.

Amino acids can also be intercalated by the co-precipitation method (AISAWA et al., 2001; TRAN; LIN; CHAO, 2018). For this type of intercalation,

pH is a determining factor, as LDHs, as already discussed, have a high charge density, facilitating the coexistence of other anions, especially (OH^- and NO_3^-) and the concentration of these ions increases with pH. For amino acid intercalation by this method, the ideal pH observed by Aisawa and collaborators for Mg-Al hydrotalcites was 10, in addition to observing that the amino acid conformation depends on the metals (M^{2+} and M^{3+}) contained in hydrotalcite, where with Mg-Al LDH the amino acids stabilize in the form of monolayers while in hydrotalcites containing Mn, Zn, among others, they stabilize in parallel to the layers (AISAWA et al., 2001), as shown in figure 8. This is due to the electrostatic force between the negative charge of the amino acid and the metallic layer of LDH, interfering with the orientation of the amino acid in the interlamellar space, causing the amino acid to change its orientation in order to compensate for the positive charge in the basal space.

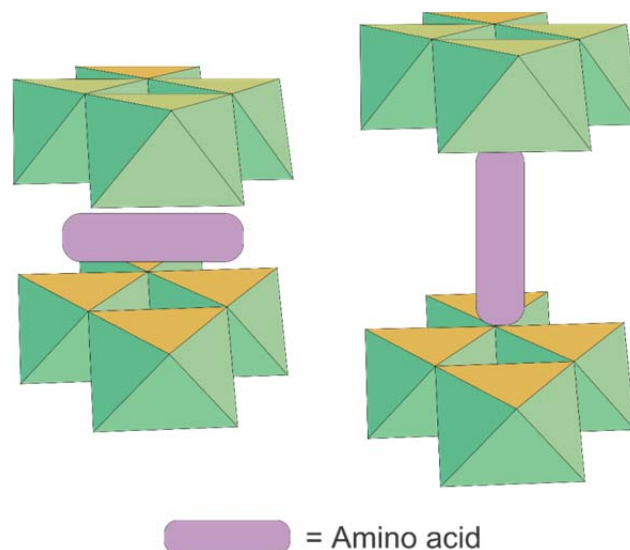


Figure 8 - Schematic representation of amino acid conformation in hydrotalcite. (Font: author)

1.4.3. Saponite and LAPONITE®

Both saponite and LAPONITE® are phyllosilicates belonging to the smectites group, with a 2:1 lamellar structure (TOT), with two tetrahedral and

one octahedral sheets, with high surface area and electrically positive charges that offer high cation exchange capacities (BISIO; CARNIATO; GATTI, 2020; DAS et al., 2019; GHADIRI et al., 2014). Both can be found in nature as in the composition of bentonite, for example, or easily synthesized in the laboratory, and these are the most common form used due to their purity, crystallinity and the possibility of stoichiometric control.

Saponite has a trioctahedral structure with small isomorphous substitutions of Si^{4+} for Al^{3+} (or other M^{3+} cations) in the tetrahedral layer generating negative charges in the surface layer, which is compensated by exchangeable cations such as Na^+ , NH_4^+ , K^+ , Li^+ or Mg^{2+} , as shown in figure 9. Its structural formula consists of $\text{M}_{x/z}^{\text{Z}+}[\text{Mg}_6][\text{Si}_{8-x}\text{Al}_x]\text{O}_{20}(\text{OH})_4 \cdot n\text{H}_2\text{O}$ where $\text{M}^{\text{Z}+}$ represents the interlamellar cations and the x ranging between 0.4 and 1.2 (BISIO; CARNIATO; GATTI, 2020; TRUJILLANO et al., 2011).

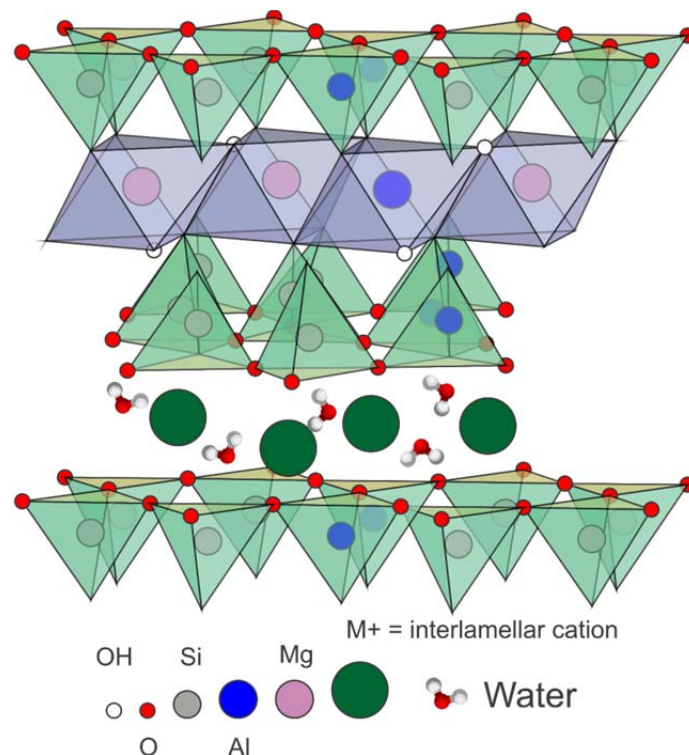


Figure 9 - Schematic representation of the saponite. (Font: author)

LAPONITE® is a synthetic clay mineral like hectorite, with morphology of plates in the form of disks with diameters of 25-30 nm and thickness of 1 nm (Figure 10-b). The substitution of Li^+ by Mg^{2+} in the octahedral layer is responsible for the negative residual charge that is compensated by interlamellar cations. Its structural formula is $\text{M}^+_x[\text{Si}_8\text{Mg}_{5,5}\text{Li}_{0,3}\text{O}_{20}(\text{OH})_4]^{-x}$ where M^+ is the interlamellar cation, as shown in figure 10.

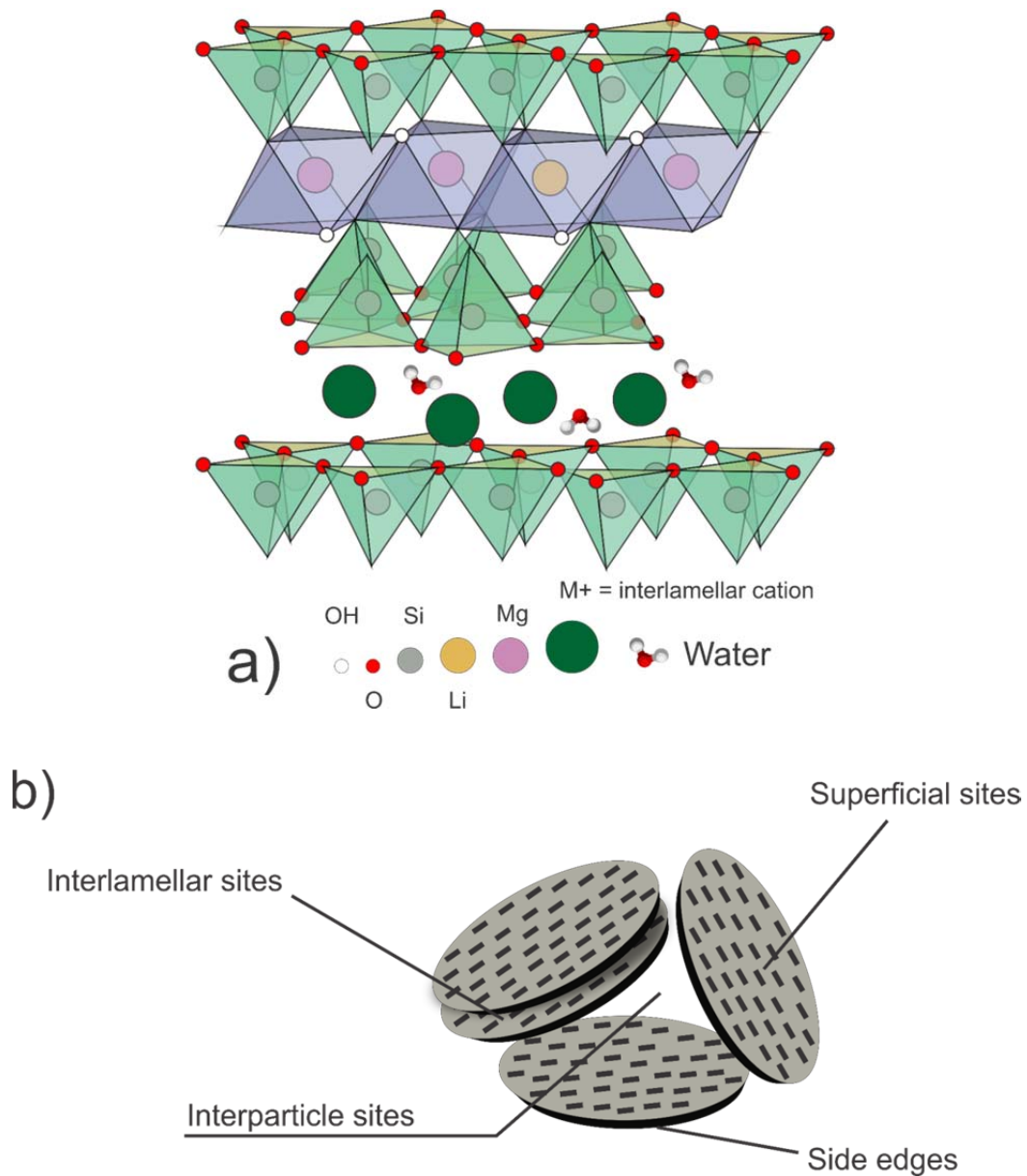


Figure 10 - a) Schematic representation of LAPONITE® and b) interaction sites. Adapted from (DAS et al., 2019).

As shown in figure 10-b, these clay minerals can interact or undergo modifications in different structural domains, the main modification strategies being by particle size modification, cation exchange between interlayer ions or by chemical modification of the lamella composition by others metal ions (BISIO; CARNIATO; GATTI, 2020).

In the context of this work, lanthanide ions can be incorporated into these clay minerals in two main ways: the first is by direct doping of the ion into the lamellar structure of the clay (MARCHESI et al., 2021a; SÁNCHEZ et al., 2006; TERTRE et al., 2006; TRONTO et al., 2009). The other way is through the intercalation of Ln^{3+} organo-complexes, which is the most used due to the expandable characteristic of smectites (LI et al., 2014; LI; LI, 2021; RYU et al., 2014; SILVA et al., 2018; WANG et al., 2019). Another less common route is by decreasing the particle size, separating the clay mineral into isolated layers (delamination) and incorporating luminescent complexes by covalent bonds (MA et al., 2019). Therefore, the intercalation of Eu^{3+} complexes with amino acids was chosen for this work due to the ease, versatility and low cost of the synthesis of obtaining these hybrid materials for application as contaminant sensors. These amino acids can interact with the complex and after being intercalated in the matrix (saponite and LAPONITE®) or the amino acid is previously functionalized in the matrix (LDH and kaolinite) and then interacts with Eu^{3+} in the formation of luminescent complexes.

1.5. Objectives

This work aims the synthesis of hybrid materials, prepared by the intercalation/functionalization of clay minerals with amino acids proline and

phenylalanine complexed with the Eu^{3+} ion and the application of these materials as fingerprint detectors, as adsorbent material and luminescent sensors of Cr^{3+} , caffeine and estrogen (β -estradiol) in aqueous phase.

Four different types of clay minerals were used, these being kaolinite, hydrotalcite, saponite and LAPONITE®, covering neutral, cationic and anionic clays, of natural (kaolinite) and synthetic origin.

The specific objectives for obtaining hybrid materials using kaolinite are:

1. Purification of natural kaolinite;
2. Expansion of the interlamellar space through intercalation with dimethylsulfoxide (DMSO);
3. Functionalization of kaolinite with the amino acids proline and phenylalanine by the DMSO displacement method (direct synthesis);
4. Functionalization of kaolinite with 3-aminopropyltriethoxysilane alkoxide (APTES) with the amino acids proline and phenylalanine through boric acid catalyzed amidation reaction;

To obtain hybrid materials with hydrotalcite, three routes are used, however, as already discussed, the ion exchange synthesis is hampered due to the zwitterionic characteristic of amino acids. Therefore, the specific objectives for obtaining materials with HDL are:

1. Synthesize pure hydrotalcite from Mg-Al in hydrothermal reactor;
2. Intercalate the amino acids proline and phenylalanine by the reconstruction method;

3. Intercalate the amino acids proline and phenylalanine by the co-precipitation method;

After the synthesized materials, to provide the luminescent properties in these materials the proposed objectives are:

1. Complex the Eu^{3+} ion in all samples containing the amino acids and study its properties (emission and excitation, lifetimes, quantum yield and amounts of water molecules in the first coordination sphere of the complexes);
2. Add the secondary ligand tenoyltrifluoroacetate (tta) to remove water molecules and improve charge transfer capacity between ligands to the central ion Eu^{3+} .

And finally, the specific objectives for obtaining hybrid materials with LAPONITE® and saponite are:

1. Obtaining pure saponite by microwave synthesis;
2. Complexation of the Eu^{3+} ion with the amino acids proline and phenylalanine;
3. Intercalation of complexes in LAPONITE® and saponite;
4. Addition of the secondary ligand tenoyltrifluoroacetate (tta) in the resulting materials.

After the preparation of all hybrid materials complexed to Eu^{3+} ion, the objective is their application in the sensing of Cr^{3+} , caffeine and estrogen contaminants by luminescence spectroscopy. Therefore, the specific goals for luminescent sensors are:

1. Perform contaminant calibration curve for later quantification;
2. Carry out a kinetic study of adsorption of contaminants in the hybrid materials obtained;
3. After identifying the maximum adsorption capacity, carry out an equilibrium study of the samples where it was possible to quantify the contaminants;
4. Analyze the radioactive emission of the samples with contaminants and evaluate their sensing capacity through the quenching effect in the interaction process of the samples with the contaminants;
5. Analyze luminescent properties for application as fingerprint detectors.

1.6. Materials and reagents use

- 17 β -estradiol 98% - Sigma-Aldrich;
- 2-thenoyltrifluoroacetone (tta) 99,0% - Aldrich
- 3-aminopropyltriethoxysilane (APTES) 97% - Synth;
- Boric Acid – Dinâmica Ltda;
- Distilled water;
- Ethyl alcohol P.A. 95,0% - Synth;
- Sodium Bicarbonate P.A. 99,9% - Synth
- Caffeine P.A. – Sigma-Aldrich;
- Kaolinite, São Simão, Mineradora Darcy R. O. Silva (Previously characterized in the group by DE FARIA et al., 2009, 2011);
- Aluminum chloride hexahydrate (AlCl₃·6H₂O) P.A. – Synth;

- Chromium chloride hexahydrate ($\text{CrCl}_3 \cdot 6\text{H}_2\text{O}$) P.A. - Sigma-Aldrich;
- Magnesium chloride hexahydrate ($\text{MgCl}_2 \cdot 6\text{H}_2\text{O}$) P.A. - Synth
- Dimethylsulfoxide (DMSO) P.A. 99,9% - Synth;
- Sodium hydroxide P.A.- Synth;
- LAPONITE® RD - BYK Additives
- L-phenylalanine – Sigma-Aldrich;
- L-proline – Sigma-Aldrich;
- Sodium metasilicate (Na_2SiO_3) - Sigma-Aldrich;
- Methylbenzene (Toluene)99,9% - J.T. Baker;
- Europium Oxide P.A. – Sigma-Aldrich;

1.7. References

AISAWA, S. et al. Direct Intercalation of Amino Acids into Layered Double Hydroxides by Coprecipitation. **Journal of Solid State Chemistry**, v. 162, n. 1, p. 52–62, nov. 2001.

ALABA, P. A. et al. Kaolinite properties and advances for solid acid and basic catalyst synthesis. **RSC Advances**, v. 5, p. 101127–101147, 2015.

ARAÚJO, F. R. et al. Versatile heterogeneous dipicolinate complexes grafted into kaolinite: Catalytic oxidation of hydrocarbons and degradation of dyes. **Catalysis Today**, v. 227, p. 105–115, maio 2014.

ATTIA, M. S. et al. Spectrofluorimetric assessment of chlorzoxazone and ibuprofen in pharmaceutical formulations by using Eu-Tetracycline HCl optical sensor doped in sol-gel matrix. **Journal of Fluorescence**, v. 22, n. 2, p. 779–788, 2012.

ATTIA, M. S.; DIAB, M.; EL-SHAHAT, M. F. Diagnosis of some diseases related to the histidine level in human serum by using the nano optical sensor Eu-Norfloxacin complex. **Sensors and Actuators, B: Chemical**, v. 207, n. PartA, p. 756–763, 2014.

BARBOSA, L. V. et al. Kaolinite-titanium oxide nanocomposites prepared via sol-gel as heterogeneous photocatalysts for dyes degradation. **Catalysis**

Today, v. 246, p. 133–142, maio 2015.

BARJA, B. C.; ARAMENDÍA, P. F. Luminescent Eu(III) hybrid materials for sensor applications. **Photochemical & photobiological**, v. 7, n. 11, p. 1391–1399, 2008.

BELTRÁN-LEIVA, M. J. et al. Theoretical Method for an Accurate Elucidation of Energy Transfer Pathways in Europium(III) Complexes with Dipyrrophenazine (dppz) Ligand: One More Step in the Study of the Molecular Antenna Effect. **Inorganic Chemistry**, v. 56, n. 15, p. 9200–9208, 7 ago. 2017.

BISIO, C.; CARNIATO, F.; GATTI, G. An overview of the recent synthesis and functionalization methods of saponite clay. **New Journal of Chemistry**, v. 44, n. 24, p. 9969–9980, 2020.

BIZAIA, N. et al. Porphyrin-kaolinite as efficient catalyst for oxidation reactions. **ACS Applied Materials & Interfaces**, v. 1, n. 11, p. 2667–2678, 2009.

BOCHEŃSKA, P.; PYKA, A. Use of TLC for the quantitative determination of acetylsalicylic acid, caffeine, and ethoxybenzamide in combined tablets. **Journal of Liquid Chromatography & Related Technologies**, v. 36, n. 17, p. 2405–2421, 21 out. 2013.

BODE, J. W. Rh(III)- and Ir(III)-Catalyzed C–C Bond Cross Couplings from C–H Bonds. **Topics in Organometallic Chemistry**, v. 48, n. June 2009, p. 11533–11542, 2015.

BODMAN, S. E.; BUTLER, S. J. Advances in anion binding and sensing using luminescent lanthanide complexes. **Chemical Science**, v. 12, n. 8, p. 2716–2734, 2021.

BRIGATTI, M. F.; GALAN, E.; THENG, B. K. G. Chapter 2 Structures and Mineralogy of Clay Minerals. In: BERGAYA, F.; THENG, B. K. G.; LAGALY, G. (Eds.). **Developments in Clay Science**. Elsevier Ltd, 2006. v. 1p. 19–86.

BÜNZLI, J.-C. G. On the design of highly luminescent lanthanide complexes. **Coordination Chemistry Reviews**, v. 293–294, p. 19–47, 2015.

BÜNZLI, J.-C. G. Lanthanide Luminescence: From a Mystery to Rationalization, Understanding, and Applications. In: JEAN-CLAUDE G. BÜNZLI; VITALIJ K. PECHARSKY (Eds.). **Handbook on the Physics and Chemistry of Rare Earths**. Elsevier Ltd, 2016. v. 50p. 141–176.

BUNZLI, J.-C. G.; PIGUET, C. Taking advantage of luminescent lanthanide ions. **Chemical Society Reviews**, v. 34, n. 12, p. 1048–1077, 2005.

CAMACHO CÓRDOVA, D. I. et al. Immobilization of laccase on hybrid layered double hydroxide. **Química Nova**, v. 32, n. 6, p. 1495–1499, 2009.

CHATTERJEE, S. et al. Design of Multifunctional Fluorescent Hybrid Materials Based on SiO₂ Materials and Core–Shell Fe₃O₄@SiO₂ Nanoparticles for Metal Ion Sensing. **Small**, v. 15, n. 44, p. 1904569, out. 2019.

CHATTERJEE, S. et al. Dendritic Fibrous Nanosilica Hybrid Materials with Near-Infrared Emission as Multifunctional Sensors for Toxic Pollutants. **Advanced Sustainable Systems**, v. 5, n. 1, p. 2000220, 19 jan. 2021.

CHEN, X.; XU, Y.; LI, H. Lanthanide organic/inorganic hybrid systems: Efficient sensors for fluorescence detection. **Dyes and Pigments**, v. 178, n. February, p. 108386, jul. 2020.

CREPALDI, E. L.; VALIM, J. B. Hidróxidos duplos lamelares: síntese, estrutura, propriedades e aplicações. **Química Nova**, v. 21, n. 3, p. 300–311, jun. 1998.

CUNHA, V. R. R. et al. Accessing the biocompatibility of layered double hydroxide by intramuscular implantation: histological and microcirculation evaluation. **Scientific Reports**, v. 6, n. 1, p. 30547, 2 set. 2016.

DA SILVA, A. F. et al. Immobilization of L-alanine into natural kaolinite via amidation catalyzed by boric acid for the development of biohybrid materials. **Journal of Solid State Chemistry**, v. 287, n. April, p. 121332, jul. 2020.

DAS, S. S. et al. Laponite-based Nanomaterials for Biomedical Applications: A Review. **Current Pharmaceutical Design**, v. 25, n. 4, p. 424–443, 3 jun. 2019.

DE ARAÚJO, D. T. et al. Luminescent properties of biohybrid (kaolinite-proline) materials synthesized by a new boric acid catalyzed route and complexed to Eu³⁺. **Applied Clay Science**, v. 192, n. April, p. 105634, jul. 2020.

DE ARAÚJO, D. T. et al. Grafting of L-proline and L-phenylalanine amino acids on kaolinite through synthesis catalyzed by boric acid. **Applied Surface Science Advances**, v. 4, n. December 2020, p. 100081, jun. 2021.

DE CASTRO SILVA, F. et al. A comparative study of alanine adsorption and condensation to peptides in two clay minerals. **Applied Clay Science**, v. 192, n. April, p. 105617, 2020.

DE FARIA, E. H. et al. Hybrid materials prepared by interlayer functionalization of kaolinite with pyridine-carboxylic acids. **Journal of Colloid and Interface Science**, v. 335, n. 2, p. 210–215, jul. 2009.

DE FARIA, E. H. **Estudo das Propriedades Luminescentes e Catalíticas de Materiais Híbridos Obtidos pela Funcionalização de uma Caulinita Natural com Complexos de Ácidos Carboxílicos.** Emerson

Henrique de Faria. Universidade de Franca, 2011.

DE FARIA, E. H. et al. New Highly Luminescent Hybrid Materials: Terbium Pyridine–Picolinate Covalently Grafted on Kaolinite. **ACS Applied Materials & Interfaces**, v. 3, n. 4, p. 1311–1318, 27 abr. 2011.

DE FARIA, E. H. et al. Green and selective oxidation reactions catalyzed by kaolinite covalently grafted with Fe(III) pyridine-carboxylate complexes. **Catalysis Today**, v. 187, n. 1, p. 135–149, jun. 2012.

DEBLONDE, T.; COSSU-LEGUILLE, C.; HARTEMANN, P. Emerging pollutants in wastewater: A review of the literature. **International Journal of Hygiene and Environmental Health**, v. 214, n. 6, p. 442–448, nov. 2011.

DEDZO, G. K.; DETELLIER, C. Functional nanohybrid materials derived from kaolinite. **Applied Clay Science**, 2015.

FLINT, S. et al. Bisphenol A exposure, effects, and policy: A wildlife perspective. **Journal of Environmental Management**, v. 104, p. 19–34, ago. 2012.

GAO, R.; KODAIMATI, M. S.; YAN, D. Recent advances in persistent luminescence based on molecular hybrid materials. **Chemical Society Reviews**, v. 50, n. 9, p. 5564–5589, 2021.

GAVRILESCU, M. et al. Emerging pollutants in the environment: present and future challenges in biomonitoring, ecological risks and bioremediation. **New Biotechnology**, v. 32, n. 1, p. 147–156, jan. 2015.

GHADIRI, M. et al. Layered silicate clay functionalized with amino acids: wound healing application. **RSC Advances**, v. 4, n. 67, p. 35332–35343, 2014.

GIRÓN, J.; ALAIZ, M.; VIOQUE, E. High-performance liquid chromatographic determination of n-ε-(2-propenal)lysine in biological samples after derivatization with diethylethoxymethylenemalonate. **Analytical Biochemistry**, v. 206, n. 1, p. 155–160, out. 1992.

GONZÁLEZ GARCÍA, S.; SÁNCHEZ CAMAZANO, M. Differentiation of kaolinite from chlorite by treatment with dimethyl-sulphoxide. **Clay Minerals**, v. 7, n. 4, p. 447–450, 9 dez. 1968.

H.A. JAHN AND E. TELLER. Stability of polyatomic molecules in degenerate electronic states - I—Orbital degeneracy. **Proceedings of the Royal Society of London. Series A - Mathematical and Physical Sciences**, v. 161, n. 905, p. 220–235, 15 jul. 1937.

HE, H. et al. Silylation of clay mineral surfaces. **Applied Clay Science**, v. 71, p. 15–20, 2013.

HESPANHOL, I. Reúso potável direto e o desafio dos poluentes emergentes. **Revista USP**, n. 106, p. 79, 2 set. 2015.

HOCQUET, D.; MULLER, A.; BERTRAND, X. What happens in hospitals does not stay in hospitals: antibiotic-resistant bacteria in hospital wastewater systems. **Journal of Hospital Infection**, v. 93, n. 4, p. 395–402, ago. 2016.

HUGGETT, J. M. Clay Minerals. In: **Reference Module in Earth Systems and Environmental Sciences**. Elsevier, 2015. p. 358–365.

JACKSON, M. L. Significance of Kaolinite Intersalation in Clay Mineral Analysis. **Clays and Clay Minerals**, v. 9, n. 1, p. 424–430, 1960.

JIA, P. et al. Selective sensing of Fe^{3+} ions in aqueous solution by a biodegradable platform based lanthanide metal organic framework. **Spectrochimica Acta Part A: Molecular and Biomolecular Spectroscopy**, v. 230, p. 118084, abr. 2020.

JIANG, G. et al. Luminescent $\text{La}_2\text{O}_2\text{S}:\text{Eu}^{3+}$ nanoparticles as non-contact optical temperature sensor in physiological temperature range. **Materials Letters**, v. 143, p. 98–100, 2015.

KOTOVA, O.; COMBY, S.; GUNNLAUGSSON, T. Sensing of biologically relevant d-metal ions using a Eu(III)-cyclen based luminescent displacement assay in aqueous pH 7.4 buffered solution. **Chemical communications**, v. 47, p. 6810–6812, 2011.

KOWALIK, P. et al. Memory effect of the CuZnAl-LDH derived catalyst precursor—In situ XRD studies. **Applied Catalysis A: General**, v. 464–465, p. 339–347, ago. 2013.

KOZAK, M. et al. Luminescent Temperature Sensor Material Based on an Eu(III) β -Diketonate Complex Incorporated into Cellulose Triacetate. **Journal of Applied Spectroscopy**, v. 81, n. 4, p. 678–683, 9 set. 2014.

LETAIEF, S.; DETELLIER, C. Application of thermal analysis for the characterisation of intercalated and grafted organo-kaolinite nanohybrid materials. **Journal of Thermal Analysis and Calorimetry**, v. 104, n. 3, p. 831–839, 2011.

LI, H. et al. Luminescent hybrid materials based on laponite clay. **Chemistry - A European Journal**, v. 20, n. 33, p. 10392–10396, 2014.

LI, P.; LI, H. Recent progress in the lanthanide-complexes based luminescent hybrid materials. **Coordination Chemistry Reviews**, v. 441, p. 213988, ago. 2021.

LIU, M. et al. Development of a ratiometric time-resolved luminescence sensor for pH based on lanthanide complexes. **Analytica Chimica Acta**, v.

761, p. 149–156, 2013.

MA, J. et al. Luminescent materials of covalent grafting lanthanide complexes to the synthetic clays. **Journal of Luminescence**, v. 212, n. November 2018, p. 126–132, 2019.

MARCHESI, S. et al. Bifunctional Europium(III) and Niobium(V)-Containing Saponite Clays for the Simultaneous Optical Detection and Catalytic Oxidative Abatement of Blister Chemical Warfare Agents. **Chemistry – A European Journal**, v. 27, n. 14, p. 4723–4730, 8 mar. 2021.

MOORE, J. D. et al. Concentration-independent pH detection with a luminescent dimetallic Eu(III)-based probe. **Journal of the American Chemical Society**, v. 134, n. 42, p. 17372–17375, 2012.

NAKAGAKI, S.; BENEDITO, F. L.; WYPYCH, F. Anionic iron(III) porphyrin immobilized on silanized kaolinite as catalyst for oxidation reactions. **Journal of Molecular Catalysis A: Chemical**, v. 217, n. 1–2, p. 121–131, 2004.

NAKAYAMA, H.; WADA, N.; TSUHAKO, M. Intercalation of amino acids and peptides into Mg-Al layered double hydroxide by reconstruction method. **International Journal of Pharmaceutics**, v. 269, n. 2, p. 469–478, 2004.

NGNIE, G.; DEDZO, G. K. A template approach for the multifunctionalization of the interlayer space of kaolinite. **Applied Clay Science**, v. 198, n. June, p. 105858, nov. 2020.

NGNIE, G.; KENNE DEDZO, G.; DETELLIER, C. Synthesis and catalytic application of palladium nanoparticles supported on kaolinite-based nanohybrid materials. **Dalton Transactions**, 2016.

NOVOTNIK, B. et al. Cytotoxic and genotoxic potential of Cr(VI), Cr(III)-nitrate and Cr(III)-EDTA complex in human hepatoma (HepG2) cells. **Chemosphere**, v. 154, p. 124–131, jul. 2016.

OLFS, H.-W. et al. Comparison of different synthesis routes for Mg–Al layered double hydroxides (LDH): Characterization of the structural phases and anion exchange properties. **Applied Clay Science**, v. 43, n. 3–4, p. 459–464, mar. 2009.

PATTABIRAMAN, V. R.; BODE, J. W. Rethinking amide bond synthesis. **Nature**, v. 480, n. 7378, p. 471–9, 2011.

PEÑA-GUZMÁN, C. et al. Emerging pollutants in the urban water cycle in Latin America: A review of the current literature. **Journal of Environmental Management**, v. 237, n. December 2018, p. 408–423, maio 2019.

PRAKRUTHI, H. R.; JAI PRAKASH, B. S.; BHAT, Y. S. Microwave

assisted synthesis of glycerol carbonate over LDH catalyst: Activity restoration through rehydration and reconstruction. **Journal of Molecular Catalysis A: Chemical**, v. 408, p. 214–220, nov. 2015.

PUSHKAR, B. et al. Chromium pollution and its bioremediation mechanisms in bacteria: A review. **Journal of Environmental Management**, v. 287, n. February, p. 112279, jun. 2021.

RIBEIRO, A. R. et al. An overview on the advanced oxidation processes applied for the treatment of water pollutants defined in the recently launched Directive 2013/39/EU. **Environment international**, v. 75, p. 33–51, 2015.

RIVES, V. **Layered Double Hydroxides: Present And Future**. 1st. ed. New York: Nova Science Publishers, 2001.

RIVES, V.; ULIBARRI, M. A. Layered double hydroxides (LDH) intercalated with metal coordination compounds and oxometalates. **Coordination Chemistry Reviews**, v. 181, n. 1, p. 61–120, 1999.

RYU, S. J. et al. Photoluminescent europium(III) complex intercalated in natural and synthetic clay minerals for enhanced latent fingerprint detection. **Applied Clay Science**, v. 101, p. 52–59, 2014.

SÁNCHEZ, A. et al. Intercalation of Europium (III) species into bentonite. **Materials Research Bulletin**, v. 41, n. 6, p. 1185–1191, jun. 2006.

SIGOLI, F. A. et al. Luminescence of Eu(III)β-diketone complex supported on functionalized macroporous silica matrix. **International Journal of Inorganic Materials**, v. 3, n. 7, p. 755–762, 2001.

SILVA, A. F. DA; DUARTE, J. L. DA S.; MEILI, L. Different routes for MgFe/LDH synthesis and application to remove pollutants of emerging concern. **Separation and Purification Technology**, v. 264, n. January, p. 118353, jun. 2021.

SILVA, J. M. et al. New organic-inorganic hybrid composites based on cellulose nanofibers and modified Laponite. **Advanced Optical Technologies**, v. 7, n. 5, p. 327–334, 2018.

SOUZA, A. S.; COUTO DOS SANTOS, M. A. The J-mixing effect in Ln³⁺ ions crystal field levels. **Chemical Physics Letters**, v. 521, p. 138–141, jan. 2012.

STUMPF, M. et al. Polar drug residues in sewage and natural waters in the state of Rio de Janeiro, Brazil. **Science of The Total Environment**, v. 225, n. 1–2, p. 135–141, jan. 1999.

TAN, H.; LIU, B.; CHEN, Y. Lanthanide Coordination Polymer Nanoparticles for Sensing of Mercury(II) by Photoinduced Electron Transfer.

ACS Nano, v. 6, n. 12, p. 10505–10511, 21 dez. 2012.

TERTRE, E. et al. Europium retention onto clay minerals from 25 to 150°C: Experimental measurements, spectroscopic features and sorption modelling. **Geochimica et Cosmochimica Acta**, v. 70, n. 18, p. 4563–4578, set. 2006.

TRAN, H. N.; LIN, C.-C.; CHAO, H.-P. Amino acids-intercalated Mg/Al layered double hydroxides as dual-electronic adsorbent for effective removal of cationic and oxyanionic metal ions. **Separation and Purification Technology**, v. 192, p. 36–45, fev. 2018.

TRONTO, J. et al. Visible and near-infrared luminescent Eu³⁺ or Er³⁺ doped laponite-derived xerogels and thick films: Structural and spectroscopic properties. **Materials Chemistry and Physics**, v. 113, n. 1, p. 71–77, jan. 2009.

TRUJILLANO, R. et al. Rapid microwave-assisted synthesis of saponites and their use as oxidation catalysts. **Applied Clay Science**, v. 53, n. 2, p. 326–330, 2011.

TUREL, M. et al. Direct UV-LED lifetime pH sensor based on a semi-permeable sol-gel membrane immobilized luminescent Eu³⁺ chelate complex. **Sensors and Actuators, B: Chemical**, v. 131, n. 1, p. 247–253, 2008.

VARGAS-BERRONES, K. et al. Emerging pollutants (EPs) in Latin América: A critical review of under-studied EPs, case of study -Nonylphenol-. **Science of The Total Environment**, v. 726, p. 138493, jul. 2020.

WAINIPEE, W. et al. The effects of oil on As(V) adsorption on illite, kaolinite, montmorillonite and chlorite. **Geochimica et Cosmochimica Acta**, v. 121, p. 487–502, 2013.

WANG, H. et al. Analysis of phenolic pollutants in human samples by high performance capillary electrophoresis based on pretreatment of ultrasound-assisted emulsification microextraction and solidification of floating organic droplet. **Journal of Chromatography A**, v. 1253, p. 16–21, ago. 2012.

WANG, K. M. et al. Multifunctional chemical sensors and luminescent thermometers based on lanthanide metal-organic framework materials. **CrystEngComm**, v. 18, n. 15, p. 2690–2700, 2016.

WANG, S. et al. Organic/inorganic hybrid sensors: A review. **Sensors and Actuators B: Chemical**, v. 182, p. 467–481, jun. 2013.

WANG, Y. et al. Recent progress in luminescent materials based on lanthanide complexes intercalated synthetic clays. **Journal of Rare Earths**, v. 37, n. 5, p. 451–467, 2019.

WHITTAKER, M. L. et al. Ion exchange selectivity in clay is controlled by nanoscale chemical–mechanical coupling. **Proceedings of the National Academy of Sciences**, v. 116, n. 44, p. 22052–22057, 29 out. 2019.

YANG, G. et al. Applications of MOFs as Luminescent Sensors for Environmental Pollutants. **Small**, v. 17, n. 22, p. 2005327, 26 jun. 2021.

YOOSEFIAN, M. et al. Ultra-low concentration protein detection based on phenylalanine–Pd/SWCNT as a high sensitivity nanoreceptor. **RSC Advances**, v. 10, n. 5, p. 2650–2660, 2020.

ZHAI, D. et al. Mesoporous silica equipped with europium-based chemosensor for mercury ion detection: Synthesis, characterization, and sensing performance. **Inorganica Chimica Acta**, v. 387, p. 396–400, 2012.

ZHAN, Z. et al. A water-stable europium-MOF as a multifunctional luminescent sensor for some trivalent metal ions (Fe^{3+} , Cr^{3+} , Al^{3+}), PO_4^{3-} ions, and nitroaromatic explosives. **Dalton Transactions**, v. 48, n. 5, p. 1786–1794, 2019.

ZHANG, Q. et al. Facile and controllable synthesis of hydroxyapatite/graphene hybrid materials with enhanced sensing performance towards ammonia. **The Analyst**, v. 140, n. 15, p. 5235–5242, 2015.

ZHOU, X.-H. et al. A flexible Eu(III)-based metal-organic framework: turn-off luminescent sensor for the detection of Fe(III) and picric acid. **Dalton transactions**, v. 42, n. 34, p. 12403–9, 2013.

2. Chapter 2 - Experimental

The hybrid materials that were used as luminescent contaminant sensors were obtained by intercalation/functionalization of clay minerals with complexes of europium (III) with amino acids proline and phenylalanine. Four clay minerals with different properties were used, namely kaolinite, hydrotalcite, LAPONITE® and saponite and the procedures for obtaining these materials are described in detail below.

2.1. Kaolinite materials

The experimental procedures for obtaining samples with kaolinite are shown in Figure 11:

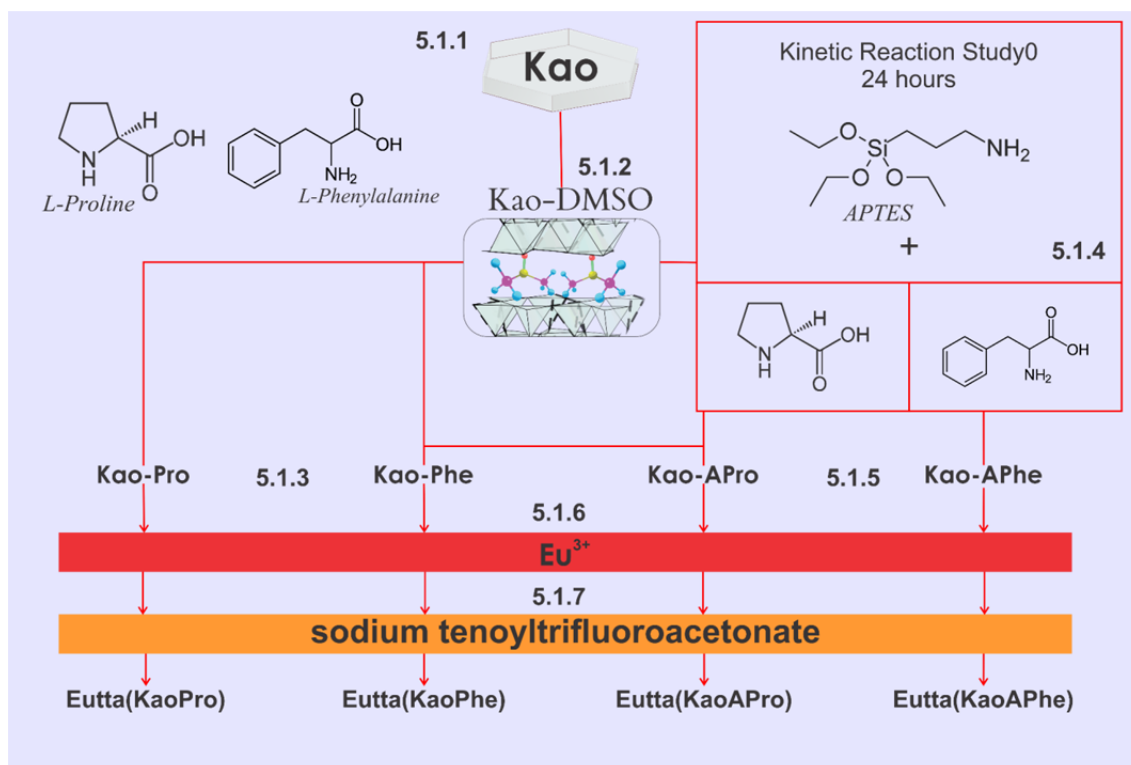


Figure 11 - Flowchart of experimental procedures for samples with kaolinite.

2.1.1. Purified kaolinite

The kaolinite samples used in this work come from São Simão, in the state of São Paulo, Brazil and were supplied by Darcy R.O. Silva and Co. (São Simão-SP, Brazil). To purify the material, the dispersion and sedimentation of natural clay in distilled water was performed, according to Stokes' Law, widely reported in the literature (AVILA et al., 2010; DE FARIA et al., 2009). The samples showed high purity content, particle size close to 2 μm , light color, high plasticity, thermal resistance and high percentage of hexagonal structure (DE ARAÚJO et al., 2021; DE FARIA, 2011; DE FARIA et al., 2012). Kaolinite had the following chemical formula: $\text{Si}_{2.04}\text{Al}_{2.00}\text{Fe}_{0.03}\text{Mg}_{0.01}\text{K}_{0.02}\text{Ti}_{0.04}\text{O}_{7.23}$, close to literature (DE ARAUJO et al., 2017), with specific surface area of 17 m^2/g and pore volume of 0.14 cm^3/g . The purified kaolinite was designated as Kao.

2.1.2. Intercalation of kaolinite with DMSO

Intercalation of kaolinite with DMSO was performed according to Castrillo (CASTRILLO; OLMOS; GONZÁLEZ-BENITO, 2015) with the method widely discussed in the literature (FROST et al., 1998, 1999; GARDOLINSKI et al., 2000; LAPIDES; YARIV, 2009; MBEY et al., 2013; PATAKFALVI; DÉKÁNY, 2004; ZHANG et al., 2012) and used by our group (AVILA et al., 2010; BIZAIA et al., 2009; DA SILVA et al., 2016; DE ARAUJO et al., 2017; DE FARIA et al., 2009, 2012; FERREIRA et al., 2017). 60 g of purified kaolinite was used with 150 mL of DMSO in suspension and 50 mL of distilled water for 48 hours. The resulting material was washed and centrifuged at 2500 rpm for 15 minutes 3 times with ethanol and oven dried at 60°C for 48 hours. The sample was designated as Kao-DMSO.

2.1.3. Functionalization by the displacement method

Kaolinite was functionalized with the amino acids proline and phenylalanine through the displacement method widely discussed in the literature and used by our research group (AVILA et al., 2010; DE ARAÚJO et al., 2020; DE FARIA et al., 2009, 2010), where 10 g of Kao-DMSO was added to 50 g of L-proline in a reflux system (ratio of 5:1) with temperature slowly rising from 60°C to 105°C, close to the melting/decomposition temperature of the amino acid. After 24h, the material was washed with ethanol by a soxhlet system for 24h and then vacuum filtered. The resulting material was designated as Kao-Pro.

The same process was carried out with the amino acid L-phenylalanine, however with the reaction temperature slowly rising between 60°C to 275°C, the resulting material being designated as Kao-Phe.

2.1.4. Kinetic study of the boric acid catalyzed amidation reaction

The boric acid catalyzed amidation reaction was adapted from Arce (ARCE et al., 2015) based on several studies on amidation reaction (EL DINE; ROUDEN; BLANCHET, 2015; MYLAVARAPU et al., 2007; PATTABIRAMAN; BODE, 2011; TANG, 2005; WANG et al., 2013a). A kinetic reaction study was carried out by modifying the alkoxide APTES with amino acids in a catalytic environment of boric acid. A reflux system was installed to prevent hydrolysis and loss of alkoxide mass, where 100 mL of toluene, 4.5 mL of APTES, 120 mg of boric acid (10% ratio of H₃BO₃:APTES on the mass) and 3.2 g of amino acid under magnetic stirring at 180°C. The synthesis was carried out by varying the

reaction times for 0, 1, 2, 4, 6, 12 and 24 hours. Subsequently, the temperature was reduced to 50°C and 1 g of Kao-DMSO added, slowly increasing the temperature to 180°C. The resulting material was washed 3 times with toluene and 3 times with ethanol and oven dried at 60°C for 24 hours.

2.1.5. Functionalization of kaolinite by boric acid catalyzed amidation reaction

After defining the best reaction time obtained by the kinetic study (24 hours), the reaction was repeated using 300 mL of toluene, 15 mL of APTES, 7.24 g of proline and 4 g of Kao-DMSO. The resulting material was designated as Kao-APro. For the sample containing the phenylalanine, 16 g of the amino acid, 300 mL of toluene, 22.4 mL of APTES, 0.59 g of boric acid and 5 g of Kao-DMSO were used. The resulting material was designated as Kao-APhe.

2.1.6. Complexation of Eu^{3+} ion

The complex $\text{EuCl}_3 \cdot 6\text{H}_2\text{O}$ was obtained with 1.76 g of Eu_2O_3 solubilized in 20 mL of distilled water and 3.04 mL of HCl (0.1 mol/L), in heating until evaporation close to the oxidation of europium (III), where ethanol is added in a dropper until the pH of the solution reaches values close to 6. Afterwards, the solution is transferred to a volumetric flask and its volume completed to 100 mL (MATOS et al., 2014; SALTARELLI et al., 2012). Afterwards, the samples were added in suspension with the europium(III) chloride solution in a molar ratio of 3:1 (amino acid: Eu^{3+}) (using the minimum formula obtained from the thermal analysis) under magnetic stirring for 24 hours, as shown in table 3.

Table 3 - Proportion between sample mass and europium(III) chloride volume in samples containing kaolinite.

Samples	<i>m</i> (g)	<i>v</i> (EuCl₃·6H₂O)(mL)
<i>Kao-Pro</i>	1,5	35
<i>Kao-APro</i>	1,5	31
<i>Kao-Phe</i>	2	40
<i>Kao-APhe</i>	1,2	26

Subsequently, the resulting materials were washed and centrifuged 3 times with ethanol and 3 times with distilled water and dried in a vacuum oven at 60°C for 24 hours. The samples were designed as Eu(KaoPro), Eu(KaoPhe), Eu(KaoAPro) and Eu(KaoAPhe).

2.1.7. Addition of the secondary ligand sodium tenoyltrifluoroacetate (tta:Na)

The 0.1 M solution containing the secondary ligand tta:Na was obtained by a reflux system containing 30 mL of ethanol, 1.2 g of NaOH and 0.7 g of tenoyltrifluoroacetone for 2 hours at a temperature of 80°C (LI; YAN, 2013). Subsequently, the content was completed with ethanol in a 100 mL volumetric flask. The resulting materials were designated as Eutta(Kao-Pro), Eutta(Kao-Phe), Eutta(KaoAPro) and Eutta(KaoAPhe) respectively.

2.2. Hydrotalcite (LDH) materials

The experimental procedures for obtaining the hydrotalcite hybrid materials are shown in Figure 12 and described below.

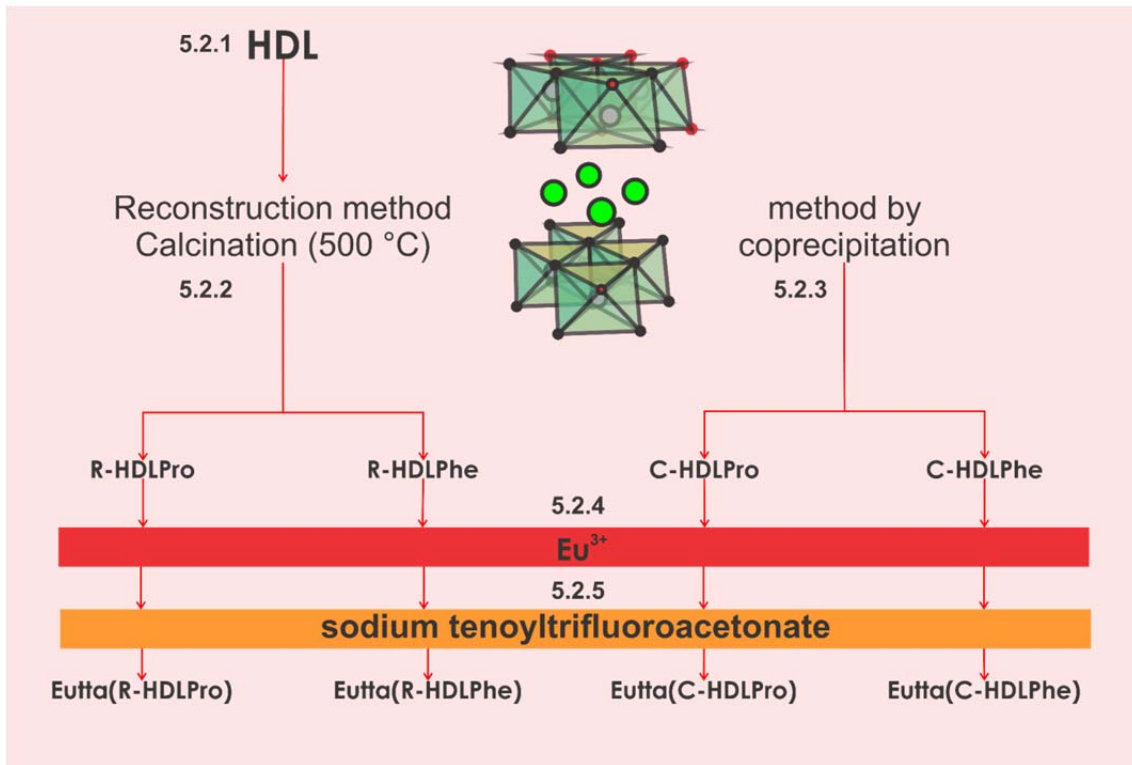


Figure 12 - Flowchart of experimental procedures for samples with hydrotalcite.

2.2.1. Synthesis of lamellar double hydroxides (LDH)

Firstly, to avoid excess carbonate ions in the interlamellar space of the hydrotalcite, argon was bubbled in water to remove CO₂ which can be converted to carbonate and easily intercalated for 3 hours, being designated as DD water. For the synthesis of synthetic hydrotalcite, the hydrothermal method already known and widely discussed in the literature was used (GUO et al., 2010; RIVES, 2001; TRAN; LIN; CHAO, 2018). A solution was made containing 0.12 mol of MgCl₂·6H₂O (24.4 g) and 0.04 mol of AlCl₃·6H₂O (9.66 g) with 60 mL of distilled water. Another solution containing 0.34 g mol of NaOH (13.4 g) and 0.022 mol of sodium bicarbonate (2.3 g of Na₂CO₃) with 60 mL of distilled water was added in a burette and slowly dripped onto the first solution at 45 °C and constant stirring for 24 hours.

Subsequently, the volume was completed with DD water up to 200 mL and kept under magnetic stirring for another hour and then transferred the contents to a teflon autoclave reactor for another 24 hours at 190 °C in the muffle. The resulting material was centrifuged and washed with ethanol 3 times and with DD water 3 more times. Afterwards, the sample was dried in an oven at 60°C for 48 hours. The sample was designated as LDH.

Pure hydrotalcite had the following chemical formula: $Mg_{4.98}(Al_{1.72})(CO_3)(OH)_{16}\cdot 4H_2O$ with particle size of 7.1 μm , 40 m^2/g of specific surface area and 0.18 cm^3/g of pore volume and hexagonal structure of 3R rhombohedral symmetry, values close to the literature (AISAWA et al., 2001; BERNARDO; RIBEIRO, 2018).

2.2.2. Addition of amino acids by reconstruction method

For amino acid intercalation by the reconstruction method, it was necessary to calcine pure hydrotalcite at 500°C for 5 hours, being designated as LDH500. Afterwards, 2.5 g of LDH500 was suspended with 100 mL of DD water and 1.84 g of phenylalanine were added (ratio of 3 mmol/g of LDH) in an inert argon environment in a reflux system and magnetic stirring for 24 hours at a temperature of 40 °C. The pH was maintained at 6 with a 0.1 M NaOH solution. Afterwards the resulting material was washed and centrifuged 5 times with DD water and oven dried being designated as R-LDHPhe.

The same procedure was repeated for the amino acid proline, however under different conditions to avoid LDH dissolution according to Nakayama (NAKAYAMA; WADA; TSUHAKO, 2004), being 2.5 g of LDH500 suspended in a reflux system with magnetic stirring with 1.26 g of proline and 100 mL of DD

water for 3 hours at a temperature of 40 °C. Subsequently, the resulting material was washed and centrifuged 5 times with DD water and dried in an oven, designated as R-LDHPro.

2.2.3. Addition of amino acids by the co-precipitation method

The intercalation of amino acids in hydrotalcite by the coprecipitation method was performed according to Tran and Chao (TRAN; LIN; CHAO, 2018) this method being widely used and discussed in the literature (CREPALDI; VALIM, 1998; DEL ARCO et al., 2004; GUO et al., 2010; MA; ZHENG; PANG, 2012; OLFS et al., 2009; RIVES, 2001; RIVES; DEL ARCO; MARTÍN, 2014; RIVES; ULIBARRI, 1999). A solution containing 3 g of $MgCl_2 \cdot 6H_2O$ and 1.2 g of $AlCl_3 \cdot 6H_2O$ with 50 mL of DD water was made. A second solution containing 0.81 g for the amino acid phenylalanine and 0.57 g for the amino acid proline with 50 ml of DD water was added slowly through a burette to the first solution under magnetic stirring and temperature of 40°C.

The pH of the resulting solution was maintained at 10 with a 0.1 M NaOH solution and argon was bubbled through the solution to avoid contact with CO_2 during the procedure. The resulting material was left to rest at room temperature for 1 hour, then washed 5 times with DD water and oven dried at 60 °C for 48 hours. The samples were designated as C-LDHPhe and C-LDHPro for the materials containing the amino acids phenylalanine and proline respectively.

2.2.4. Complexation of Eu^{3+} with hydrotalcite samples

For this procedure, a solution of $EuCl_3 \cdot 6H_2O$ was made with DD water and 0.55 mmol of the solution (35 mL) in 2 g of HDL-AA (AA = amino acid, 1:1

AA:Eu³⁺ ratio) added in an inert argon atmosphere at 80 °C for 6 hours for the amino acid proline and at room temperature for 18 hours for the amino acid phenylalanine according to Gago et al. (GAGO et al., 2005). Afterwards the samples were washed and centrifuged 5 times with DD water and dried in a vacuum oven at 60°C for 24 hours. The samples were designated as Eu(R-LDHPPro) and Eu(R-LDHPhe) for the samples containing the amino acids proline and phenylalanine by the reconstruction method respectively and Eu(C-HDLPro) and Eu(C-HDLPhe) for the samples containing proline and phenylalanine by the coprecipitation method respectively.

2.2.5. Addition of the tenoyltrifluoroacetate (tta) ligand in HDL complexes

2 g of samples obtained by both methods were added in suspension with 100 mL of 0.1M tta:Na for 3 hours at 80°C for samples containing the amino acid proline and in 24 hours at room temperature for samples containing the amino acid phenylalanine. Both in magnetic stirring and in a reflux system with an inert argon atmosphere. Afterwards the samples were washed and centrifuged 3 times with ethanol and 3 times with DD water, dried in an oven at 60°C for 24 hours. The samples obtained were designated as Eutta(R-LDHPPro) and Eutta(R-LDHPhe) for the samples containing the amino acids proline and phenylalanine through the reconstruction method respectively and Eutta(C-LDHPPro) and Eutta(C-LDHPhe) for the samples containing the amino acids proline and phenylalanine by the co-precipitation method respectively.

2.3. Saponite and LAPONITE® materials

The experimental procedures for obtaining hybrid materials of LAPONITE® and saponite are shown in Figure 13 and described below.

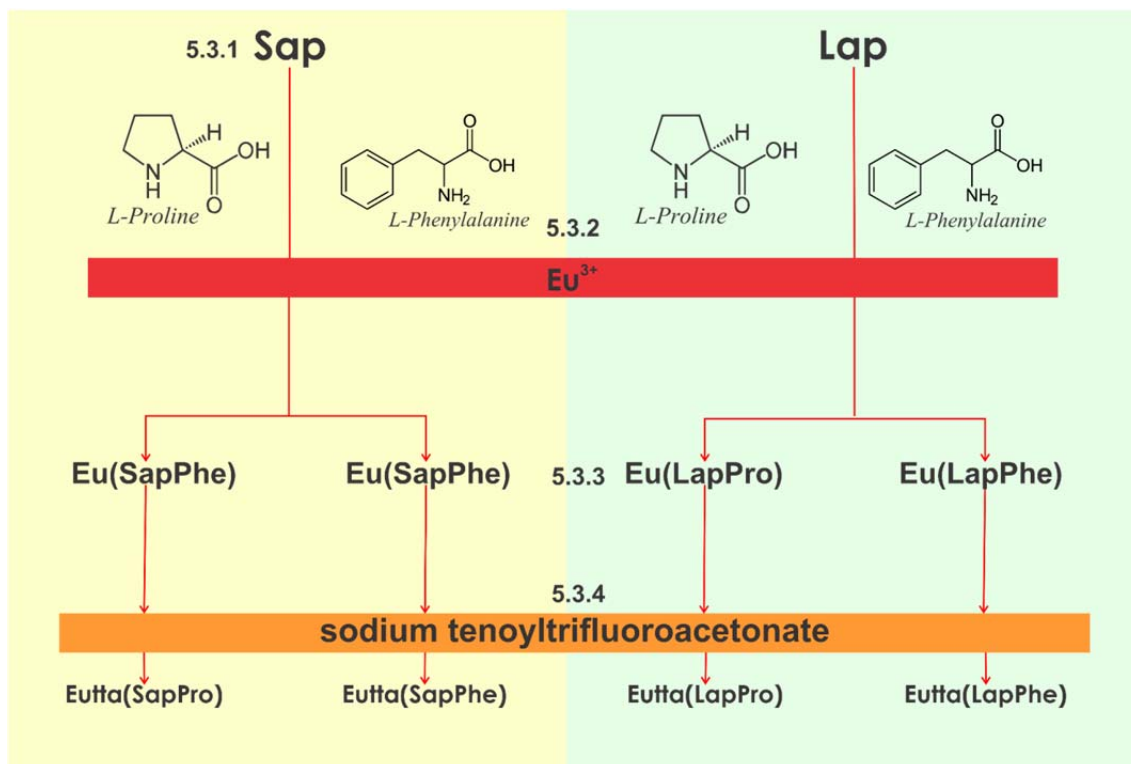


Figure 13 - Flowchart of experimental procedures for samples with saponite and LAPONITE®.

2.3.1. Commercial LAPONITE® RD and Pure Saponite (microwave)

LAPONITE® RD was provided by BYK Additives with specific surface area of 370 m²/g, pore volume of 0.03 cm³/g, particle size of 25 nm, cation exchange capacity of 0.35 eq/unit cell and chemical formula Na⁺_{0.7}[(Si_{6.47}Mg_{4.39}Li_{0.4})O₂₀(OH)₄]^{-0.7}, values close to literature (DAS et al., 2019). The sample was designated as Lap.

The saponite was synthesized by the microwave method according to Trujillano (TRUJILLANO et al., 2010, 2011). A solution containing 3.8 g of sodium hydroxide (NaOH), 7.0 g of sodium bicarbonate (NaHCO₃) and 4.5 g of sodium silicate (Na₂SiO₃) was made with 50 mL of distilled water and a second solution in a burette containing 1.6 g of aluminum(III) chloride (AlCl₃·6H₂O), 6.6 g of magnesium(II) chloride (MgCl₂·6H₂O) in 25 mL of distilled water. The

second solution was slowly added by a burette (10 ml/min) over the first under magnetic stirring. Subsequently, the resulting content was placed in a microwave reactor with a 10 min heating rate and 30 minutes of synthesis at 180 °C. Afterwards, the resulting solution was washed and centrifuged 5 times with distilled water and dried in an oven at 60°C for 48 hours. The pure saponite was designated as Sap. The material had 370 m²/g of specific surface area, cation exchange capacity of 1.0 meq/g, average particle size of 156 µm and structural formula [Si_{7,1}Al_{0,88}][Mg_{6,0}]O₂₀(OH)₄[Na_{1,7}].18H₂O, values close to literature (BISIO; CARNIATO; GATTI, 2020; TRUJILLANO et al., 2011).

2.3.2. Complexation of Eu³⁺ with the amino acids proline and phenylalanine

Due to the ease of expansion of the interlamellar space of the smectites, the Eu³⁺ ion was complexed with the amino acids and subsequently intercalated in saponite and LAPONITE® clay minerals (MA et al., 2019; RYU et al., 2014; WANG et al., 2019). 4.0 g of phenylalanine amino acid were suspended with 82 ml of EuCl₃·6H₂O 0.1 M (molar ratio of 3:1 amino acid:Eu³⁺) in 100 mL of water/ethanol (1:1) with magnetic stirring and temperature of 80 °C. The amount of water was reduced by the constant addition of ethanol. Subsequently, 100 mL of benzene was added to the concentrated solution and placed in refrigeration for 7 days. The resulting solution was vacuum filtered and dried in a vacuum oven at 50°C for 48 hours (CARUBELLI; MASSABNI; LEITE, 1997). The complex was designated as Eu(Phe)₃.

For complex involving phenylalanine the pH of the solution was maintained at 6, however, for proline there was no precipitation of the complex at low pH values. Therefore, for the synthesis of complexation of the L-proline

amino acid with Eu^{3+} , a solution containing 2.82 g of proline was made with 82 mL of 0.1 M $\text{EuCl}_3 \cdot 6\text{H}_2\text{O}$ (3:1 molar ratio amino acid: Eu^{3+}) in 100 mL of water with the pH maintained at 9 with a 0.1 M NaOH solution. The resulting solution was stored under refrigeration for 24 hours until complex precipitation. The resulting material was vacuum filtered and dried in a vacuum oven at 60°C for 48 hours (ZHENG, 2012). The resulting complex was designated as $\text{Eu}(\text{Pro})_3$.

2.3.3. Intercalation of Eu^{3+} complexes in saponite and LAPONITE®

For intercalation of the complexes in saponite, 2 g of the clay mineral was suspended with 75 mL of ethanol for 24 hours under magnetic stirring and at room temperature. Subsequently, 7.1 g of the $\text{Eu}(\text{Phe})_3$ complex was solubilized in 100 mL water/ethanol (1:1) and mixed with the solution containing saponite under magnetic stirring at room temperature for 24 hours (Molar ratio 1:1 $\text{Na}^+ : \text{Eu}^{3+}$). The resulting material was washed and centrifuged 5 times with ethanol and oven dried at 60°C. The sample was designated as $\text{Eu}(\text{SapPhe})$. This procedure was repeated with the $\text{Eu}(\text{Pro})_3$ complex (3.9 g), the resulting sample being designated as $\text{Eu}(\text{SapPro})$.

For intercalation in LAPONITE®, the same procedure as the intercalation of complexes in saponite was used, using 2 g of LAPONITE®, 7 g of $\text{Eu}(\text{Phe})_3$ and 4 g of $\text{Eu}(\text{Pro})_3$ in a molar ratio of 1:1 between $\text{Na}^+ : \text{Eu}^{3+}$. The resulting material was designated as $\text{Eu}(\text{LapPhe})$ for the sample containing phenylalanine and $\text{Eu}(\text{LapPro})$ for the sample containing the amino acid proline.

2.3.4. Addition of the tta ligand in the complexes intercalated in saponite and LAPONITE®

Samples of saponite and LAPONITE® intercalated with the complexes were suspended with the tta:Na solution for 24 hours at room temperature and magnetic stirring in the approximate molar ratio of 3:1 tta:Eu³⁺ as shown in table 4.

Table 4 - Ratio of sample mass to volume of tta:Na 0.1 M added.

Sample	<i>m</i> (g)	<i>v</i> (mL) (tta:Na 0,1 M)
Eu(LapPro)	2,1	60
Eu(LapPhe)	1,2	25
Eu(SapPro)	3,8	100
Eu(SapPhe)	3,7	100

After this process, the samples were washed and centrifuged 3 times with ethanol and 3 times with water and dried in an oven at 60°C for 24 hours. The samples were named as Eutta(LapPhe) and Eutta(LapPro) for the LAPONITE® samples and Eutta(SapPhe) and Eutta(SapPro) for the saponite samples respectively.

2.4. Leaching tests

The samples Kao-Pro; Kao-Phe; Kao-APro; Kao-APhe; R-LDHPro; R-LDHPhe; C-HDLPro and C-HDLPhe were subjected to a leaching test, where the samples were suspended at a mass ratio of 10:1 (distilled water:sample) for 7 days under magnetic stirring and at room temperature. Afterwards, the samples were centrifuged and dried in an oven at 60°C for 24 hours.

2.5. Adsorption tests for Estrogen, Caffeine and Cr³⁺ contaminants

2.5.1. Calibration curves

Solutions of Cr³⁺ in distilled water were prepared at the following concentrations: 60, 100, 200, 400, 600, 800, 1000, 2000, 4000, 8000, 12000, 16000, 20000 mg/L. Afterwards, its calibration curve was constructed using the spectra obtained by analyzing the absorbance at 408 nm. The 1000 mg/L solution was chosen as the base solution for analysis in the adsorption tests.

Caffeine solutions were made in distilled water at the following concentrations: 1, 5, 10, 15, 20 and 25 mg/L. The samples were analyzed in a UV-Vis spectrometer and their calibration curve was constructed, fixing the absorbance at 273 nm. The 25 mg/L solution was chosen as the base solution for the adsorption tests.

Estrogen, on the other hand, had very low solubility in water, so solutions were made in absolute ethanol at the following concentrations: 5, 10, 15, 30, 65, 136, 150 mg/L. Afterwards, the spectra were analyzed and its calibration curve constructed, analyzing the absorbance at 280 nm. The 150 mg/L solution was chosen as the base solution for the adsorption tests.

2.5.2. Adsorption Kinetics

To perform the adsorption kinetics, the mass quantity of sample obtained from the final materials was considered. The mass ratio per sample is shown in table 5.

Table 5 - Mass ratio used at each time in the kinetic adsorption study.

Sample	<i>m</i> per time (mg)	Sample	<i>m</i> per time (mg)*
Kao-Pro	20	R-LDHPro	20
Kao-Apro	10	C-HDLPro	15
Kao-Phe	10	R-LDHPhe	10
Kao-Aphe	10	C-HDLPhe	15
Lap-Pro	20	Sap-Pro	20
Lap-Phe	20	Sap-Phe	20

* The amount of material used in each sample was based on the total amount obtained by the syntheses, to perform the kinetics, balance and characterization.

The samples were separated in the amounts shown in table 5 in a falcon tube and the solid added in suspension with 5 mL of base solution of the contaminant under magnetic stirring and at room temperature in the following times: 1, 3, 7, 15, 30, 60 and 120 minutes. Afterwards, the material was centrifuged, and the supernatant separated for analysis in the UV-Vis spectrometer and the resulting solid dried in an oven at 60°C for 24 hours for analysis in the luminescence spectrometer.

2.5.3. Chemical equilibrium in the adsorption process

For the equilibrium tests, the time in the adsorption kinetics where the highest adsorption rate occurs was observed and this same time was used to repeat the experimental kinetics process in 10 mg of material and 5 mL of contaminant, varying the concentration of the adsorbate between 5-250 mg/L for estrogen, 1-25 mg/L for caffeine and 15-800 mg/L for Cr³⁺. Afterwards, the supernatant of the material was analyzed in the UV/Vis spectrophotometer and the dry solid analyzed in the fluorimeter to evaluate the luminescent properties.

2.6. Characterization Techniques

The characterizations of the materials were carried out both at the University of Franca-BR and at the University of Salamanca-ES and are described below.

2.6.1. X-ray diffraction (XRD)

X-ray diffractions were obtained in a Rigaku equipment, at 40 kV, 30 mA (1200 W) and 0.4° increment in 2θ at the University of Franca-BR. The diffractograms obtained at the University of Salamanca-ES were performed in a Siemens D500 equipment with 40 kV and 30 mA and scanning speed of 1.5 and 0.05° increment in 2θ . In both equipments, the diffractograms were evaluated varying the angle between 2 to 70° in 2θ with solids ground in an agate mortar and analyzed by the powder method (Debye-Scherrer).

2.6.2. Fourier Transform Infrared Molecular Spectroscopy (FTIR)

Universidade de Franca-BR: The spectra were obtained on a Perkin-Elmer 1730 Frontier spectrophotometer with a Fourier transform in the range of 400-4000 cm^{-1} .

Universidad de Salamanca-ES: the analyzes were carried out in a Monohaz Perkin-Elmer 1600 spectrophotometer with Fourier transform in the range of 400-4000 cm^{-1} .

The samples were analyzed using the diffuse reflectance (DR) technique, with 32 resolution scans, by diluting the sample in KBr in an agate mortar and using KBr as a Background.

2.6.3. Thermal analysis (TG/DTG/DTA)

The same model of equipment was used at both universities, this being a TA Instruments SDT Q600 thermal analysis equipment, with an oxidizing atmosphere (synthetic air) at a flow of 100 mL/min, heating rate of 20 °C/min and a ramp heating from 25°C to 900°C.

2.6.4. Specific surface by BET isotherms (Brunauer, Emmett e Teller)

Universidade de Franca-BR: Measurements were performed on a Micrometrics ASAP 2020 equipment using N₂ gas. The samples were heat treated at 140°C for 24 hours to avoid interference with the analysis.

Universidad de Salamanca-ES: Measurements were made on a Micrometrics 2010 ASAP using N₂ gas with samples being treated at 140°C for 6 hours.

2.6.5. Determination of particle size

To determine the particle size, a Malvern Mastersizer 2000 analyzer at the University of Salamanca was used, using 6 cycles, laser intensity between 60 to 80% and using water as background. For the acquisition of the measurements, an ultrasound was used that kept the samples suspended during the time intervals of 5, 10 and 15 minutes in agitation of 920 rpm and pump (pump) of 2250 ppm.

2.6.6. Electron microscopy (SEM/TEM)

Universidade de Franca-BR: Images were taken on a Tescan See 3 SBH Model EasyProbe (U.K.) microscope. The samples were dispersed with ethanol in an aluminum cell with adhesive made of colloidal graphite and then coated with a thin layer of gold by a Quorum SC7620 coating system.

Universidad de Salamanca-ES: Scanning electron microscopy was performed on a Zeiss DSM 940 microscope while transmission electron microscopy was performed on a Zeiss-902 microscope by *Servicio General de Microscopía Electrónica de la Universidad de Salamanca*.

2.6.7. Absorption spectroscopy in the UV-Visible region

The absorption spectra in the ultraviolet/visible region were obtained in a Diode Array UV-Vis HP 8453 spectrophotometer, using a quartz cuvette with an optical path of 10 mm in the *Universidade de Franca-BR*.

2.6.8. Luminescence spectroscopy

The luminescence spectra (emission and excitation) were performed by a Fluorolog Horiba Jobinyvon spectrofluorimeter at *Universidade de Franca-BR*. Excitation and emission spectra in continuous and pulsed light (resolved in time) were obtained and measurements of the emission lifetimes of the samples were obtained. The measurements were carried out at room temperature, using Corning 97202 filters with transmittance less than 0.2% below 470 nm and with a detection angle of 90°.

2.7. References

AISAWA, S. et al. Direct Intercalation of Amino Acids into Layered Double Hydroxides by Coprecipitation. **Journal of Solid State Chemistry**, v. 162, n. 1, p. 52–62, nov. 2001.

ARCE, G. et al. Greener Synthesis of an Amide by Direct Reaction of an Acid and Amine under Catalytic Conditions. **World Journal of Chemical Education**, v. 3, n. 1, p. 27–29, 7 mar. 2015.

AVILA, L. R. et al. New synthesis strategies for effective functionalization of kaolinite and saponite with silylating agents. **Journal of Colloid and Interface Science**, v. 341, n. 1, p. 186–193, jan. 2010.

BERNARDO, M. P.; RIBEIRO, C. [Mg-Al]-LDH and [Zn-Al]-LDH as Matrices for Removal of High Loadings of Phosphate. **Materials Research**, v. 21, n. 3, 15 mar. 2018.

BISIO, C.; CARNIATO, F.; GATTI, G. An overview of the recent synthesis and functionalization methods of saponite clay. **New Journal of Chemistry**, v. 44, n. 24, p. 9969–9980, 2020.

BIZAIA, N. et al. Porphyrin-kaolinite as efficient catalyst for oxidation reactions. **ACS Applied Materials & Interfaces**, v. 1, n. 11, p. 2667–2678, 2009.

CARUBELLI, C. R.; MASSABNI, A. M. G.; LEITE, S. R. DE A. Study of the binding of Eu^{3+} and Tb^{3+} to L-phenylalanine and L-tryptophan. **Journal of the Brazilian Chemical Society**, v. 8, n. 6, p. 597–602, 1997.

CASTRILLO, P. D.; OLMOS, D.; GONZÁLEZ-BENITO, J. Kinetic study of the intercalation process of dimethylsulfoxide in kaolinite. **International Journal of Mineral Processing**, v. 144, p. 70–74, 2015.

CREPALDI, E. L.; VALIM, J. B. Hidróxidos duplos lamelares: síntese, estrutura, propriedades e aplicações. **Química Nova**, v. 21, n. 3, p. 300–311, jun. 1998.

DA SILVA, A. C. et al. Influence of physical/chemical treatments to delamination of nanohybrid kaolinite-dipicolinate. **Applied Clay Science**, v. 126, p. 251–258, 2016.

DAS, S. S. et al. Laponite-based Nanomaterials for Biomedical Applications: A Review. **Current Pharmaceutical Design**, v. 25, n. 4, p. 424–443, 3 jun. 2019.

DE ARAUJO, D. T. et al. Eu^{3+} - and Tb^{3+} -Dipicolinate Complexes Covalently Grafted into Kaolinite as Luminescence-Functionalized Clay Hybrid Materials. **The Journal of Physical Chemistry C**, v. 121, n. 9, p. 5081–5088, 9 mar. 2017.

DE ARAÚJO, D. T. et al. Luminescent properties of biohybrid (kaolinite-proline) materials synthesized by a new boric acid catalyzed route and complexed to Eu^{3+} . **Applied Clay Science**, v. 192, n. April, p. 105634, jul. 2020.

DE ARAÚJO, D. T. et al. Grafting of L-proline and L-phenylalanine amino acids on kaolinite through synthesis catalyzed by boric acid. **Applied Surface Science Advances**, v. 4, n. December 2020, p. 100081, jun. 2021.

DE FARIA, E. H. et al. Hybrid materials prepared by interlayer functionalization of kaolinite with pyridine-carboxylic acids. **Journal of Colloid**

and Interface Science, v. 335, n. 2, p. 210–215, jul. 2009.

DE FARIA, E. H. et al. Novel reactive amino-compound: Tris(hydroxymethyl)aminomethane covalently grafted on kaolinite. **Applied Clay Science**, v. 48, n. 3, p. 516–521, abr. 2010.

DE FARIA, E. H. **Estudo das Propriedades Luminescentes e Catalíticas de Materiais Híbridos Obtidos pela Funcionalização de uma Caulinita Natural com Complexos de Ácidos Carboxílicos**. Emerson Henrique de Faria. Universidade de Franca, 2011.

DE FARIA, E. H. et al. Green and selective oxidation reactions catalyzed by kaolinite covalently grafted with Fe(III) pyridine-carboxylate complexes. **Catalysis Today**, v. 187, n. 1, p. 135–149, jun. 2012.

DEL ARCO, M. et al. Synthesis and characterization of layered double hydroxides (LDH) intercalated with non-steroidal anti-inflammatory drugs (NSAID). **Journal of Solid State Chemistry**, v. 177, n. 11, p. 3954–3962, 2004.

EL DINE, T. M.; ROUDEN, J.; BLANCHET, J. Borinic acid catalysed peptide synthesis. **Chemical Communications**, v. 51, n. 89, p. 16084–16087, 2015.

FERREIRA, B. F. et al. Kaolinite-polymer compounds by grafting of 2-hydroxyethyl methacrylate and 3-(trimethoxysilyl)propyl methacrylate. **Applied Clay Science**, v. 146, n. May, p. 526–534, set. 2017.

FROST, R. L. et al. Molecular Structure of Dimethyl Sulfoxide Intercalated Kaolinites. **The Journal of Physical Chemistry B**, v. 102, n. 43, p. 8519–8532, 1998.

FROST, R. L. et al. Molecular Structure of Dimethyl Sulfoxide in DMSO-Intercalated Kaolinites at 298 and 77 K. **The Journal of Physical Chemistry A**, v. 103, n. 48, p. 9654–9660, 1999.

GAGO, S. et al. Immobilization of Lanthanide Ions in a Pillared Layered Double Hydroxide. **Chemistry of Materials**, v. 17, n. 23, p. 5803–5809, 2005.

GARDOLINSKI, J. E. et al. Layered polymer-kaolinite nanocomposites. **Journal of Materials Science**, v. 35, n. 12, p. 3113–3119, 2000.

GUO, X. et al. Layered double hydroxide films: synthesis, properties and applications. **Chemical Communications**, v. 46, n. 29, p. 5197, 2010.

LAPIDES, I.; YARIV, S. Thermo-X-ray-diffraction analysis of dimethylsulfoxide-kaolinite intercalation complexes. **Journal of Thermal Analysis and Calorimetry**, v. 97, n. 1, p. 19–25, 27 jul. 2009.

LI, Q.-P.; YAN, B. Novel luminescent hybrids by incorporating rare earth β -diketonates into polymers through ion pairing with an imidazolium counter ion. **Photochemical & Photobiological Sciences**, v. 12, n. 9, p. 1628, 2013.

MA, J. et al. Luminescent materials of covalent grafting lanthanide complexes to the synthetic clays. **Journal of Luminescence**, v. 212, n. November 2018, p. 126–132, 2019.

MA, X.; ZHENG, J.; PANG, H. Intercalation of Mg-Al layered double hydroxides by L-proline: Synthesis and characterization. **Research on Chemical Intermediates**, v. 38, n. 2, p. 629–638, 2012.

MATOS, M. G. et al. Synthesis and photoluminescent properties of yttrium vanadate phosphor prepared by the non-hydrolytic sol-gel process. **Journal of Luminescence**, v. 147, p. 190–195, 2014.

MBEY, J. A. et al. An insight on the weakening of the interlayer bonds in a Cameroonian kaolinite through DMSO intercalation. **Applied Clay Science**, v. 83–84, p. 327–335, out. 2013.

MYLAVARAPU, R. K. et al. Boric Acid Catalyzed Amidation in the Synthesis of Active Pharmaceutical Ingredients. **Organic Process Research & Development**, v. 11, n. i, p. 1065–1068, 2007.

NAKAYAMA, H.; WADA, N.; TSUHAKO, M. Intercalation of amino acids and peptides into Mg-Al layered double hydroxide by reconstruction method. **International Journal of Pharmaceutics**, v. 269, n. 2, p. 469–478, 2004.

OLFS, H.-W. et al. Comparison of different synthesis routes for Mg-Al layered double hydroxides (LDH): Characterization of the structural phases and anion exchange properties. **Applied Clay Science**, v. 43, n. 3–4, p. 459–464, mar. 2009.

PATAKFALVI, R.; DÉKÁNY, I. Synthesis and intercalation of silver nanoparticles in kaolinite/DMSO complexes. **Applied Clay Science**, v. 25, n. 3–4, p. 149–159, 2004.

PATTABIRAMAN, V. R.; BODE, J. W. Rethinking amide bond synthesis. **Nature**, v. 480, n. 7378, p. 471–9, 2011.

RIVES, V. **Layered Double Hydroxides: Present And Future**. 1st. ed. New York: Nova Science Publishers, 2001.

RIVES, V.; DEL ARCO, M.; MARTÍN, C. Intercalation of drugs in layered double hydroxides and their controlled release: A review. **Applied Clay Science**, v. 88–89, p. 239–269, 2014.

RIVES, V.; ULIBARRI, M. A. Layered double hydroxides (LDH) intercalated with metal coordination compounds and oxometalates.

Coordination Chemistry Reviews, v. 181, n. 1, p. 61–120, 1999.

RYU, S. J. et al. Photoluminescent europium(III) complex intercalated in natural and synthetic clay minerals for enhanced latent fingerprint detection. **Applied Clay Science**, v. 101, p. 52–59, 2014.

SALTARELLI, M. et al. Influence of Catalyses on the Preparation of $\text{YVO}_4:\text{Eu}^{3+}$ Phosphors by the Sol–gel Methodology. **Journal of Fluorescence**, v. 22, n. 3, p. 899–906, 30 maio 2012.

TANG, P. Boric acid catalyzed amide formation from carboxylic acids amines: n-benzyl-4-phenylbutyramide. **Organic Syntheses**, v. 81, n. September, p. 262, 2005.

TRAN, H. N.; LIN, C.-C.; CHAO, H.-P. Amino acids-intercalated Mg/Al layered double hydroxides as dual-electronic adsorbent for effective removal of cationic and oxyanionic metal ions. **Separation and Purification Technology**, v. 192, p. 36–45, fev. 2018.

TRUJILLANO, R. et al. Microwave radiation and mechanical grinding as new ways for preparation of saponite-like materials. **Applied Clay Science**, v. 48, n. 1–2, p. 32–38, mar. 2010.

TRUJILLANO, R. et al. Rapid microwave-assisted synthesis of saponites and their use as oxidation catalysts. **Applied Clay Science**, v. 53, n. 2, p. 326–330, 2011.

WANG, C. et al. Mechanism of arylboronic acid-catalyzed amidation reaction between carboxylic acids and amines. **Organic and Biomolecular Chemistry**, v. 11, n. 13, p. 2140–2146, 2013.

WANG, Y. et al. Recent progress in luminescent materials based on lanthanide complexes intercalated synthetic clays. **Journal of Rare Earths**, v. 37, n. 5, p. 451–467, 2019.

ZHANG, Y. et al. Thermal behavior analysis of kaolinite–dimethylsulfoxide intercalation complex. **Journal of Thermal Analysis and Calorimetry**, v. 110, n. 3, p. 1167–1172, 2 dez. 2012.

ZHENG, Z. Lanthanides: Amino Acid Compounds. In: **Encyclopedia of Inorganic and Bioinorganic Chemistry**. Chichester, UK: John Wiley & Sons, Ltd, 2012.

3. Chapter 3 – Results published in journals

As it is a reliable reproduction of the articles, the formatting, references and captions do not follow the formatting of this thesis, which continues in chapter 4.

ARTICLE I

Applied Surface Science Advances 4 (2021) 100081



Contents lists available at ScienceDirect

Applied Surface Science Advances

journal homepage: www.elsevier.com/locate/apsadv



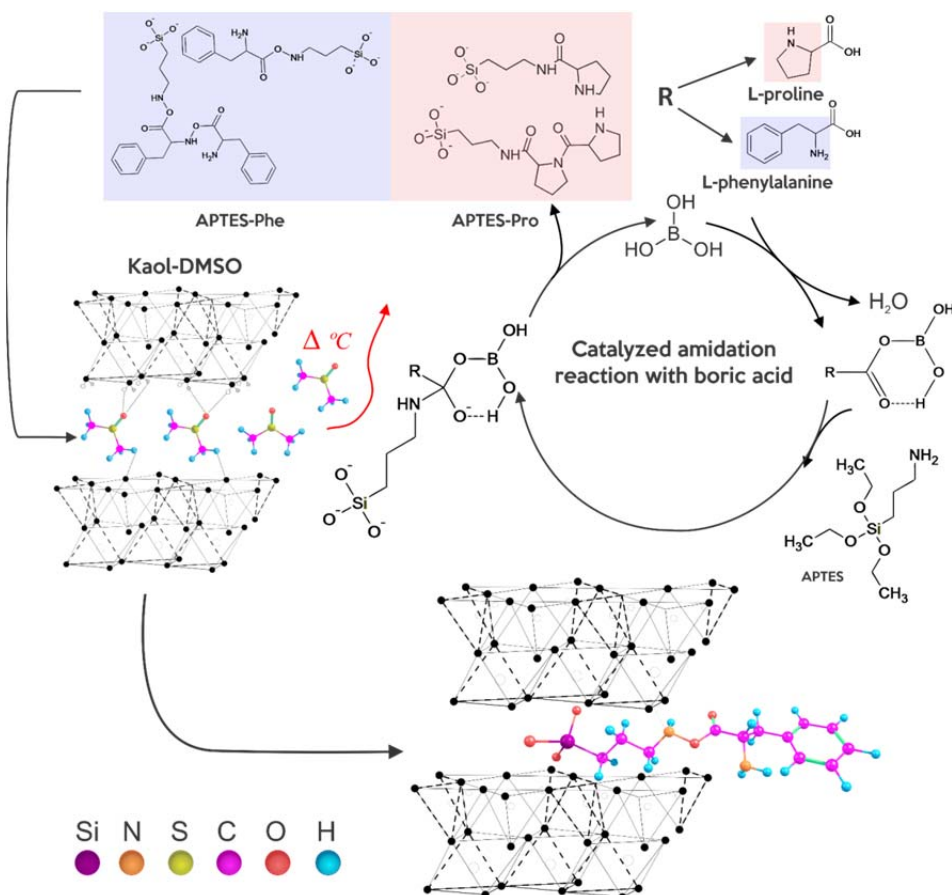
Grafting of L-proline and L-phenylalanine amino acids on kaolinite through synthesis catalyzed by boric acid



Denis T. de Araújo^a, Katia J. Ciuffi^a, Eduardo J. Nassar^a, Miguel A. Vicente^b, Raquel Trujillano^b, Vicente Rives^b, Elena P. Bernal^b, Emerson H. de Faria^{a,*}

^a Grupo de Pesquisas em Materiais Lamelares Híbridos (GPMatLam). Universidade de Franca, Av. Dr. Armando Salles Oliveira, Parque Universitário, 201, 14404-600 Franca, SP, Brazil

^b GIR-QUESCAT, Departamento de Química Inorgánica, Universidad de Salamanca, 37008 Salamanca, Spain



Abstract

The amidation reaction catalyzed by boric acid between the amino acids proline and phenylalanine and the alkoxide 3-aminopropyltriethoxysilane was studied. Afterwards, the modified alkoxide was used to functionalize the clay mineral kaolinite. The hybrid material was characterized by powder X-ray diffraction, molecular absorption spectroscopy in the infrared region, thermal analysis and scanning electron microscopy, to understand the influence of the reaction time on the kaolinite intercalation process, in order to improve this functionalization route for both amino acids considered. The reaction times evaluated varied from 0 to 24 hours, keeping the reflux temperature fixed at 180 °C, being then reacted with kaolinite previously intercalated with dimethyl sulfoxide (DMSO). After 24 hours of reaction the modified alkoxide interacted effectively, replacing the DMSO molecules and resulting in the formation of covalent bonds between the modified alkoxide and the clay. The material showed greater dispersion of the organic phase along the layered matrix, and significantly increased its thermal stability, with maximum loss at 320°C. The sample containing phenylalanine was more agglomerated than that containing proline, with 2.4 times in mol number. In all cases, the crystallinity of the material decreased by the interaction of the modified alkoxide with the kaolinite matrix, the modified alkoxide being partially outside the interlayer space because of its large molecular size.

Keywords: Kaolinite; Functionalization; Phenylalanine; Organically modified; kaolinite

1. Introduction

Organic-inorganic hybrid materials have attracted interest among researchers due to their broad variety of properties. Consequently, hybrid materials synthesized from layered clay minerals as inorganic matrixes have been studied extensively in recent years for the most diverse applications such as catalysis (ALABA et al., 2015; BIZAIA et al., 2009), luminescent sensors (SATO; TAMURA; YAMAGISHI, 2014), adsorption (DE CASTRO SILVA et al., 2020), and controlled drug release (GARCÍA-VILLÉN et al., 2019), among others. Among these clay minerals, kaolinite has received scarce attention due to its difficult intercalation caused by the interlayer aluminol groups that maintain the cohesive hydrogen bond, resulting in a small specific external surface area in relation to the interlayer area, being considered for a long time non-expandable (YANG et al., 2012).

With minimal formula $\text{Al}_2\text{Si}_2\text{O}_5(\text{OH})_4$, kaolinite consists of a tetrahedral layer of silica and another octahedral of alumina, with a hydroxyl surface responsible for the interactions; however, to outline the strong interaction between the layers, it is necessary to intercalate a small and highly polar molecule such as dimethylsulfoxide (DMSO), thus swelling the interlayer space and facilitating the access of molecules of interest to the interlayer space, which can form covalent bonds through condensation reactions (TAO et al., 2014). In the context of this work, the amino acids L-proline and L-phenylalanine were chosen because they are molecules with high potential for different applications,

being already widely used in the pharmaceutical industry, in addition to show low toxicity, being of low cost and non-polluting.

The most common route for grafting is the displacement method (DEDZO; DETELLIER, 2016; HE et al., 2013; TUNNEY; DETELLIER, 1993), which provides a greater concentration of the functionalized material, which remains aggregated in the interlayer space and increases the thermal stability of the amino acid. On the other hand, in previous studies (DA SILVA et al., 2020; DE ARAÚJO et al., 2020), a new route for the functionalization of amino acids in kaolinite was presented, through an amidation reaction between the amino acid and an alkoxide (3-aminopropyltriethoxylane), catalyzed by boric acid, which causes a greater dispersion of the amino acid, and with even greater thermal stability, increasing the organophilicity of the material and the solubility of the amino acid, an important aspect for biological applications.

When the alkoxide modified by the amino acid is incorporated into the kaolinite, covalent bonds are formed on the interlayer surface, being arranged parallel to the layer with part of the structure outside the basal space, on the sides of the kaolinite particles, providing greater structural mobility to the modified alkoxide, facilitating both its interaction with organic molecules in processes involving adsorption (DA SILVA et al., 2020), as well as its complexation with metal cations (DE ARAÚJO et al., 2020). This range of properties developed by this route can raise the interest in kaolinite as an inorganic matrix for hybrid materials, bypassing its “non-expandable” characteristic in relation to other clay minerals and making it a platform for subsequent reactions.

As this route catalyzed by boric acid can be used on a large scale and in different applications, a well-founded basis on the method used is necessary. For this, the aim of this work is the study of the grafting of kaolinite with a modified alkoxide, produced by the modification of 3-aminopropyltriethoxsilane alkoxide (APTES) with the amino acids L-proline and L-phenylalanine by an amidation reaction catalyzed with boric acid, at times ranging from 0 to 24 hours. To evaluate the functionalization conditions, powder X-ray diffraction, molecular spectroscopy in the infrared region and thermal analyzes were used.

Materials and methods

2.1. Materials

For the experimental part, 3-aminopropyltriethoxysilane (APTES) 97% - Synth; Sodium acetate - Synth (99%); Boric Acid - Dinâmica Ltda; Distilled water; Ethyl alcohol 95.0% - Synth; Dimethylsulfoxide (DMSO) 99.9% - Synth; Sodium hydroxide P.A.- Synth; L-proline - Sigma-Aldrich; L-phenylalanine - Sigma-Aldrich; Methylbenzene (Toluene) 99.9% - J.T. Baker were used, all of them as received, without any further purification.

The kaolinite used in this work came from the city of São Simão, in the state of São Paulo, Brazil, kindly provided by Darcy R.O. Silva e Cia. (São Simão-SP, Brazil). Removal of impurities, and the consequent obtention of purified kaolinite, was carried out through dispersion and sedimentation of natural clay in distilled water, based on the Stokes' Law; the solid obtained was denoted as Kaol (AVILA et al., 2010; DE FARIA et al., 2009; FERREIRA et al., 2017). It was highly pure, with granulometry in the order of 2 μm , light color, high percentage of crystals with hexagonal structure, high plasticity and resistance under thermal and humidity conditions, showing the chemical formula $\text{Si}_{2.04}\text{Al}_{2.00}\text{Fe}_{0.03}\text{Mg}_{0.01}\text{K}_{0.02}\text{Ti}_{0.04}\text{O}_{7.23}$, very close to the theoretical one (DE ARAÚJO et al., 2020). The specific surface area of the solid was 17 m^2/g , with a total pore volume 0.14 cm^3/g , close to literature results (DE FARIA et al., 2010; SONG et al., 2014).

The intercalation of kaolinite with DMSO was based on methods well reported in the literature (BRANDT; ELBOKL; DETELLIER, 2003; DEDZO; DETELLIER, 2016; TAO et al., 2014), mixing 60 g of Kaol with 150 ml of DMSO

and 50 ml of H₂O. The resulting suspension was stirred at 60° for 48h. The material was centrifuged at 2000 rpm for 15 min and washed three times with ethanol and dried in an oven at 60° C for 48 h, being designated as Kaol-DMSO.

Kaolinite functionalization was carried out by modifying the APTES alkoxide in a boric acid catalytic environment. Initially, a reflux system was installed to prevent loss of the alkoxide. 100 ml of toluene, 4.5 ml of APTES, 120 mg of boric acid (10% H₃BO₃:APTES mass ratio) and 3.2 g of amino acid were used and left stirring at a temperature of 180°C for 0, 1, 2, 4, 6, 12 and 24h. Subsequently, the temperature was lowered to 50°C, 1 g of Kaol-DMSO was added, and then the temperature was slowly raised to 180 °C. The resulting material was washed with toluene and ethanol and dried in an oven at 60°C for 24h. The materials were designated as Kaol-APTES-Phe for the amino acid L-phenylalanine and Kaol-APTES-Pro for L-proline. All organofunctionalized materials were placed under magnetic stirring for 7 days in a sample/distilled water m/v ratio of 1:10 to check the chemical stability of the organofunctionalized material and leaching of solvents and adsorbed material.

2.2. Characterization techniques

Powder -ray diffraction analysis was performed on a Rigaku equipment using Cu K α filtered radiation (40 kV, 30 mA), between 2 to 70° (in 2 θ), with scan speed of 0.04° (2 θ) at room temperature. Infrared absorption spectra were obtained by a Fourier transform Perkin-Elmer 1730 Frontier spectrometer, in the 4000-400 cm⁻¹ range. The samples were analyzed by the diffuse reflectance technique by mixing with KBr, with 32 scans using KBr as background. Thermal

analyses were performed on a TA Instruments SDT Q600 thermal analysis device, with a 100 mL/min flow of synthetic air, heating rate of 10° C/min and heating range from 25 to 900° C.

Selected materials were also characterized by scanning electron microscopy, obtained in a Zeiss DSM 940 apparatus over samples coated with a thin gold layer by a Quorum SC7620 coating system and in a Zeiss-902 apparatus, over samples dispersed with ethanol in a colloidal graphite aluminum cell.

3. Results and discussion

The amidation reaction time was a key factor in the intercalation of the modified alkoxide between the kaolinite sheets, as shown in the diffractograms of the solids (Figure 1). Kaolinite peaks were the most important in the diffractograms, although a first wide peak was recorded at low angle for all materials, swelling as reaction time increases and probably due to a very low smectite admixture.

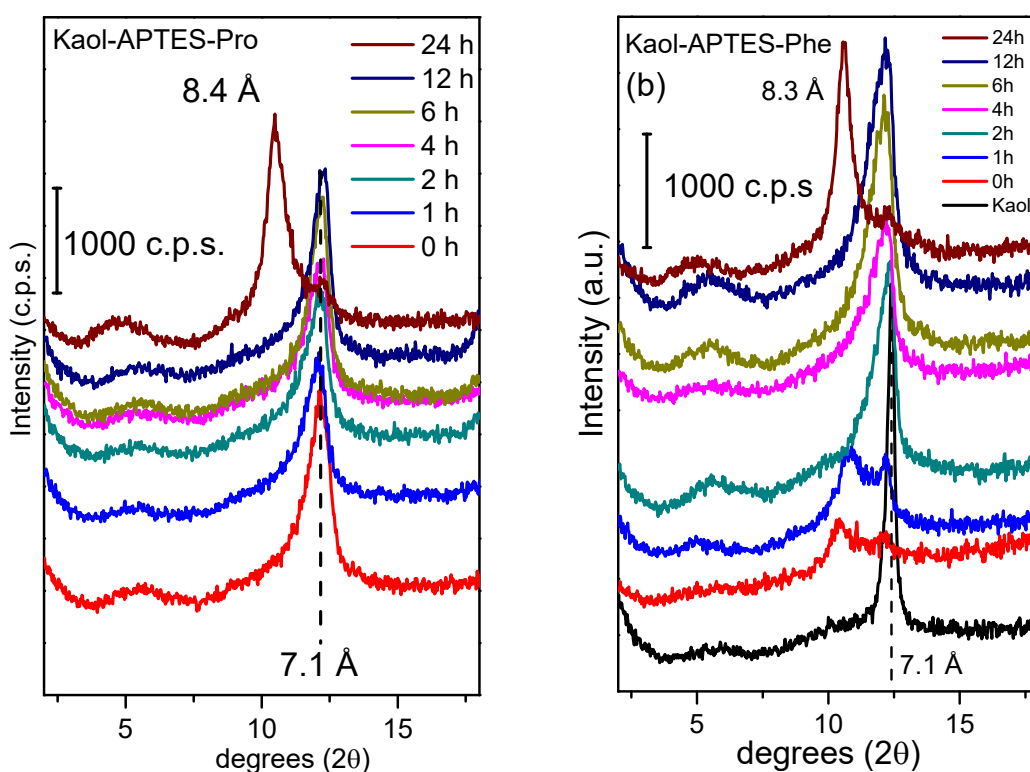


Figure 1. Low-angle X-ray diffractograms of the hybrid materials Kaol-APTES-Pro and Kaol-APTES-Phe after reaction from 0 to 24h. 0h denotes the sample immediately after putting in contact the reagents.

Purified kaolinite had 7.1 Å of interlayer spacing, which was expanded to 11.2 Å by intercalation with DMSO (not shown). After incorporation of the modified alkoxide, it was possible to verify a drop in crystallinity evidenced by several factors. When dealing specifically with kaolinite, it was possible to analyze the crystallinity through the degree of particle orientation (R), calculated

as $R=I_{d001}/I_{d020}$ where the higher the value, the greater the crystallinity (DA SILVA et al., 2016), because reflection 020 of this clay shows no significant changes under several treatments (SMRČOK et al., 2010). The FWHM index, denoting the width at half peak maximum, was also indicative of changes in the crystallinity; both indexes are given in Table 1.

Materials involving the amino acid proline showed an increase in basal space only after 24 h of amidation, while the materials involving phenylalanine already showed a basal spacing expansion to 8.5 Å after 0h (the amidation reaction occurs in contact with the clay mineral) and 1h of reaction. However, this intercalation did not continue at increasing times, suggesting that this interaction was not stable. After 24h of treatment, a new peak appeared at 8.3 Å, with a swelling of 1.2 Å with respect to kaolinite, and suggesting that the modified alkoxide interacted with the interlayer of kaolinite only at the space through the sides of the lamellae, justifying the low expansion (YANG et al., 2012).

In all the intercalated samples, the characteristic peak of non-intercalated kaolinite at 7.1 Å was still observed. Thus, it was possible to analyze the intensities of the 001 reflection of the intercalated material and the non-intercalated kaolinite to define an intercalated rate of each material using the equation $\alpha= I_1/(I_1 + I_0)$, where α is the intercalation rate, I_1 is the peak intensity of the 001 reflection of the intercalated material and I_0 in original kaolinite (MBEY et al., 2013). In the case of the Kaol-APTES-Pro sample, only with 24 h of catalyzed reaction the material showed a 72% intercalation rate, while for the Kaol-APTES-Phe sample at the same time it was 71% intercalated.

Table 1 - Basal spacing (d); variation of basal spacing (Δd); intercalation/grafting ratio (α); degree of particle orientation (R) and d_{001} reflection peak widths (FWHM) of kaolinite and functionalized hybrid materials.

Sample	d (Å)	Δd (Å)	α (%)	$R=d_{001}/d_{020}$	FWHM ($^{\circ}2\theta$)
Kaol	7.1	-	-	3.7	0.4
Kaol-APTES-Pro (24h)	8.4	1.3	72	1.3	1.1
Kaol-APTES-Phe					
0 h	8.5	1.4	53	0.6	1.9
1 h	8.2	1.1	51	0.7	1.6
24 h	8.3	1.2	71	1.0	0.7

The crystallinity of Kaol-APTES-Phe samples, although low in relation to the non-intercalated kaolinite, increased with the amidation reaction time. With a short reaction time and steric hinderance caused by the concentration of kaolinite in the solution, it was more likely that the amino acid and APTES preferentially interacted with the matrix, which may have caused an increase in the concentration of phenylalanine and alkoxide in kaolinite in relation to modified alkoxide. On the other hand, in the Kaol-APTES-Pro samples, this increase did not occur, because proline had a smaller molecular diameter, facilitating the contact with the alkoxide and consequently facilitating the amidation reaction.

In all cases, the decrease in crystallinity occurred due to the influence of organic matter in the stacking of the layers, resulting in a lower stacking that decreased the crystallinity of the material. Upon removal of DMSO by leaching and grafting, the hydrogen bonds between the layers were recovered, promoting a small folding of the layers causing its delamination (DA SILVA et al., 2016). When the reflections not related to this stacking were analyzed,

particularly the 060 reflection, it was verified that the crystalline structure of the kaolinite remained unchanged (Figure 2).

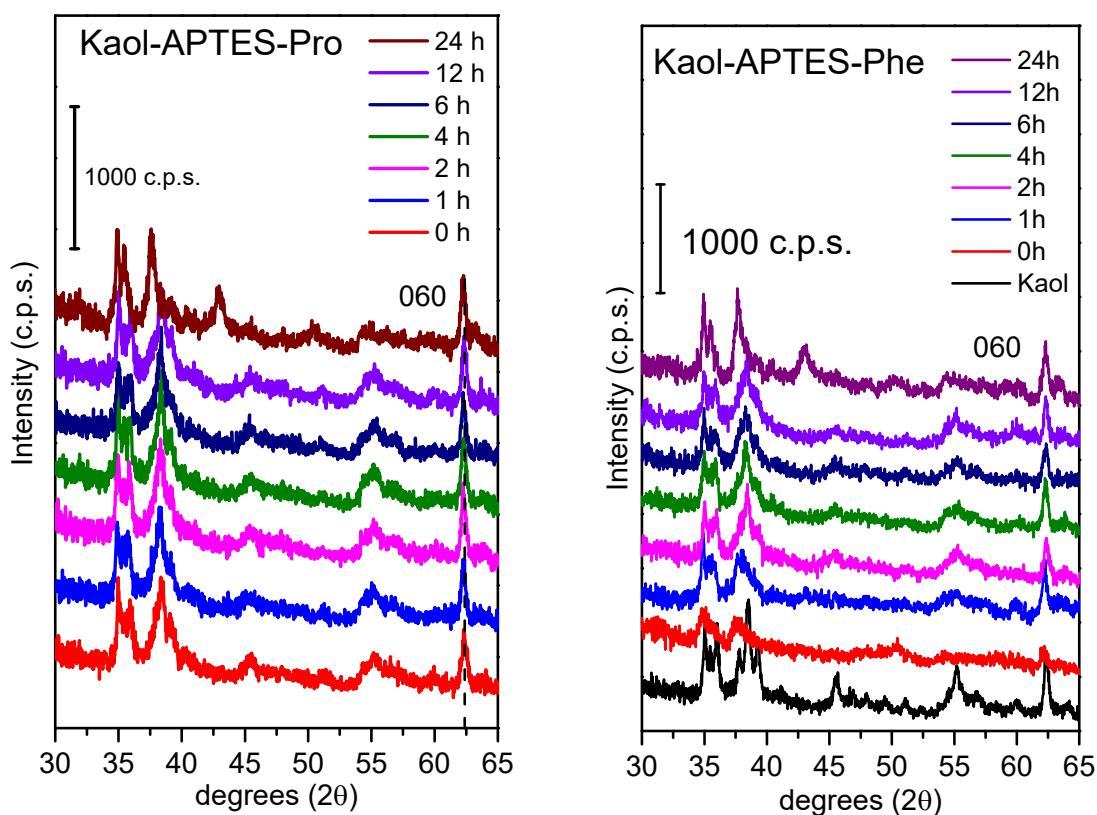


Figure 2. X-ray diffractograms of the hybrid materials K-APTES-Pro and K-APTES-Phe in the 0 to 24h time range.

Aluminol groups have an intralamellar hydroxyl group and three interlamellar ones, which are responsible for the interactions, according to Figure 3. In the molecular absorption spectra in the infrared region, the bands related to these hydroxyls have been reported at 3696, 3563 and 3668 cm^{-1} for interlamellar hydroxyls and at 3620 cm^{-1} for intralamellar hydroxyl, respectively (TOSONI; DOLL; UGLIENGO, 2006).

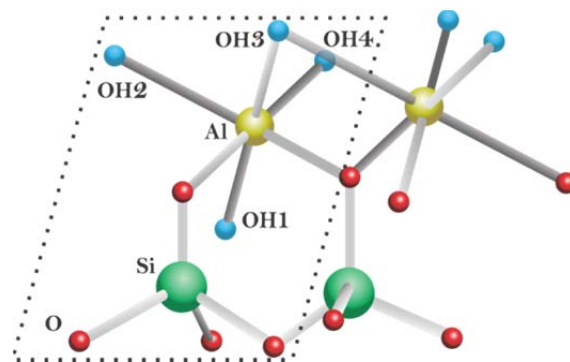


Figure 3. Schematic representation of hydroxyls present in aluminol groups.

In the intercalation process, the interlamellar hydroxyl bands can change in position and intensity or even new bands can appear, while in the functionalization process they can change in intensity or even disappear. Intralaminar hydroxyl did not participate in interactions due to its steric hindrance. The absorption spectra in the infrared region are shown in Figures 4 and 5.

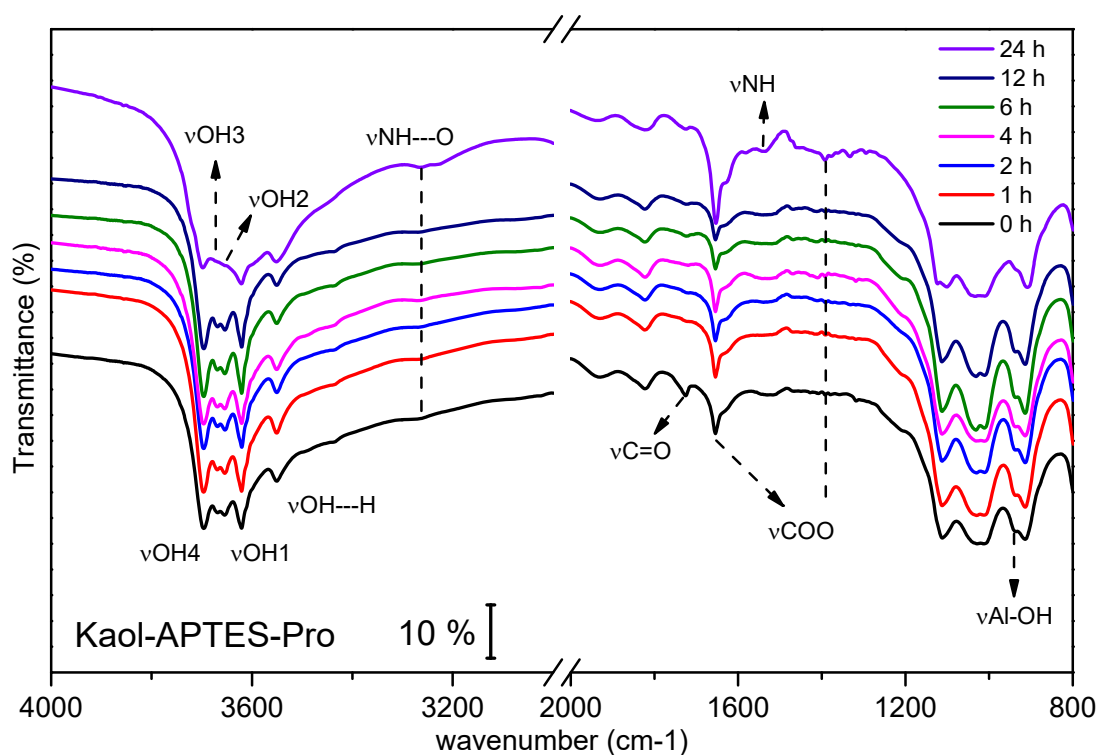


Figure 4. Infrared absorption spectra (FTIR) of Kaol-APTES-Pro solids, from 4000-800 cm^{-1} with a break at 3000-2000 cm^{-1} .

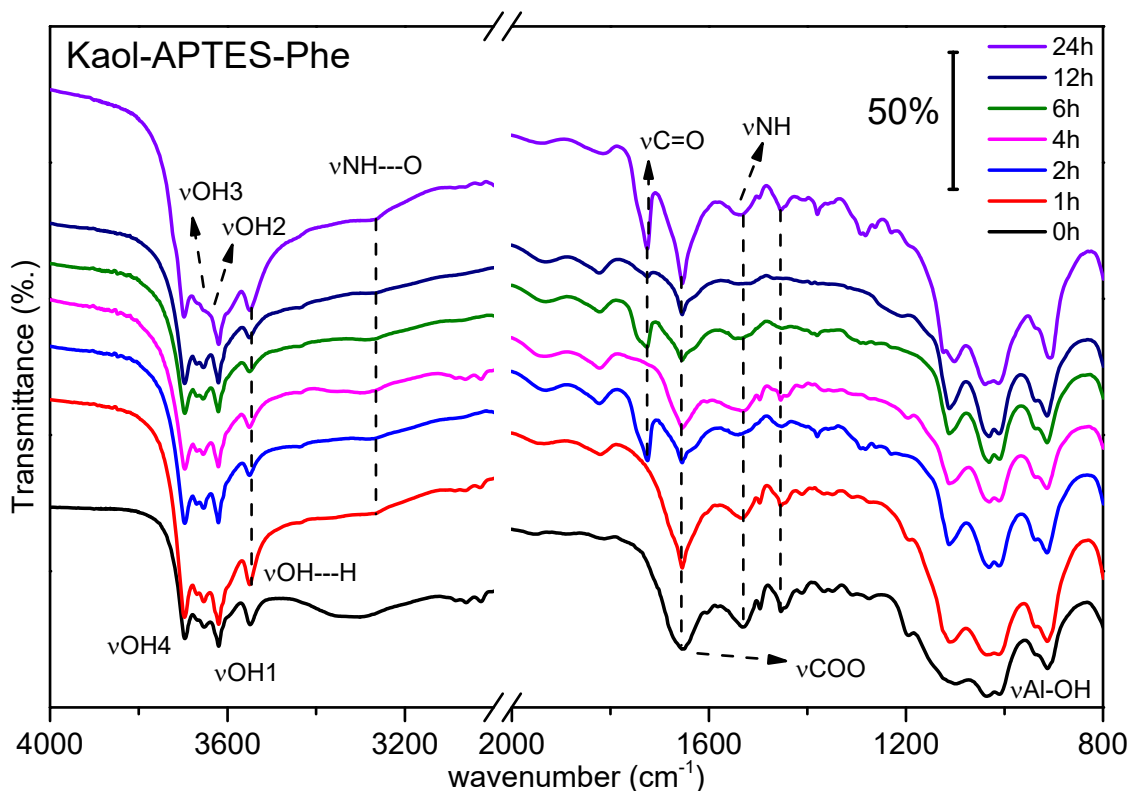


Figure 5. Infrared absorption spectra (FTIR) of the Kaol-APTES-Phe from 4000-800 cm^{-1} with break at 3000 a 2000 cm^{-1} .

In the Kaol-APTES-Pro samples, the hydroxyls remained unchanged until 24 h of reaction, when two interlamellar hydroxyls disappeared, and at the same time the characteristic band of axial vibration of aluminol at 938 cm^{-1} also disappeared, indicating that these hydroxyls were removed, leading to formation of covalent bonds, characteristic of the functionalization process. In the Kaol-APTES-Phe samples, the aluminol band remained with less intensity, indicating the presence of both intercalated and grafted material. On the other hand, organic matter was detected in all the samples, indicating that it was adsorbed on the surface of the clay; the hydroxyl at 3551 cm^{-1} present in the spectra of all the samples indicated this weaker interaction by means of hydrogen bonding or other van der Waals forces.

The fact that the intralamellar aluminol band did not participate in the interactions allowed it to be considered as a standard to analyze the intensity of the interlayer aluminol band and thus to evaluate its interactions, where the greater the difference in transmittance between the intra and interlayer aluminol bands, the greater the strength of the interactions (Table 2).

Table 2 - Relation of position and transmittance between the intralamellar and interlamellar aluminol bands.

Sample		OH intra		OH inter	$\Delta\%$	$\text{OH}_{\text{inter}}/\text{OH}_{\text{intra}}$
Time (h)	Transmittance (%)	Wavenumber (cm^{-1})	Transmittance 938 cm^{-1} (%)			
Kaol	19.6	914	24.8		5.2	1.3
Kaol-APTES-Pro						
0	7.9	913	11.0		3.1	1.4
1	11.5	914	16.1		4.6	1.4
2	13.0	914	17.9		4.9	1.4
4	8.9	914	12.5		3.6	1.4
6	20.5	914	26.7		6.2	1.3
12	14.9	914	19.8		4.9	1.3
24	9.2	909	-		-	-
Kaol-APTES-Phe						
0	47.9	912	53.1		5.2	1.1
1	14.1	912	19.4		5.3	1.4
2	38.8	914	43.4		4.6	1.1
4	26.0	914	30.1		4.1	1.2
6	49.9	914	55.0		5.1	1.1
12	48.3	914	54.0		5.7	1.1
24	26.4	908	37.5		11.1	1.4

In both series, the interaction occurred via the interlamellar hydroxyls during the initial amidation reaction times, due to the concentration of amino acid and APTES in contact with the kaolinite. However, only after 24h of reaction the interlayer aluminol band disappeared in the sample with proline and the transmittance of the sample with phenylalanine greatly changed, being at

this time the highest probability of covalent bond between the modified alkoxide and the kaolinite interlamellar hydroxyls. Another factor that proved this interaction force was a slight displacement of the intralamellar aluminol band to lower wavenumbers, proving a slight increase in the structural rigidity, characteristic of stronger interactions such as covalent bonds.

The absence of hydroxyl bands 2 and 3 (3663 and 3668 cm^{-1}) indicated that the modified alkoxide interacted in the interlayer space; however, due to the steric hindrance caused by the size of the molecule in relation to the increase in the basal space shown in the X-ray diffraction, it was most likely that this interaction occurred preferably with part of the molecule outside the basal space, when the alkoxide reacted with a peptide, causing a small exfoliation in the matrix structure. Phenylalanine has a greater facility for peptide formation in the amidation reaction in relation to proline, which resulted in a larger structure of the organic part in the Kaol-APTES-Phe samples, causing steric hindrance for its complete intercalation in the matrix. This factor explains the oscillation in the ratio between intra and interlamellar transmittances and the difficulty of the modified alkoxide in removing the two interlamellar hydroxyls and consequently in the disappearance of the band at 938 cm^{-1} . Most likely, this interaction occurred in only one hydroxyl group in the kaolinite unit cell for this sample.

A very broad band close to 3266 cm^{-1} indicated several distinct interactions between the amines of APTES and amino acids in the form of a hydrogen bond, in addition to overlapping bands of axial C-H vibrations that extended up to 2500 cm^{-1} . The amine stretching band of the amino acids can be seen close to 1550 cm^{-1} and the vibrations of the COO^- symmetric and antisymmetric stretching modes were close to 1650 and 1400 cm^{-1} .

The stretching vibrations of the COO^- carbonyl group occurred at lower wavenumbers in these amino acids due to their conjugation (SILVERSTEIN; WEBSTER; KIEMLE, 2005), however, a new stretching band due to $\text{C}=\text{O}$ appeared at 1725 cm^{-1} indicating interactions in the carbonyl group that can be attributed both to the amidation reaction and to the interaction of the COO^- group with kaolinite, appearing as low intensity bands in the Kaol-APTES-Pro series and higher intensities at times 2, 6 and 24h in the Kaol-APTES-Phe series.

The carbonyl band was not observed at 1725 cm^{-1} after 0 and 1h of amidation between APTES and phenylalanine, indicating that this group remained unchanged in the amino acid, interacting directly with kaolinite, thus reducing the efficiency in the amidation reaction catalyzed by boric acid, as also evidenced by the powder X-ray diffraction data. This band appeared again only after 6 h of reaction, its intensity increasing over time; however, with the bands of interlamellar hydroxyls and aluminol disappearing only after 24 hours, it is evident that the modified APTES-Phe alkoxide strongly interacted with kaolinite only after 24 hours of amidation reaction.

The stretching vibrations of the water molecules in the non-intercalated kaolinite are recorded in the 3435 cm^{-1} region and the angular vibrations in the 1630 cm^{-1} region. The axial vibrations of the connections between Si and O appeared at 1000 to 1200 cm^{-1} , while the O bridge between the Si outside and in the plane can be found at 701 and 473 cm^{-1} , respectively. Bands due to traces of silica and quartz can be found at 795 cm^{-1} . The vibrations of intralamellar stretching of the aluminum were at 912 cm^{-1} while the vibrations of the Si-O-Al bonds of the octahedral lamella were at 795 and 543 cm^{-1} , and

finally the angular vibration between Si and O was located at 431 cm^{-1} (BRANDT; ELBOKL; DETELLIER, 2003; FROST, 1996; TOSONI; DOLL; UGLIENGO, 2006).

Under heat treatment, kaolinite react up to form mullite ($\text{Al}_2\text{O}_3\cdot 2\text{SiO}_2$) (SAHNOUNE et al., 2012). As already described in previous studies (DE ARAÚJO et al., 2020), kaolinite has a small mass loss at $65\text{ }^\circ\text{C}$ due to removal of adsorbed water, the first endothermic dehydroxylation close to $510\text{ }^\circ\text{C}$ and the second one at $900\text{ }^\circ\text{C}$. Thermogravimetric analysis (TG) and its derivative (DTG) are shown in Figures 6 and 7.

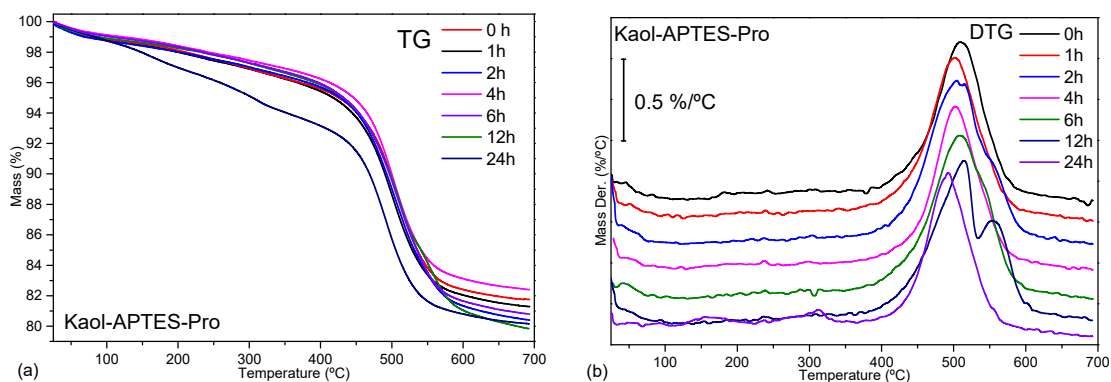


Figure 6. Thermogravimetric analysis and its derivative for Kaol-APTES-Pro series. Ramp of $10\text{ }^\circ\text{C}/\text{min}$, from 25 to $700\text{ }^\circ\text{C}$ in an oxidant atmosphere, with DTG results normalized between 0 and 1.

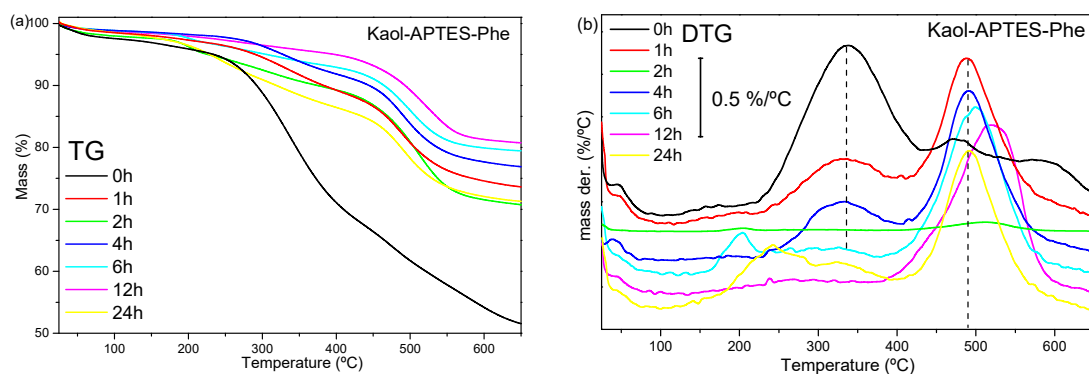


Figure 7. Thermogravimetric analysis and its derivative for Kaol-APTES-Phe series. Ramp of $10\text{ }^\circ\text{C}/\text{min}$, from 25 to $700\text{ }^\circ\text{C}$ in an oxidant atmosphere, with DTG results normalized between 0 and 1.

When kaolinite was functionalized, the temperature of the first dehydroxylation was slightly decreased. Solvents and adsorbed molecules had

been removed by means of a small effect at low temperature. In the Kaol-APTES-Pro sample after 1 h of amidation reaction, it was already possible to see a slight endothermic decrease close to 502 °C, with the greatest decrease after 24 hours of reaction, with maximum loss of mass at 493 °C. In the Kaol-APTES-Phe series, the decrease of this temperature was already observed in the sample at 0h amidation time with maximum loss temperature at 489 °C. This temperature increased up to 12 h of reaction and returned to 489 °C with 24 hours of reaction, showing together with the other techniques that kaolinite was functionalized already at the beginning of the amidation reaction, but separately without the alkoxide being modified, however, this interaction was weaker than that which occurred in longer times (24h), when the alkoxide was already modified.

On the other hand, proline only succeeded in functionalizing the matrix when already modified with APTES after long reaction times, when it had a large content of organic matter. All the proline solids showed a single mass loss (with a small previous loss of solvent), but the solid reacted for 12 hours showed two mass losses above 500 °C and higher thermal stability. These suggested that the proline-modified alkoxide can be completely intercalates in the basal space providing greater thermal stability than for phenylalanine samples; the modified alkoxide structure may remain parallel to the matrix layers causing a low expansion of the interlayer space.

Decomposition of the amino acids occurred in a large step beginning above 200 °C, the matrix offered the amino acid a greater thermal resistance compared to the isolated amino acid (MA; ZHENG; PANG, 2012).

From the values of mass losses of the materials, the content of organic matter per mol of kaolinite was calculated (Table 3), taking into account the modification of the alkoxide with the amino acid and the peptide, as shown in figure 9 (DA SILVA et al., 2016).

Table 3 - Experimental number of moles of modified alkoxide per mol of kaolinite for Kaol-APTES-Pro and Kaol-APTES-Phe solids, obtained from thermogravimetry.*

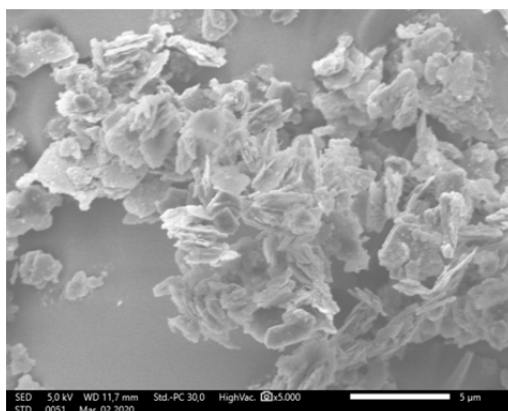
Kaol-APTES-Pro		Kaol-APTES-Phe	
time (h)	Modified alkoxide/kaolinite	time (h)	Modified alkoxide/kaolinite
0	0.063	0	0.711
1	0.071	1	0.171
2	0.085	2	0.220
4	0.053	4	0.121
6	0.078	6	0.085
12	0.093	12	0.067
24	0.088	24	0.211

* The molecular mass of kaolinite was calculated by means of the formula given in Materials section, while the molecular mass of the modified alkoxide was calculated as the media of the two formulae proposed in Figure 9.

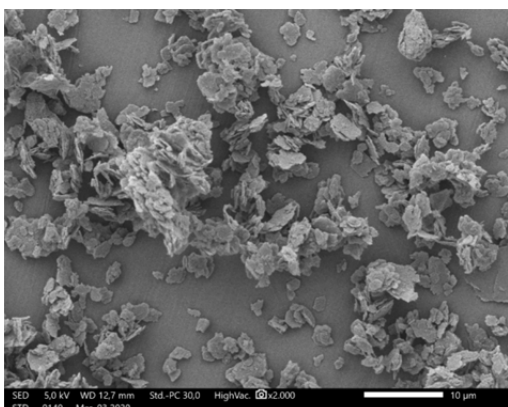
After 24 hours of amidation reaction, the Kaol-APTES-Phe solid showed ca. 2.4 times the number of mol of modified alkoxide compared to the corresponding Kaol-APTES-Pro counterpart, bonded by covalent bonding. Conventional syntheses lead to larger amounts of organic matter per kaolinite unit cell. A recent study of kaolinite functionalization with the amino acid alanine showed that the greater the clumping of the amino acid in the matrix, the greater the thermal resistance offered to it (DE CASTRO SILVA et al., 2020). However, the functionalization of alanine in kaolinite by this amidation reaction catalyzed by boric acid (DA SILVA et al., 2020), resulted in a greater thermal

stability than by conventional syntheses, even at a low agglomeration environment of the modified alkoxide.

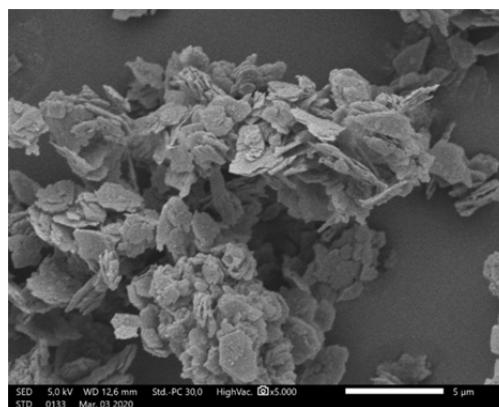
Morphologically, kaolinite has a structural organization in the form of tactoids and when functionalized, they can change in the 001 reflection plane, fracturing the lamellae, decreasing the crystallinity and consequently causing the tactoids to overlap, an effect called delamination (VALÁŠKOVÁ et al., 2007), or may suffer the total loss of unit cell structure in individual layers, resulting in a loss of crystallinity, an effect called exfoliation (TÁBOROSI; SZILÁGYI, 2016). All the samples prepared in the present study showed the presence of kaolinite agglomerated tactoids. In some cases, the increase in the basal space caused by the functionalization weakened the hydrogen bonds between the layers, limiting their overlap and that, after the leaching process, eliminating the organic molecules that were only adsorbed, the force of attraction was reestablished causing a displacement of the structure of the layers further decreasing the morphological ordering (LI et al., 2015).



a) Kaol



b) Kaol-APTES-Pro



c) Kaol-APTES-Phe

Figure 8. SEM micrographs of the indicated solids.

Due to the modification of the APTES alkoxide with the amino acid, the peptide reaction between the amino acids can also occur, further increasing the size of the molecule and the steric hindrance for intercalation in the interlayer space of kaolinite, making even more difficult to insert it in this region during the step of displacement of DMSO. If the amidation reaction resulted in the formation of peptides, the concentration of the amino acid decreased in relation to APTES, favoring the amidation reaction again between the peptide and the alkoxide (Figure 9).

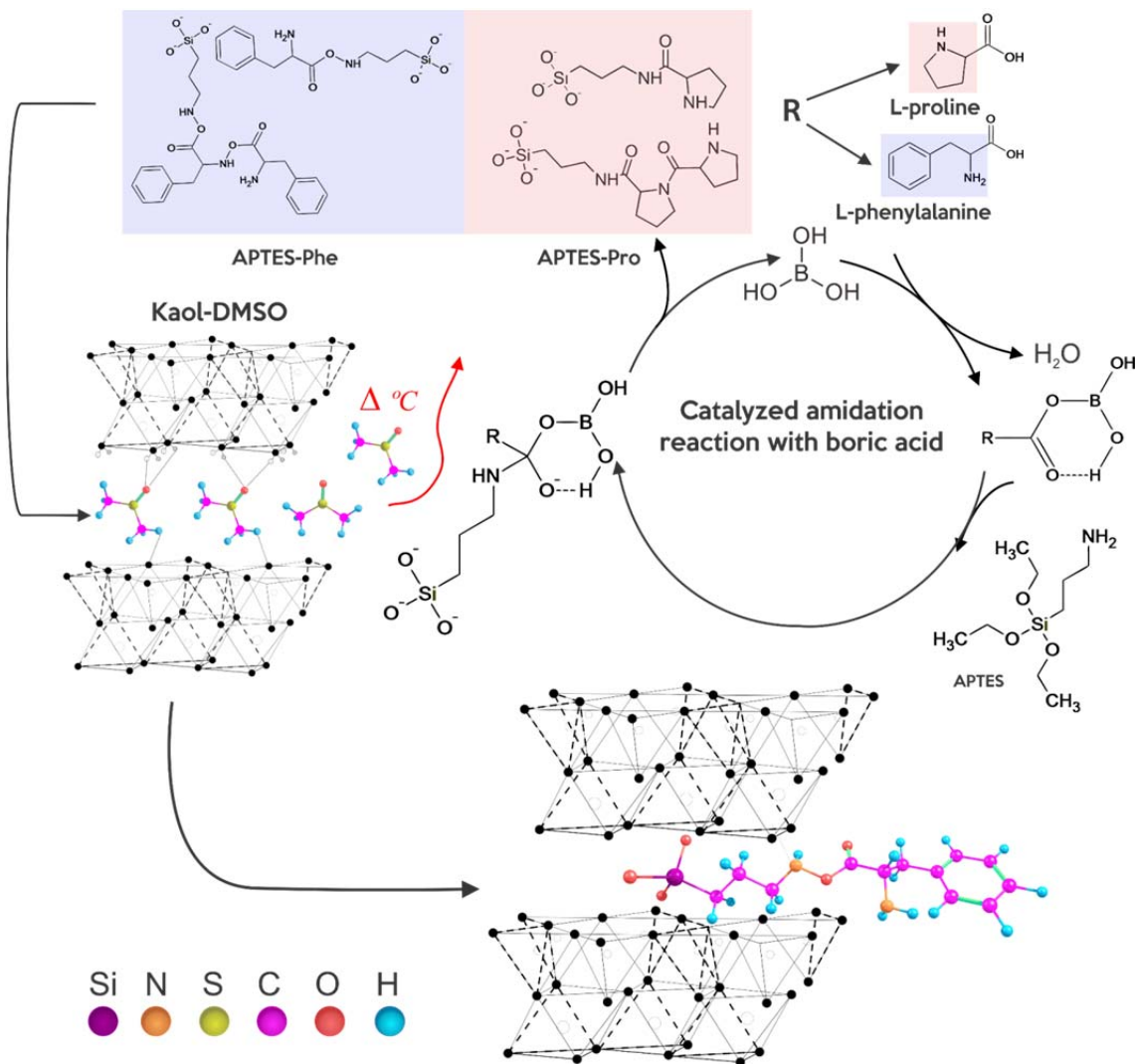


Figure 9. Schematic representation of the reaction flowchart between the modified alkoide and kaolinite.

4. Conclusions

The amidation between the amino acids proline and phenylalanine catalyzed by boric acid was studied as a function of the time or reaction, for further functionalization in kaolinite. In both cases, the interaction by covalent bonding between kaolinite and the modified alkoide only occurred after 24 hours of amidation reaction.

Kaol-APTES-Phe system showed a greater interaction of the amino acid and the alkoxide at the initial times, although with a weaker interaction, being leached at larger amidation times, while after 24 hours the covalent interaction with the modified alkoxide was favored. For the Kaol-APTES-Pro series, this interaction did not occur at the initial times, but also after 24 hours of amidation, the interaction with the modified alkoxide was favored. For phenylalanine, the possible formation of peptides in the modification of the alkoxide caused a steric hindrance for complete intercalation in the interlayer space. Proline, due to its smaller size and its chiral carbon participating in a cyclic chain can hinder the peptide formation in these conditions, making possible its intercalation inside the layers.

The functionalized solids showed greater thermal resistance than isolated materials and greater dispersion of the amino acid compared to conventional syntheses. The catalyzed synthesis may lead several properties different from conventional syntheses, such as greater organophilicity, dispersion of functionalized material and greater structural mobility, which may give these materials applications as luminescent sensors, catalysts, or adsorbents, among others.

5. Acknowledgements

The authors thank a Cooperation Grant jointly financed by Universidad de Salamanca (Spain) and FAPESP (Brazil), reference 2016/50322- 2. The Spanish group acknowledges the support from MINECO and ERDF (MAT2016-78863-C2-R). The Brazilian group acknowledges the support from research funding agencies Fundação de Amparo à Pesquisa do Estado de São Paulo, FAPESP (2013/19523-3, 2018/26569-3, 2017/01719-0 and 2017/15482-1), and

Coordenação de Aperfeiçoamento de Pessoal de Nível Superior (CAPES) and Conselho Nacional de Desenvolvimento Científico e Tecnológico, CNPq (311767/2015-0 and 303135/2018-2). The equipment of Brazilian group has been financed by FAPESP (1998/11022-3, 2005/00720-7, 2011/03335-8, 2012/11673-3 and 2016/01501-1). DTA and EHF thanks Universidade de Franca and Universidad de Salamanca for a “Cotutela PhD” facilities.

References

- [1] P.A. Alaba, Y.M. Sani, W. Mohd, A.W. Daud, Kaolinite properties and advances for solid acid and basic catalyst synthesis, *RSC Adv.* 5 (2015) 101127–101147. doi:10.1039/c5ra18884a.
- [2] N. Bizaia, E.H. De Faria, G.P. Ricci, P.S. Calefi, E.J. Nassar, K.A.D.F. Castro, S. Nakagaki, K.J. Ciuffi, R. Trujillano, M.A. Vicente, A. Gil, S.A. Korili, Porphyrin-kaolinite as efficient catalyst for oxidation reactions, *ACS Appl. Mater. Interf.* 1 (2009) 2667–2678. doi:10.1021/am900556b.
- [3] H. Sato, K. Tamura, A. Yamagishi, Luminescent Oxygen Gas Sensors Based on Nanometer-Thick Hybrid Films of Iridium Complexes and Clay Minerals, *Chemosen.* 2 (2014) 41–55. doi:10.3390/chemosensors2010041.
- [4] F. de Castro Silva, L.C.B. Lima, E.C. Silva-Filho, M.G. Fonseca, J.F. Lambert, M. Jaber, A comparative study of alanine adsorption and condensation to peptides in two clay minerals, *Appl. Clay Sci.* 192 (2020) 105617. doi:10.1016/j.clay.2020.105617.
- [5] F. García-Villén, E. Carazo, A. Borrego-Sánchez, R. Sánchez-Espejo, P. Cerezo, C. Viseras, C. Aguzzi, Clay minerals in drug delivery systems, in: *Modified Clay and Zeolite Nanocomposite Materials: Environmental and Pharmaceutical Applications*. Elsevier, 2019: pp. 129–166. doi:10.1016/B978-0-12-814617-0.00010-4.
- [6] S.-q. Yang, P. Yuan, H.-p. He, Z.-h. Qin, Q. Zhou, J.-x. Zhu, D. Liu, Effect of reaction temperature on grafting of γ -aminopropyl triethoxysilane (APTES) onto kaolinite, *Appl. Clay Sci.* 62–63 (2012) 8–14. doi:10.1016/j.clay.2012.04.006.
- [7] Q. Tao, L. Su, R.L. Frost, D. Zhang, M. Chen, W. Shen, H. He, Silylation of mechanically ground kaolinite, *Clay Miner.* 49 (2014) 559–568. doi:10.1180/claymin.2014.049.4.06.

- [8] G.K. Dedzo, C. Detellier, Functional nanohybrid materials derived from kaolinite, *Appl. Clay Sci.* 130 (2015) 33–39. doi:10.1016/j.clay.2016.01.010.
- [9] J.J. Tunney, C. Detellier, Interlamellar covalent grafting of organic units of kaolinite, *Chem. Mater.* 5 (1993) 747–748. doi:10.1021/cm00030a002.
- [10] H. He, Q. Tao, J. Zhu, P. Yuan, W. Shen, S. Yang, Silylation of clay mineral surfaces, *Appl. Clay Sci.* 71 (2013) 15–20. doi:10.1016/j.clay.2012.09.028.
- [11] A.F. da Silva, G.S. de Pádua, D.T. de Araújo, C.A. Vieira, E.H. de Faria, Immobilization of L-alanine into natural kaolinite via amidation catalyzed by boric acid for the development of biohybrid materials, *J. Solid State Chem.* 287 (2020) 121332. doi:10.1016/j.jssc.2020.121332.
- [12] D.T. de Araújo, G.S. de Pádua, V.G. Peixoto, K.J. Ciuffi, E.J. Nassar, M.A. Vicente, R. Trujillano, V. Rives, M.E. Pérez-Bernal, E.H. de Faria, Luminescent properties of biohybrid (kaolinite-proline) materials synthesized by a new boric acid catalyzed route and complexed to Eu^{3+} , *Appl. Clay Sci.* 192 (2020) 105634. doi:10.1016/j.clay.2020.105634.
- [13] E.H. de Faria, O.J. Lima, K.J. Ciuffi, E.J. Nassar, M.A. Vicente, R. Trujillano, P.S. Calefi, Hybrid materials prepared by interlayer functionalization of kaolinite with pyridine-carboxylic acids, *J. Colloid Interface Sci.* 335 (2009) 210–215. doi:10.1016/j.jcis.2009.03.067.
- [14] B.F. Ferreira, K.J. Ciuffi, E.J. Nassar, M.A. Vicente, R. Trujillano, V. Rives, E.H. de Faria, Kaolinite-polymer compounds by grafting of 2-hydroxyethyl methacrylate and 3-(trimethoxysilyl)propyl methacrylate, *Appl. Clay Sci.* 146 (2017) 526–534. doi:10.1016/j.clay.2017.07.009.
- [15] L.R. Avila, E.H. de Faria, K.J. Ciuffi, E.J. Nassar, P.S. Calefi, M.A. Vicente, R. Trujillano, New synthesis strategies for effective functionalization of kaolinite and saponite with silylating agents, *J. Colloid Interface Sci.* 341 (2010) 186–193. doi:10.1016/j.jcis.2009.08.041.
- [16] E.H. de Faria, K.J. Ciuffi, E.J. Nassar, M.A. Vicente, R. Trujillano, P.S. Calefi, Novel reactive amino-compound: Tris(hydroxymethyl)aminomethane covalently grafted on kaolinite, *Appl. Clay Sci.* 48 (2010) 516–521. doi:10.1016/j.clay.2010.02.017.
- [17] S. Song, L. Dong, Y. Zhang, S. Chen, Q. Li, Y. Guo, S. Deng, S. Si, C. Xiong, Lauric acid/intercalated kaolinite as form-stable phase change material for thermal energy storage, *Energy.* 76 (2014) 385–389. doi:10.1016/j.energy.2014.08.042.
- [18] K.B. Brandt, T.A. Elbokl, C. Detellier, Intercalation and interlamellar

- grafting of polyols in layered aluminosilicates. D-Sorbitol and adonitol derivatives of kaolinite, *J. Mater. Chem.* 13 (2003) 2566-2572. doi:10.1039/b306468a.
- [19] A.C. da Silva, K.J. Ciuffi, M.J. dos Reis, P.S. Calefi, E.H. de Faria, Influence of physical/chemical treatments to delamination of nanohybrid kaolinite-dipicolinate, *Appl. Clay Sci.* 126 (2016) 251–258. doi:10.1016/j.clay.2016.03.023.
- [20] L. Smrčok, D. Tunega, A.J. Ramirez-Cuesta, A. Ivanov, J. Valúchová, The combined inelastic neutron scattering (INS) and solid-state DFT study of hydrogen-atoms dynamics in kaolinite-dimethylsulfoxide intercalate, *Clays Clay Miner.* 58 (2010) 52–61. doi:10.1346/CCMN.2010.0580105.
- [21] J.A. Mbey, F. Thomas, C.J. Ngally Sabouang, Liboum, D. Njopwouo, An insight on the weakening of the interlayer bonds in a Cameroonian kaolinite through DMSO intercalation, *Appl. Clay Sci.* 83–84 (2013) 327–335. doi:10.1016/j.clay.2013.08.010.
- [22] S. Tosoni, K. Doll, P. Ugliengo, Hydrogen bond in layered materials: Structural and vibrational properties of kaolinite by aperiodic B3LYP approach, *Chem. Mater.* 18 (2006) 2135–2143. doi:10.1021/cm060227e.
- [23] R.M. Silverstein, F.X. Webster, D.J. Kiemle, Spectrometric identification of organic compounds, 7th ed., John Wiley & Sons, Ltd, Hoboken, 2005. <http://linkinghub.elsevier.com/retrieve/pii/002228607687024X>.
- [24] R.L. Frost, A.M. Vassallo, The dehydroxylation of the kaolinite clay minerals using infrared emission spectroscopy, *Clays Clay Miner.* 44 (1996) 635–651. doi:10.1346/CCMN.1996.0440506.
- [25] F. Sahnoune, N. Saheb, B. Khameh, Z. Takkouk, Thermal analysis of dehydroxylation of Algerian kaolinite, *J. Therm. Anal. Calorim.* 107 (2012) 1067–1072. doi:10.1007/s10973-011-1622-6.
- [26] X. Ma, J. Zheng, H. Pang, Intercalation of Mg-Al layered double hydroxides by L-proline: Synthesis and characterization, *Res. Chem. Intermed.* 38 (2012) 629–638. doi:10.1007/s11164-011-0376-x.
- [27] M. Valášková, M. Rieder, V. Matějka, P. Čapková, A. Slíva, Exfoliation/delamination of kaolinite by low-temperature washing of kaolinite-urea intercalates, *Appl. Clay Sci.* 35 (2007) 108–118. doi:10.1016/j.clay.2006.07.001.
- [28] A. Táborosi, R.K. Szilágyi, Behaviour of the surface hydroxide groups of exfoliated kaolinite in the gas phase and during water adsorption, *Dalton Trans.* 45 (2016) 2523–2535. doi:10.1039/C5DT03785A.

- [29] X. Li, Q. Liu, H. Cheng, S. Zhang, R.L. Frost, Mechanism of kaolinite sheets curling via the intercalation and delamination process, *J. Colloid Interface Sci.* 444 (2015) 74–80. doi:10.1016/j.jcis.2014.12.039.

ARTICLE II

Applied Clay Science 192 (2020) 105634



Contents lists available at ScienceDirect

Applied Clay Science

journal homepage: www.elsevier.com/locate/clay



Research Paper

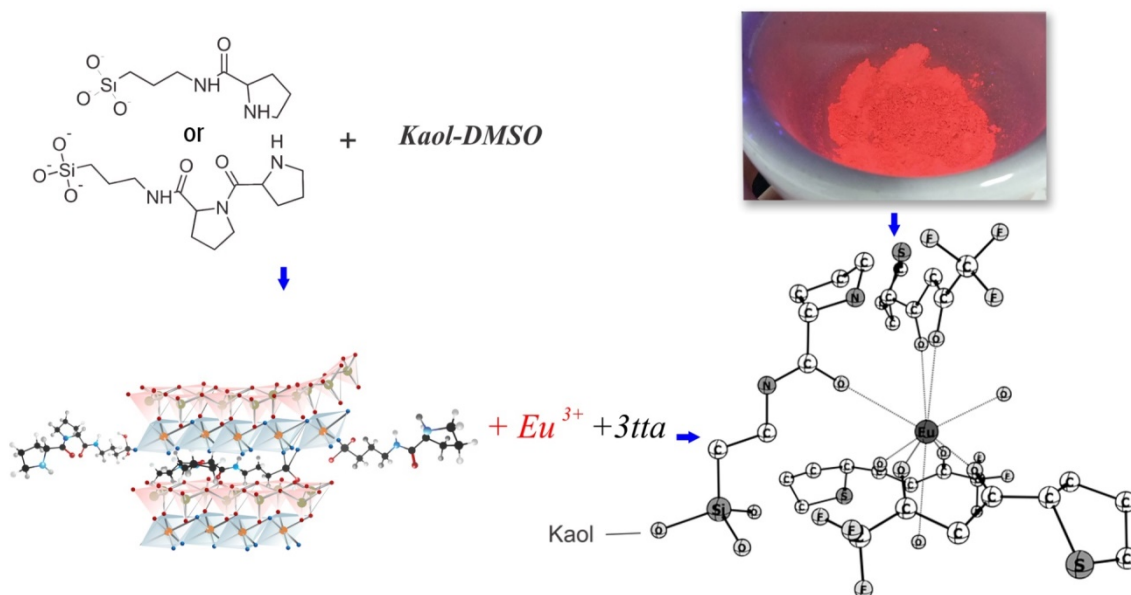
Luminescent properties of biohybrid (kaolinite-proline) materials synthesized by a new boric acid catalyzed route and complexed to Eu^{3+}

D.T. de Araújo^a, G.S. de Pádua^a, V.G. Peixoto^a, K.J. Ciuffi^a, E.J. Nassar^a, M.A. Vicente^{b,*}, R. Trujillano^b, V. Rives^b, M.E. Pérez-Bernal^b, E.H. de Faria^a

^a Universidade de Franca, UNIFRAN. Grupo de Pesquisas em Materiais Lamelares Híbridos (GPMatLam), Av. Dr. Armando Salles Oliveira, Parque Universitário, 201,

14404-600 Franca, São Paulo, Brazil

^b GIR-QUESCAT, Departamento de Química Inorgánica, Universidad de Salamanca, 37008 Salamanca, Spain



ABSTRACT

The properties of Eu^{3+} -biohybrid (kaolinite-proline) materials were investigated by powder X-ray diffraction, vibrational spectroscopy, scanning electron microscopy, nitrogen adsorption and photoluminescence to understand how Eu^{3+} interacts with the biohybrid matrices. Biohybrids were obtained through the conventional route and by two new catalytic routes for functionalization of clay minerals, and were then complexed to Eu^{3+} ions at a constant proline: Eu^{3+} molar ratio of 3:1, while the water molecules originally existing in the first coordination sphere of Eu^{3+} ions in the kaolinite-grafted complexes were replaced by 2-thenoyltrifluoroacetone (tta). The typical Eu^{3+} emission spectra for solids containing tta revealed the characteristic Eu^{3+} transitions from fundamental $^5\text{D}_0$ state to excited $^7\text{F}_J$ ($J = 0, 1, 2, 3$ and 4) states. The lifetime measurements also confirmed that water molecules were exchanged, increasing the emission efficiency. The time-resolved spectra allowed to remove the matrix and ligand emissions and thus to evaluate their influence on the emission of the lanthanide ion. After incorporation of Eu^{3+} , the thermal stability of the solids improved. The intercalated europium complexes did not show the same ligand/ Eu^{3+} molar ratio as the free complexes, due the restricted mobility of the ligands grafted within the interlayer of kaolinite. On the contrary, these complexes showed high internal quantum yield, low luminescence suppression (after tta coordination), preserved the kaolinite layered structure and also showed a low water molecules coordination number, which made them very attractive for luminescent applications, in addition to bringing high added value, due to its low cost, non-toxicity, non-polluting and high efficiency.

Keywords: Kaolinite, L-Proline, Biohybrids, Amidation, Europium, Luminescence.

1. Introduction

Lanthanide ions have been the subject of research in luminescent applications for many years due to their [Xe] 4fⁿ electronic configuration, the 4f shells are shielded by outer filled 5s and 5p orbitals, which gives a stable configuration to rare earth cations, resulting in unique spectroscopic and magnetic properties (Binnemans, 2009; Ryu et al., 2014). This results in sharp lines in the spectra, increasing the selectivity in various applications such as LEDs, OLEDs, lasers, and sensors, among others (BLASSE; GRABMAIER, 1994; YU et al., 2016). The trivalent oxidation state is the most stable for most of the lanthanide cations and their coordination numbers range from 6 even to 12. All trivalent lanthanides are classified as Pearson hard acids, thus binding to hard bases where the donor atom is highly electronegative and has low polarizability, as nitrogen, oxygen and sulfur (PEARSON, 1968).

Rare earths have low direct excitation luminescence efficiency, due to the low molar absorptivity, low ion concentration and the parity-selection rule, which prohibits these transitions that can be 10⁶ times weaker than the permitted transitions (BLASSE; GRABMAIER, 1994). This factor makes these ions to require a ligand with good absorptivity to transfer the received energy to the ion; this phenomenon is known as an “antenna effect” (BELTRÁN-LEIVA et al., 2017; SIGOLI et al., 2001). Organic ligands with aromatic rings or highly conjugated units are very promising for these materials providing greater electron resonance and consequently improving the energy transfer to the central ion. Therefore, the formation of organic-inorganic hybrid materials using lanthanide ions for luminescent purposes has been extensively studied in Material Chemistry in recent decades, combining the thermal stability and

structural stiffness of inorganic materials with the flexibility of organic compounds (DE FARIA et al., 2011).

A new class of these materials has aroused the interest of researchers in recent years, combining an inorganic matrix with biomolecules such as amino acids, proteins, carbohydrates, peptides and nucleic acids, being classified as biohybrids (DIRKS et al., 2007). These biomolecules derive from abundant, ecological and low-cost sources, which make them more attractive. In the context of this work, cyclic amino acids such as L-proline (L-Pro), L-phenylalanine and L-tryptophan, are very attractive for the formation of luminescent biohybrids because of their high molar absorptivity, and when complexed to lanthanide ions they increase the absorption of the molecule, bypassing the low coefficient of these isolated atoms, increasing their quantum yield and making them promising compounds for luminescent applications (BÜNZLI, 2015; BUNZLI; PIGUET, 2005). Despite the observed improvements in photoluminescent properties, these isolated complexes have low thermal and mechanical stability, requiring their incorporation in matrices such as aluminosilicates and polymers, among others (RYU et al., 2014).

Kaolinite has been used as an inorganic matrix in this work. Kaolinite is a 1:1 (TO) clay mineral containing tetrahedral and octahedral sheets with general minimum formula $\text{Al}_2\text{Si}_2\text{O}_5(\text{OH})_4$ (ALABA et al., 2015). It has a layered structure and between the lamellae it contains a hydroxylic surface from the octahedral sheet of aluminol $[\text{Al}(\text{OH})_3]$, which can form covalent bonds by condensation reactions (ZULFIQAR et al., 2015). Preparation of luminescent materials from smectite clays by simple methods, such as cationic exchange, has been widely explored (BERGAYA; VAN DAMME, 1983; OKADA; EHARA; OGAWA, 2007;

TRONTO et al., 2009). However, these systems present certain disadvantages, such as the weak absorption of Eu^{3+} above 250 nm due to forbidden f-f transitions, the presence of water in these matrices, requiring additional heat treatment for its removal, low quantum yields for emissive states below $30,000 \text{ cm}^{-1}$ and the loss of radiative emission resulting from the charge transfer (CT) originated by the interaction of the lanthanide with oxygen ions of the matrices (LEZHNINA et al., 2007). Opposite to smectite clay minerals, the kaolinite intercalation process is hampered as the clay is non-swellable, due to the hydrogen bonds between Al-OH and Si-O units, requiring pre-swelling by intercalating small, highly polar molecules such as dimethyl sulfoxide (DMSO), this process being almost compulsory for further functionalization (DEDZO; DETELLIER, 2016; HE et al., 2013). Once DMSO has been intercalated, larger molecules can be incorporated by displacing it, while maintaining the integrity of the crystalline structure (DE FARIA et al., 2009, 2012). Thus, the intercalated molecules act as precursors for the functionalization by organic or organometallic compounds finally producing materials for different applications, such as luminescent sensors, catalysts, contaminant adsorbent, among others (BARBOSA et al., 2015; MORETTI et al., 2012; WAINIPEE et al., 2013). This process contributes to reduce the influence of the environment in relation to smectites and provides stronger interactions such as covalent bonds preventing material from leaching.

Organosilane alkoxides, such as 3-aminopropyltriethoxysilane (APTES), have been recently used for kaolinite functionalization, aiming at some versatile properties such as organophilicity or metallic affinity, among others (YANG et al., 2012; ZHANG et al., 2015b). The organophilicity of silane is very convenient

for the incorporation of other molecules, such as amino acids. The immobilization of the silylating agent on the surface is called organic functionalization, a process that requires to activate the silanol groups eliminating the residual water molecules, and forming monodentate, bidentate or tridentate covalent bonds, the most common ones being mono and bidentate. Following incorporation of the silylating agent into the matrix, the alkoxide may be modified by an amidation reaction where condensation occurs by deprotonation of the aminosilane agent with the hydroxyl group of the carboxylic end of the amino acid.

The amidation reaction is responsible for the formation of peptides, indispensable to life and widely used in the pharmaceutical industry (BODE, 2015). Living organisms carry out the amidation reaction naturally through enzymes; however, for the amidation reaction to take place synthetically, an activator for carboxylic acid is required, such as high temperatures or a catalyst, which can generate many undesired by-products and increase the costs for treating these residues. To avoid this, several amidation procedures have been described in the literature to diminish costs and make the process feasible for green chemistry (Tang, 2012). The use of boric acid as a catalyst becomes feasible because it is low cost, non-toxic and high efficiency, being better than most of the reported amidation reaction catalysts (MYLAVARAPU et al., 2007). Boric acid reacts with the carboxylic acid to form a mixed anhydride and after reaction with the amine, boric acid is regenerated, leading to formation of the desired carboxamide (Fig. 1).

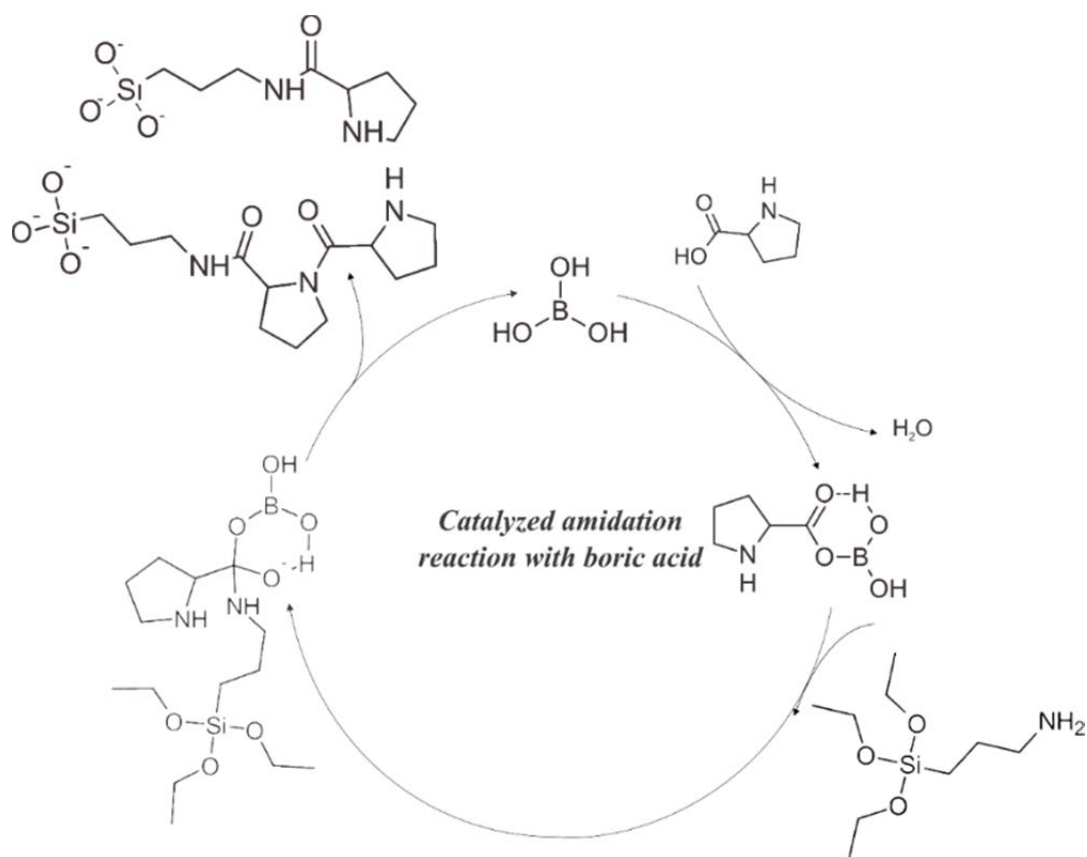


Fig. 1. Amidation reaction catalyzed by boric acid (Adapted from Arce et al., 2015).

The modification of the alkoxide with the amino acid through the amidation reaction catalyzed by boric acid is a new route for functionalization of clay minerals, different from conventional ones, and generating new possibilities of application. Therefore, the aim of this work was the development and study of new luminescent hybrid materials prepared by the functionalization of natural kaolinite with the amino acid L-Pro complexed to the europium ion, seeking to verify the spectroscopic and photophysical properties of the prepared materials, such as quantum yield, number of molecules of water in the first coordination sphere and lifetime of the excited state. These materials may be better suited for luminescent applications compared to materials obtained by the conventional routes, as biomarkers, sensors of contaminants, among others (Fig. S1). These materials were characterized by infrared spectrometry, powder

X-ray diffraction, element chemical analysis, thermal analysis and scanning electron microscopy (SEM). Luminescence spectroscopy evaluated the quantum emission yields of europium, the lifetime, the amount of water molecules in the first coordination sphere and the Judd-Ofelt intensity parameters.

2. Materials and Methods

2.1. Materials

The kaolinite used in this work came from the city of São Simão, in the state of São Paulo, Brazil, kindly provided by Darcy R.O. Silva and Cia. (São Simão-SP). The kaolinite was purified by dispersing and settling the natural clay in distilled water, as reported in previous studies (AVILA et al., 2010; DE FARIA et al., 2009); 2-thenoyltrifluoroacetone (tta) 99.0%; L-proline (99%) and Europium Oxide, Eu_2O_3 (99%), were provided by Sigma-Aldrich; 3-aminopropyltriethoxysilane, APTES, 97% and dimethyl sulfoxide, DMSO (99.9%) were provided by Synth; boric acid (99%) was provided by Dinâmica Ltda. and toluene (99.9%) was provided by J.T. Baker. Eu_2O_3 , insoluble in water, was transformed into $\text{EuCl}_3 \cdot \text{H}_2\text{O}$ by dissolving with HCl and further crystallization, while all the other reagents were used without further purification.

2.2. Characterization Techniques.

The powder X-ray diffraction analysis was performed on the solids obtained in a Rigaku equipment using Cu $\text{K}\alpha$ filtered radiation (40 kV, 30 mA). 2θ angle was scanned from 2 to 70° , with a scan speed of $0.04^\circ 2\theta$ per second at room temperature. The FTIR absorption spectra were recorded by the transmission method, in the range $400\text{-}4000\text{ cm}^{-1}$, averaging 32 scans to improve the signal-to-noise ratio, in a Perkin-Elmer Spectrum One spectrometer, on samples mixed with KBr (ca. 1:300 ratio sample/KBr), using KBr itself as background. Thermal analyses were performed in a TA Instruments SDT Q600 thermal analysis apparatus, using a standard mass of

10 mg of sample, under a 100 mL/min flow of synthetic air, and with a heating ratio of 20°C/min from 25°C to 900°C. The scanning electron microscopy (SEM) images were obtained in a Tescan Vega 3 SBH Model EasyProbe microscope, over samples dispersed with ethanol in a colloidal graphite aluminum cell and then coated with a thin gold layer by a Quorum SC7620 coating system. The nitrogen adsorption–desorption isotherms were obtained at – 196°C from a Micromeritics ASAP 2010; specific surface area was determined by the BET method while the total pore volume was determined from the nitrogen adsorbed at a relative pressure of 0.95 (ROUQUEROL; ROUQUEROL; SING, 1999).

The luminescence spectra (excitation and emission) in continuous light, time-resolved and lifetime measurements were obtained on the Fluorolog Horiba Jobin Yvon fluorometer. Measurements were carried out at room temperature. For the excitation spectra, the Corning 97202 filters with transmittance less than 0.2% below 470 nm were used, the inlet and outlet slots are described in the caption of each spectrum and all analyses were performed with an angle of detection of 45°.

3. Experimental

3.1. Synthesis of bio-hybrid materials

Kaolinite was intercalated with DMSO according to the Tunney and Detellier method (LETAIEF; DETELLIER, 2011; TUNNEY; DETELLIER, 1993, 1996). An amount of 30 g of purified kaolinite was mixed in a reflux system with 150 mL of DMSO and 50 mL of water and stirred for 10 days at 80°C. The material was then washed with ethanol several times and dried at 60°C. The intermediate thus obtained was designated Kaol-DMSO. This solid was functionalized with proline by three different methods:

i) Displacement method (de Faria et al., 2009, 2010): heating a 5:1 (w/w) mixture of amino acid and kaolinite near the amino acid melting temperature for 48 hours. The resulting material was washed in a Soxhlet system with ethanol for 24 hours, dried and designated Kaol-P.

ii) Functionalization of Kaol-DMSO with APTES alkoxide (molar ratio APTES:Kaol-DMSO 1:1) by dispersing their mixture at 180°C (YANG et al., 2012) (no solvent was used, as APTES is liquid), obtaining the solid Kaol-APS. This solid was then submitted to amidation with L-Pro catalyzed by boric acid, with molar ratios L-Pro:Kaol-APS 5:1 and boric acid:Kaol-APS 0.1:1 (ARCE et al., 2015; MYLAVARAPU et al., 2007). The resulting material was washed with toluene and ethanol six times and dried; the material was designated Kaol-AP1.

iii) APTES was first submitted to amidation with L-Pro catalyzed by boric acid (molar ratios L-Pro:APTES 1:1 and boric acid:APTES 0.1:1), and after 24 h of reaction, 4 g of Kaol-DMSO was added and the mixture was stirred for 24 h

at 180°C. The resulting material was washed with toluene and ethanol six times and dried, being designated as Kaol-AP2.

The three solids obtained were agitated for 7 days in aqueous dispersions, with a solid/water w/w ratio 1:100 to verify that the structures of the solids were maintained.

3.2. Eu³⁺ ion complexation

The Eu (III) ion was complexed to the hybrid materials using a ligand/cation molar ratio of 3:1 (after determination of the chemical analysis of the hybrids). The samples were stirred for 24 h at a fixed pH of 6, being then centrifuged and dried. Subsequently, 0.071 mol/L solution of tta in 1:2.5 water/ethanol was added, with a 3:1 molar ligand/cation ratio. The samples were named Eutta-Kaol-P; Eutta-Kaol-AP1 and Eutta-Kaol-AP2 for the samples derived from Kaol-P, Kaol-AP1 and Kaol-AP2 samples, respectively.

4. Results and Discussion

4.1. Hybrid materials

Purified Kaol had the chemical formula, referred to Al content, $\text{Si}_{2.04}\text{Al}_{2.00}\text{Fe}_{0.03}\text{Mg}_{0.01}\text{K}_{0.02}\text{Ti}_{0.04}\text{O}_{7.23}$. This formula was very close to the kaolinite theoretical one, $\text{Si}_2\text{Al}_2\text{O}_7$, suggesting very small amounts of admixtures (DE FARIA et al., 2009). Fe^{III} and Ti^{IV} may be present in the octahedral sheet of the clay or forming segregated minerals, while Mg^{2+} and K^+ may be part of other clay minerals existing in the sample (DE FARIA et al., 2009). The specific surface area of the solid was $17 \text{ m}^2/\text{g}$, and the total pore volume $0.14 \text{ cm}^3/\text{g}$, similar to literature results for kaolinite from this deposit and from other deposits (DE FARIA et al., 2009, 2010; SONG et al., 2014).

Purified kaolinite has a basal spacing of 0.71 nm (Fig. 2), which correctly expands to 1.12 nm with DMSO intercalation (LETAIEF; DETELLIER, 2007) (diffractogram not shown). A very weak reflection due to non-intercalated kaolinite was also recorded, allowing to calculate the amount of reacted kaolinite (MBEY et al., 2013; OLEJNIK et al., 1968; SMRČOK et al., 2010) (Table S1, Supplementary Data).

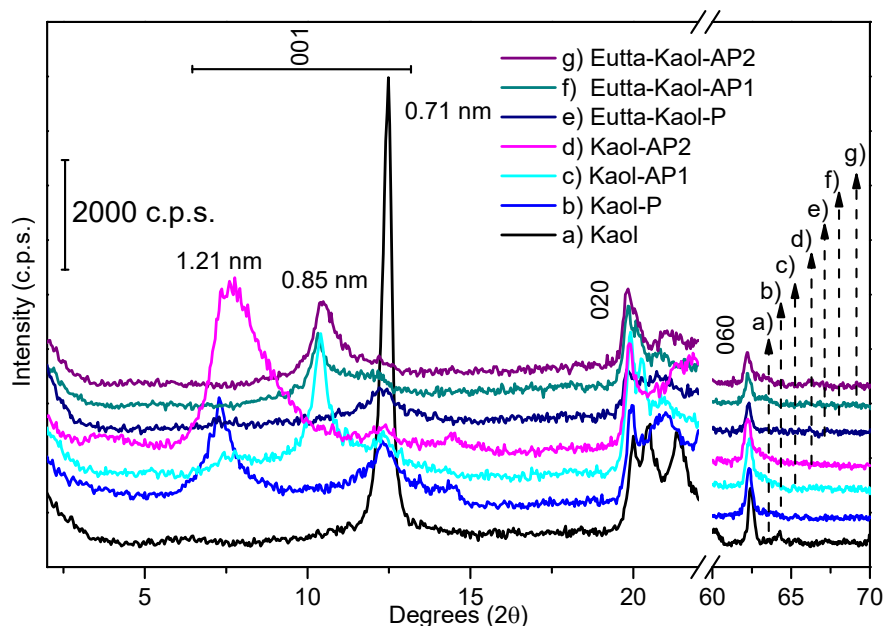


Fig. 2. X-ray diffractograms of the different solids, in the 2-25° and 60-70° (2θ) regions.

The crystallinity, evaluated by the FWHM index, increased from purified kaolinite to the solid treated with DMSO, showing that intercalation with this molecule favored the long-distance stacking of the layers, but incorporation of the other molecules decreased the stacking degree. The ratio between the intensities of the peaks due to the diffraction by planes (001) and (020) allowed to evaluate the orientation of the particles, again obtaining the maximum value for the DMSO-intercalated sample, and strongly decreased when treating it with the other compounds. The (020) plane was used as a reference because its reflection showed a high intensity and was not significantly altered by the different treatments (SMRČOK et al., 2010).

The sample functionalized with L-Pro without the use of APTES (Kaol-P) had a basal spacing of 1.21 nm, larger than those for the other samples. The increase of the interlayer spacing, 0.5 nm, matches the size of the L-Pro molecule (0.5 nm size, calculated by ACD ChemSketch software, <http://www.acdlabs.com/resources/freeware/chemsketch/>), confirming the

intercalation of the amino acid. However, this sample showed the lowest intercalation rate (59%), with a significant decrease in crystallinity with respect to parent kaolinite and to the DMSO-intercalated sample.

Amidation reactions led to solids with basal spacings of 0.85 and 1.14 nm, respectively. In the first case, the basal spacing was the same as that of Kaol-APS, suggesting that its arrangement was maintained, again with a low crystallinity and a decrease of the intercalation degree. For sample Kaol-AP2, the previous reaction of the alkoxide and the amino acid in the presence of boric acid led to a larger basal spacing and a higher intercalation degree, suggesting a perpendicular orientation of the molecules in the kaolinite interlayer, as previously reported by Yang et al. (2012). This conformation was lost after incorporation of the europium (III) cations, resulting in the displacement of the 1.13 nm peak in the precursor to 0.84 nm in the complexed samples. The reflections not related to the layers stacking remained unchanged in all samples, particularly the in-plane 060 reflection at 62.5° (2θ), suggesting that the layers were not affected by the treatments (TONLÉ et al., 2007), and these only affected to the height of the basal spacing and to the stacking of the layers along the c-axis.

The nitrogen adsorption isotherms of the solids (Fig. S2) showed a small curve concave to the p/p^0 axis, referring to the formation of an adsorption monolayer and a second broader region convex to the p/p^0 axis, attributed to the formation of adsorption multilayers. A slight displacement of the desorption curve in the region of multilayer formation caused the isotherms to be classified as type IV, characteristic of mesoporous materials, which may contain micropores (ROUQUEROL; ROUQUEROL; SING, 1999). There was a

decrease in the specific surface area (Table S2) when forming the biohybrids, indicating the presence of organic matter which would decrease the adsorption of nitrogen gas, Kaol-AP2 showing the lowest value.

The signals in the FTIR spectrum of kaolinite (Fig. 3) were ascribed to axial vibrations of its different types of OH groups (Fig. S3), at 3620 cm^{-1} (OH1), 3668 cm^{-1} (OH2), 3653 cm^{-1} (OH3), and 3696 cm^{-1} (OH4) (Table S3). These positions were very close to the values (3620 , 3668 , 3651 and 3694 cm^{-1} , respectively) reported by Tosoni et al. (2006), and thus it was possible to verify that OH1 species did not participate in the bonds because of the steric hindrance derived from its intramolecular location. The Si-O-Al-O-Si vibrations were recorded in the $1000\text{-}1100\text{ cm}^{-1}$ range, without significant changes for the treated samples. Axial vibrations of the interlamellar and intralamellar aluminol groups were recorded at 938 and 912 cm^{-1} , respectively (DE FARIA et al., 2009; FROST, 1996; TOSONI; DOLL; UGLIENGO, 2006).

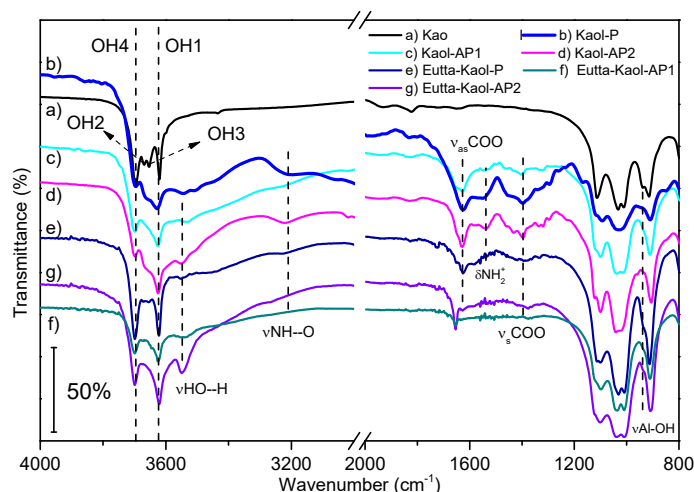


Fig. 3. Infrared absorption spectra of the different solids.

After intercalation with DMSO, two new bands were recorded at 3540 and 3504 cm^{-1} , resulting from the hydrogen bonds between the hydroxyl groups of the interlamellar region of kaolinite and the DMSO molecules (Zhang et al.,

2015a). The interactions through hydrogen bonds were confirmed by the shifting of the characteristic aluminol vibration from 938 cm^{-1} in kaolinite to 953 cm^{-1} in Kaol-DMSO, along with the development of a new signal at 959 cm^{-1} . The characteristic bands related to C–H bonds were recorded at 3023 and 2936 cm^{-1} . The antisymmetric Si–O stretching band shifted from 1034 to 1030 cm^{-1} , showing now a shoulder, suggesting that water molecules entered into the hexagonal cavities of the tetrahedral silicon disturbing these bonds (MA; ZHENG; PANG, 2012). For the Pro-treated sample, Kaol-P, bands related to CH_2 and C–H stretching became very broad. The OH₂ and OH₃ signals disappeared, suggesting a strong interaction between kaolinite and L-Pro, as confirmed by the development of bands at 3544 and 3510 cm^{-1} , attributed to stretching of HO–H and/or CH–O bonds, and NH-stretching vibrations (SILVERSTEIN; WEBSTER; KIEMLE, 2005; WAGNER; TORRE; BARAN, 2008).

Bands assigned to angular in-plane NH_2 vibration and NH and/or HO–H stretching bands were observed in the spectrum of sample Kaol-AP1. Broadening of the bands between 3000 – 2000 cm^{-1} as well as the characteristic bands of L-Pro –COOH group at 1628 and 1400 cm^{-1} were also recorded. For the Kaol-AP2 sample, the out-of-plane vibration band due to NH_2 shifted to 1538 cm^{-1} , suggesting its participation in the interaction. The signal at 1432 cm^{-1} was attributed to the shift of the band due to the symmetric stretching mode of the COO^- group, characteristic of the interaction via this group. Interaction with L-Pro was also evidenced by the development of an Al–O band at 960 cm^{-1} and modifications in the bands of the OH₂ and OH₃ hydroxyl groups. In the L-Pro-containing samples, the stretching bands due to hydrogen bonds between the

amine and the carboxylate groups were recorded close to 3220 cm^{-1} , evidencing L-Pro condensation (that is, L-Pro- L-Pro) or the interaction between L-Pro and APTES (SIFFERT; KESSAISSIA, 1978).

The molecular formula of the organic matter involved in the functionalization routes was proposed from the chemical composition of the solids, taking into account the possible reactions between the functional groups of the different compounds, and referring this amount to kaolinite unit cells (Table S4). Thus, for the Kaol-P sample, the C/N ratio in the solid was similar to that in pure L-Pro, confirming that the amino acid was incorporated in its molecular form, in a ratio of one L-Pro molecule per 3 kaolinite cells. When both APTES and L-Pro were involved in the synthesis, various reactions were possible. When kaolinite had been previously functionalized with APTES and then submitted to amidation with L-Pro, sample Kaol-AP1, three main chemical possibilities can be proposed: i) L-Pro and APTES interact with kaolinite separately; ii) the alkoxide incorporated to the clay reacts with L-Pro; and iii) the amount of APTES functionalized in the kaolinite is larger in relation to the L-Pro. From the calculated average C/N ratio, it was concluded that one organic moiety was fixed per 12 kaolinite unit cells. For the Kaol-AP2 sample, the APTES- L-Pro catalytic amidation took place before being in contact with the clay, and four main possibilities were considered: i) formation of the modified alkoxide; ii) formation of a peptide bond between two L-Pro molecules; iii) reaction between APTES and the two- L-Pro peptide; and iv) APTES and L-Pro interact separately with kaolinite. The average value of these possibilities led to the presence of one organic moiety per 17 kaolinite unit cells.

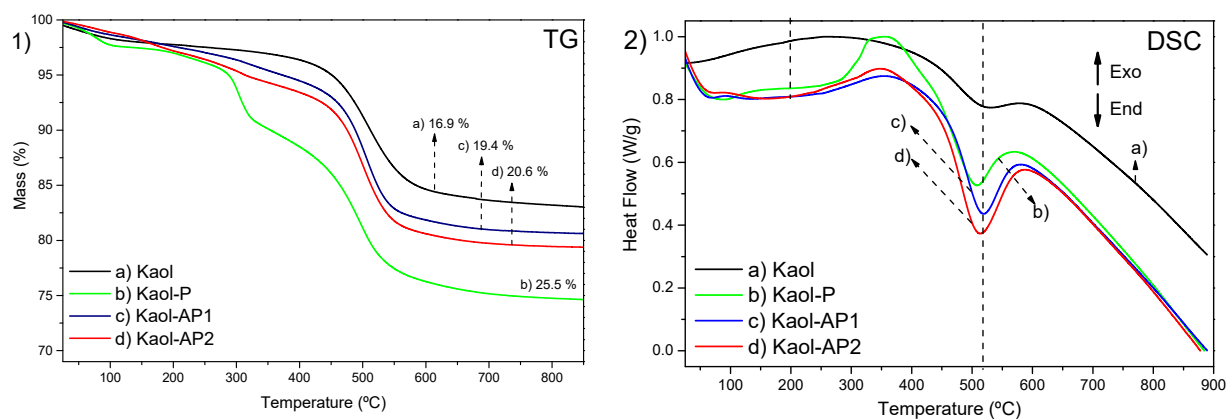


Fig. 4. TG (1) and DSC (2) curves for samples Kaol, Kaol-P, Kaol-AP1 and Kaol-AP2 in oxidizing atmosphere, from 25 to 900°C, with heat flow results normalized between 0 and 1.

The thermogravimetric curve of kaolinite (Fig. 4) showed a small mass loss near 65°C due to removal of adsorbed water, another mass loss due to endothermic dehydroxylation of the structure near 510°C, resulting in the formation of metakaolinite, and finally, the loss of the remaining hydroxyl groups near 900°C occurred, leading to the formation of mullite (DE FARIA et al., 2009; LETAIEF; DETELLIER, 2007) (DTG curves in Fig. S4). In all cases, after removal of the organic matter, the main effect was the dehydroxylation of kaolinite near 500°C, essentially identical to that observed in natural kaolinite (LETAIEF; DETELLIER, 2011), but in all cases showing a decrease in the dehydroxylation temperature, which agreed with functionalization, as this made the solid surface more hydrophobic, favoring the elimination of water generated from condensation of hydroxyl groups. Kaol-P showed the largest mass loss of the L-Pro-containing samples, 25.5%. After an initial mass loss (2.3%, 78°C), due to removal of adsorbed water, the combustion of L-Pro was clearly observed as an effect located at 304°C, with 7.2% of mass loss, suggesting that the access of L-Pro to the interlayer space was relatively easy. This loss was observed as a broad exothermic effect in the DSC curve, probably because L-

Pro adopted different conformations in the interlayer and the temperature at which L-Pro was desorbed was not high enough to complete its combustion. The last mass loss (16%) was centered at 495°C, and in addition to kaolinite dehydroxylation, it should also include the last stage of L-Pro decomposition (MA; ZHENG; PANG, 2012).

For samples Kaol-AP1 and Kaol-AP2, where a reaction under catalytic conditions had taken place, removal of L-Pro was almost negligible. It was detected as a very small effect in the DSC curve near 310°C (Fig. 4); however, a continuous mass loss was observed until dehydroxylation. In both cases, dehydroxylation seemed to occur at the same time as the end of the decomposition of the organic matter (MA; ZHENG; PANG, 2012), probably due to the presence of the silylated part of the alkoxide. Formation of silica from the alkoxide also decreased the total mass loss, as silica formed was not removed upon heating. The amount of organic matter determined by both thermogravimetric analysis and element chemical analysis showed similar results (LETAIEF; DETELLIER, 2011).

Kaolinite preferably oriented towards the formation of microcrystals of hexagonal shape parallel to the (001) plane, agglomerating in tactoids, in which changes can undergo by intercalation/functionalization (Fig. 5). On increasing the interlayer space, the hydrogen bonds were weakened, which limited the lamella overlapping, consequently modifying the initial kaolinite morphology. But despite this slight modification, the kaolinite plate-like morphology was maintained in the three samples, not lost by delamination, explaining the broadening in the peaks from (001) reflection in the diffractograms.

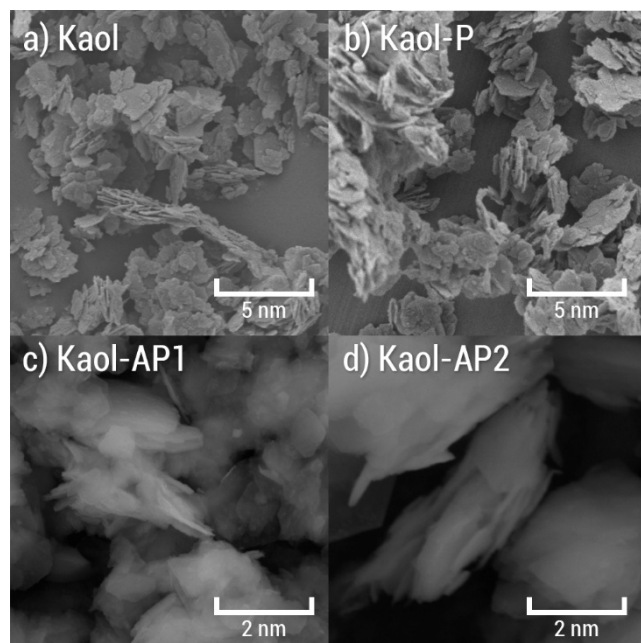
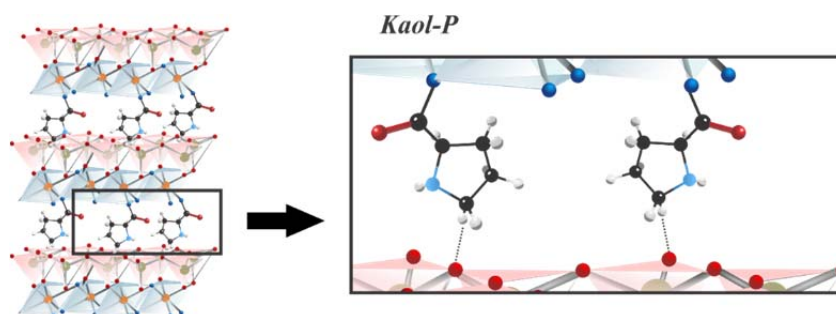


Fig. 5. SEM micrographs of the solids indicated.

Considering all the characterization results, structural models can be proposed for the biohybrid materials. Thus, the direct intercalation of L-Pro in the interlayer space is proposed for Kaol-P; FTIR and PXRD results confirmed that L-Pro was located in the interlayer region and it bound in the covalent form, thermal analyses indicated that with one L-Pro molecule for every three kaolinite unit cells (Fig. 6). L-Pro molecules should be oriented perpendicular to the layers, and their carboxylate groups may be bonded to the layers.



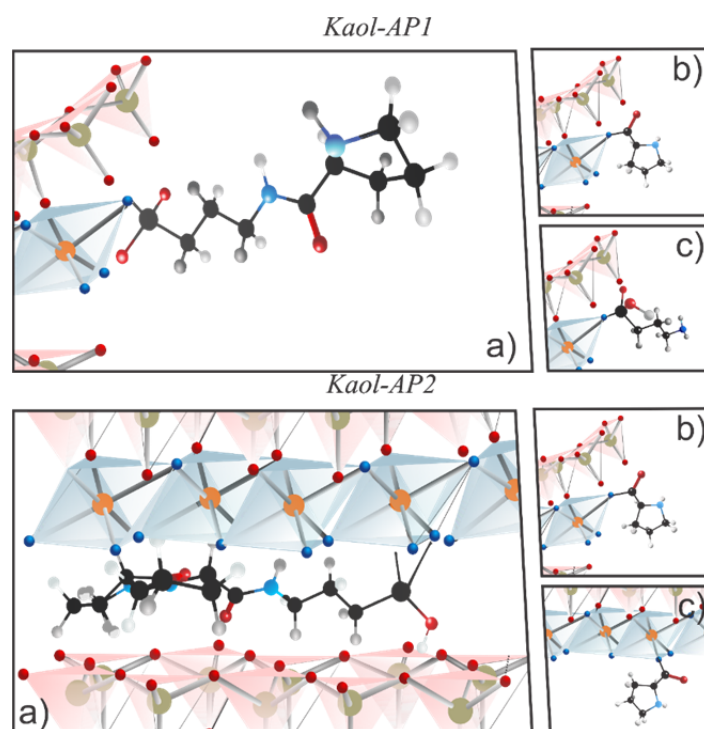


Fig. 6. Proposed models for the samples Kaol-P, Kaol-AP1: a) functionalized modified alkoxide, b) functionalized proline in kaolinite and c) unreacted functionalized APTES alkoxide produced in the amidation reaction and Kaol-AP2: a) modified alkoxide in the interlayer space functionalized and/or interacting by hydrogen bonding; b) unmodified proline parallel to the layer, c) unmodified proline in the interlayer space.

For Kaol-AP1 material, individual APTES and L-Pro molecules and the product of their amidation reaction can modify kaolinite (Fig. 6), as more than one 001 reflection were observed in its PXRD diagram, with the same basal spacings that Kaol-APS and Kaol-P, but more dispersed on the inorganic matrix. While for the Kaol-AP2 material the decrease in the dehydroxylation temperature of kaolinite evidenced functionalization, the IR band of the aluminol species confirmed the presence of kaolinite without interaction by covalent bonds. The presence of a basal reflection in the same position as for sample

Kaol-P indicated that this solid contained unmodified L-Pro in the interlayer space (Fig. 6).

4.2. Luminescence spectroscopy

Trivalent europium emits photons in the visible region, mainly in the red region (610 nm) (BINNEMANS, 2015), relaxing from the excited state 5D_0 to the 7F_J ($J = 0, 1, 2, 3$ and 4) ground states, featuring a long decay time and thin bands due to the shielding of f-f transitions, very attractive properties for luminescent applications. Ligands with efficient absorption and efficiency in the intramolecular ligand-metal energy transfer process are required (SABBATINI; GUARDIGLI; MANET, 1996). Bidentate organic ligands and aromatics effectively contribute to energy absorption acting as "antennae" transferring energy to Eu^{3+} (DEOLIVEIRA et al., 2007; LEZHNINA et al., 2007), consequently, Eu^{3+} can be used as an activator in L-Pro-functionalized kaolinite (organic ligand) providing a material with luminescent properties.

The secondary ligand tta acts on energy levels, contributing to the transport of energy between the singlet states to the triplet and the excited states of the Eu^{3+} ion, being able to either absorb and transfer directly to the central ion or receive energy from the amino acid L-Pro, resulting in increased energy transfer efficiency between the ligands and the central ion (LI et al., 2009). In addition, tta contributes to the decrease of water molecules in the first coordination sphere, consequently decreasing quenching (WAYCHUNAS, 2014).

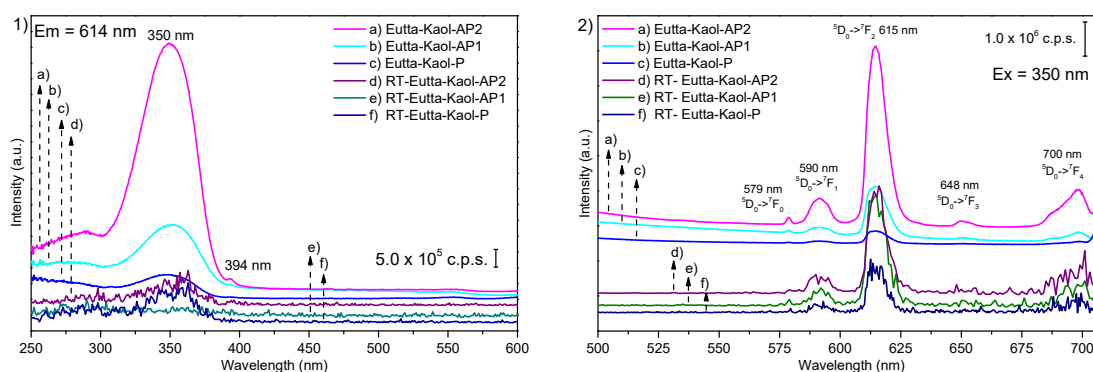


Fig. 7. Excitation (1) and emission (2) spectra of complexed precursors with europium (III) in continuous light and time-resolved (RT).

The broad excitation bands in the luminescence spectra of the Eu^{3+} complexed samples (Fig. 7) were attributed to a charge transfer process between the ligand and the central ion (BINNEMANS, 2009, 2015; BÜNZLI, 2015; REINHARD; GÜDEL, 2002; ZOLIN et al., 2004). The ligands absorbed energy from their ground state (S_0) to an excited state, which return may occur via various radiative (fluorescence) or non-radiative transitions by molecular rotations or vibrations; however, the energy can be also transferred from the excited state of the ligand (S_1) to a triplet state (T_1) that can itself relax to the ground state (S_0) through radiation (phosphorescence) or vibrations/rotations, transferring energy to the other species in the case of the excited state 5D_0 of the Eu^{3+} ion which when relaxing to the fundamental states 7F_J ($J = 0-4$) emits in the red region, the 7F_2 transition generally with greater intensity (BINNEMANS, 2015; BÜNZLI, 2015; DE SÁ et al., 2000). This fact can be observed in the emission spectra of the samples, where they were excited in the charge transfer bands and in the characteristic regions of the Eu^{3+} ion.

Kaolinite had a band with a maximum peak at 250 nm that was slightly displaced after the organic phase was functionalized (Fig. S5), which was wrongly ascribed to the ligand-metal charge transfer (LMCT) allowed by Laporte's rule (BÜNZLI et al., 2007). Two other broad bands at 358 nm and 376

nm were related to the matrix absorption which, after complexation, and gave rise to a single broad band related to the ligand-metal charge transfer (LMCT) between the complex and the matrix, showing great intensity (DE FARIA et al., 2011). The Eutta-Kaol-AP2 sample showed a higher intensity for the charge transfer $tta \rightarrow Eu^{3+}$ band, indicating an easy energy transfer to the Eu^{3+} ion emission. As already mentioned, the influence of tta on the complex was decisive for the intensity of emission; however, the difference in intensities of the Eutta-Kaol-AP2 sample in relation to the others can be explained by several reasons, such as a greater intercalation ratio (77%) of the other precursors and a lower ligand concentration of the precursor, increasing the dispersion and removing the oscillator, evidenced in the X-ray diffractograms and thermal analysis. The larger (0.43 nm) interlayer space than in the precursor favored an easier and larger mobility in the reaction between the ligand and the Eu^{3+} ion, facilitating the interaction between the secondary ligand and the Eu^{3+} complex, thus removing the water molecules originally coordinated to the central ion, decreasing the luminescence suppression and consequently increasing the emission intensity.

The transition ${}^5D_0 \rightarrow {}^7F_0$ showed a single broad band (2 nm, 0.2 nm increment) in all samples, indicating the presence of complexes distributed in different sites or in compounds of polymeric structure (BUENZLI; CHOPPIN, 1989). The emission intensity of this transition was also related to the symmetry of the compound, its increase indicated that the ion occupied distinct environments (CICCONI et al., 2017). Since the transition ${}^5D_0 \rightarrow {}^7F_0$ is a typical electric dipole transition, it is very sensitive to the Eu^{3+} ion symmetry site, but the ${}^5D_0 \rightarrow {}^7F_1$ is a transition of magnetic dipole, so it is hardly influenced by the

chemical environment; as a result, it is possible to establish an analysis between intensities through the ratio of the intensities of the bands due to the transitions $I(^5D_0 \rightarrow ^7F_0)/I(^5D_0 \rightarrow ^7F_1)$ (R_0) and $I(^5D_0 \rightarrow ^7F_2)/I(^5D_0 \rightarrow ^7F_1)$ (R_2) (Table 1), serving as an indicator of the chemical environment where the higher the ratio, the lower the symmetry and the greater the degree of covalence in the interaction between the ion and the ligand (DE ARAUJO et al., 2017; ZHOU et al., 2013). The intensities of the characteristic dipole-electric transitions related to the $^5D_0 \rightarrow ^7F_1$ transition, allowed by a magnetic dipole mechanism, indicated an environment of low symmetry caused by the formation of the complex with different stoichiometries. The samples synthesized by catalyzed amidation showed lower symmetries for the complexes in relation to the traditional route.

Table 1

Spectroscopic parameters obtained by luminescence spectroscopy. *

	R_0	R_2	Ω_2 (10^{-20} cm^2)	Ω_4 (10^{-20} cm^2)	A_{rad} (s^{-1})	A_{nrad} (s^{-1})	τ_{obs} (ms)	τ_{rad} (ms)	q	$Q_{\text{Ln}}^{\text{Ln}}$ (%)
TR-Eutta-Kaol-P	0.37	4.79	10.10	7.27	2930	27100	0.21	1.89	4	11
Eutta-Kaol-P	0.74	3.01	5.25	12.00	3290	12700	0.21	3.11	4	66
TR-Eutta-Kaol-AP1	0.34	6.79	12.35	5.82	4160	12100	0.26	1.74	3	15
Eutta-Kaol-AP1	0.83	3.19	4.55	2.66	273	793	0.26	3.54	3	7
TR-Eutta-Kaol-AP2	0.18	5.82	10.30	7.00	4100	21900	0.16	1.91	1	28
Eutta-Kaol-AP2	0.41	5.62	8.41	4.92	4400	24500	0.16	0.23	2	69

* Ratio between the areas of the bands corresponding to $I(^5D_0 \rightarrow ^7F_0)/I(^5D_0 \rightarrow ^7F_1)$ (R_0) and $I(^5D_0 \rightarrow ^7F_2)/I(^5D_0 \rightarrow ^7F_1)$ (R_2); Judd-Ofelt parameters Ω_2 and Ω_4 ; total radiation (A_{rad}) and non-radiation (A_{nrad}) emission rate; obtained lifetime ratio (τ_{obs}) and lifetime of radiative emission (τ_{rad}); number of water molecules in the first coordination sphere (q) and internal quantum yield of radiative emission ($Q_{\text{Ln}}^{\text{Ln}}$).

These $4f \rightarrow 4f$ transitions also provided information about the chemical environment of the Eu^{3+} ion such as ion microsymmetry, bond covalence, influence of vibration transitions, among others, through the Judd-Ofelt intensity

parameters (MOURA et al., 2016): the higher value for the intensity parameter Ω_2 , lower the symmetry, and it is sensitive to small angular variations. As for the higher ranks intensity parameter of Ω_4 , they are more sensitive to the distance between the Eu^{3+} and the ligands.

According to Supkowski and Horrocks (2002), for trivalent lanthanide ions, especially Eu^{3+} and Tb^{3+} , it is possible to identify the influence of each functional group in the complex on non-radiative relaxation. These functional groups release the energy absorbed in the form of vibration and are called oscillators. The amino acid groups such as amine and carboxylate contribute to the non-radiative relaxation of the complex. The Eutta-Kaol-AP2 sample showed a greater mobility of the organic phase in the matrices, allowing to form a complex with greater rigidity due to the coordination of these groups, decreasing their oscillation and improving the efficiency in radiative emission.

The time resolved spectra are intended to remove matrix and ligand emissions and thus to evaluate their influence on the Eu^{3+} emission. The emission efficiency of the Eu^{3+} ion in these spectra was reduced, except for sample Eutta-Kaol-AP1, which presented a low efficiency compared to the others, 7% (Table 1). This was due to the high concentration of isolated L-Pro and APTES molecules in kaolinite compared to modified alkoxide (See three samples in Fig. 8), which greatly decreased the ligand conjugation, in addition to the increase of oscillating groups contributing to suppression of luminescence. This showed that low conjugation molecules such as APTES did not contribute significantly to radiative emission, even though they did not have a longer lifetime, since besides providing a low energy transfer to the central

ion, the number of oscillating groups still increased, which did not occur for the other complex samples.

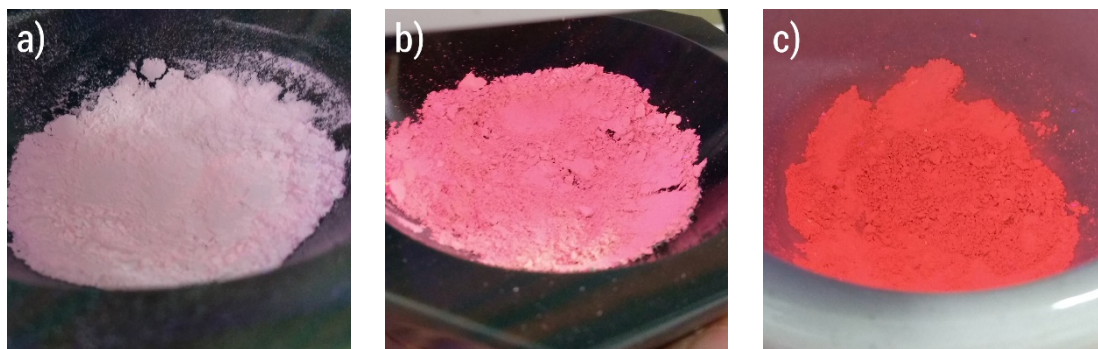


Fig. 8. Photographs of solids a) Eutta-Kaol-P, b) Eutta-Kaol-AP1 and c) Eutta-Kaol-AP2.

The Eutta-Kaol-AP2 sample showed higher quantum efficiency (69%) and lower hydration number (2) in the first coordination sphere, showing that this boric acid-catalyzed route was the most suitable for Eu^{3+} ion complexation and consequently for luminescent applications. Higher dispersion of organic molecules in the matrix combined with higher efficiency of APTES alkoxide modification with amino acid provided better complexation of Eu^{3+} ion by the hybrid material. The modified alkoxide increased the molecule mobility for complexation, the changes in the PXRD peak strongly supported that the modified alkoxide located within the kaolinite interlayer space went out of this region for favoring coordination. In the Eutta-Kaol-P sample, unlike Eutta-Kaol-AP2, where the alkoxide remained bound to the matrix, amino acids were removed from the interlayer space in the complexation process, interacting with the matrix by intermolecular forces such as hydrogen bond and van der Waals forces (Fig. 9).

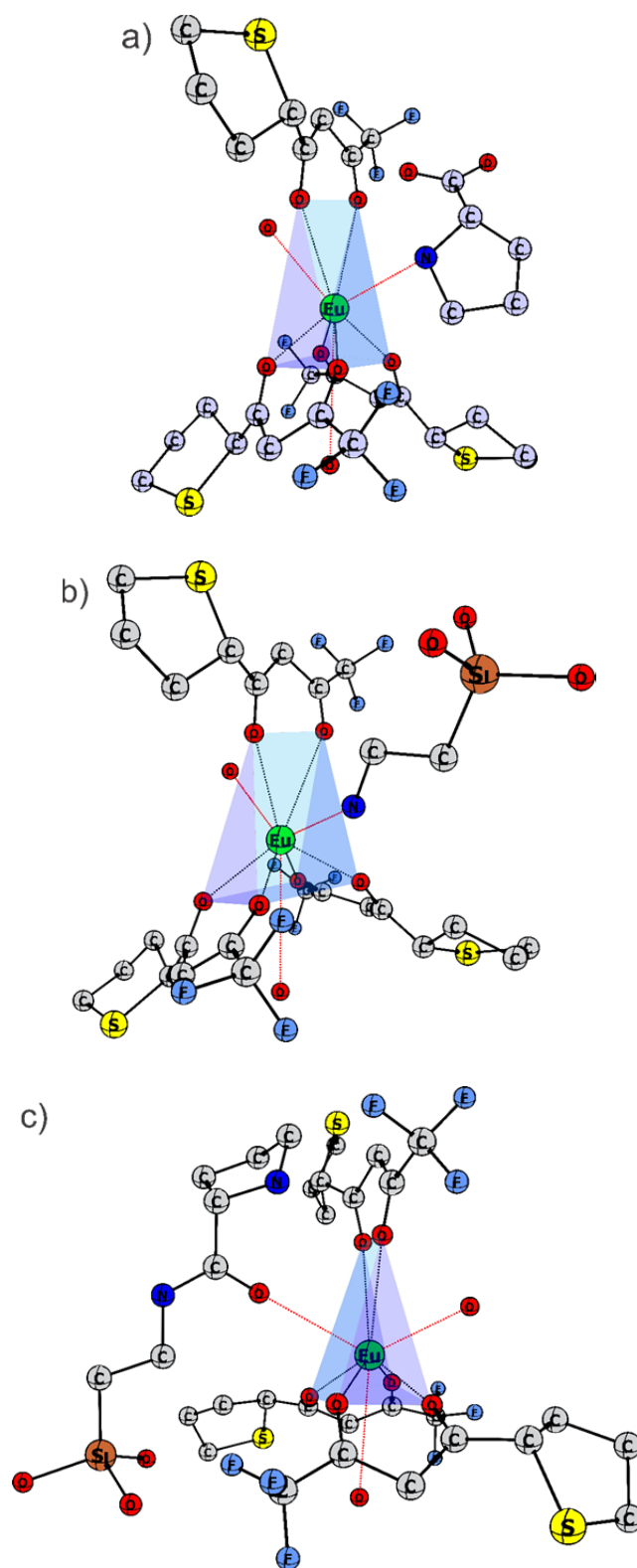


Fig. 9. Schematic model of the main proposals of the Eu^{3+} complexes for a) Eutta-Kaol-P, b) Eutta-Kaol-AP1 and c) Eutta-Kaol-AP2.

Europium(III) complexes with organic ligands generally have high mobility and can form different coordination compounds with different

symmetries (BINNEMANS, 2005). When added to the tta ligand, they tend to adopt a slightly distorted trigonal prism symmetry or slightly distorted quadrangular antiprism, stabilizing with 8 or 9 coordination sites according to reported similar studies (BINNEMANS, 2005; LI et al., 2009; STANLEY et al., 2010), with the formula $[\text{Eu}(\text{tta})_3(\text{H}_2\text{O})_q\text{L}]$ where q is the hydration number and L are the organic-inorganic hybrid ligands. As they had different complexing environments, the symmetry values of the complexes changed. Analyzing the intensities of $4f \rightarrow 4f$ transitions, for both R_0 and R_2 intensities, in relation to the magnetic dipole transition and Judd-Ofelt parameters, low symmetries were observed, resulting in environments without center of symmetry, except for the Eutta-Kaol-P sample, which indicated higher intensity parameter values among the complexes. The Eutta-Kaol-AP2 sample showed the smallest R_2 and Ω_2 values among all the hybrid materials here studied, indicating a lower symmetry and a larger covalence degree between the metal ion and the ligand (MOURA et al., 2016). From time-resolved spectroscopy the intensity values of the parameters increased, that is, when emissions from the ligand containing the modified kaolinite were not considered, the symmetry was even lower.

5. Conclusions

Kaolinite was successfully functionalized by three different routes and complexed with Eu^{3+} , and the photoluminescent properties of the obtained solids were studied. A new route for kaolinite functionalization through the boric acid catalyzed amidation reaction between APTES and the amino acid L-Pro proved to be efficient for increasing kaolinite organophilicity, being a reaction route suitable for Green Chemistry, with low cost, and easily reproducible. The

physical properties of sample Eutta-Kaol-AP2, obtained by this new route, such as dispersion, thermal resistance, and improved radiative emission efficiency of the complex, make these materials better suited for luminescent applications compared to materials obtained by the conventional routes, as biomarkers, sensors of contaminants, among others. The new material has high added value and may be applicable in a variety of related areas, due to its low cost, non-toxicity, non-polluting activity and high efficiency.

Declaration of Competing Interest

None.

Acknowledgements

The authors thank a Cooperation Grant jointly financed by Universidad de Salamanca (Spain) and FAPESP (Brazil), reference 2016/50322-2. The Spanish group acknowledges the support from MINECO and ERDF (MAT2016-78863-C2-R). The Brazilian group acknowledges the support from research funding agencies Fundação de Amparo à Pesquisa do Estado de São Paulo, FAPESP (2013/19523-3, 2018/26569-3 and 2017/15482-1), and Coordenação de Aperfeiçoamento de Pessoal de Nível Superior (CAPES) and Conselho Nacional de Desenvolvimento Científico e Tecnológico, CNPq (311767/2015-0 and 303135/2018-2). The equipment of Brazilian group has been financed by FAPESP (1998/11022-3, 2005/00720-7, 2011/03335-8, 2012/11673-3 and 2016/01501-1). DTA thanks Universidade de Franca and Universidad de Salamanca for a “Cotutela PhD” facilities.

References

Alaba, P.A., Sani, Y.M., Mohd, W., Daud, A.W., 2015. Kaolinite properties and advances for solid acid and basic catalyst synthesis. RSC Adv. 5, 101127–

101147. <https://doi.org/10.1039/c5ra18884a>
- Arce, G., Carrau, G., Bellomo, A., González, D., 2015. Greener Synthesis of an Amide by Direct Reaction of an Acid and Amine under Catalytic Conditions. *World J. Chem. Educ.* 3, 27–29. <https://doi.org/10.12691/wjce-3-1-4>
- Avila, L.R., de Faria, E.H., Ciuffi, K.J., Nassar, E.J., Calefi, P.S., Vicente, M.A., Trujillano, R., 2010. New synthesis strategies for effective functionalization of kaolinite and saponite with silylating agents. *J. Colloid Interf. Sci.* 341, 186–193. <https://doi.org/10.1016/j.jcis.2009.08.041>
- Barbosa, L.V., Marçal, L., Nassar, E.J., Calefi, P.S., Vicente, M.A., Trujillano, R., Rives, V., Gil, A., Korili, S.A., Ciuffi, K.J., De Faria, E.H., 2015. Kaolinite-titanium oxide nanocomposites prepared via sol-gel as heterogeneous photocatalysts for dyes degradation. *Catal. Today* 246, 133–142. <https://doi.org/10.1016/j.cattod.2014.09.019>
- Beltrán-Leiva, M.J., Cantero-López, P., Zúñiga, C., Bulhões-Figueira, A., Páez-Hernández, D., Arratia-Pérez, R., 2017. Theoretical Method for an Accurate Elucidation of Energy Transfer Pathways in Europium(III) Complexes with Dipyrrophenazine (dppz) Ligand: One More Step in the Study of the Molecular Antenna Effect. *Inorg. Chem.* 56, 9200–9208. <https://doi.org/10.1021/acs.inorgchem.7b01221>
- Bergaya, F., Van Damme, H., 1983. Luminescence of Eu^{3+} and Tb^{3+} ions adsorbed on hydrated layer-lattice silicate surfaces. *J. Chem. Soc. Faraday Trans. 2* 79, 505. <https://doi.org/10.1039/f29837900505>
- Binnemans, K., 2015. Interpretation of europium(III) spectra. *Coord. Chem. Rev.* 295, 1–45. <https://doi.org/10.1016/j.ccr.2015.02.015>
- Binnemans, K., 2009. Lanthanide-based luminescent hybrid materials. *Chem. Rev.* 109, 4283–4374. <https://doi.org/10.1021/cr8003983>
- Binnemans, K., 2005. Rare-earth beta-diketonates. *Handb. Phys. Chem. Rare Earths* 35, 107–272. [https://doi.org/10.1016/S0168-1273\(05\)35003-3](https://doi.org/10.1016/S0168-1273(05)35003-3)
- Blasse, G., Grabmaier, B.C., 1994. *Luminescent Materials*, Springer Handbooks. <https://doi.org/10.1007/978-3-642-79017-1>
- Bode, J.W., 2015. Rh(III)- and Ir(III)-Catalyzed C–C Bond Cross Couplings from C–H Bonds. *Top. Organomet. Chem.* 48, 11533–11542. <https://doi.org/10.1007/3418>
- Bünzli, J.-C.G., 2015. On the design of highly luminescent lanthanide

- complexes. *Coord. Chem. Rev.* 293–294, 19–47. <https://doi.org/10.1016/j.ccr.2014.10.013>
- Bünzli, J.-C.G., Comby, S., Chauvin, A.-S., Vandevyver, C.D.B., 2007. New Opportunities for Lanthanide Luminescence. *J. Rare Earths* 25, 257–274. [https://doi.org/10.1016/S1002-0721\(07\)60420-7](https://doi.org/10.1016/S1002-0721(07)60420-7)
- Bünzli, J.-C.G., Piguet, C., 2005. Taking advantage of luminescent lanthanide ions. *Chem. Soc. Rev.* 34, 1048–1077. <https://doi.org/10.1039/b406082m>
- Bünzli, J.C.G., Choppin, G.R., 1989. Lanthanide Probes in Life, Chemical and Earth Sciences: Theory and Practice, in: Bünzli, J.C.G., Choppin, G.R. (Eds.), *Chemical and Earth Sciences*. Elsevier, Amsterdam, p. 127.
- Cicconi, M.R., Veber, A., de Ligny, D., Rocherullé, J., Lebullenger, R., Tessier, F., 2017. Chemical tunability of europium emission in phosphate glasses. *J. Lumin.* 183, 53–61. <https://doi.org/10.1016/j.jlumin.2016.11.019>
- de Araujo, D.T., Ciuffi, K.J., Nassar, E.J., Vicente, M.A., Trujillano, R., Calefi, P.S., Rives, V., de Faria, E.H., 2017. Eu³⁺- and Tb³⁺-Dipicolinate Complexes Covalently Grafted into Kaolinite as Luminescence-Functionalized Clay Hybrid Materials. *J. Phys. Chem. C* 121, 5081–5088. <https://doi.org/10.1021/acs.jpcc.6b12308>
- de Faria, E.H., Lima, O.J., Ciuffi, K.J., Nassar, E.J., Vicente, M.A., Trujillano, R., Calefi, P.S., 2009. Hybrid materials prepared by interlayer functionalization of kaolinite with pyridine-carboxylic acids. *J. Colloid Interf. Sci.* 335, 210–215. <https://doi.org/10.1016/j.jcis.2009.03.067>
- de Faria, E.H., Ciuffi, K.J., Nassar, E.J., Vicente, M.A., Trujillano, R., Calefi, P.S., 2010. Novel reactive amino-compound: Tris(hydroxymethyl)aminomethane covalently grafted on kaolinite. *Appl. Clay Sci.* 48, 516–521. <https://doi.org/10.1016/j.clay.2010.02.017>
- De Faria, E.H., Nassar, E.J., Ciuffi, K.J., Vicente, M.A., Trujillano, R., Rives, V., Calefi, P.S., 2011. New highly luminescent hybrid materials: Terbium pyridine-picolinate covalently grafted on kaolinite. *ACS Appl. Mater. Interf.* 3, 1311–1318. <https://doi.org/10.1021/am2001086>
- De Faria, E.H., Ricci, G.P., Marçal, L., Nassar, E.J., Vicente, M.A., Trujillano, R., Gil, A., Korili, S.A., Ciuffi, K.J., Calefi, P.S., 2012. Green and selective oxidation reactions catalyzed by kaolinite covalently grafted with Fe(III) pyridine-carboxylate complexes. *Catal. Today* 187, 135–149.

- <https://doi.org/10.1016/j.cattod.2011.11.029>
- de Sá, G.F., Malta, O.L., de Mello Donegá, C., Simas, A.M., Longo, R.L., Santa-Cruz, P.A., da Silva, E.F., 2000. Spectroscopic Properties and Design of Highly Luminescent Lanthanide Coordination Complexes. *Coord. Chem. Rev.* 196, 165–195. [https://doi.org/10.1016/S0010-8545\(99\)00054-5](https://doi.org/10.1016/S0010-8545(99)00054-5)
- Dedzo, G.K., Detellier, C., 2015. Functional nanohybrid materials derived from kaolinite. *Appl. Clay Sci.* 130, 33–39. <https://doi.org/10.1016/j.clay.2016.01.010>
- DeOliveira, E., Neri, R., Serra, O.A., Prado, A.G.S., 2007. Antenna Effect in Highly Luminescent Eu^{3+} Anchored in Hexagonal Mesoporous Silica. *Chem. Mater.* 19, 5437–5442. <https://doi.org/10.1021/cm701997y>
- Dirks, A.J., Cornelissen, J.J.L.M., Van Delft, F.L., Van Hest, J.C.M., Nolte, R.J.M., Rowan, A.E., Rutjes, F.P.J.T., 2007. From (bio)molecules to biohybrid materials with the click chemistry approach. *QSAR Comb. Sci.* 26, 1200–1210. <https://doi.org/10.1002/qsar.200740085>
- Frost, R.L., Vassallo, A.M., 1996. The dehydroxylation of the kaolinite clay minerals using infrared emission spectroscopy. *Clays Clay Miner.* 44, 635–651. <https://doi.org/10.1346/CCMN.1996.0440506>
- He, H., Tao, Q., Zhu, J., Yuan, P., Shen, W., Yang, S., 2013. Silylation of clay mineral surfaces. *Appl. Clay Sci.* 71, 15–20. <https://doi.org/10.1016/j.clay.2012.09.028>
- Jung, J., Islam, A., Pecoraro, V.L., Mallah, T., Berthon, C., Bolvin, H., 2019. Derivation of lanthanide series crystal field parameters from first principles. *Chem. Eur. J.* 25, 15112–15122. <https://doi.org/10.1002/chem.201903141>
- Kodaira, C.A., Brito, H.F., Felinto, M.C.F.C., 2003. Luminescence investigation of Eu^{3+} ion in the $\text{RE}_2(\text{WO}_4)_3$ matrix (RE=La and Gd) produced using the Pechini method. *J. Solid State Chem.* 171, 401–407. [https://doi.org/10.1016/S0022-4596\(02\)00221-9](https://doi.org/10.1016/S0022-4596(02)00221-9)
- Letaief, S., Detellier, C., 2011. Application of thermal analysis for the characterisation of intercalated and grafted organo-kaolinite nanohybrid materials. *J. Therm. Anal. Calorim.* 104, 831–839. <https://doi.org/10.1007/s10973-010-1269-8>
- Letaief, S., Detellier, C., 2007. Nanohybrid materials from the intercalation of imidazolium ionic liquids in kaolinite. *J. Mater. Chem.* 17, 1476.

<https://doi.org/10.1039/b616922h>

- Lezhnina, M., Benavente, E., Bentlage, M., Echevarri, Y., Klumpp, E., Kynast, U., 2007. Luminescent Hybrid Material Based on a Clay Mineral. *Chem. Mater.* 19, 1098–1102. <https://doi.org/10.1021/cm061031h>
- Li, X.-N., Wu, Z.-J., Si, Z.-J., Zhou, L., Liu, X.-J., Zhang, H.-J., 2009. Effect of secondary ligands' size on energy transfer and electroluminescent efficiencies for a series of europium(III) complexes, a density functional theory study. *Phys. Chem. Chem. Phys.* 11, 9687–9695. <https://doi.org/10.1039/b912243e>
- Ma, X., Zheng, J., Pang, H., 2012. Intercalation of Mg-Al layered double hydroxides by L-proline: Synthesis and characterization. *Res. Chem. Intermed.* 38, 629–638. <https://doi.org/10.1007/s11164-011-0376-x>
- Mbey, J.A., Thomas, F., Ngally Sabouang, C.J., Liboum, Njopwouo, D., 2013. An insight on the weakening of the interlayer bonds in a Cameroonian kaolinite through DMSO intercalation. *Appl. Clay Sci.* 83–84, 327–335. <https://doi.org/10.1016/j.clay.2013.08.010>
- Moretti, E., Storaro, L., Chessa, G., Talon, A., Callone, E., Mueller, K.J., Enrichi, F., Lenarda, M., 2012. Stepwise dansyl grafting on the kaolinite interlayer surface. *J. Colloid Interf. Sci.* 375, 112–117. <https://doi.org/10.1016/j.jcis.2012.02.033>
- Moura, R.T., Carneiro Neto, A.N., Longo, R.L., Malta, O.L., 2016. On the calculation and interpretation of covalency in the intensity parameters of 4f–4f transitions in Eu^{3+} complexes based on the chemical bond overlap polarizability. *J. Lumin.* 170, 420–430. <https://doi.org/10.1016/j.jlumin.2015.08.016>
- Mylavarapu, R.K., Gcm, K., Kolla, N., Veeramalla, R., Koilkonda, P., 2007. Boric Acid Catalyzed Amidation in the Synthesis of Active Pharmaceutical Ingredients. *Org. Process Res. Dev.* 11, 1065–1068. <https://doi.org/10.1021/op700098w>
- Okada, T., Ehara, Y., Ogawa, M., 2007. Adsorption of Eu^{3+} to smectites and fluoro-tetrasilicic mica. *Clays Clay Miner.* 55, 348–353. <https://doi.org/10.1346/CCMN.2007.0550402>
- Olejnik, S., Aylmore, L.A.G., Posner, A.M., Quirk, J.P., 1968. Infrared spectra of kaolin mineral-dimethyl sulfoxide complexes. *J. Phys. Chem.* 72, 241–249.

- <https://doi.org/10.1021/j100847a045>
- Pearson, R.G., 1968. Hard and soft acids and bases, HSAB, part 1: Fundamental principles. *J. Chem. Educ.* 45, 581–586. <https://doi.org/10.1021/ed045p581>
- Reinhard, C., Güdel, H.U., 2002. High-Resolution Optical Spectroscopy of $\text{Na}_3[\text{Ln}(\text{dpa})_3] \cdot 13\text{H}_2\text{O}$ with $\text{Ln} = \text{Er}^{3+}, \text{Tm}^{3+}, \text{Yb}^{3+}$. *Inorg. Chem.* 41, 1048–1055. <https://doi.org/10.1021/ic0108484>
- Rouquerol, F., Rouquerol, J., Sing, K., 1999. Adsorption by Powders and Porous Solids. Elsevier. <https://doi.org/10.1016/b978-0-12-598920-6.x5000-3>
- Ryu, S.J., Kim, A., Kim, M.D., Hong, S.W., Min, S.S., Lee, J.H., Lee, J.K., Jung, H., 2014. Photoluminescent europium(III) complex intercalated in natural and synthetic clay minerals for enhanced latent fingerprint detection. *Appl. Clay Sci.* 101, 52–59. <https://doi.org/10.1016/j.clay.2014.07.010>
- Sabbatini, N., Guardigli, M., Manet, I., 1996. Antenna effect in encapsulation complexes of lanthanide ions. Chapter 154 in: *Handbook on the Physics and Chemistry of Rare Earths*. Elsevier. [https://doi.org/10.1016/S0168-1273\(96\)23005-3](https://doi.org/10.1016/S0168-1273(96)23005-3)
- Siffert, B., Kessaissia, S., 1978. Contribution au mecanisme d'adsorption des α -amino-acides par la montmorillonite. *Clay Miner.* 13, 255–270.
- Sigoli, F.A., Brito, H.F., Jafelicci, M., Davolos, M.R., 2001. Luminescence of Eu(III) β -diketone complex supported on functionalized macroporous silica matrix. *Int. J. Inorg. Mater.* 3, 755–762. [https://doi.org/10.1016/S1466-6049\(01\)00053-8](https://doi.org/10.1016/S1466-6049(01)00053-8)
- Silverstein, R.M., Webster, F.X., Kiemle, D.J., 2005. Spectrometric identification of organic compounds, 7th ed. John Wiley & Sons, Hoboken.
- Smrčok, L., Tunega, D., Ramirez-Cuesta, A.J., Ivanov, A., Valúchová, J., 2010. The combined inelastic neutron scattering (INS) and solid-state dft study of hydrogen-atoms dynamics in kaolinite-dimethylsulfoxide intercalate. *Clays Clay Miner.* 58, 52–61. <https://doi.org/10.1346/CCMN.2010.0580105>
- Song, S., Dong, L., Zhang, Y., Chen, S., Li, Q., Guo, Y., Deng, S., Si, S., Xiong, C., 2014. Lauric acid/intercalated kaolinite as form-stable phase change material for thermal energy storage. *Energy* 76, 385–389. <https://doi.org/10.1016/j.energy.2014.08.042>

- Stanley, J.M., Zhu, X., Yang, X., Holliday, B.J., 2010. Europium complexes of a novel ethylenedioxythiophene-derivatized bis(pyrazolyl)pyridine ligand exhibiting efficient lanthanide sensitization. *Inorg. Chem.* 49, 2035–2037. <https://doi.org/10.1021/ic902481y>
- Supkowski, R.M., Horrocks, W.D., 2002. On the determination of the number of water molecules, q , coordinated to europium(III) ions in solution from luminescence decay lifetimes. *Inorg. Chim. Acta* 340, 44–48. [https://doi.org/10.1016/S0020-1693\(02\)01022-8](https://doi.org/10.1016/S0020-1693(02)01022-8)
- Tang, P., 2012. Discussion Addendum for: Boric acid catalyzed amide formation from carboxylic acids and amines: *n*-benzyl-4-phenylbutyramide. *Org. Synth.* 89, 432. <https://doi.org/10.15227/orgsyn.089.0432>
- Tonlé, I.K., Diaco, T., Ngameni, E., Detellier, C., 2007. Nanohybrid kaolinite-based materials obtained from the interlayer grafting of 3-aminopropyltriethoxysilane and their potential use as electrochemical sensors. *Chem. Mater.* 19, 6629–6636. <https://doi.org/10.1021/cm702206z>
- Tosoni, S., Doll, K., Ugliengo, P., 2006. Hydrogen bond in layered materials: Structural and vibrational properties of kaolinite by aperiodic B3LYP approach. *Chem. Mater.* 18, 2135–2143. <https://doi.org/10.1021/cm060227e>
- Tronto, J., Ribeiro, S.J.L., Valim, J.B., Gonçalves, R.R., 2009. Visible and near-infrared luminescent Eu^{3+} or Er^{3+} doped laponite-derived xerogels and thick films: Structural and spectroscopic properties. *Mater. Chem. Phys.* 113, 71–77. <https://doi.org/10.1016/j.matchemphys.2008.07.030>
- Tunney, J.J., Detellier, C., 1996. Chemically modified kaolinite. Grafting of methoxy groups on the interlamellar aluminol surface of kaolinite. *J. Mater. Chem.* 6, 1679–1685. <https://doi.org/10.1039/jm9960601679>
- Tunney, J.J., Detellier, C., 1993. Interlamellar covalent grafting of organic units of kaolinite. *Chem. Mater.* 5, 747–748. <https://doi.org/10.1021/cm00030a002>
- Wagner, C.C., Torre, M.H., Baran, E.J., 2008. Vibrational spectra of copper(II) complexes of L-proline. *Lat. Am. J. Pharm.* 27, 197–202.
- Wainipée, W., Cuadros, J., Sephton, M.A., Unsworth, C., Gill, M.G., Strekopytov, S., Weiss, D.J., 2013. The effects of oil on As(V) adsorption on illite, kaolinite, montmorillonite and chlorite. *Geochim. Cosmochim. Acta*

- 121, 487–502. <https://doi.org/10.1016/j.gca.2013.07.018>
- Waychunas, G.A., 2014. Luminescence Spectroscopy. *Rev. Mineral. Geochem.* 78, 175–217. <https://doi.org/10.2138/rmg.2014.78.5>
- Yan, Z., Zhang, Z., Yu, Y., Liu, Z., Chen, J., 2016. Chemiluminescence determination of potassium bromate in flour based on flow injection analysis. *Food Chem.* 190, 20–24. <https://doi.org/10.1016/j.foodchem.2015.05.076>
- Yang, S.Q., Yuan, P., He, H.P., Qin, Z.H., Zhou, Q., Zhu, J.X., Liu, D., 2012. Effect of reaction temperature on grafting of γ -aminopropyl triethoxysilane (APTES) onto kaolinite. *Appl. Clay Sci.* 62–63, 8–14. <https://doi.org/10.1016/j.clay.2012.04.006>
- Zhang, S., Liu, Q., Cheng, H., Zeng, F., 2015a. Combined experimental and theoretical investigation of interactions between kaolinite inner surface and intercalated dimethyl sulfoxide. *Appl. Surf. Sci.* 331, 234–240. <https://doi.org/10.1016/j.apsusc.2015.01.019>
- Zhang, S., Liu, Q., Cheng, H., Zhang, Y., Li, X., Frost, R.L., 2015b. Intercalation of γ -aminopropyl triethoxysilane (APTES) into kaolinite interlayer with methanol-grafted kaolinite as intermediate. *Appl. Clay Sci.* 114, 484–490. <https://doi.org/10.1016/j.clay.2015.06.035>
- Zhou, X.-H., Li, L., Li, H.-H., Li, A., Yang, T., Huang, W., 2013. A flexible Eu(III)-based metal-organic framework: turn-off luminescent sensor for the detection of Fe(III) and picric acid. *Dalton Trans.* 42, 12403–12409. <https://doi.org/10.1039/c3dt51081f>
- Zolin, V.F., Puntus, L.N., Tsaryuk, V.I., Kudryashova, V.A., Legendziewicz, J., Gawryszewska, P., Szostak, R., 2004. Spectroscopy of europium and terbium pyridine-carboxylates. *J. Alloys Compd.* 380, 279–284. <https://doi.org/10.1016/j.jallcom.2004.03.055>
- Zulfiqar, S., Sarwar, M.I., Rasheed, N., Yavuz, C.T., 2015. Influence of interlayer functionalization of kaolinite on property profile of copolymer nanocomposites. *Appl. Clay Sci.* 112–113, 25–31. <https://doi.org/10.1016/j.clay.2015.04.010>

Supplementary Data

Luminescent properties of biohybrid (kaolinite-proline) materials synthesized by a new boric acid catalyzed route and complexed to Eu³⁺

D.T. de Araújo^a, G.S. de Pádua^a, V.G. Peixoto^a, K.J. Ciuffi^a, E.J. Nassar^a, M.A. Vicente^{*,b}, R. Trujillano^b, V. Rives^b, M.E. Pérez-Bernal^b, E.H. de Faria^{*,a}

^a Universidade de Franca, UNIFRAN. Grupo de Pesquisas em Materiais Lamelares Híbridos (GPMatLam)- Av. Dr. Armando Salles Oliveira, Parque Universitário, 201, 14404-600 Franca, SP (Brazil)

^b *GIR-QUESCAT*, Departamento de Química Inorgánica, Universidad de Salamanca, 37008 Salamanca (Spain)

Fundamentals for the calculation of spectroscopic luminescence parameters.

The experimental intensity parameters can be determined from the emission spectrum of the Eu^{3+} ion, specifically from transitions ${}^5\text{D}_0 \rightarrow {}^7\text{F}_2$ and ${}^5\text{D}_0 \rightarrow {}^7\text{F}_4$ for parameters Ω_2 and Ω_4 , respectively (NASSAR et al., 2007). These transitions were estimated according to (PARRA et al., 2002):

$$A_{0J} = \frac{4e^2\omega^3}{3hc^3} \frac{n(n^2 + 2)^2}{9} \sum_{\lambda} \Omega_{\lambda} \langle {}^7\text{F}_J || U^{(\lambda)} || {}^5\text{D}_0 \rangle^2 \quad (1)$$

where $\lambda = 2$ and 4 ; A_{0J} is the spontaneous emission coefficient; n is the refractive index (1.5 for the solid state sample Eu^{3+}); ${}^7\text{F}_J || U^{(\lambda)} || {}^5\text{D}_0$ are the reduced matrix elements for which the values are 0.0032 and 0.0023 for $J = 2$ and 4 , respectively (CARNALL; FIELDS; RAJNAK, 1968). The value of A_{0J} can be determined experimentally according to equation 2 (BALA et al., 2018):

$$A_{0J} = A_{01} \frac{(I_{0J}/I_{01})}{(\nu_{01}/\nu_{0J})} \quad (2)$$

where I_{01} and I_{0J} are the integrated intensities and ν_{01} and ν_{0J} are the energy ($1/\lambda$) of the barycenter of the transitions ${}^5\text{D}_0 \rightarrow {}^7\text{F}_1$ and ${}^5\text{D}_0 \rightarrow {}^7\text{F}_J$, respectively. The integrated intensity of the transition ${}^5\text{D}_0 \rightarrow {}^7\text{F}_1$ is considered as a reference because it is insensitive to the ligand environment and its value is estimated to be 50 s^{-1} . Each electric dipole transition depends exclusively on a squared matrix element, so we can calculate the intensities across the area of the ${}^5\text{D}_0 \rightarrow {}^7\text{F}_J$ dividing by the transition area ${}^5\text{D}_0 \rightarrow {}^7\text{F}_1$, according to equation 3 (ĐAČANIN et al., 2011):

$$\Omega_{\lambda} = \frac{D_{\text{MD}}\nu_1^3}{e^2\nu_{\lambda}^3} \frac{9n^3}{n(n^2 + 2)^2 \langle {}^7\text{F}_J || U^{(0)} || {}^5\text{D}_0 \rangle^2} \frac{\int I_J(\nu) d\nu}{\int I_{01}(\nu) d\nu} \quad (3)$$

where D_{MD} is the intensity of the transition ${}^5D_0 \rightarrow {}^7F_1$, being $9.6 \times 10^{-42} \text{ esu}^2 \text{ cm}^2$, $\int I_J(\nu)d\nu$ and $\int I_{01}(\nu)d\nu$ are the areas of transitions ${}^5D_0 \rightarrow {}^7F_J$ and ${}^5D_0 \rightarrow {}^7F_1$, respectively.

With the sum of all radiation emission rates (A_{0J}) from ion Eu^{3+} , the total radiation emission rate (A_{rad}) can be determined. Through it, it was possible to evaluate the rate of non-radiative emissions and therefore the internal quantum yield of radiative emission (Q_{Ln}^{Ln}), that is, the ratio of photon absorbed by the photons emitted by the Eu^{3+} ion (PARRA et al., 2002):

$$A_{NRAD} = 1/\tau - A_R \quad (4)$$

$$Q_{Ln}^{Ln} = \frac{A_{RAD}}{(A_{RAD} + A_{NRAD})} \quad (5)$$

where τ is the lifetime of radiative emission. The value of τ can be obtained by the following equation (WERTS; JUKES; VERHOEVEN, 2002):

$$\frac{1}{\tau_{RAD}} = A_{MD}n^3 \left(\frac{I_{tot}}{I_{01}} \right) \quad (6)$$

where I_{tot} is the total integrated area of the experimentally obtained emission intensities, I_{01} is the integrated area of the magnetic dipole transition ${}^5D_0 \rightarrow {}^7F_1$, and A_{MD} is the probability of spontaneous emission under vacuum for the transition ${}^5D_0 \rightarrow {}^7F_1$, which has a calculated value of 14.65 s^{-1} . From the value of τ_{rad} , it is also possible to obtain the internal quantum efficiency through the experimentally obtained lifetime ratio (τ_{obs}) for the lifetime of radiative emission (τ_{rad}) (BÜNZLI, 2015):

$$Q_{Ln}^{Ln} = \frac{\tau_{OBS}}{\tau_{RAD}} \quad (7)$$

Finally, with the experimentally obtained lifetime (Fig. S6) and the radiative lifetime, it is possible to calculate the amount of water molecules in the first coordination sphere through the following formula (HORROCKS; SUDNICK, 1979; SUPKOWSKI; HORROCKS, 2002):

$$q = A \left(\frac{1}{\tau_{\text{H}_2\text{O}}} - \frac{1}{\tau_{\text{D}_2\text{O}}} - \alpha \right) \quad (8)$$

Where q is the number of water molecules in the first coordination sphere, $A = 1.1$, $\alpha = 0.31$ (oscillator contribution), $\tau_{\text{H}_2\text{O}}$ is the experimentally obtained lifetime and $\tau_{\text{D}_2\text{O}} = \tau_{\text{rad}}$ for the Eu^{3+} ion (BOSSHARD et al., 2016).

References

- Bala, M., Kumar, S., Devi, R., Taxak, V.B., Boora, P., Khatkar, S.P., 2018. Synthesis and photoluminescence properties of europium(III) complexes sensitized with β -diketonato and N, N-donors ancillary ligands. *Spectrochim. Acta A* 196, 67–75. <https://doi.org/10.1016/j.saa.2018.02.013>
- Bosshard, G.Z., Brito, G.A., Monteiro, J.H.S.K., De Bettencourt-Dias, A., Mazali, I.O., Sigoli, F.A., 2016. Photophysical properties of asymmetric and water-soluble dinuclear lanthanide complexes of poly glycol chain functionalized-benzoic acid derivative: Experimental and theoretical approaches. *RSC Adv.* 6, 101133–101141. <https://doi.org/10.1039/c6ra21487h>
- Bünzli, J.-C.G., 2015. On the design of highly luminescent lanthanide complexes. *Coord. Chem. Rev.* 293–294, 19–47. <https://doi.org/10.1016/j.ccr.2014.10.013>
- Carnall, W.T., Fields, P.R., Rajnak, K., 1968. Electronic Energy Levels in the Trivalent Lanthanide Aquo Ions. I. Pr^{3+} , Nd^{3+} , Pm^{3+} , Sm^{3+} , Dy^{3+} , Ho^{3+} , Er^{3+} , and Tm^{3+} . *J. Chem. Phys.* 49, 4424–4442. <https://doi.org/10.1063/1.1669893>
- Dačanin, L., Lukić, S.R., Petrović, D.M., Nikolić, M., Dramićanin, M.D., 2011. Judd-Ofelt analysis of luminescence emission from $\text{Zn}_2\text{SiO}_4:\text{Eu}_3$ nanoparticles obtained by a polymer-assisted solgel method. *Phys. B Condens. Matter* 406, 2319–2322.

<https://doi.org/10.1016/j.physb.2011.03.068>

- Horrocks, W.D., Sudnick, D.R., 1979. Lanthanide Ion Probes of Structure in Biology. Laser-Induced Luminescence Decay Constants Provide a Direct Measure of the Number of Metal-Coordinated Water Molecules. *J. Am. Chem. Soc.* 101, 334–340. <https://doi.org/10.1021/ja00496a010>
- Nassar, E.J., Dos Santos Pereira, P.F., De Oliveira Nassor, E.C., Ávila, L.R., Ciuffi, K.J., Calefi, P.S., 2007. Nonhydrolytic sol-gel synthesis and characterization of YAG. *J. Mater. Sci.* 42, 2244–2249. <https://doi.org/10.1007/s10853-006-0077-9>
- Parra, D.F., Brito, H.F., Matos, J.D.R., Dias, L.C., 2002. Enhancement of the luminescent intensity of the novel system containing Eu^{3+} - β -diketonate complex doped in the epoxy resin. *J. Appl. Polym. Sci.* 83, 2716–2726. <https://doi.org/10.1002/app.10252>
- Supkowski, R.M., Horrocks, W.D., 2002. On the determination of the number of water molecules, q , coordinated to europium(III) ions in solution from luminescence decay lifetimes. *Inorg. Chim. Acta* 340, 44–48. [https://doi.org/10.1016/S0020-1693\(02\)01022-8](https://doi.org/10.1016/S0020-1693(02)01022-8)
- Werts, M.H.V., Jukes, R.T.F., Verhoeven, J.W., 2002. The emission spectrum and the radiative lifetime of Eu^{3+} in luminescent lanthanide complexes. *Phys. Chem. Chem. Phys.* 4, 1542–1548. <https://doi.org/10.1039/b107770h>

Table S1

Basal spacing (d); change in the basal spacing (Δd), intercalation ratio (α), full width at half maximum (FWHM) index of (001) reflections and particle orientation (R) of the samples analyzed by PXRD

	d (nm)	Δd (nm)	α (%)*	FWHM ($^\circ 2\theta$)	R^{**}
Kaol	0.71	-	-	0.40	3.73
Kaol-DMSO	1.12	0.41	92	0.32	7.27
Kaol-APS	1.12/0.85	0.14	77	0.96	1.09
Kaol-P	1.21	0.50	59	1.36	1.06
Kaol-AP1	0.85	0.14	65	1.24	1.00
Kaol-AP2	1.14	0.43	77	1.66	1.46
Eutta-Kaol-P	1.21	0.50	36	1.44	0.45
Eutta-Kaol-AP1	0.85	0.14	64	0.72	0.76
Eutta-Kaol-AP2	0.85	0.14	68	1.16	0.89

* Calculated as $\alpha = I/[I + I_0]$, I being the intensity of the reflection in an intercalated sample and I_0 the intensity of the same reflection in unreacted kaolinite. **Calculated as $R = I_{001}/I_{020}$; I_{001} and I_{020} being the intensities of the corresponding reflections.

Table S2

Textural parameters of the solids obtained from nitrogen adsorption isotherms.

Sample	SSA (m ² /g)	Pore volume (cm ³ /g)	Pore size (Å)
Kaol	17	0.14	344
Kaol-P	13	0.11	334
Kaol-AP1	18	0.11	255
Kaol-AP2	12	0.10	319

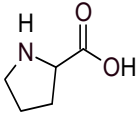
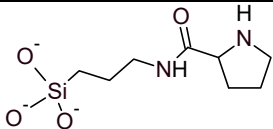
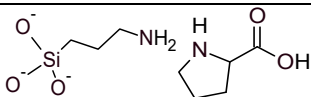
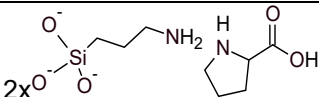
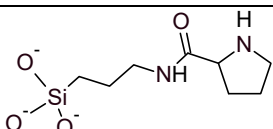
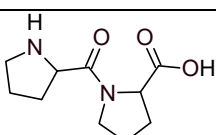
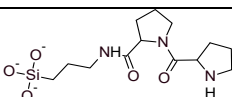
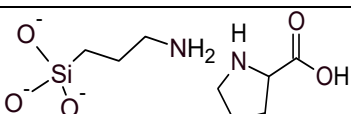
Table S3

Assignment of infrared absorption bands (cm^{-1}) characteristic of the kaolinite structure for parent kaolinite and the derived materials

	Kaol	Kaol-P	Kaol-AP1	Kaol-AP2	Eutta-Kaol-P	Eutta-Kaol-AP1	Eutta-Kaol-AP2
$\nu\text{OH}_{\text{intra}}$	3620	3628	3626	3624	3620	3620	3621
$\nu\text{OH}_{\text{inter}}$	3668, 3653, 3696	3696	3698	3698	3652, 3698, 3668	3699	3699
$\nu\text{HO}\cdots\text{H}$	3435	3544, 3510	3534	3550, 3504	-	-	3548
δHOH	1823	1823	1823	1823	1823	1823	1823
$\nu\text{Si-O}$	1113, 1032, 1011	1092, 1026	1100, 1038, 1014	1100, 1042, 1024	1105, 1034, 1017	1009, 1035, 1097	1008, 1039, 1100
$\nu\text{Al-OH}_{\text{inter}}$	938	-	-	960	-	-	-
$\nu\text{Al-OH}_{\text{intra}}$	914	910	910	906	906	907	909

Table S4

Relative theoretical carbon (C_t) and nitrogen (N_t) amounts for differently functionalized species (when more than one species can be proposed, the average values are given), compared to the experimental relative amounts of carbon (C_e) and nitrogen (N_e), and number of kaolinite unit cells that share one organic species (UC/OM).

Sample	Proposal	C_t	N_t	$\bar{x} C$	$\bar{x} N$	C_e	N_e	UC/OM
Kaol-P		5	1	-	-	5	1	3
		8	2					
Kaol-AP1		8	2	9	2	9	2	12
		11	3					
		8	2					
Kaol-AP2		10	2	10	2	10	2	17
		13	3					
		8	2					

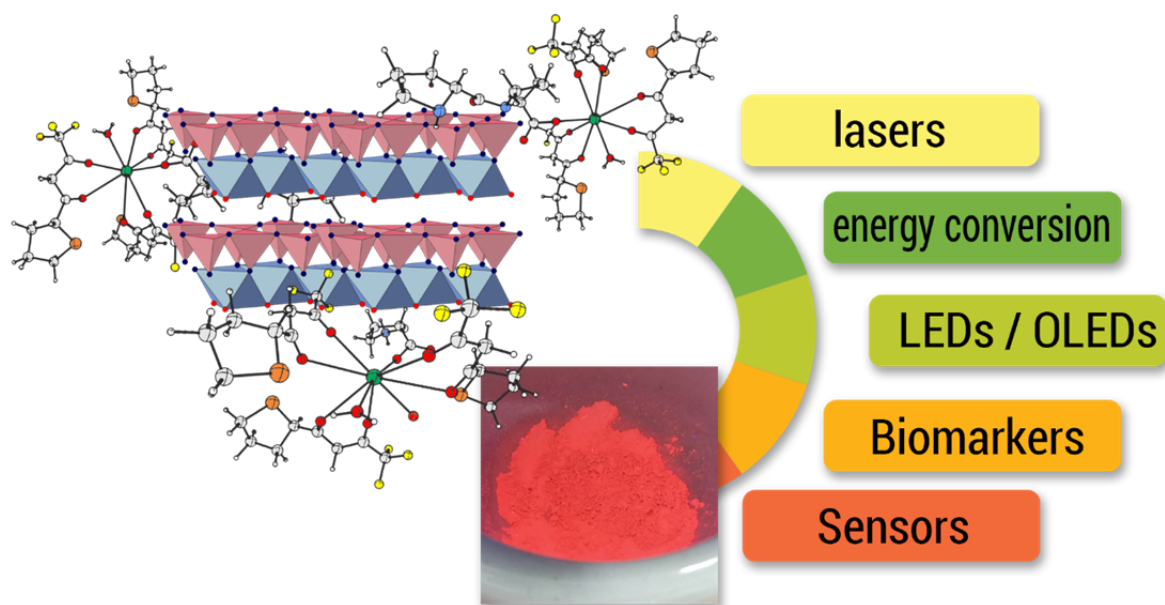


Fig. S1. Possible applications for the synthesized luminescent materials.

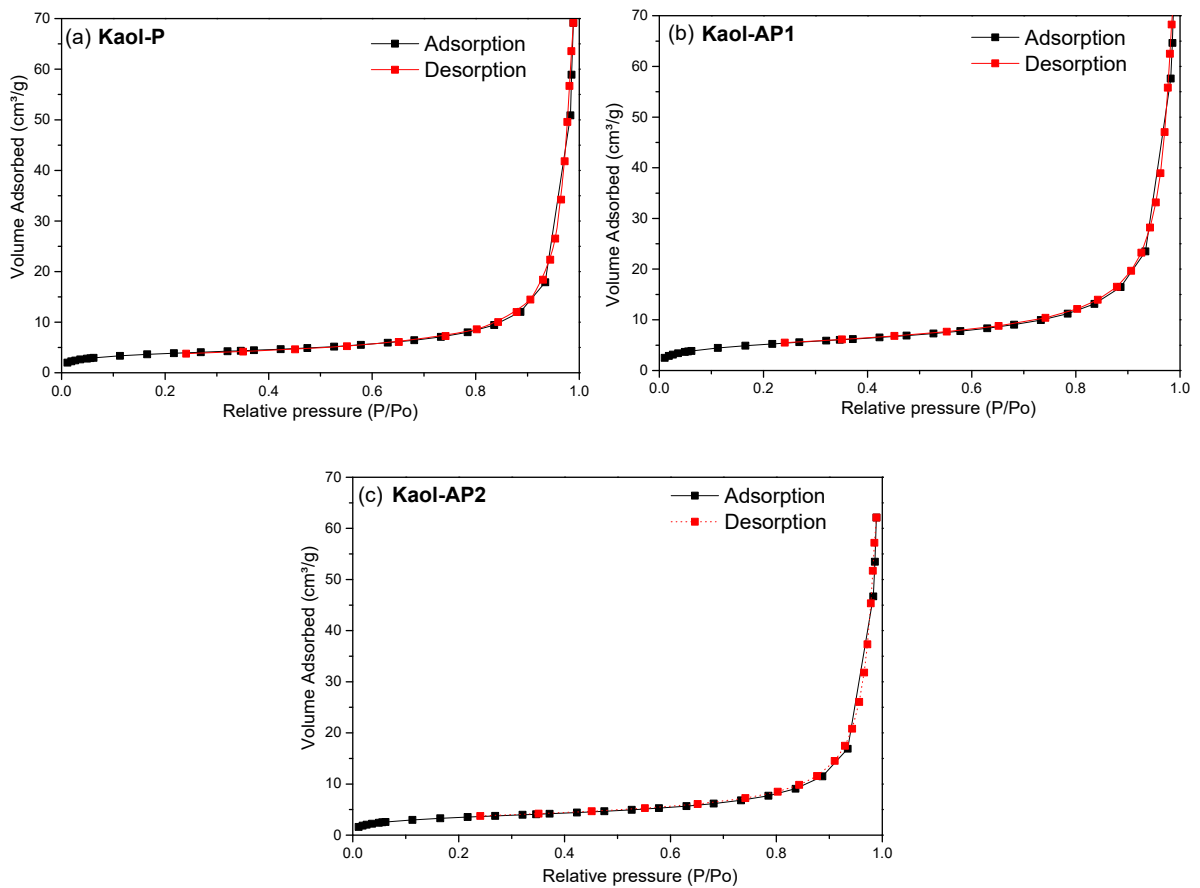


Fig. S2. Nitrogen gas adsorption isotherms for samples a) Kaol-P, b) Kaol-AP1 and c) Kaol-AP2.

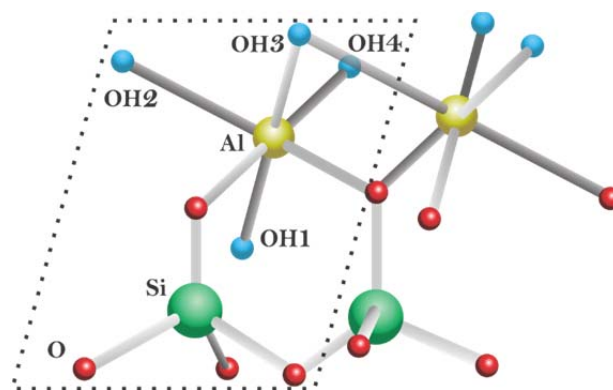


Fig. S3. Schematic representation of kaolinite describing the hydroxyl positions (adapted from Tosoni et. al, 2006).

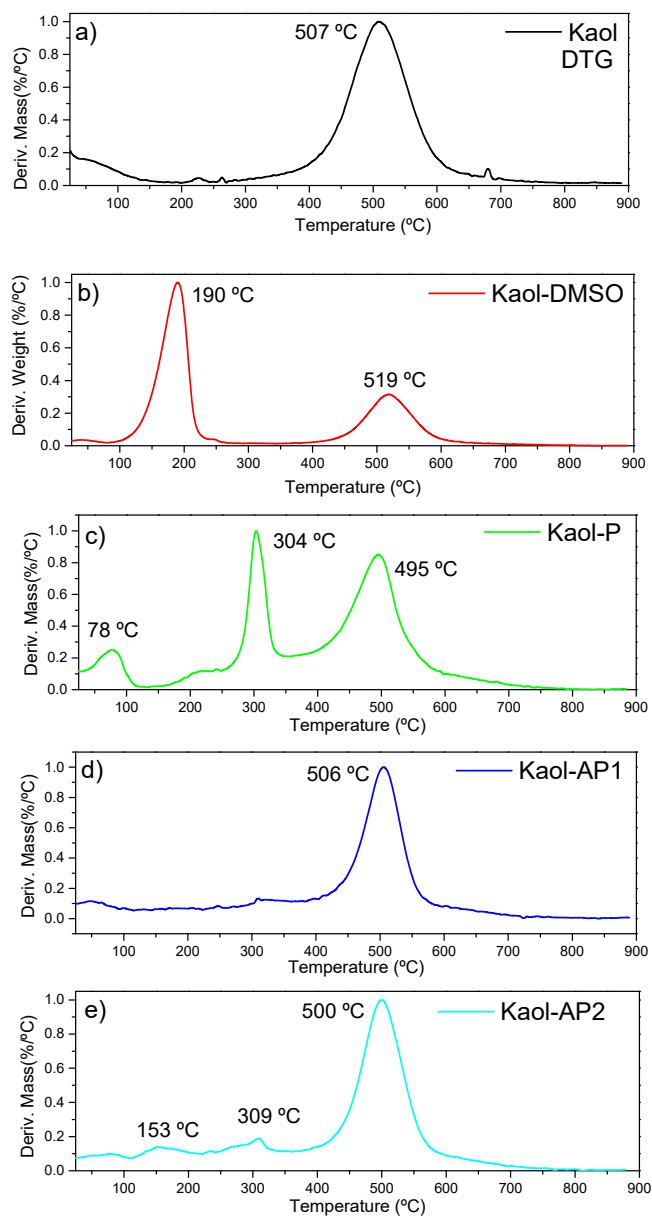


Fig. S4. DTG of samples a) Kaol, b) Kaol-DMSO, c) Kaol-P, d) Kaol-AP1 and e) Kaol-AP2.

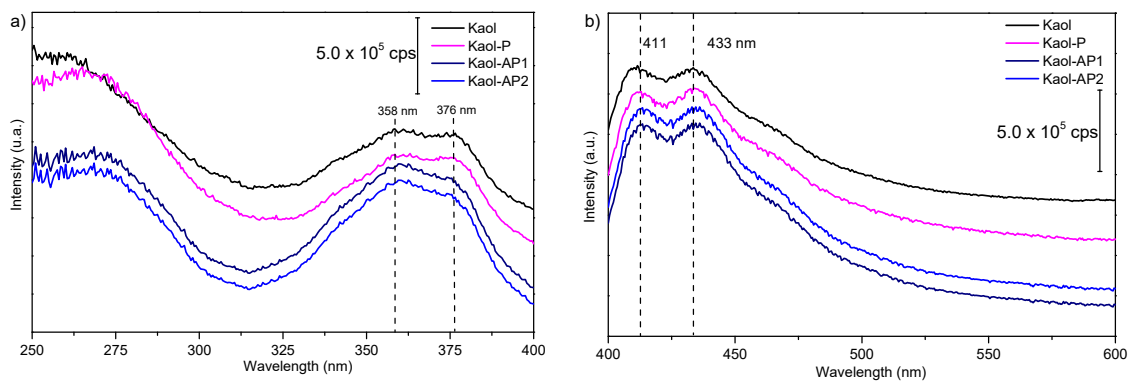


Fig. S5. (a) Excitation ($E_m = 411$ nm) and (b) emission ($E_x = 250$ nm) spectra of complexed precursors without Eu^{3+} in continuous light.

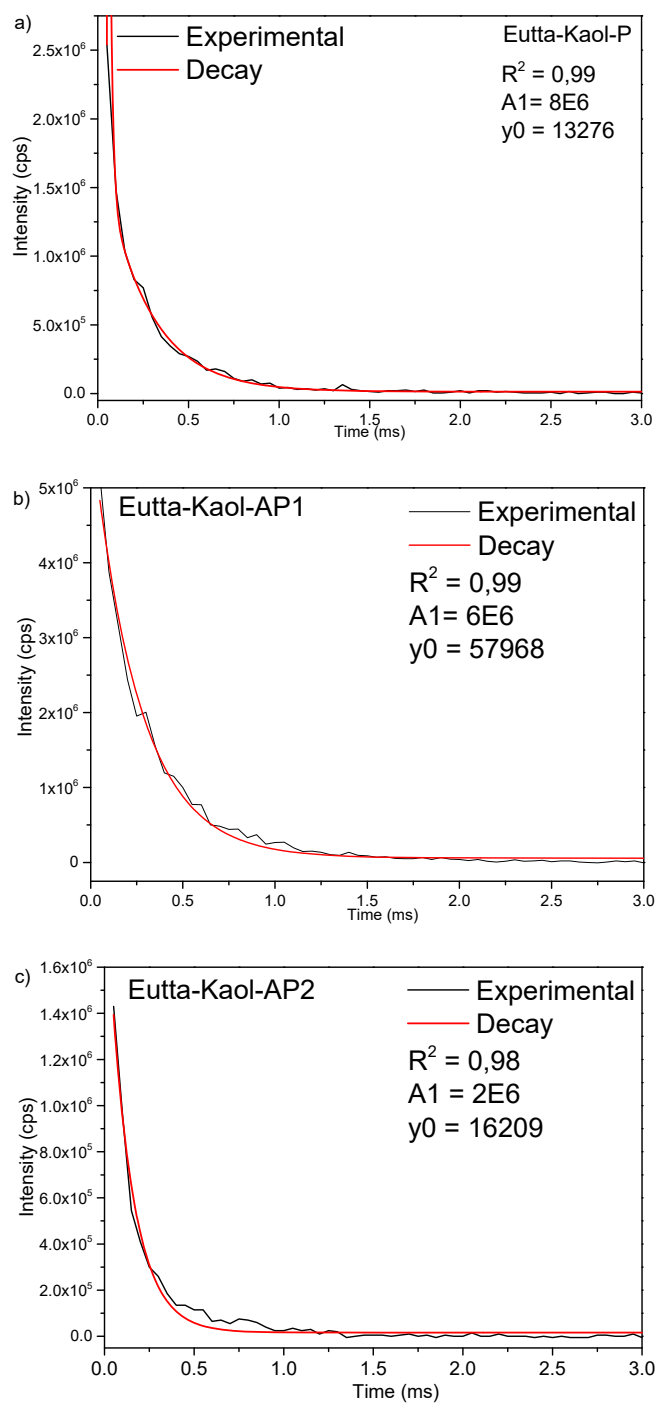


Fig. S6. Lifetime of samples with excitation set at 350 nm and emission set at 615 nm for samples a) Eutta-Kaol-P, b) Eutta-Kaol-AP1 and c) Eutta-Kaol-AP2.

4. Chapter 4 – Results not published in journals

The discussion of the results was divided into three parts, the first on the discussions and characterization of the hybrid materials obtained by the intercalation and functionalization of clay minerals with the amino acids proline and phenylalanine. The second part is about the discussion of the luminescent properties of the obtained materials, and the last one is about the use of these fingerprint detector materials, as adsorbent and luminescent sensors of the emerging contaminants caffeine and estrogen and the potentially toxic ion Cr^{3+} .

4.1. Discussion and characterization of hybrid materials

4.1.1. Materials obtained with kaolinite

4.1.1.1. X-ray diffraction

This characterization technique allows obtaining information on the crystallinity of materials, including the increase in the basal space of clay minerals and other information on structural organization. These crystallographic regions are determined by the Miller index, which is based on vector projections located in each of the three axes of the Cartesian plane, these being measured in terms of lattice parameters (a,b,c), where a (1, 0,0); b (0,1,0) and c (0,0,1), as shown in Figure 14 (KAMEDA; YAMAGISHI; KOGURE, 2005).

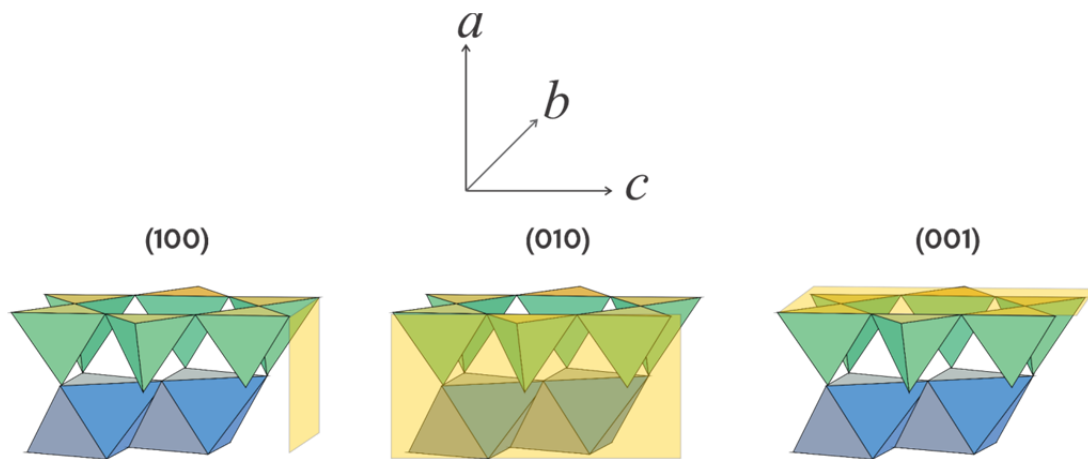


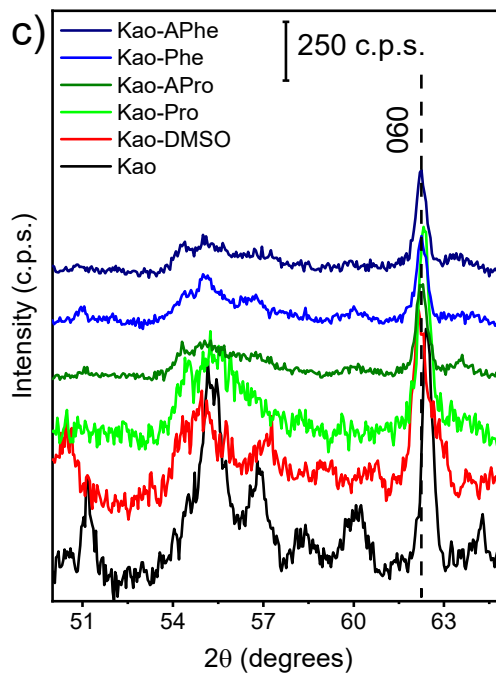
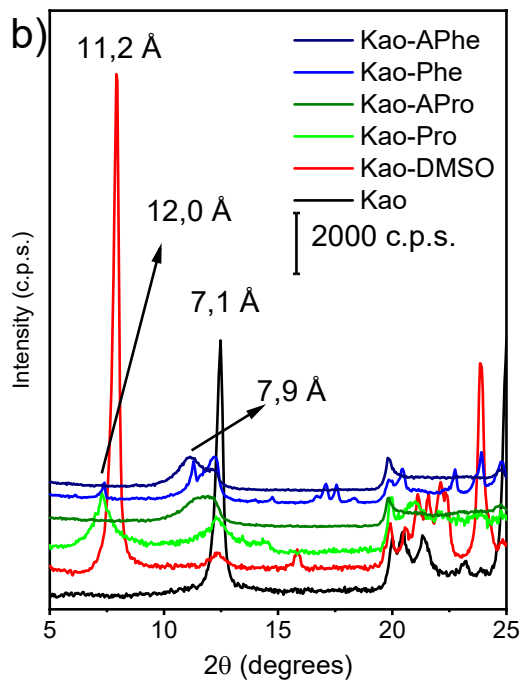
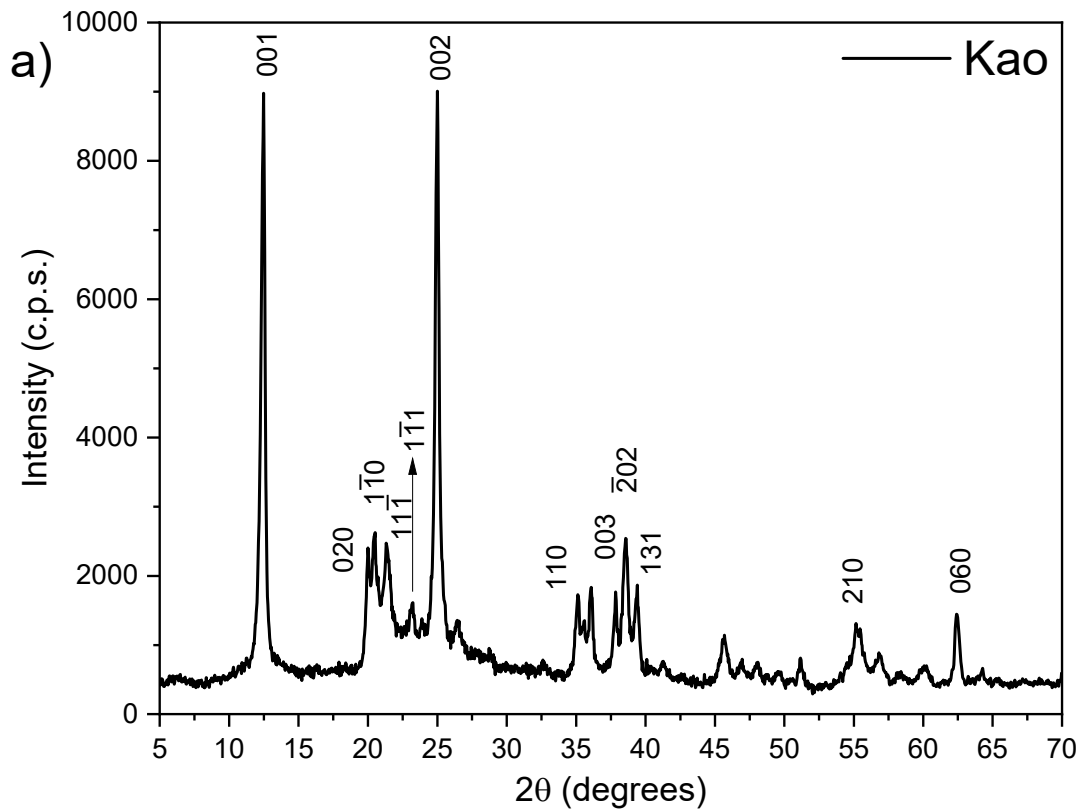
Figure 14 – Examples of Kaolinite network parameters.

Kaolinite has a triclinic structure and the most common Miller indices are: (001), (110), (020), ($1\bar{1}0$), ($\bar{1}10$), (210) e (060) (DA SILVA et al., 2014; DRITS et al., 2019; KREMLEVA; KRÜGER; RÖSCH, 2011). Reflection 001 is assigned to the horizontal plane and is used to determine the basal space between the kaolinite lamellae. This information is obtained using Bragg's Law, adapting to the X-ray diffractogram used with copper incident radiation wavelength ($\lambda=1.54$ nm), as shown in equation 1 and 2:

$$n \cdot \lambda = 2d \cdot \sin \theta \quad \text{Equation 1}$$

$$d = \frac{1,54}{2 \sin \theta} \quad \text{Equation 2}$$

where d is the distance between planes in a crystal and λ is the incident wavelength. X-ray diffractograms of purified kaolinite and resulting materials are shown in Figure 15.



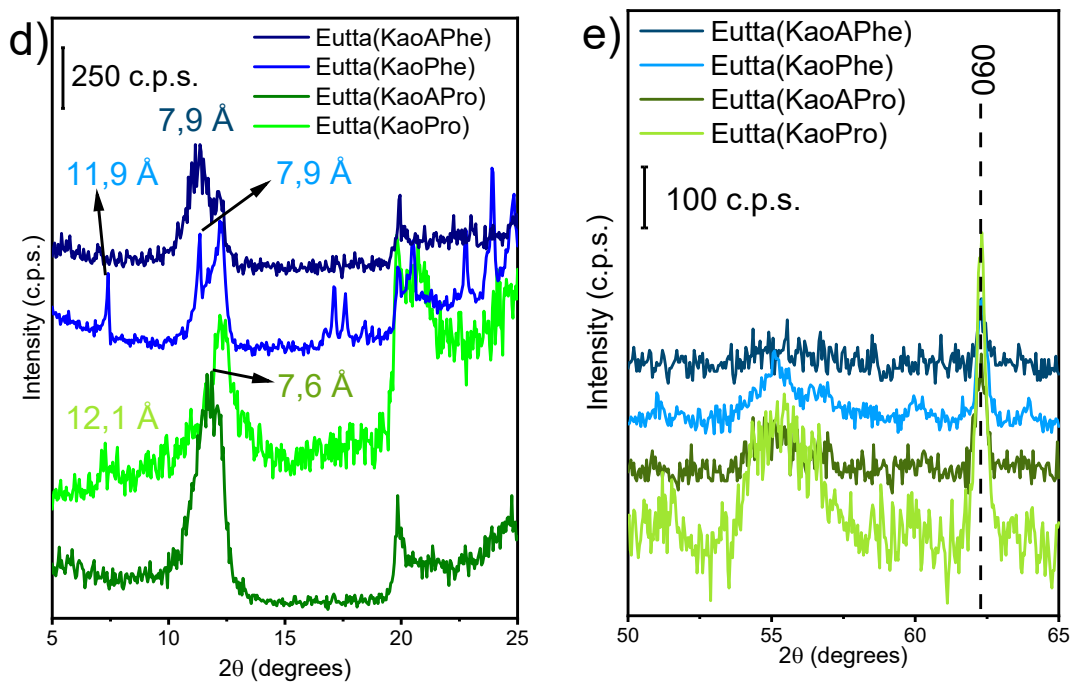


Figure 15 - X-ray diffractograms of the samples: a) kaolinite purified with main Miller's reflections; b) functionalized materials with 2θ degrees at 5-25; c) 50-65 degrees at 2θ; d) of complexed materials at 5-25 degrees at 2θ and d) 50-65 degrees at 2θ.

Purified kaolinite has 7.1 Å of interlamellar spacing, and after incorporation of the modified alkoxide, a drop in crystallinity is evidenced by several factors. When dealing specifically with kaolinite, it is possible to analyze the crystallinity through the degree of orientation of the particles (R), calculated as $R = I_{d001} / I_{d020}$ where the higher the value, the greater the crystallinity (DA SILVA et al., 2016), because the 020 reflection of this clay mineral does not undergo significant changes in several treatments (SMRČOK et al., 2010). Another factor that can be analyzed in relation to crystallinity is the FWHM index (full-width half maximum) which analyzes the width of the peaks at medium height (ALABA et al., 2015; DE ARAÚJO et al., 2020).

In all samples, it is possible to observe the reflection 001 of non-intercalated kaolinite (7.1 Å), indicating the presence of non-intercalated material even where there was expansion of the interlayer space. Therefore, it

is possible to analyze the intercalation rate through the intensities of these 001 reflections of the intercalated material compared to non-intercalated kaolinite, through the formula $\alpha = I_1 / (I_1 + I_0)$, where α is the intercalation rate, I_1 is the peak intensity of the 001 reflection of the intercalated material and I_0 the peak intensity of the 001 reflection of the non-intercalated kaolinite (MBEY et al., 2013).

Kaolinite has 4 peaks between 20 to 25° in 2θ , which are attributed to reflections (020) in 20° (2θ), ($1\bar{1}0$) in 20.5° (2θ), ($11\bar{1}$) located at 21.3° in 2θ and the reflection ($1\bar{1}1$) in 23.2° (2θ). These peaks allow to obtain information about the structural order of kaolinite through the Hinckley index (HI) through the formula $HI = (A+B)/A_h$, where A and B are the intensity from the peak to the overlap region of the reflections ($1\bar{1}0$) and ($11\bar{1}$) respectively and A_h is the intensity of the reflection peak ($1\bar{1}0$) (ALABA et al., 2015), as shown in figure 16.

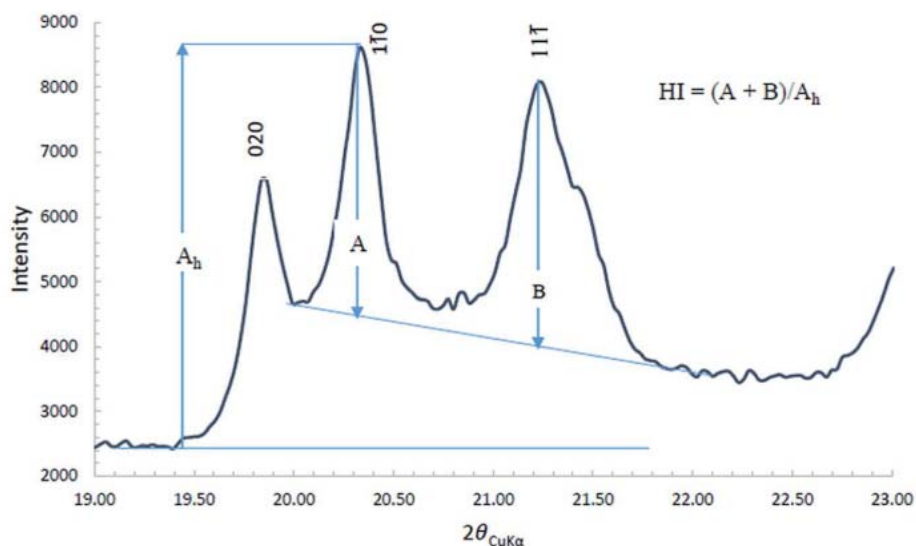


Figure 16 - Representation of obtaining data for calculating the Hinckley index. Reproduced from ALABA et al. (2015).

To corroborate the HI, the Aparicio-Galan-Ferrel index (AGFI) can also be used, which is obtained from the sum of the reflection intensities ($1\bar{1}0$) (I_A) and ($11\bar{1}$) (I_B) due to the double the intensity of the reflection (020) (I_C) [$AGFI = (I_A+I_B)/2I_C$]. In addition to these, another index used to analyze the degree of structural order is the weighting intensity ratio index (WIRI), which ranges from 0 to 1, where WIRI values ≤ 0.4 are assigned to kaolinite with low structural order, values above 0.4 and below 0.7 are considered structural medium order and values ≥ 0.7 are considered high-order structural (ALABA et al., 2015). WIRI values are obtained through equation 3:

$$WIRI = 1 - e^{\left(\frac{w_1 I_{(1\bar{1}0)} + w_2 I_{(11\bar{1})} + w_3 I_{(1\bar{1}1)}}{w_4 I_{(020)}}\right)} \quad \text{Equation 3}$$

Where w_1 , w_2 , w_3 and w_4 are the FWHM indices of the reflections ($1\bar{1}0$), ($11\bar{1}$), ($1\bar{1}1$) and (020) respectively and I is the intensity of these reflections. The results on the structural order of kaolinite are shown in table 5.

Table 6 - Structural order properties of purified kaolinite.

	<i>HI</i>	<i>AGFI</i>	<i>FWHM (2θ)</i>				<i>WIRI</i>
			w_1	w_2	w_3	w_4	
Kao	0,74	1,06	0,4	0,72	0,44	0,32	0,64

As seen in table 6, the purified kaolinite used in this work has a medium structural order, being below 1 in HI and considered median by WIRI, with high crystallinity, as evidenced by low FWHM values. The organofunctionalized materials did not show all the peaks indicated to obtain the WIRI values,

evidencing the low structural order of these materials, characteristic of kaolinite after delamination (ALABA et al., 2015).

After intercalation with DMSO, kaolinite increases its basal space to 11.2 Å, values close to the literature (DEDZO; DETELLIER, 2016; FROST et al., 1999; ZHANG et al., 2018). This 4.1 Å increase corresponds to the presence of DMSO between the lamellae. DMSO needs to exceed 2.7 kcal/mol before starting the intercalation, being attributed to the attraction force of the kaolinite edge, which explains the need for intercalation synthesis at high temperatures (ZHANG et al., 2018), as shown in figure 17.

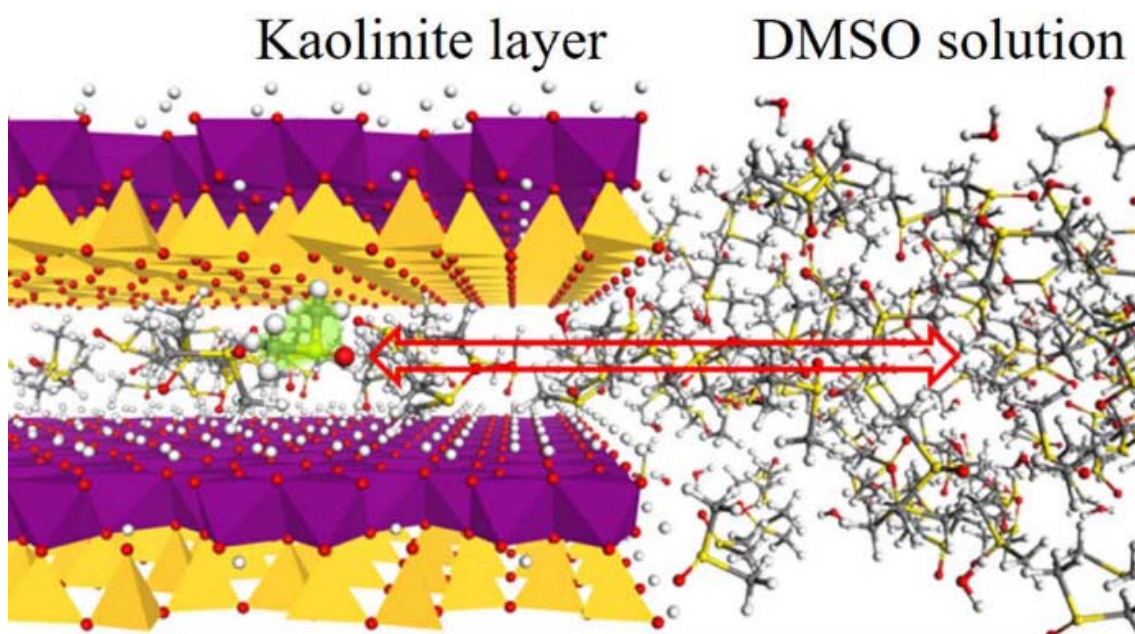


Figure 17 - Schematic representation of the intercalation process of kaolinite with DMSO. (Reproduced from ZHANG et al., 2018)

The strong interaction by hydrogen bonds between S=O and Al-OH is responsible for maintaining the crystallinity of kaolinite and the intercalation of kaolinite with DMSO obtained 92.5% of intercalation rate, showing the efficiency

of the method and the quality of the material for functionalization with amino acids.

The Kao-Pro sample presented greater basal spacing among the others with approximately 12 Å, obtaining a variation of 0.5 Å which is very close to the diameter of the proline molecule (0.5 nm, as calculated in the ACD ChemSketch program¹), indicating the presence of the molecule within the interlamellar space, with a 59% intercalation rate and a drop in crystallinity in relation to the Kao-DMSO sample, as shown in table 6.

Table 7 - Basal spacing (d); basal spacing variation (Δd); intercalation/functionalization ratio (α); particle orientation degree (R) and the ratio of the peak widths of the reflection d001 (FWHM) kaolinite samples, kaolinite intercalated with DMSO and organofunctionalized kaolinite samples.

Sample	d (Å)	Δd (Å)	α (%)	R (u.a.)	FWHM₀₀₁ (2θ)
Kao	7.1	-	-	3.7	0.4
Kao-DMSO	11.2	0.4	92	7.3	0.3
Kao-Pro	12.1	5.0	59	1.1	1.0
Kao-APro	7.5	0.4	51	1.1	1.5
Eutta(KaoPro)	12.1	5	36	0.4	0.7
Eutta(KaoAPro)	7.6	0.5	53	2.0	1.5
Kao-Phe	12.0/7.8	5.0/0.7	32/48	0.9/1.7	0.2/0.3
Kao-APhe	7.9	0.8	60	1.0	1.9
Eutta(KaoPhe)	12.0/7.9	5.0/0.8	41/48	0.9/1.3	0.2/0.3
Eutta(KaoAPhe)	7.9	0.8	60	1.6	1.2

The amidation reaction between the amino acid proline and the alkoxide APTES raises 0.4 Å of the kaolinite interlamellar space, indicating an interaction of the modified alkoxide in this region of the clay mineral, however, due to the diameter of the molecule, the modified alkoxide preferentially interacts with the

¹ The download of the program was done on 20/05/2021 from the URL: <http://www.acdlabs.com/resources/freeware/chemsketch/>

kaolinite through the sides of the lamellae (YANG et al., 2012) at a 51% intercalation rate. After complexation with the Eu^{3+} ion, the interactions of the modified alkoxide with the matrix are maintained, showing a strong interaction between them, with only a low change in crystallinity.

For the Kao-Phe sample, it is possible to observe 3 peaks related to the 001 reflection: one with 12 Å, which is attributed to the amino acid intercalated in the interlamellar space of the matrix, another peak close to 8 Å of the basal space related to the amino acid interaction with aluminol on the sides of the matrix and finally the reflection peak of non-intercalated kaolinite. Due to the large diameter of the amino acid phenylalanine in relation to proline, it interacts in the interlamellar space in the form of monolayers, parallel to the orientation of the layers, this conformation with a low intercalation rate (32%) while the higher concentration of the modified alkoxide interacts through the sides of the lamellae, with an intercalation rate of approximately 50%, where there is no steric hindrance and where the kaolinite lamellae remain with the original orientation.

For the Kao-APhe sample, where the modified alkoxide has a large molecule diameter compared to the others, only the interaction on the sides of the kaolinite is observed, with a 60% intercalation rate and a reduction in crystallinity, indicating delamination and decreased tactoid sizes. After incorporation of the Eu^{3+} ion, the properties observed by X-ray diffraction are maintained, with a slight increase in crystallinity in the complexed samples.

In all organofunctionalized samples, delamination was observed, with a decrease in crystallinity, however it is also possible to observe the peaks related

to the 060 reflection in all these same materials (Figure 15-c/e), close to 60° in 2θ , attributed to the dioctahedral clay minerals, showing that there was no exfoliation (TONLÉ et al., 2007).

4.1.1.2. Infrared molecular absorption spectroscopy

This technique is generally used to identify organic groups through the vibrations of molecules and is widely used qualitatively within the 400 to 4000 cm^{-1} regions. Radiation is absorbed by the molecule and energy is dissipated in the form of vibrations and the frequency of these vibrations are dependent on several factors such as relative mass, bond strength and geometry, being essential for identifying organic compounds (SILVERSTEIN; WEBSTER; KIEMLE, 2005). However, this technique is also widely used to identify vibrations in clay minerals, especially hydroxyl groups in solids.

Tosoni and collaborators performed a series of computational studies to define the hydroxyl vibrations in kaolinite and to study their properties. They were able to identify 4 main hydroxyls present in kaolinite, where one is in the intramolecular region (OH1) close to 3620 cm^{-1} and the other 3 in the interlamellar regions 3696 (OH4), 3653 (OH3) and 3668 cm^{-1} (OH2), being responsible for the interactions (TOSONI; DOLL; UGLIENGO, 2006), as shown in figure 18.

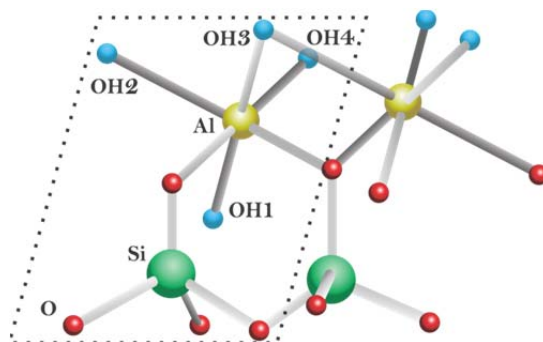


Figure 18 - Schematic representation of kaolinite with hydroxyl positions. Adapted from TOSONI; DOLL; UGLIENGO, (2006).

In purified kaolinite, water bands can be found in the region of 3435 and 1823 cm^{-1} corresponding to stretch and angular vibrations respectively. Si-O stretch vibrations are found between 1000 to 1200 cm^{-1} , while vibrations outside and in the plane of the Si-O-Si oxygen bridge are seen at 701 and 473 cm^{-1} . Finally, as already seen, the intermolecular and intramolecular aluminol stretch vibration bands are found at 938 and 912 cm^{-1} (DE FARIA et al., 2009; FROST, 1996; TOSONI; DOLL; UGLIENGO, 2006). The absorption spectra in the infrared region are shown in Figure 19 and 20.

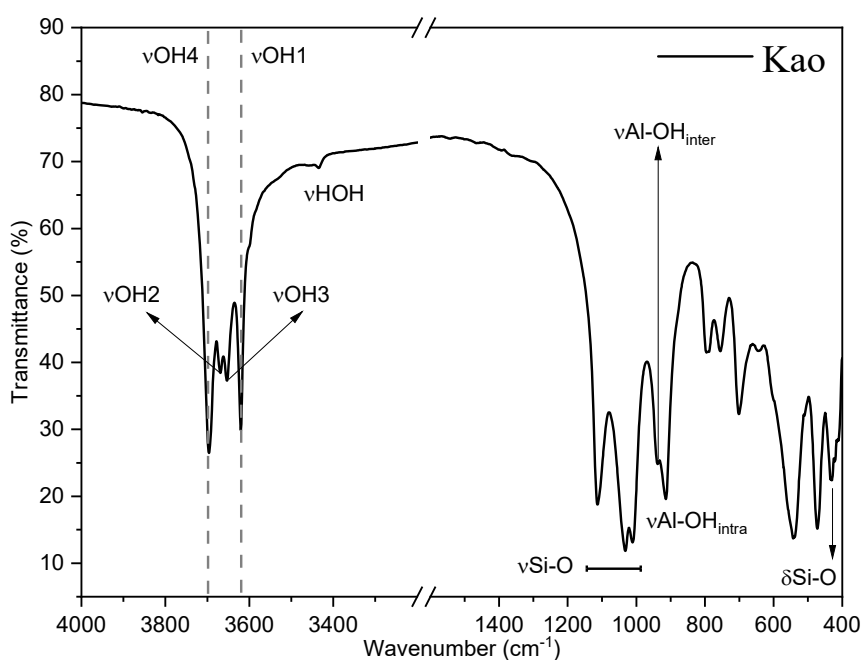


Figure 19 - Infrared absorption spectroscopy of purified kaolinite between 4000 to 400 cm^{-1} with break in 3200-1600 cm^{-1} .

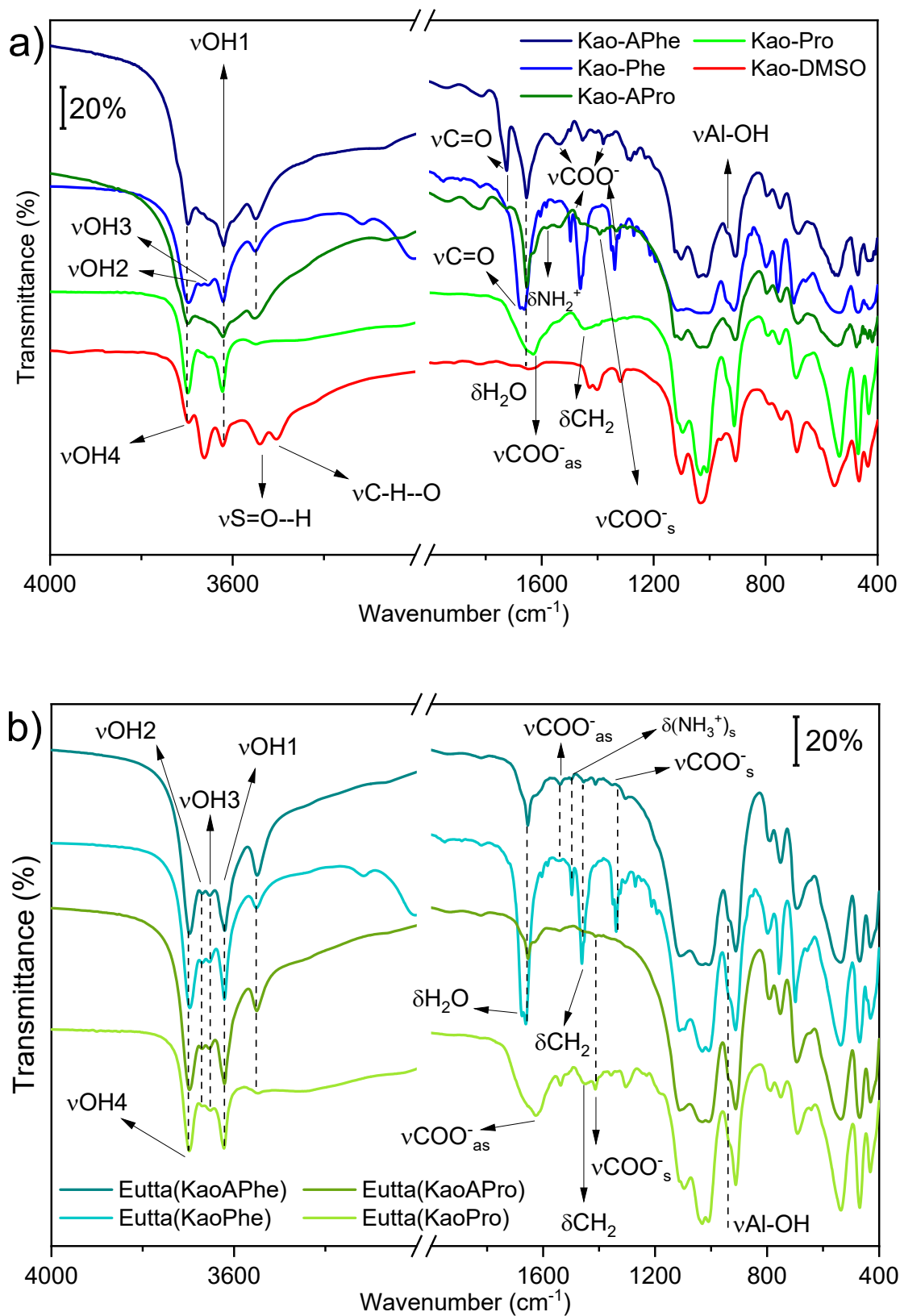


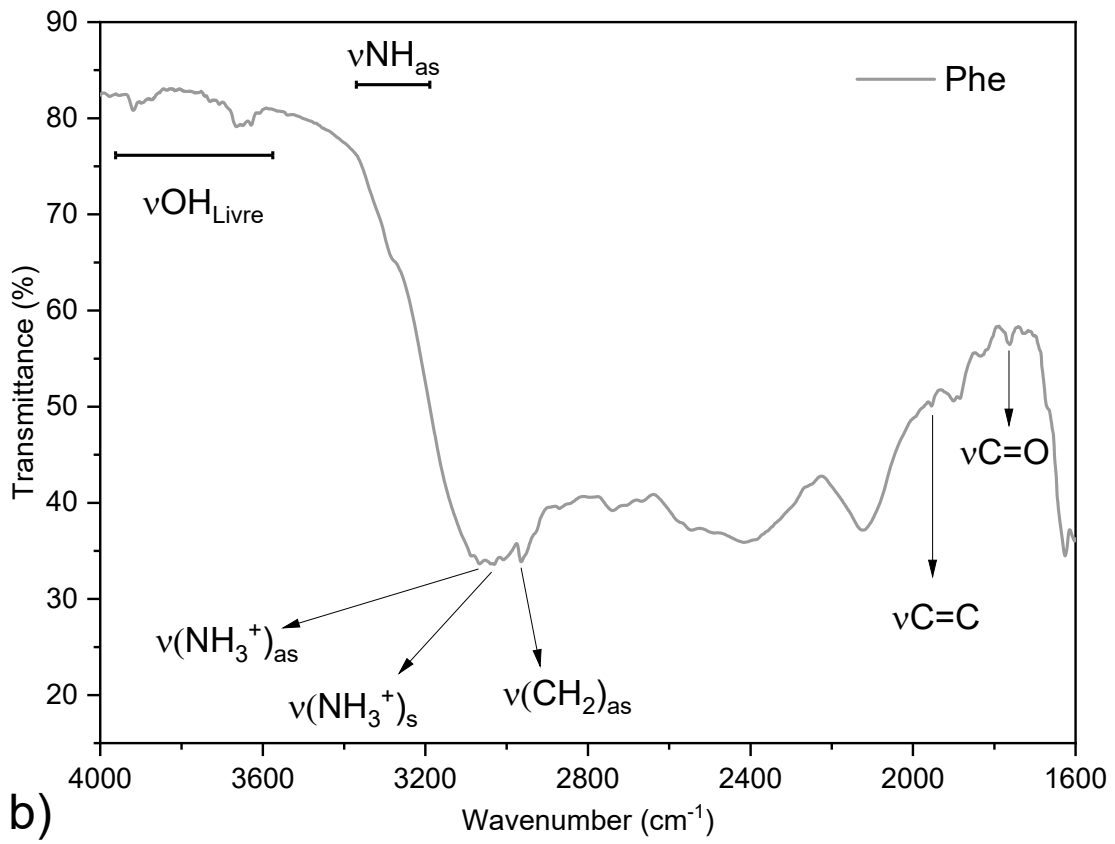
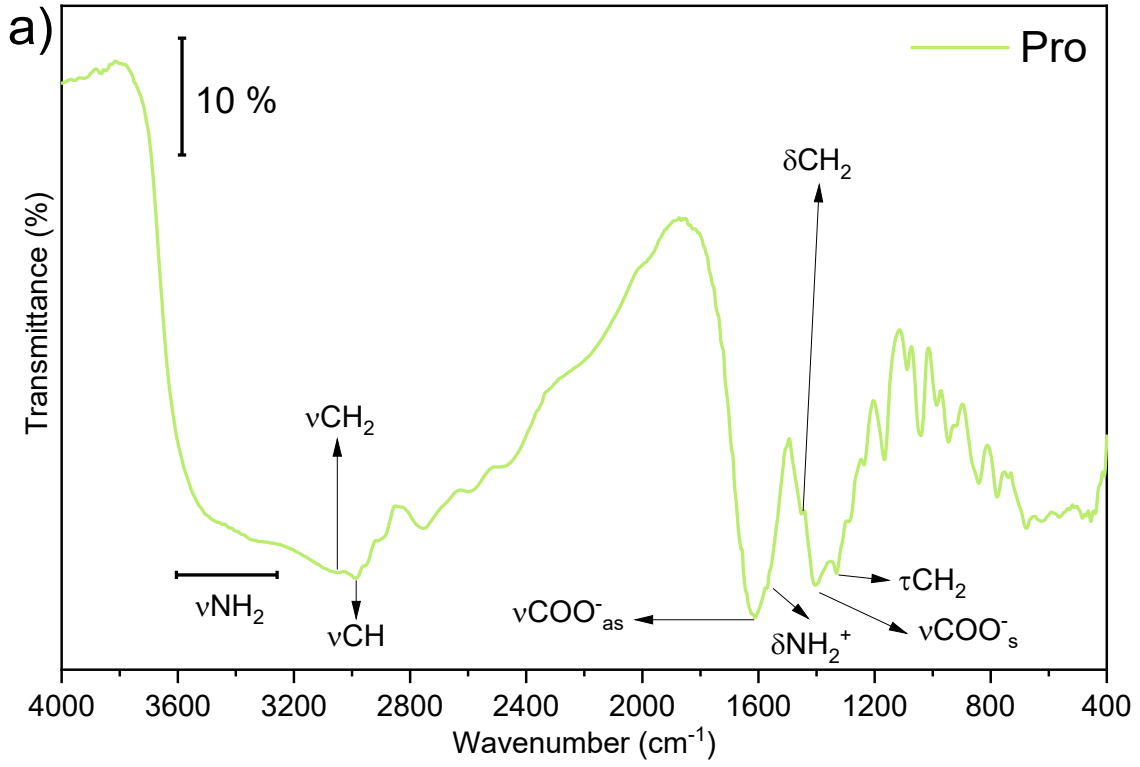
Figure 20 - Infrared absorption spectroscopy of organofunctionalized materials between 4000 to 400 cm^{-1} with breakage of 3200-2000 cm^{-1} (a) and of materials after complexation of europium III ion with breakage of 3200-2000 cm^{-1} (b).

After intercalation with DMSO, two new bands appeared at 3540 and 3504 cm^{-1} , resulting from the hydrogen bond between the kaolinite interlamellar region and the DMSO molecules (ZHANG et al., 2015c). These hydrogen bonds can also be confirmed by shifting the characteristic band of interlamellar aluminol at 938 to 960 cm^{-1} . The characteristic bands of C-H bonds were identified at 3023 and 2936 cm^{-1} . The Si-O antisymmetric stretch vibrations of the matrix shifted from 1034 to 1030 cm^{-1} , in a “shoulder” shape, suggesting that water molecules entered the hexagonal cavities of the tetrahedral silica disturbing these interactions (MA; ZHENG; PANG, 2012). The assignment of kaolinite bands in the pure sample and in the organofunctionalized ones are shown in table 8.

Table 8 - Assignment of infrared absorption bands characteristic of kaolinite structure to purified kaolinite (Kao) and organofunctionalized materials.

	Kao (cm ⁻¹)	Kao-DMSO (cm ⁻¹)	Kao-Pro (cm ⁻¹)	Kao-APRO (cm ⁻¹)	Kao-Phe (cm ⁻¹)	Kao-APhe (cm ⁻¹)	Eutta(KaoPro) (cm ⁻¹)	Eutta(KaoAPro) (cm ⁻¹)	Eutta(KaoPhe) (cm ⁻¹)	Eutta(KaoAPhe) (cm ⁻¹)
vOH1	3620	3621	3632	3628	3626	3624	3622	3621	3621	3620
vOH2	3668	3664	-	-	-	-	3670	3670	3670	3669
vOH3	3653	-	-	-	-	-	3652	3654	3654	3653
vOH4	3696	3698	3698	3698	3697	3698	3698	3698	3698	3697
vHOH	3435	3424	-	-	-	-	-	-	-	-
δHOH	1823	1642	1653	1661	1653	1653	-	1654	1661	1654
vSi-O	1113; 1032; 1011; 431	1100; 1034; 434	1099; 1035; 1011; 432	1092; 1026; 1011; 434	1115; 1031; 1008; 430	1102; 1040; 1012; 435	1096; 1032; 1008; 432	1112; 1031; 1008; 431	1113; 1031; 1008; 431	1111; 1031; 1008; 431
vAl-OH inter	938	960	-	-	-	-	-	-	-	-
vAl-OH intra	914	906	912	909	912	907	912	912	912	912
δSi-O-Al	755	744	751	747	757	748	751	753	757	752
δSi-O-Si in plane	473	468	469	475	469	470	469	470	470	470
δSi-O-Si out plane	701	688	691	684	684	683	691	694	699	693

There is a structural difference between proline and phenylalanine in the amine group of the molecule, as the amine in proline is classified as a secondary amine because it is found in a cyclic chain in the amino acid, whereas in phenylalanine the amine is primary. Thus, in the zwitterionic form, the amines tend to be in the form of NH_2^+ and NH_3^+ for proline and phenylalanine respectively. For the amino acid proline, secondary amine stretch vibrations are found between 3200 to 3600 cm^{-1} , with overlapping CH and CH_2 stretch vibrations forming a wide band extending up to 2000 cm^{-1} , while angular vibration of NH_2^+ is found in 1572 cm^{-1} (JACOBS et al., 2018; NEACSU et al., 2019; WAGNER; TORRE; BARAN, 2008). As for the amino acid phenylalanine, the primary amine (NH_3^+) symmetric and antisymmetric stretch vibrations are observed at 3031 and 3066 cm^{-1} respectively, while the NH stretch vibrations are observed between 3200 to 3400 cm^{-1} and are superimposed by stretches of CH_2 and CH that appear as broad bands extending up to 2000 cm^{-1} . The angular vibrations of symmetrical and antisymmetrical primary amine are observed at 1495 and 1626 cm^{-1} respectively (KACZOR et al., 2006; LI et al., 2001; MAHALAKSHMI; JESURAJA; DAS, 2006; POLFER et al., 2006; RAVIKUMAR; RAJARAM; RAMAKRISHNAN, 2006). Infrared absorption spectra of free amino acids and their main attributions are shown in Figure 21.



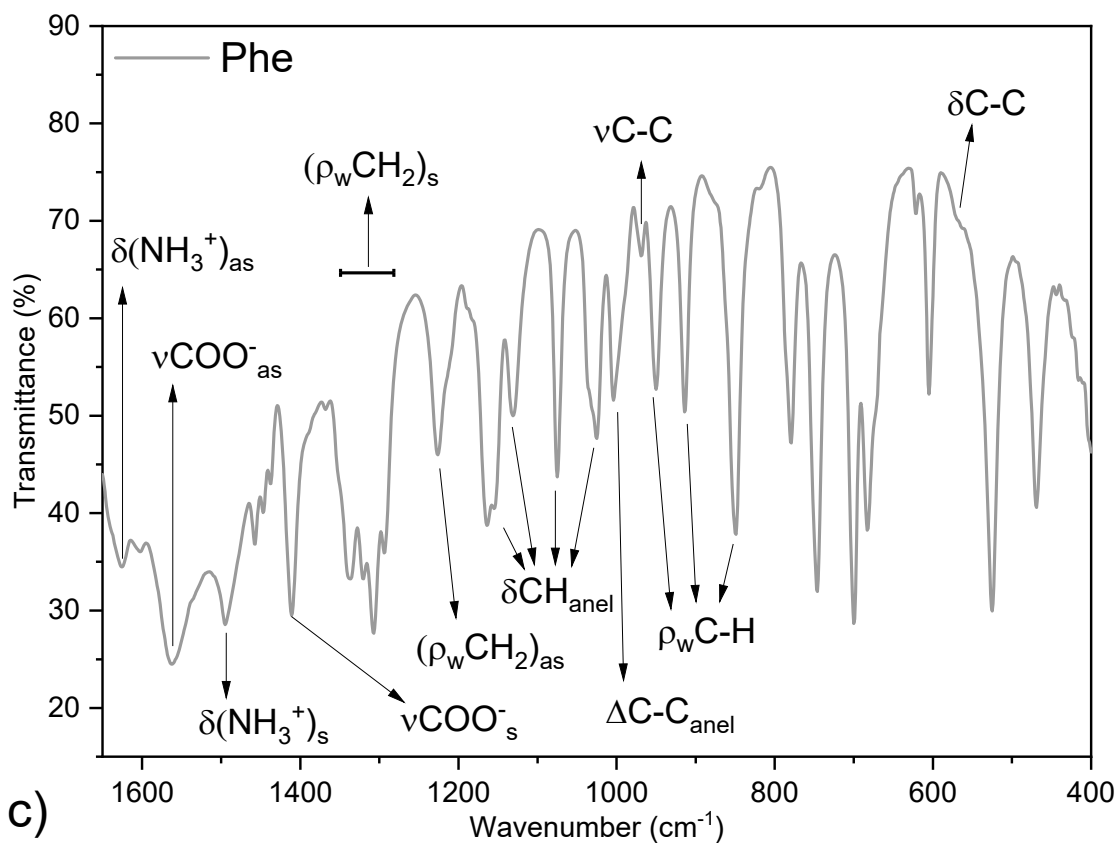


Figure 21 - Infrared spectra of amino acids a) Proline (between 4000 to 400 cm^{-1}) and phenylalanine between b) 4000 to 1600 cm^{-1} and c) 1600 to 400 cm^{-1} .

The carboxylate group in amino acids is mainly characterized by two bands of stretch vibration, a symmetrical and an antisymmetrical vibration, being assigned in proline at 1612 cm^{-1} for antisymmetric stretch vibration and 1404 cm^{-1} for the symmetrical one, while for phenylalanine these bands are seen at 1563 cm^{-1} and 1411 cm^{-1} for symmetrical and antisymmetrical stretch vibrations respectively.

For the Kao-Pro sample, the wide bands between 3400 to 2000 cm^{-1} are related to overlapping stretch bands between CH_2 and C-H. Signals of OH2 and OH3 disappeared indicating a strong interaction between kaolinite and the amino acid proline, confirmed by the appearance of stretch bands of hydrogen bonds between proline and kaolinite at 3544 and 3510 cm^{-1} , related to HO-H

vibrations and/or CH-O and NH stretch bands (SILVERSTEIN; WEBSTER; KIEMLE, 2005; WAGNER; TORRE; BARAN, 2008). At 1630 and 1380 cm^{-1} are the vibrations relative to the proline carboxylate and the disappearance of the aluminol band at 938 cm^{-1} indicate strong interactions between the amino acid and kaolinite.

In the Kao-Phe sample, the hydroxyls OH2 and OH3 did not disappear, nor the interlamellar aluminol band at 938 cm^{-1} which indicates a weaker interaction between the amino acid phenylalanine and the matrix such as hydrogen bonding or Van der Waals forces. The hydroxyl band relative to the hydrogen bond between the amino acid and the matrix at 3550 cm^{-1} and the presence of NH_3^+ bands at 1462 cm^{-1} and COO^- at 1497 and 1339 cm^{-1} confirm the presence of the amino acid phenylalanine and the interaction between the amino acid and the matrix, proven by the displacement of COO^- vibration bands from phenylalanine (1563 and 1411 cm^{-1}) to lower wavenumbers.

In the modified alkoxides of the Kao-APro and Kao-APhe samples, the COO^- bands are slightly shifted with proline and greatly shifted to phenylalanine in relation to the free amino acid, indicating different interactions in this region. For phenylalanine, the ease of peptide formation increased by catalysis with boric acid indicates an amidation reaction between amino acids in addition to the amidation reaction between APTES and phenylalanine, evidenced by the appearance of carbonyl stretch bands (C=O) of the amide COO-N at 1725 cm^{-1} for both Kao-APro and Kao-APhe. Carbonyl bands from peptide bond are found at 1676 cm^{-1} for the Kao-Phe sample. The characterization of the vibration bands of amino acids in the kaolinite samples are shown in table 9.

Table 9 - Assignment of infrared absorption bands characteristic of the amino acids proline and phenylalanine to organofunctionalized kaolinite materials.

	Pro (cm ⁻¹)	Phe (cm ⁻¹)	Kao-Pro (cm ⁻¹)	Kao- APRO (cm ⁻¹)	Kao-Phe (cm ⁻¹)	Kao- APhe (cm ⁻¹)	Eutta(KaoPro) (cm ⁻¹)	Eutta(KaoAPro) (cm ⁻¹)	Eutta(KaoPhe) (cm ⁻¹)	Eutta(KaoAPhe) (cm ⁻¹)
v CH₂	3048	-	-	-	-	-	-	-	-	-
v CH	2988	-	-	-	-	-	-	-	-	-
v COO⁻_{as}	1612	1563	1630	1630	1497	1540	1629	1534	1542	1538
v COO⁻_s	1404	1411	1379	1392	1339	1380	1413	1412	1339	1350
v NH₂⁺	3600- 3200	-	-	-	-	-	-	-	-	-
δ NH₂⁺	1572	-	1540	1582	-	-	1537	1544	-	-
δ CH₂	1452	-	1446	1460	-	-	1448	1442	-	-
τ CH₂	1332	-	1337	1332	-	-	1357	-	-	-
v NH₃⁺_{as}	-	3066	-	-	3063	3065	-	-	3063	3071
v NH₃⁺_s	-	3031	-	-	3029	3030	-	-	3029	3031
v CH₂_{as}	2958	2963	2950	2952	2966	2968	2952	2944	2966	2937
v C=C	-	1955	-	-	1951	1937	-	-	1951	1943
v C=O	-	1762	-	1725	1770	1725	-	1751	1725, 1676	-
δ NH₃⁺_{as}	-	1626	-	-	1662	1654	-	-	1605	1624
δ NH₃⁺_s	-	1495	-	-	1497	1454	-	-	1497	1498
ρ_w CH₂_{as}	-	1226	-	-	1213	1229	-	-	1212	-
ρ_w CH₂_s	-	1250-	-	-	1300-1350	1250-	-	-	1240-1390	1305

Continues on the next page

		1350			1340				
δ CH _{ring}	-	1010- 1200	-	-	1020-1290	1020- 1200	-	-	1020-1205 1111,1031
Δ C-C _{ring}	-	1004	-	-	1008	1013	-	-	1008 1007
ν C-C	-	969	-	-	-	-	-	-	- -
δ C-C	-	564	-	-	537	542	-	-	- -
ρ_w C-H	-	963-800	-	-	850		-	-	- -

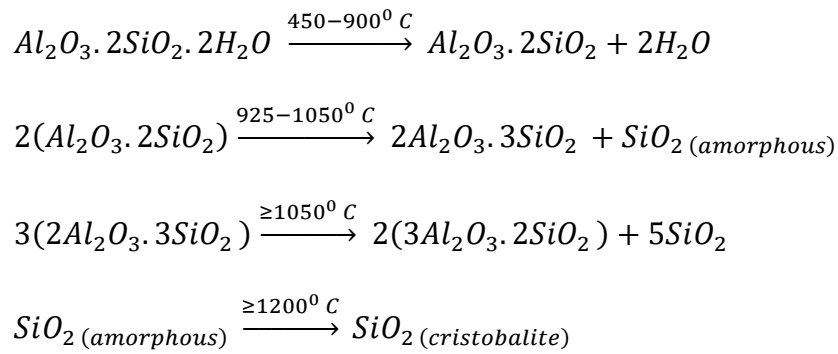
The symbols *as* and *s* mean antisymmetric and symmetric respectively; ν are stretch vibrations; δ are angular vibrations; τ means torsion movement; ρ_w are scissor-shaped angular vibrations (wagging); Δ are breath-shaped movements (breathing).

After complexation of the europium (III) ion, the OH2 and OH3 bands reappeared in all samples indicating leaching of material intercalated in kaolinite in the complexation process (Table 9), a factor also evidenced by the "shoulder" at 938 cm^{-1} of aluminol interlamellar. However, it is possible to verify that the amino acid remains interacting with the matrix through the characteristic bands of the amino acids present in the samples, especially the bands related to the carboxylate and amine groups (Table 9).

4.1.1.3. Thermal analysis

Thermal analysis is an important characterization technique where the physical and chemical properties of samples are studied by submitting them to a treatment with temperature programming. Among the most used techniques are thermogravimetry (TG), derivative thermogravimetry (DTG), Differential thermal analysis (DTA) and Differential scanning calorimetry (DSC) (BERNAL et al., 2002). The samples are subjected to a temperature ramp while the sample is heated on a balance. The TG and the DTG is to study the physical properties related to the mass, while the DTA is analyzed the temperature and finally by the DSC it is possible to obtain information about the enthalpy of the samples.

In the case of kaolinite, it has an initial formula $\text{Al}_2\text{Si}_2\text{O}_5(\text{OH})_4$ and that after thermal treatment, it suffers from several reactions until the formation of mullite (SAHNOUNE et al., 2012), which consists of 1 mol of AlO_3 and 2 mols of silica (SiO_2). In this process, two dehydroxylations occur, losing 2 moles of water, the first dehydroxylation occurring at temperatures close to $520\text{ }^\circ\text{C}$ and the second around $900\text{ }^\circ\text{C}$. Thus, the thermal behavior of kaolinite can be represented by equation 4 (AVILA et al., 2010):



Equation 4

The kaolinite used in this work showed a small loss of mass relative to water molecules adsorbed on the surface between 50 and 100 °C. The first dehydroxylation of kaolinite occurs at a temperature of greater mass loss at 520 °C (endothermic) causing the formation of metakaolinite and the second dehydroxylation (exothermic) occurs near 1000 °C forming mullit (AVILA et al., 2010; DE FARIA et al., 2012). The kaolinite TG, DTG and DTA curves are shown in Figure 22.

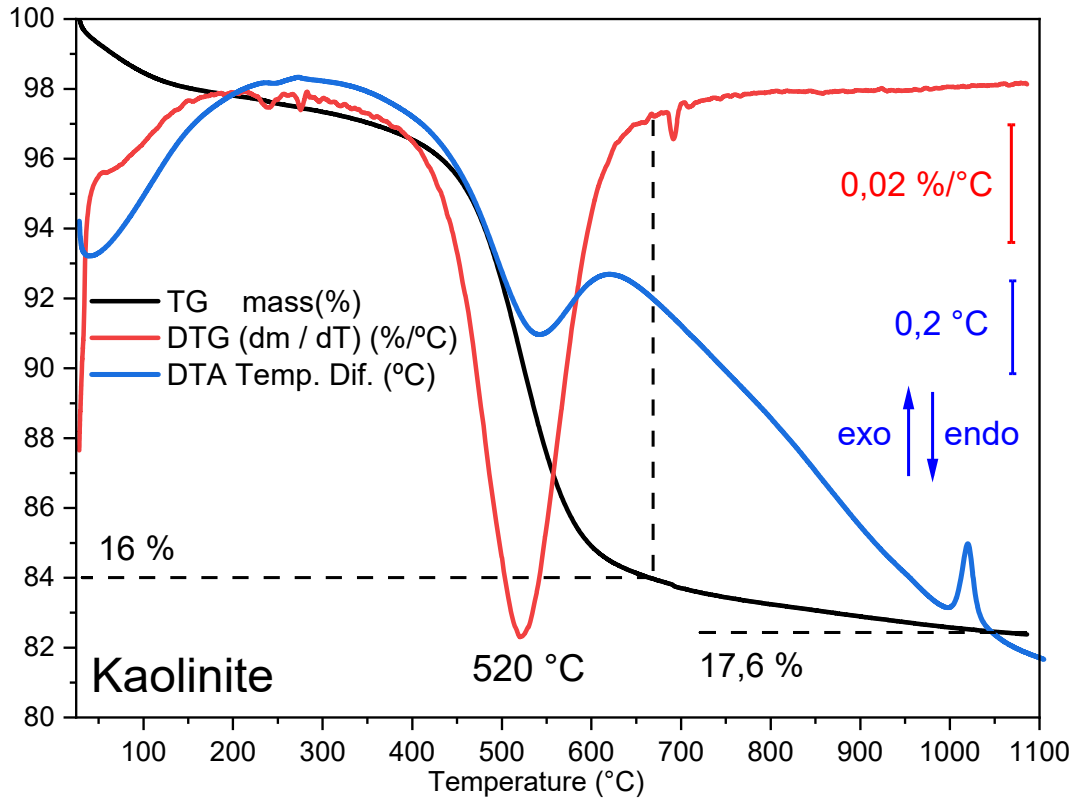
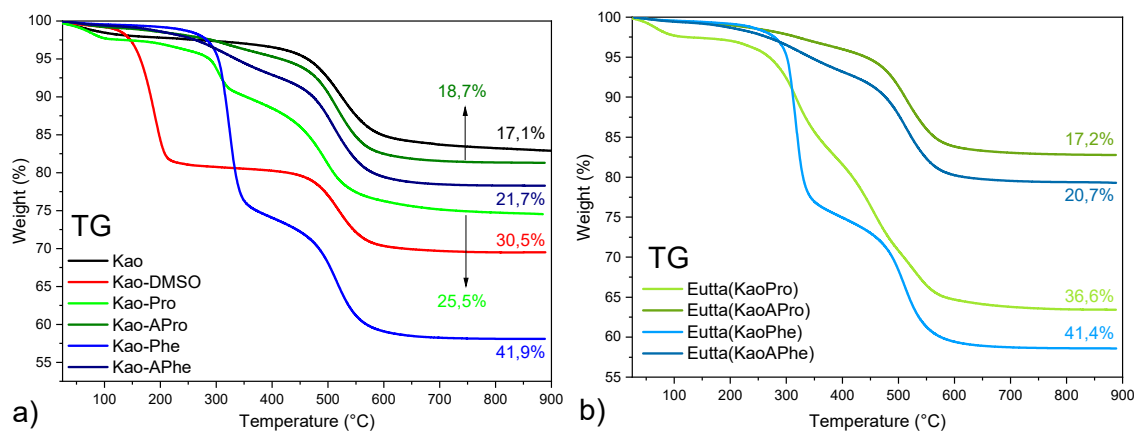
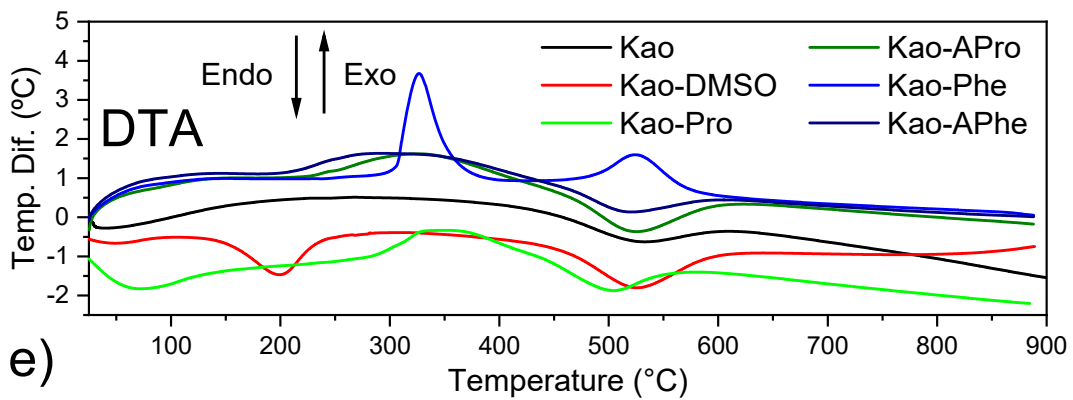
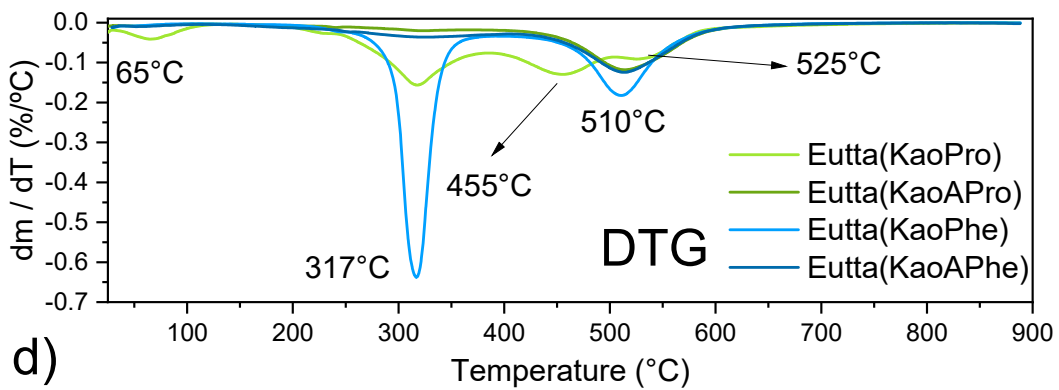
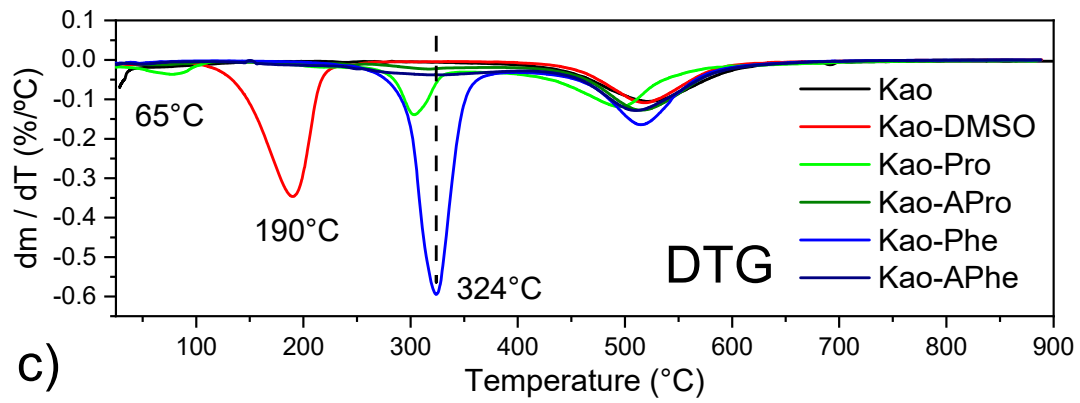


Figure 22 - TG, DTG and DTA curves of purified kaolinite obtained in an oxidizing atmosphere (O_2) with a heating rate of $20^\circ C/min$.

When kaolinite is functionalized, the temperature of the first dehydroxylation is slightly lowered. Solvents and molecules adsorbed on the matrix surface are removed at low temperatures (close to $100^\circ C$). Thermal analyzes of purified kaolinite intercalated with DMSO and organofunctionalized kaolinite materials are shown in Figure 23.





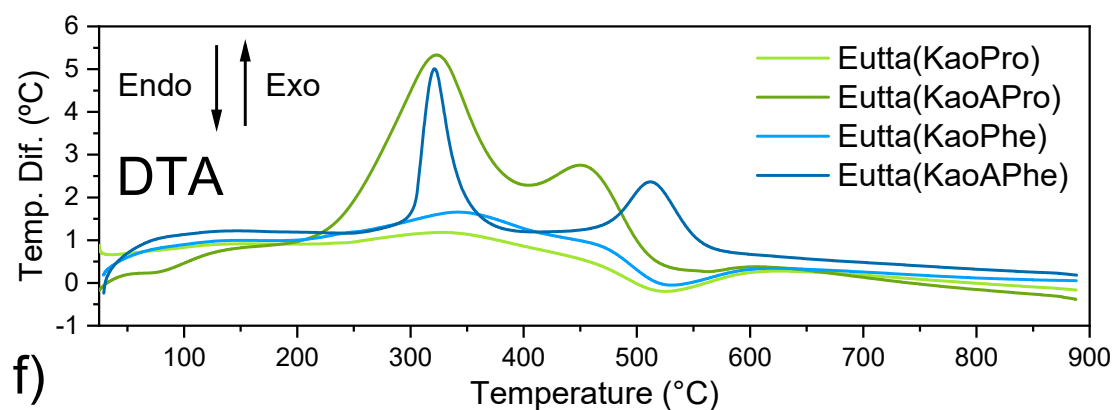
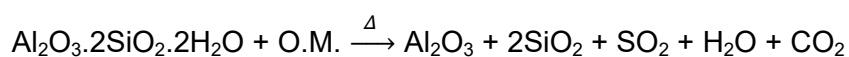


Figure 23 - Thermal analysis of kaolinite samples being: TG, DTG and DTA before (a, c, and respectively) and (b, d, f respectively) after complexation of the europium ion (III).

In kaolinite intercalated with DMSO, three mass losses are observed, the first being related to water adsorbed on the surface close to 100 °C, the second endothermic loss at 190 °C and attributed to the removal and decomposition of DMSO molecules and the last loss of relative mass, also endothermic dehydroxylation occurs at 519 °C. In all organofunctionalized samples, a small mass loss is observed between 25 and 100 °C relative to solvents adsorbed on the material. For the Kao-Pro sample, an endothermic mass loss occurs close to 303 °C and is attributed to a proline decomposition phase, greater than its decomposition temperature, resulting from the increase in the thermal resistance of the material, which is mainly found within the interlamellar space, while in the kaolinite dehydroxylation region there is a loss of endothermic mass close to 495 °C, the lowest temperature among the organofunctionalized samples, also attributed to the last phase of proline decomposition, indicating a large concentration of functionalized material. After complexation of the Eu^{3+} ion, it is possible to observe a loss at 455 °C relative to the decomposition of the complex and at 525 °C the dehydroxylation of kaolinite together with the last stage of organic matter decomposition.

In the Kao-Phe sample among all organofunctionalized kaolinite materials, it is the sample that obtained the greatest mass loss with approximately 42% loss, relative to the size of the molecule and its concentration in the kaolinite. The decomposition of most of the molecule occurs with the highest loss temperature of 324 °C and with the dehydroxylation temperature (endothermic) and the last stage of organic matter decomposition (exothermic) occurring at 517 °C. After complexation with the lanthanide ion, the material properties were maintained, with a drop in the temperature of greater loss of kaolinite dehydroxylation to 510 °C. The highest concentration of organic matter occurs in the samples obtained by conventional synthesis, a fact evidenced by the higher energy released (exothermic) in the last stage of organic matter decomposition, overlapping the energy absorption in the kaolinite dehydroxylation reaction close to 500 °C, the which does not occur in samples obtained by amidation reaction between APTES and amino acids.

Knowing the amount of mass lost at a given temperature, it is possible to calculate the amount of organic matter per mole of kaolinite, taking into account the modification of the APTES alkoxide with the amino acids and the formation of a peptide bond between the amino acids, as shown in the equation 5.



$$258,16 + \text{MM(O.M.)}x - \text{B(O.M.)}x - 18x \xrightarrow{\Delta} 222,13$$

$$1 \qquad \qquad \qquad \longrightarrow \%/100 \text{ r}$$

Equation 5

Where MM (O.M.) is the molar mass of organic matter; B(O.M.) is the molar mass of lost organic matter; 18x is the molar mass ratio of water due to

dehydroxylation of kaolinite by functionalization; %/100r is experimental percentage of waste divided by 100, obtained by heat treatment.

For the Kao-APro and Kao-APhe samples, the arithmetic average of the modified alkoxide and the alkoxide modified by the equivalent peptide was considered as molar mass. For the Kao-Pro sample, the presence of only proline as a monomer was proposed, while for the Kao-Phe sample, both the monomer and the dimer were proposed. It is possible to observe this difference in functionalized material by calculating the molarity between the organic matter and the kaolinite unit cell, as shown in table 10.

Table 10 - Relative mol number for kaolinite samples according to proposed structures for the interaction between matrix and organic matter.

Sample	relative mol number	\bar{x}	U.C./O.M.
Kao-DMSO	0.84	-	1
Kao-Pro	0.41	-	2
Kao-APro	x ₁ : 0.16 x ₂ : 0.05	0.11	10
Eutta(KaoPro)	0.30	-	3
Eutta(KaoAPro)	x ₁ : 0.07 x ₂ : 0.06	0.07	14
Kao-Phe	x ₁ : 0.84 x ₂ : 0.42	0.63	1,5
Kao-APhe	x ₁ : 0.10 x ₂ : 0.06	0.08	13
Eutta(KaoPhe)	x ₁ : 0.37 x ₂ : 0.30	0.34	3
Eutta(KaoAPhe)	x ₁ : 0.09 x ₂ : 0.08	0.09	11

x₁: alkoxide modified with an amino acid; x₂: alkoxide modified with the corresponding amino acid dimer; \bar{x} : arithmetic average of x₁ and x₂. U.C./O.M.: Approximate value of kaolinite unit cell per organic matter.

This result allows to modulate the concentration of intercalated amino acid according to the application to be assigned, obtaining a material with greater agglomeration for conventional synthesis or a material with the amino acid dispersed in the matrix, through the amidation reaction between the amino acid and the alkoxide APTES.

4.1.1.4. Electron Microscopy (SEM)

The electron microscope uses an electron beam in place of photons (common optical microscope), in order to increase the resolution of the images obtained, with extremely short wavelengths of approximately 5×10^{-4} nm, which can increase (zoom) up to 300,000 times. Through this technique it is possible to obtain information mainly on the morphology of materials, in addition to collecting information on microstructural characteristics and even identifying chemical elements in solids (DEDAVID; GOMES; MACHADO, 2007; INKSON, 2016).

The microscope emits a highly focused beam of electrons onto the sample in a vacuum chamber, microscopes that are primarily designed to examine the surfaces of the sample (such as the common optical microscope) are referred to as a scanning electron microscope (SEM) while microscopes that are primarily designed to examine the internal structure of the sample are known as a transmission electron microscope (TEM) (INKSON, 2016). Electron microscopy of kaolinite and organofunctionalized materials are shown in Figure 24.

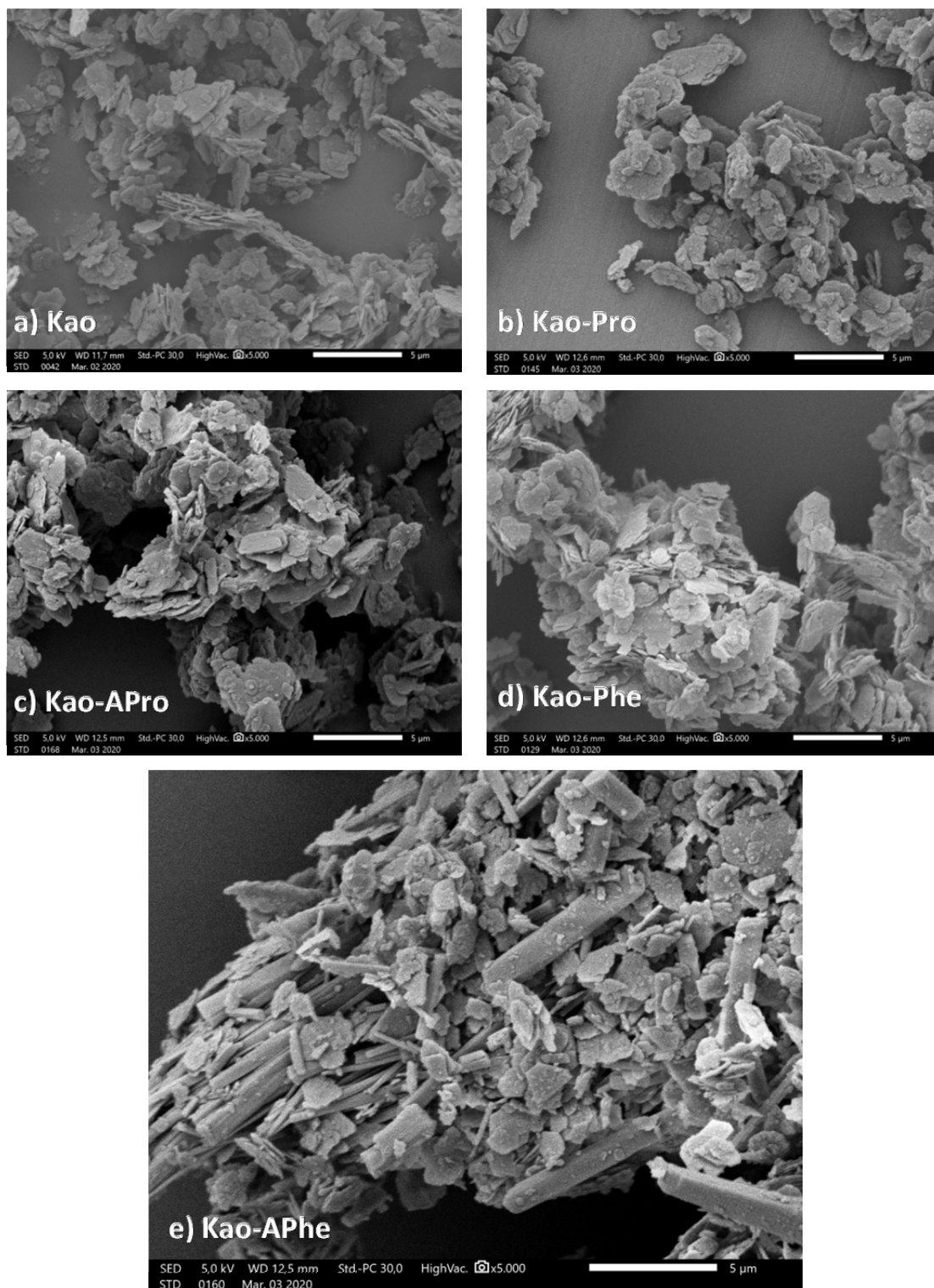


Figure 24 - Scanning electron microscopy of purified kaolinite and organofunctionalized samples. Images taken with a working distance of approximately 12.5 mm and beam energy of 5.0 kV.

Kaolinite has a morphology with hexagonal microcrystals parallel to the 001 plane, which remains agglomerated in tactoids that can reduce their stacking or have their size changed in the intercalation and functionalization

process (DE FARIA et al., 2010). This morphological organization remains in the samples after functionalization, with the exception of the Kao-APhe sample, which presented, in addition to the tactoids, a tubular morphology of various diameters and lengths, caused by the weakening of the hydrogen bonds in the intercalation process which, when leached from space, interlamellar causes displacement in the structure of the layers promoting the rolling of the lamellae offering this tubular appearance (LI et al., 2015).

4.1.2. Hydrotalcite Materials (LDH)

Hydrotalcite is a clay mineral with exchangeable anions in the interlamellar space, in the case of this work with Cl^- ions. However, the zwitterionic characteristic of amino acids hinders the intercalation of proline or phenylalanine by ion exchange (NAKAYAMA; WADA; TSUHAKE, 2004). In addition to ion exchange, two main amino acid intercalation routes in LDH have been reported, being them by the reconstruction method (NAKAYAMA; WADA; TSUHAKE, 2004) and by co-precipitation method (TRAN; LIN; CHAO, 2018). Therefore, the intercalation of the amino acids proline and phenylalanine were performed by these two methods.

4.1.2.1. X-ray diffraction

In the analysis of X-ray diffraction for hydrotalcite, Bragg's law is also used, however, a series of reflections 001 are observed as fine and intense lines at low angles, limiting its analysis in conventional X-ray diffraction techniques, thus the main reflections for obtaining crystallographic information are reflections 003, 006 and 110. The 003 reflections demonstrate the distance between two adjacent metal-hydroxide layers. The X-ray diffractions of the samples with hydrotalcite are shown in Figure 25.

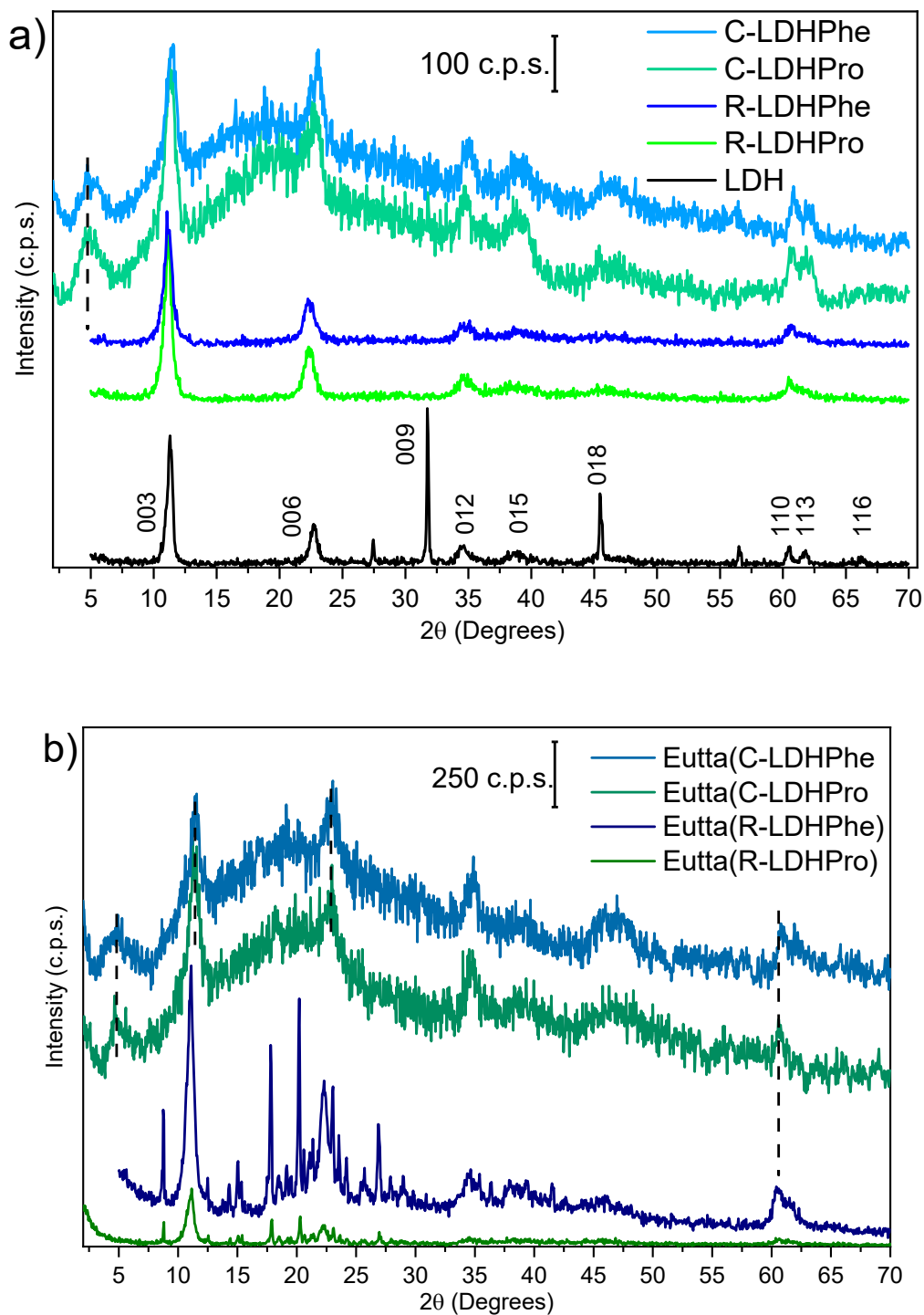


Figure 25 - X-ray diffractograms of LDH samples, a) purified LDH and intercalated with amino acids and b) complexed with europium ion (III).

The X-ray diffractogram profile of hydrotalcite used in this work presented a typical LDH structure with hexagonal rhombohedral symmetry (3R) (CAVANI; TRIFIRÒ; VACCARI, 1991).

Through the diffractions, it is possible to obtain structural organization information through the parameters "a" and "c", according to equation 6 and 7.

$$a = 2 \times \left(\frac{\lambda}{2 \sin \theta} \right)_{(110)} \quad \text{Equation 6}$$

$$c = 3 \times \left(\frac{\lambda}{2 \sin \theta} \right)_{(003)} \quad \text{Equation 7}$$

With parameter "a" it is possible to obtain the distance between the cations within the LDH layer (brucite type), while parameter "c" reveals the distance adjacent to the hydroxide layer (SILVA; DUARTE; MEILI, 2021). The information of the parameters obtained by the diffractograms is shown in table 11. The parameter "a" obtained indicates that there were no significant changes on the brucite-type structure in the samples, while the parameter "c" reveals a greater adjacent distance in the samples obtained by the co-precipitation method.

Table 11 - Network and basal space parameters of X-ray diffractograms of samples with hydrotalcite.

Sample	2θ			d (Å)		a (Å)	c (Å)
	003	006	110	003	006		
LDH	11.3	22.7	60.55	7.8	3.9	3.05	23.46
R-LDHPro	11.2	22.3	60.45	7.9	4.0	3.06	23.67
Eutta(R-LDHPro)	11.1	22.2	30.35	7.9	4.0	3.06	23.76
	8.8			10.0			30.12
R-LDHPhe	11.0	22.2	60.6	8.0	4.0	3.05	23.99
Eutta(R-LDHPhe)	11.1	22.3	60.4	8.0	4.0	3.06	23.88
	8.75			10.1			30.27
C-LDHPro	11.2	22.6	60.6	7.9	3.9	3.05	23.58
	4.6			19.3			58.05
Eutta(C-LDHPro)	11.3	23.0	60.7	7.8	4.0	3.05	23.43
	4.6			19.0			57.07
C-LDHPhe	11.6	22.8	60.8	7.6	3.9	3.04	22.92
	4.7			18.7			56.10

Eutta(C-LDHPhe)	11.4	23.0	30.8	7.7	3.8	3.04	23.16
	4.9			17.9			53.82

After the intercalation of amino acids and complexation of the Eu^{3+} ion, the samples maintained the characteristic peaks of hydrotalcite with hexagonal structure and rhombohedral symmetry. For the samples obtained by the reconstruction method, a slight change in the reflection peaks 003 and 006 is observed, being $d_{003} = 7.9 \text{ \AA}$ and $d_{006} = 4.0 \text{ \AA}$ for the sample R-LDHPro, $d_{003} = 8.0 \text{ \AA}$ and $d_{006} = 4.0 \text{ \AA}$ for the R-LDHPhe sample, the presence of the amino acid being attributed parallel to the layer, together with the anions Cl^- and/or OH^- (AISAWA et al., 2001).

The theoretical thickness of the brucite layer is approximately 4.8 \AA , while the theoretical basal space for Mg-Al(Cl^-) LDH is approximately 7.6 \AA (CAMACHO CORDOVA et al., 2009; TRAN; LIN; CHAO, 2018). The amino acid proline is approximately 4.9 \AA long and 3.0 \AA thick², while phenylalanine is 9.4 \AA long and 4.0 \AA thick approximately (CHOI et al., 2015). In all samples intercalated by the reconstruction method, amino acids were intercalated parallel to the layer and/or interacting on the sides of the lamellae. For the samples obtained by the reconstruction method (C-LDHPro and C-LDHPhe) it presents two reflection peaks 003 indicating two types of interactions between the amino acid and the hydrotalcite, being preferably oriented perpendicular to the matrix. The basal space of these samples expanded between 18 to 19 \AA indicating an interaction between two phenylalanine molecules through the π - π

² Calculated from the software Chemcraft, version 1.8, obtained from the URL: <https://www.chemcraftprog.com>. Calculated on 16/August/2021.

interaction between the aromatic rings (CHOI et al., 2015), while proline organizes itself into a pileup caused by hydrogen bonds, as shown in figure 26.

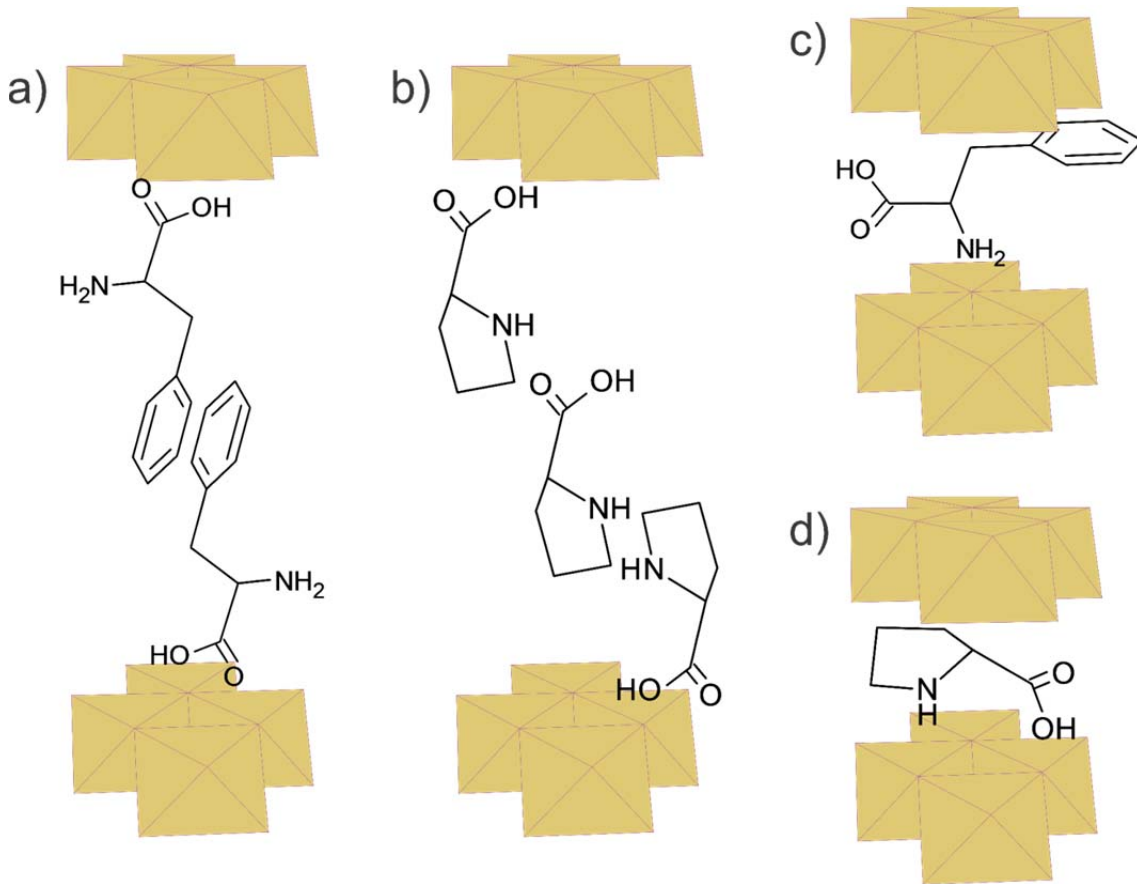


Figure 26 - Proposed schematic representation of the structure of amino acids intercalated in hydrotalcite for a) C-LDHPhe, b) C-LDHPro, c) R-LDHPhe and d) R-LDHPro.

For a better understanding of the structural properties, it is possible to calculate the approximate crystallite size of hydrotalcite using the Scherrer equation, where the *FWHM* index of the 003 reflection is analyzed through equation 8 (HERALDY; NUGRAHANINGTYAS; HERIYANTO, 2017; LIN et al., 2017):

$$t = \frac{0.9 \times \lambda}{\beta \cos \theta} \quad \text{Equation 8}$$

Where *t* is the mean size of the ordered domain, which can be equal to or smaller than the crystallite size, which in turn can be equal to or smaller than

the particle size; 0.9 is the form factor; λ is the Cu K α radiation (0.1540) and β is the *FWHM* index of the 003 reflection. The crystallite sizes are shown in table 12.

Table 12 - *FWHM* index of reflection 003 and the respective crystallite sizes of samples with LDH.

Sample	<i>FWHM</i>₀₀₃ (2θ)	<i>t</i> (Å)	Sample	<i>FWHM</i>₀₀₃ (2θ)	<i>t</i> (Å)
LDH	0.65	21.19			
R-LDHPro	0.75	18.36	C-LDHPro	2.24 1.24	6.12 11.11
Eutta(R-LDHPro)	0.75	18.36	Eutta(C-LDHPro)	1.96 1.40	6.70 9.84
R-LDHPhe	0.75	18.36	C-LDHPhe	2.08 1.12	6.59 12.30
Eutta(R-LDHPhe)	0.75	18.36	Eutta(C-LDHPhe)	2.16 1.48	6.35 9.31

It was observed that the lower the crystallinity, the smaller the crystallite size and that the samples obtained by the co-precipitation method had smaller crystallite sizes, while the samples obtained by the reconstruction method practically did not change the size of the hydrotalcite crystallite, with only a slight change between pure and intercalated LDH. The complexed samples were also not observed significant changes in the sizes of crystallites in relation to their precursors (18.36 Å).

4.1.2.2. Molecular spectroscopy in the infrared region (FTIR)

The FTIR spectra of the hydrotalcite samples are shown in Figure 27. In the region between 3200 and 3800 cm⁻¹ are the stretch vibrations of the hydrotalcite hydroxyls, while water stretch vibrations are observed in the region

of 1650 cm^{-1} . At approximately 1375 cm^{-1} are located the stretching vibrations of CO_3^{2-} related to the contact between the synthesis solution with the atmosphere (SILVA; DUARTE; MEILI, 2021).

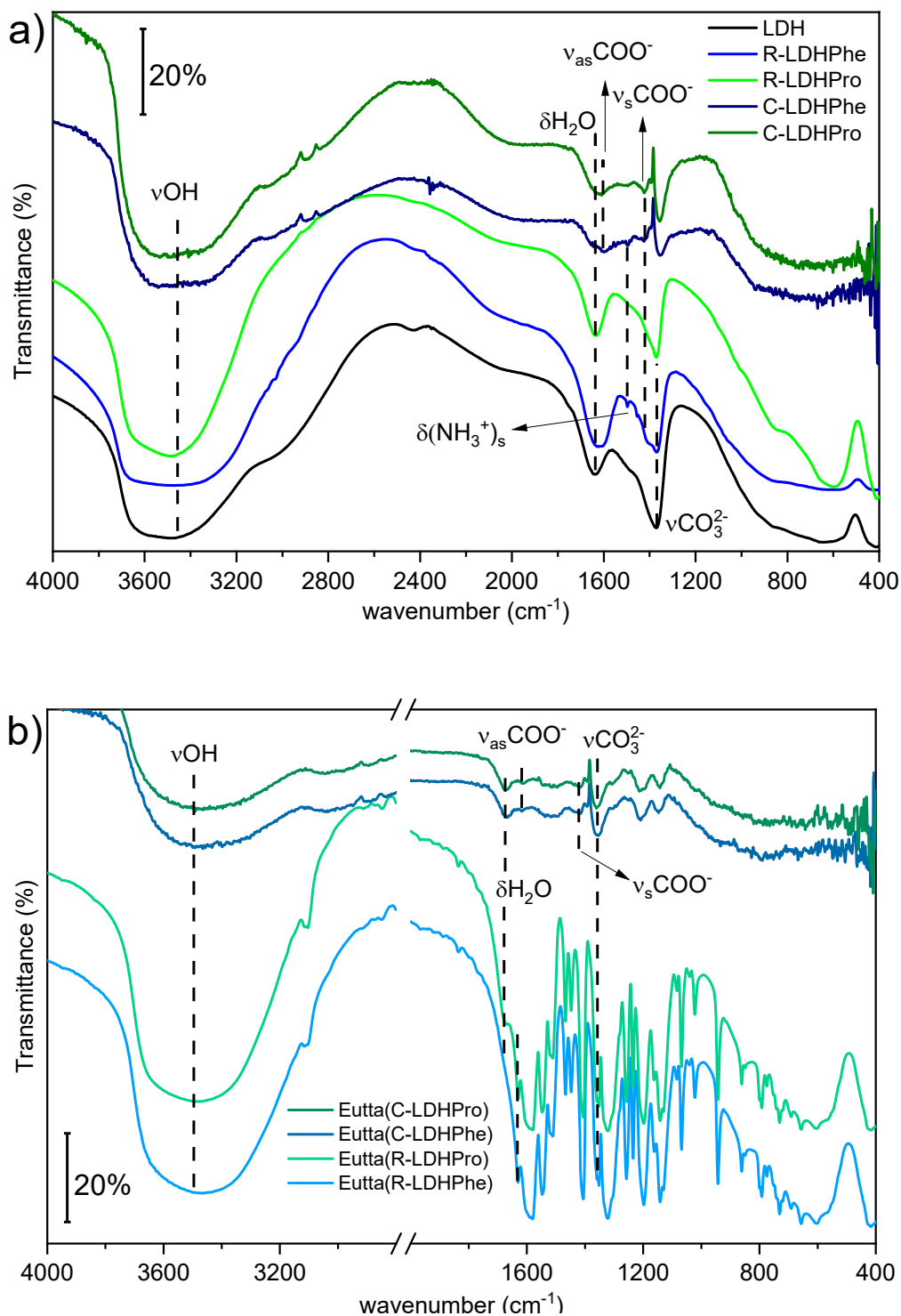


Figure 27 - Infrared spectra (FTIR) of samples with a) hydrotalcite and b) after complexation of Eu(III) ion.

The most definitive bands to identify the presence of amino acids in the FTIR spectra are the symmetrical and antisymmetrical vibrations of the carboxylate group (COO^-), however, these vibrations are found in regions close to the vibrations of the carbonate anion and angular vibrations of water present in the hydrotalcite, resulting in the possibility of overlapping of these characteristic amino acid bands, as seen in the R-LDHP sample (figure 27-a). In the samples obtained by the coprecipitation method, the characteristic amino acid bands are more visible. In all samples with phenylalanine it is possible to observe the angular vibration of amine (NH_3^+) close to 1497 cm^{-1} , while in 1423 and 1600 cm^{-1} symmetrical and antisymmetrical stretch vibrations of the carboxylate are observed (CHOI et al., 2015). For the C-LDHP sample these vibrations are at 1424 and 1610 cm^{-1} respectively.

After complexation of the intercalated samples with the europium (III) ion and addition of the secondary ligand tta, the characteristic bands of the carboxylate are maintained. In the samples obtained by the reconstruction method, the vibrations of the complex, as well as of the tta, are more intense and defined by superimposing the main vibrations of the amino acid, which does not happen in the samples obtained by the co-precipitation method. The most intense vibrations are recorded at 1585 cm^{-1} relative to the stretch of $\text{C}=\text{O}$ in coordination with the Eu^{3+} ion. The free $\text{C}=\text{O}$ bands are observed at 1630 cm^{-1} and shifted to lower wavenumbers when interacting with the lanthanide due to a resonance between $\text{C}-\text{O}-\text{Eu}$ and $\text{C}=\text{O}\cdots\text{Eu}$ (ZHAO et al., 2006).

4.1.2.3. Thermal analysis

$\text{Mg}-\text{Al}-\text{CO}_3$ hydrotalcite has a very defined mass loss profile, the first mass loss starting at $35\text{ }^\circ\text{C}$ to $200\text{ }^\circ\text{C}$ is attributed to water adsorbed on the

material surface. In the 220 °C region, the dehydroxylation of LDH occurs, remaining together with double hydroxide oxide, and a strong peak related to the decomposition of the intercalated carbonate in the form of CO₂. Above 400 °C, the remaining hydroxyls decompose, forming double oxides of magnesium and aluminum, with the last stage of this decomposition occurring at 800 °C, resulting in the collapse of the lamellar structure. The curves of the thermal analysis of materials with hydroxalcite are shown in figures 28 to 32.

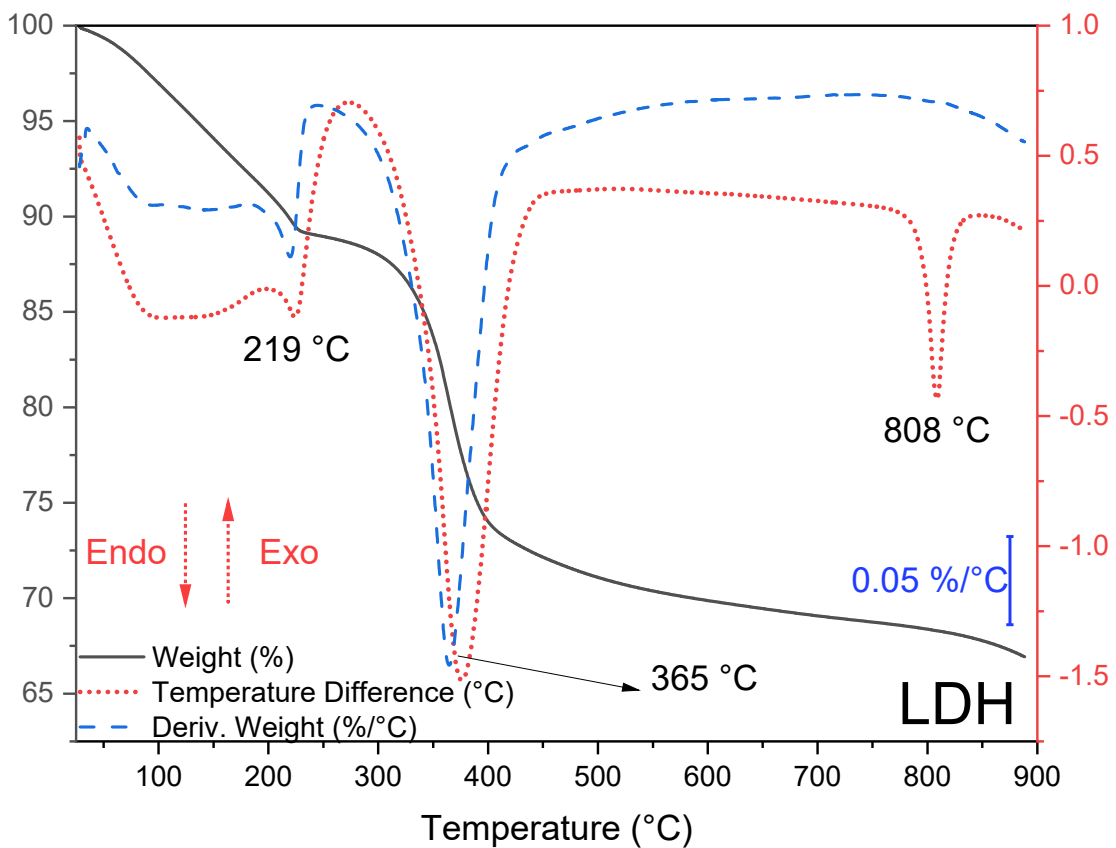


Figure 28 – Thermal analysis of synthetic LDH. With ramp from 25 to 900 °C, at 20 °C per min and in an oxidizing atmosphere.

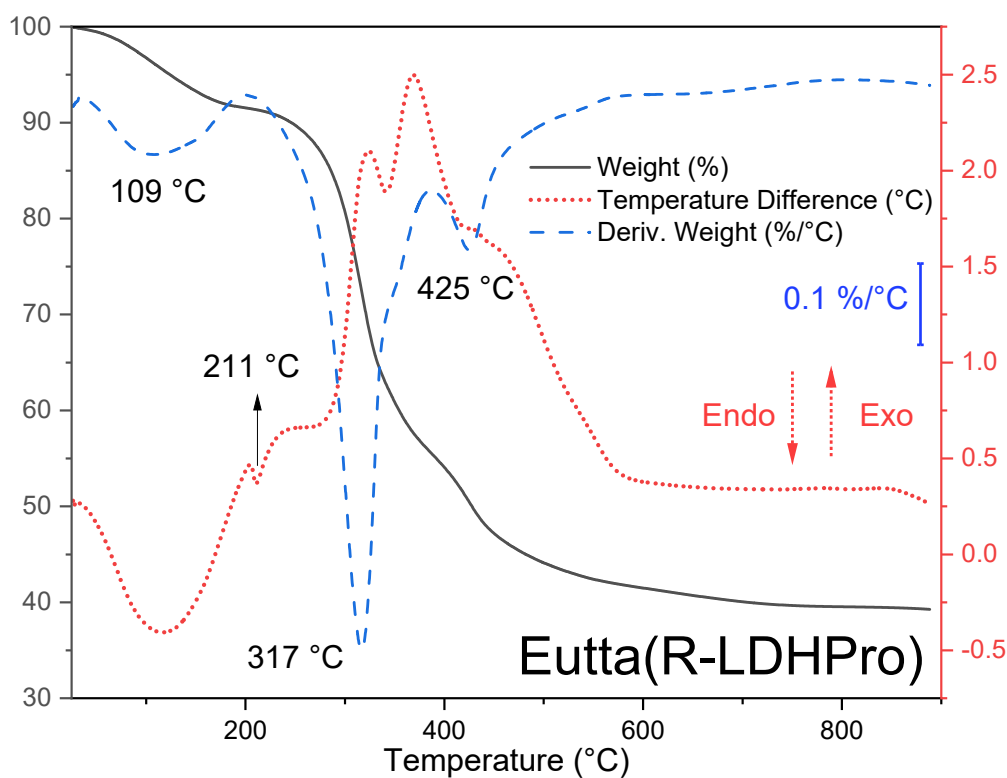
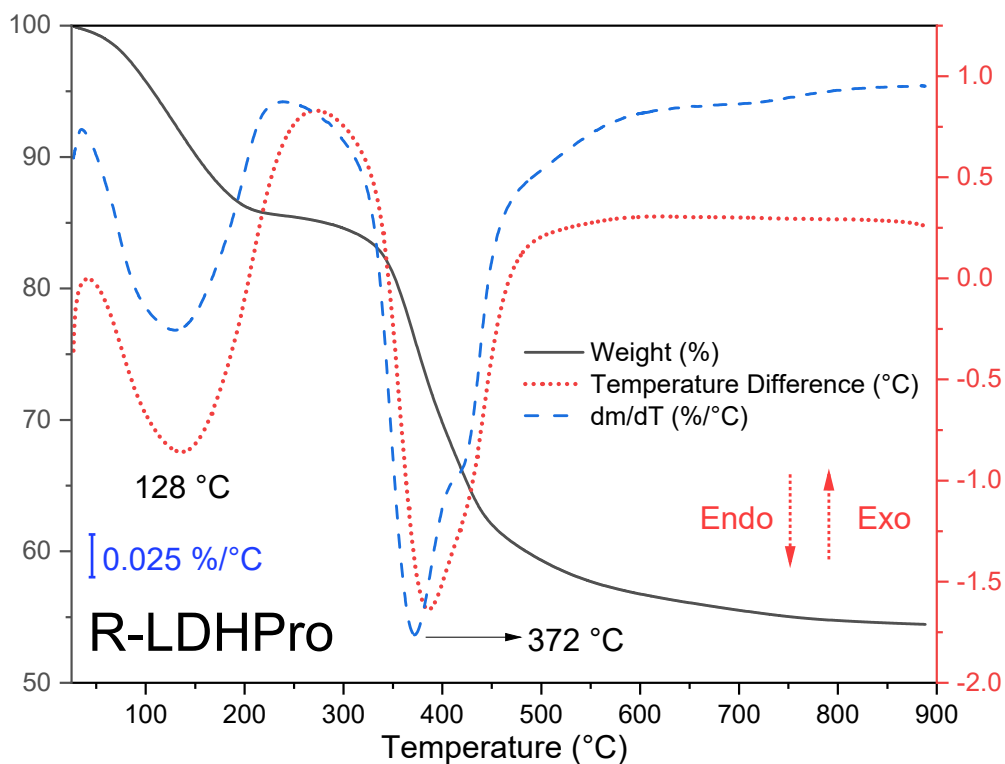


Figure 29 - TG of R-LDHPPro samples before and after complexation with Eu^{3+} ion, with a ramp from 25 to 900 °C, at 20 °C per min and in an oxidizing atmosphere.

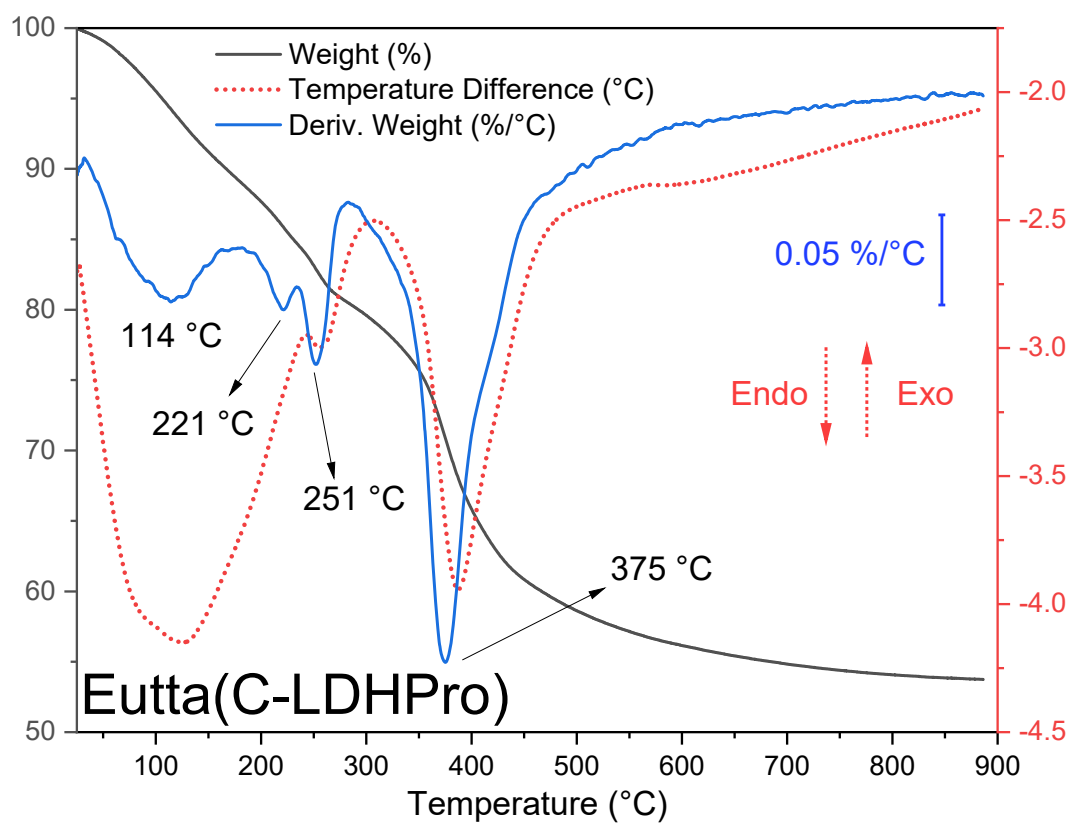
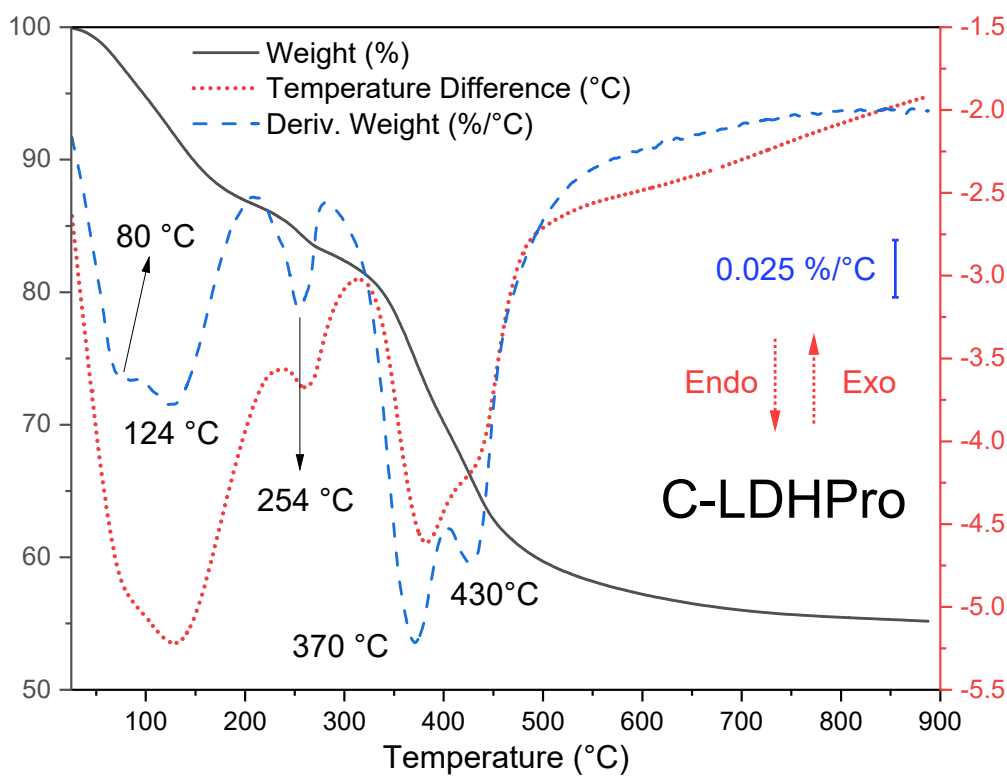


Figure 30 – Thermal analysis of C-LDHPPro samples before and after complexation with Eu^{3+} ion, with a ramp from 25 to 900 °C, at 20 °C per min and in an oxidizing atmosphere.

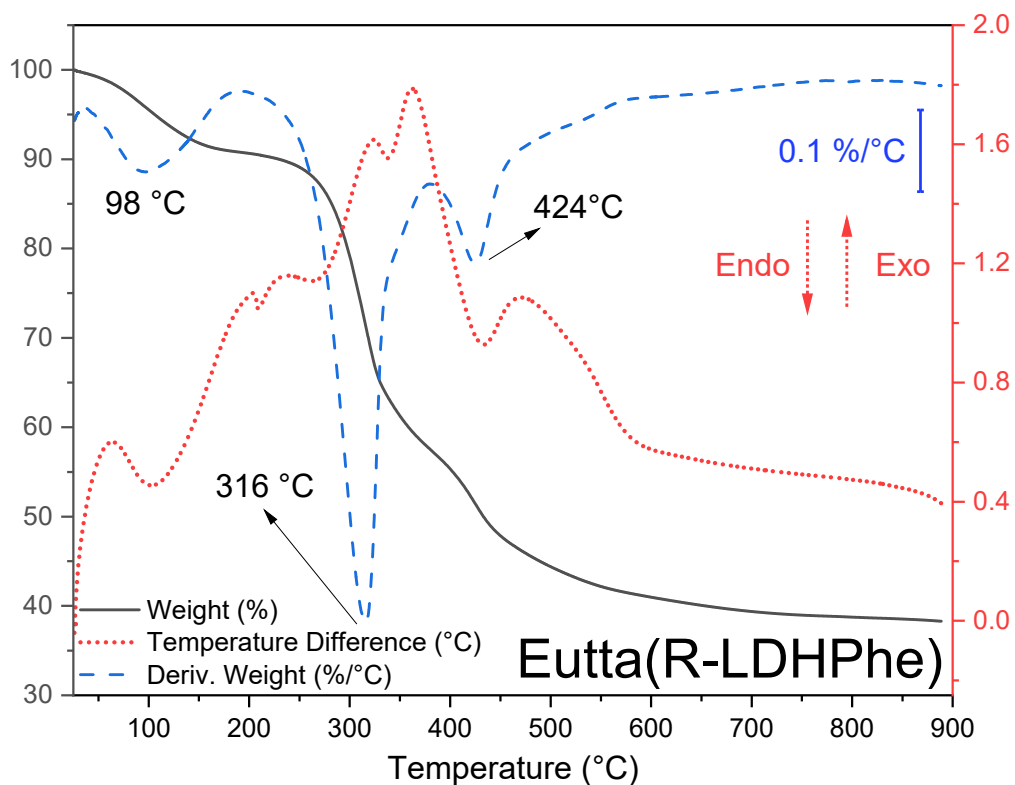
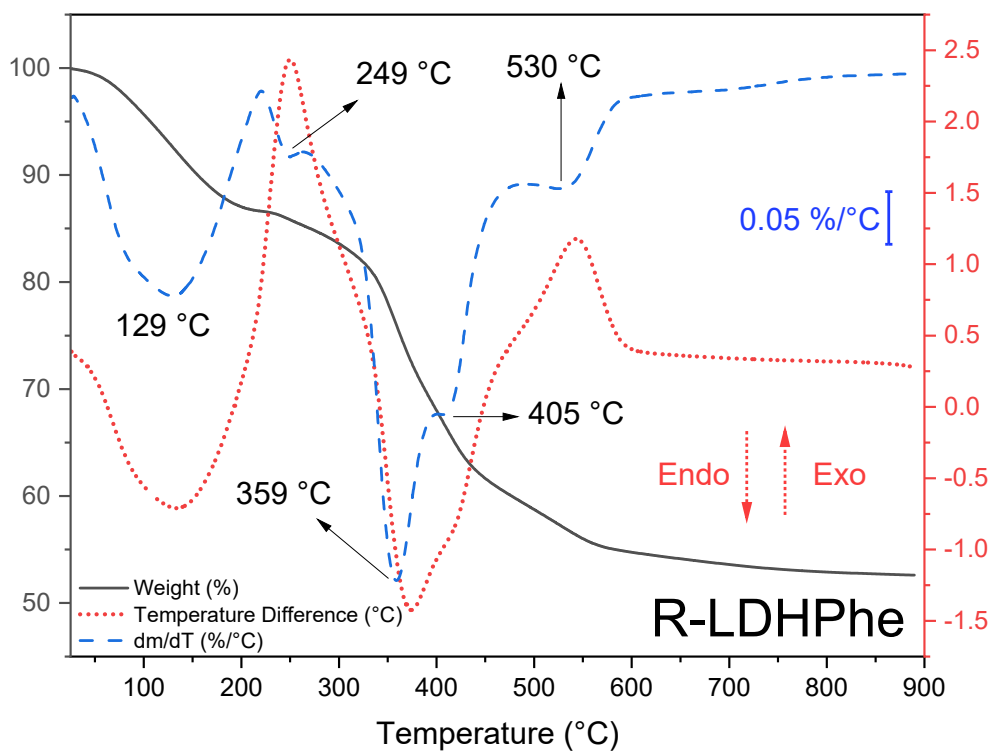


Figure 31 - Thermal analysis of R-LDHPhe samples before and after complexation with Eu^{3+} ion, with a ramp from 25 to 900 °C, at 20 °C per min and in an oxidizing atmosphere.

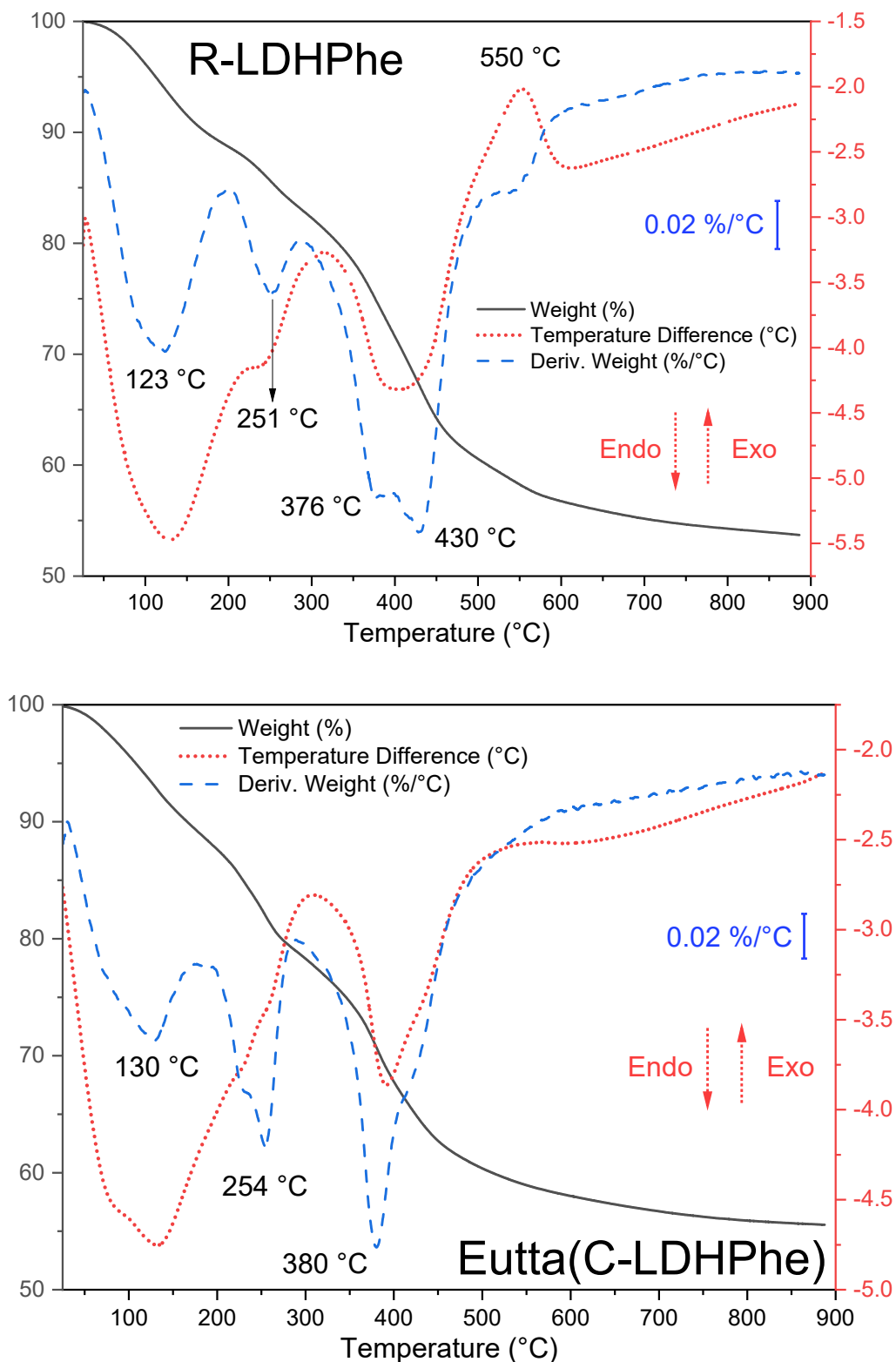
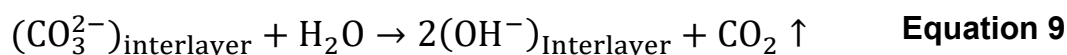


Figure 32 - Thermal analysis of C-LDHPhe samples before and after complexation with Eu^{3+} ion, with a ramp from 25 to 900 °C, at 20 °C per min and in an oxidizing atmosphere.

In the R-LDHPhe sample, there is a mass loss with maximum loss peak close to 128 °C of large width starting at 35 °C up to 220 °C, attributed both to the removal of adsorbed water and the first phase of melting and decomposition

of proline and the LDH dehydroxylation phase. At 372 °C, the endothermic decomposition of $[\text{CO}_3]^-$ occurs and the last stage of proline decomposition occurs at peaks close to 420 °C. The decomposition of carbonate is endothermic because it reacts with a nearby water molecule, resulting in volatile CO_2 and an interlamellar hydroxyl, as shown in equation 9 (KANEZAKI, 1998):

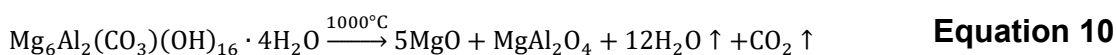


The process of transformation of CO_3^{2-} into CO_2 is endothermic while that of proline decomposition is exothermic, with the superposition of energy of these processes occurring in the DTA peaks, with the resulting peak being the one with the highest energy. After the complexation of the Eu^{3+} ion, with the increase of organic matter from tta, the energy release resulting from the decomposition, mainly from the aromatic rings of tta and the cyclic radical of proline, overlaps with the endothermic process of $[\text{CO}_3]^{2-}$, resulting in two exothermic peaks in the regions of 317 to 400 °C.

In the proline sample obtained by the coprecipitation method, there is an increase in the temperature of the LDH dehydroxylation mass loss peak to 254 °C, also attributed to the melting of proline. Removal of water adsorbed on the surface of the C-LDHPro sample occurs between 35 to 100 °C with a mass loss peak at 75 °C, as well as the onset of melting and proline decomposition occurring at 125 °C. The mass loss peak of the interlamellar anion decomposition also increases to 371 °C with the last stage of proline decomposition occurring at 429 °C (MA; ZHENG; PANG, 2012). After complexation, the mass loss peak for dehydroxylation shifts to 221 °C, closer to pure LDH, while proline fusion appears with maximum mass loss at 251 °C.

For samples containing phenylalanine, 5 peaks of mass losses are observed. The first, between 100 and 130 °C, is related to water adsorbed on the surface of the material, while the second loss in mass close to 254 °C is attributed to the beginning of melting and decomposition of the intercalated phenylalanine, starting with the removal of the aromatic ring, in the form of toluene, with overlapping of LDH dehydroxylation. The peak of mass loss at 360 °C is related to the decomposition of $[\text{CO}_3]^-$, while the last two steps of phenylalanine decomposition occur at approximately 405 and 530 °C. In the sample obtained by the co-precipitation method, the temperature of these last two phases shifts to 430 and 550 °C indicating an increase in the thermal stability of the material.

In general, the decomposition of LDH Mg-Al is described according to equation 10 (ZHITOVA et al., 2020):



Which can be readjusted to calculate the molarity of lost organic matter, through the initial and final molar mass, as shown in equation 11:

$$\%m[\text{M.M.LDH} + (\text{O.M.})_x - (\text{CO}_3^- + (\text{OH})_{10} + \text{H}_2\text{O})_x] = \text{Mg}_6\text{Al}_2(\text{O}_2)_{4.5} \quad \text{Equation 11}$$

Where $\%m$ is the percentage of mass remaining after heat treatment, M.M.LDH is the molar mass of hydrotalcite, x is the molarity of organic matter and O.M. is the molar mass of the intercalated organic molecule. The chemical compositions calculated by thermal and elemental analyzes are shown in table 13.

Table 13 - Calculated chemical formulas for hydrotalcite samples intercalated with amino acids.

Sample	Chemical formula
LDH	$[\text{Mg}_{2.49}\text{Al}_{0.87}(\text{OH})_{6.67}](\text{CO}_3)_{0.77} \cdot 1.67\text{H}_2\text{O}$
R-LDHPro	$[\text{Mg}_{2.49}\text{Al}_{0.87}(\text{OH})_{6.67}](\text{CO}_3)_{0.24}(\text{Pro})_{0.08} \cdot 1.67\text{H}_2\text{O}$
R-LDHPh	$[\text{Mg}_{2.49}\text{Al}_{0.87}(\text{OH})_{6.67}](\text{CO}_3)_{0.10}(\text{Phe})_{0.22} \cdot 1.67\text{H}_2\text{O}$
C-LDHPro	$[\text{Mg}_{2.49}\text{Al}_{0.87}(\text{OH})_{6.67}](\text{CO}_3)_{0.12}(\text{Pro})_{0.20} \cdot 1.67\text{H}_2\text{O}$
C-LDHPh	$[\text{Mg}_{2.49}\text{Al}_{0.87}(\text{OH})_{6.67}](\text{CO}_3)_{0.06}(\text{Pro})_{0.38} \cdot 1.67\text{H}_2\text{O}$

As shown in table 15, the samples obtained by the coprecipitation method showed approximately twice the amino acid concentration compared to the reconstruction method. With the increase of the interlamellar space evidenced by the X-ray diffractograms, the amino acids obtained greater mobility in relation to the reconstruction synthesis, facilitating the intercalation. The low concentration of proline in relation to the amino acid phenylalanine is due to the chemical environment and affinity between the amino acid and the matrix. Proline is very soluble and has greater affinity with carbonate than with hydrotalcite, making substitution difficult in both applied methods. On the other hand, the same does not happen with phenylalanine, which has low affinity with both water and carbonate, facilitating intercalation, even using ethanol as a solvent (TRAN; LIN; CHAO, 2018).

4.1.2.4. Scanning electron microscopy

The scanning electron microscopy images of the samples with hydrotalcites are shown in Figure 33.

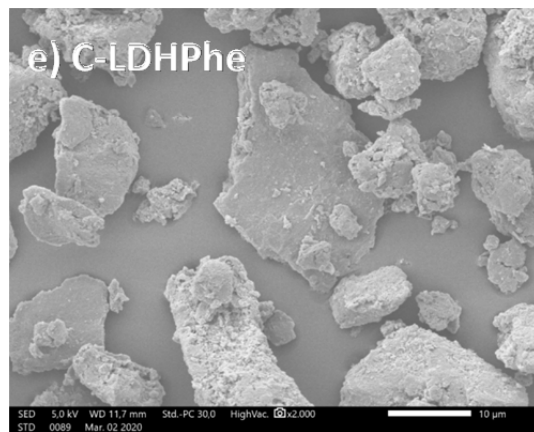
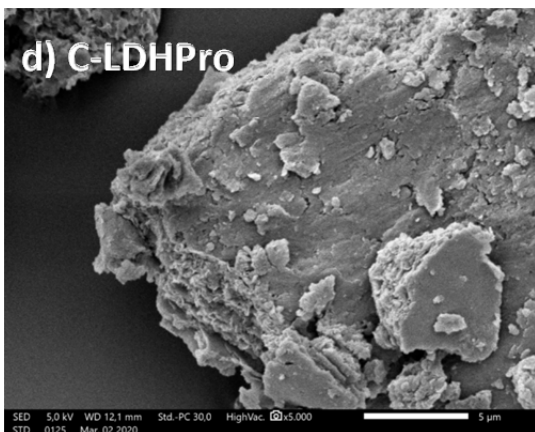
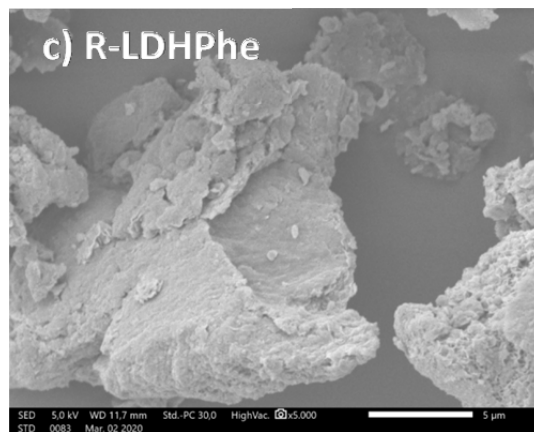
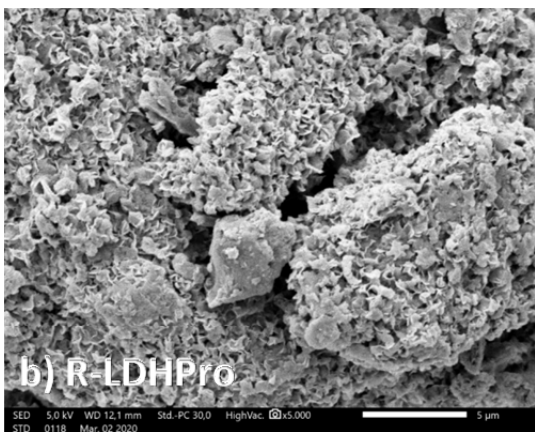
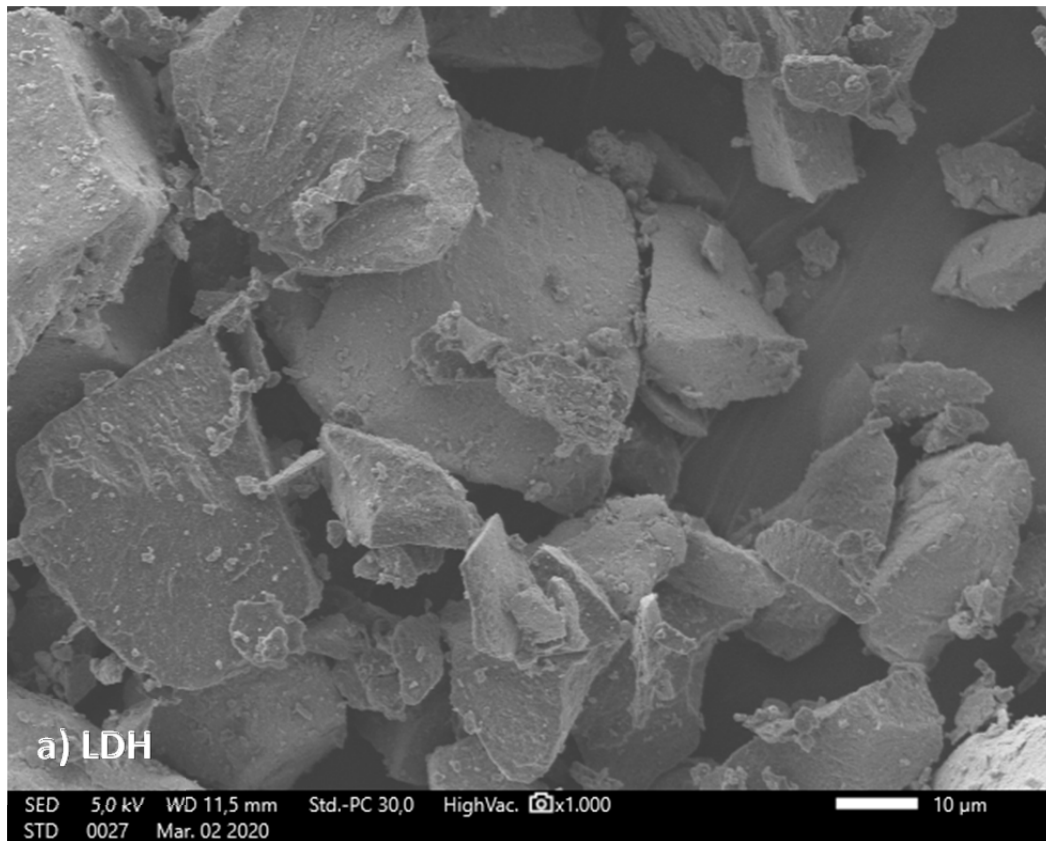


Figure 33 - SEM images for pure and amino acid intercalated LDH samples.

The material has a typical morphology of hydrotalcite hexagonal structure, in the form of plates that remain in the materials intercalated with the amino acids proline and phenylalanine. However, the R-LDHPro sample presents a kind of surface exfoliation, with a rough characteristic, indicating the region of interaction of the complex with the matrix. The samples obtained by the coprecipitation method had a more "smooth" and more distributed surface compared to the samples obtained by the reconstruction method, being even more distributed in the samples with phenylalanine, due to the influence of the solvent and the hydrophobic character of the amino acid. In all samples, the characteristic of material stacked in the form of tactoids was observed, maintaining the initial characteristic of LDH.

4.1.3. Materials obtained from LAPONITE® and saponite (smectites)

Due to the relative ease of expansion of the basal space of smectites, the lanthanide complex with amino acids was synthesized and intercalated directly in LAPONITE® and saponite and studied their properties.

4.1.3.1. X-ray diffraction

The X-ray diffractograms of the samples obtained by LAPONITE® and saponite are shown in Figure 34.

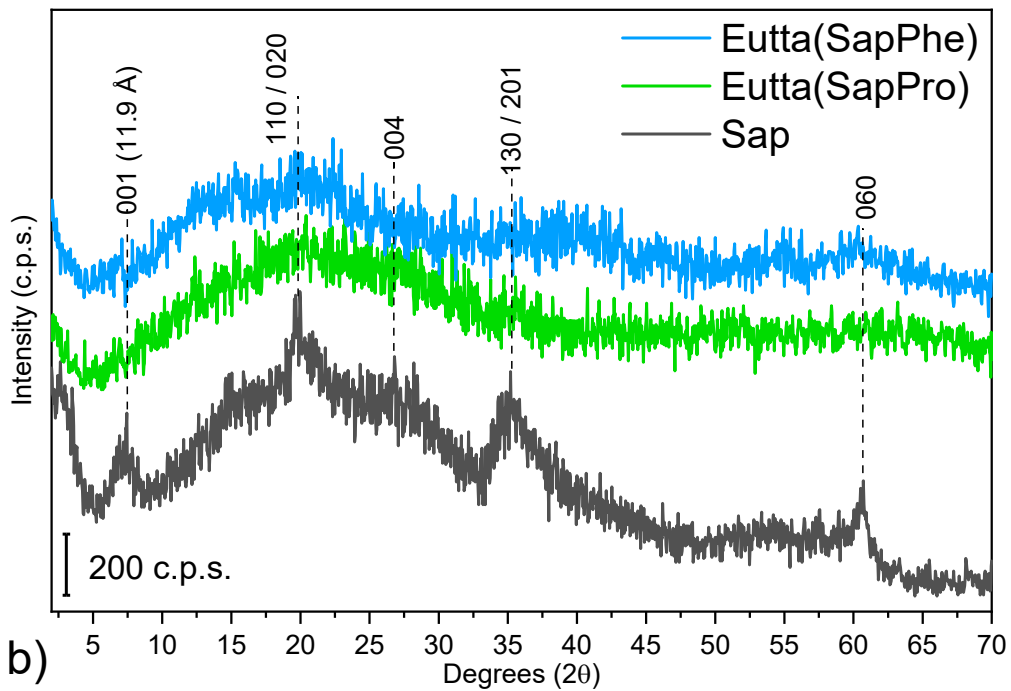
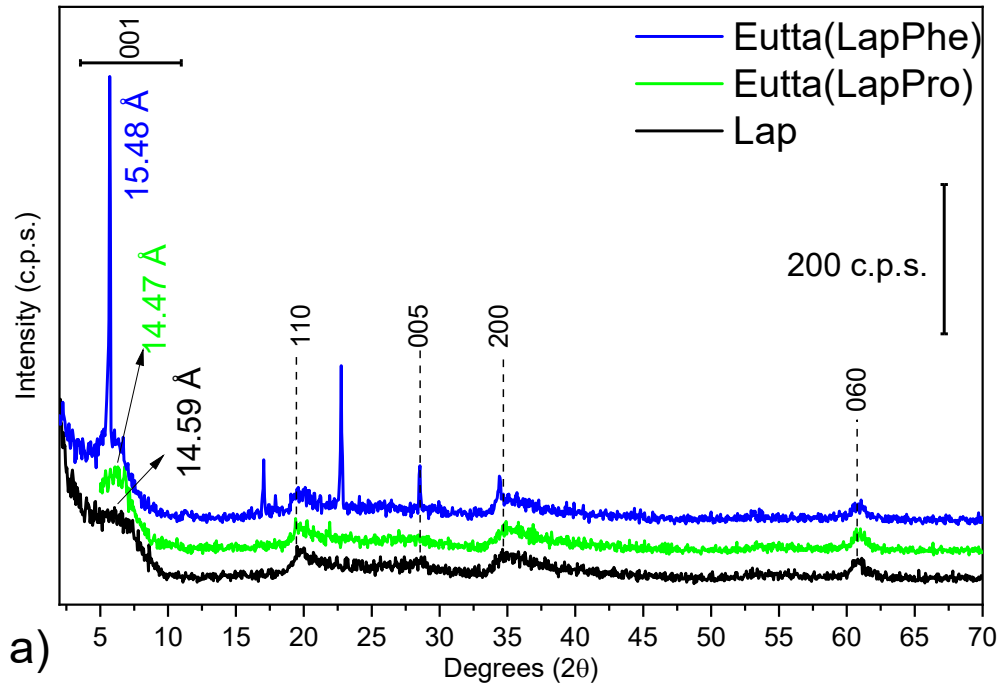


Figure 34 - X-ray diffractograms of LAPONITE® (a) and saponite (b) samples.

Both pure clay mineral samples showed a typical structure of smectites with the main reflections present, these being reflection 001 (between 5 to 8° in 2θ), 110 (close to 20° in 2θ) and 060 (near 60° in 2θ), with the other reflections shown in Figure 38 being particular to each clay mineral (MARCHESI et al.,

2021b; SILVA et al., 2018). The pure saponite synthesized by the microwave method showed lower crystallinity related to other similar works in the literature (AVILA et al., 2010; TRUJILLANO et al., 2011; VOGELS; KLOPROGGE; GEUS, 2005), factor evidenced by the *FWHM* index, as shown in table 14.

Table 14 - Basal space (*d*) and *FWHM* index of X-ray diffractograms of samples obtained by LAPONITE® and saponite.

Sample	<i>2θ</i> (degree)			<i>d</i> (Å)	<i>FWHM</i> ₀₀₁ (2θ)
	001	110	060		
Lap	6.1	19.5	60.8	14.6	3.45
Sap	7.4	19.6	60.7	11.9	1.96
Eutta(LapPro)	6.1	19.4	61.0	14.6	2.35
Eutta(LapPhe)	5.7	19.5	61.0	15.5	0.10
Eutta(SapPro)	6.9	-	-	12.7	1.64
Eutta(SapPhe)	7.1	-	60.4	12.5	1.84

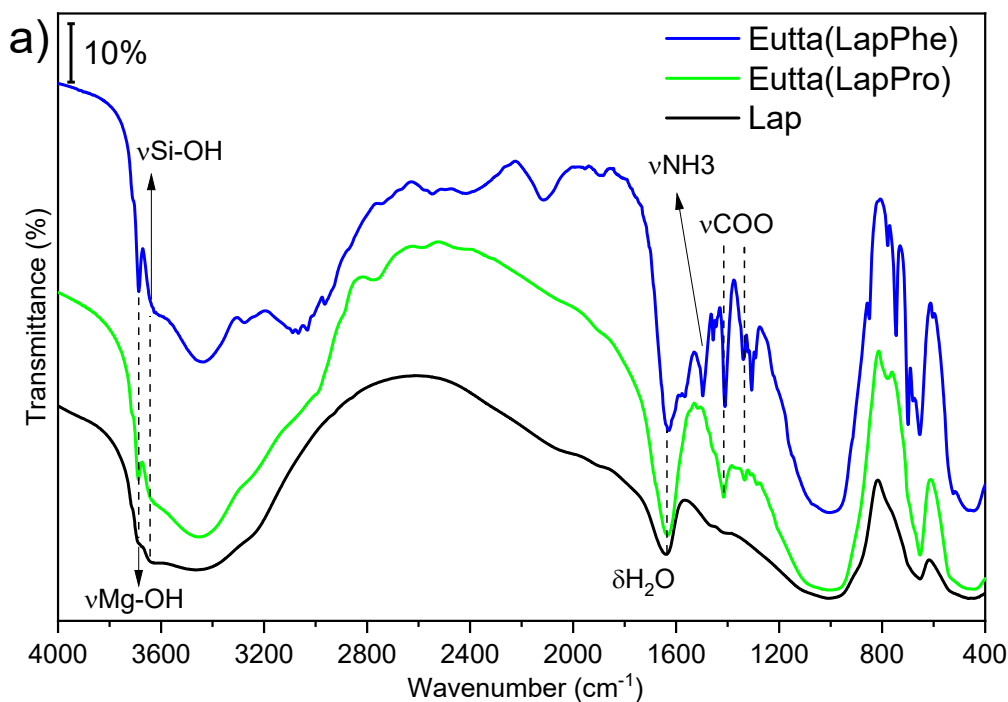
X-ray diffraction is an established method for studying the structures and intercalation of species in clay minerals such as the smectites group. The 001 plane had an increase from 14.6 Å to 15.5 Å in the phenylalanine sample, while the proline sample remained with the same spacing, however with a finer peak compared to pure LAPONITE®. The sample with phenylalanine presented an intense and fine peak in reflection 001, in addition to relatively fine peaks in reflections 005 and 200, indicating an increase in the crystallinity of the material with the intercalation of the complex with phenylalanine. The results suggest that the interactions between amino acid and the matrix occur at the

interparticle sites, on the sides of the lamellae or on the surface of the lamellae rather than in the interlayer space.

On the other hand, samples intercalated in saponite had a significant loss of crystallinity. The Eutta(SapPro) sample did not show the peak relative to the 060 reflection attributed to the bonding planes between the tetrahedral and octahedral layers. The absence of this plane may indicate crystallite exfoliation or the total loss of the lamellar structure. As for the Eutta (SapPhe) sample, despite having low crystallinity, it was possible to identify the 001 and 060 reflection planes, maintaining the characteristic of smectites. Similarly to LAPONITE®, with the approximate increase of 0.8 Å suggests that interactions occur at interparticle sites, on the surface or on the sides of the lamellae.

4.1.3.2. Infrared spectroscopy (FTIR)

The vibrational spectra in the infrared region are shown in Figure 35.



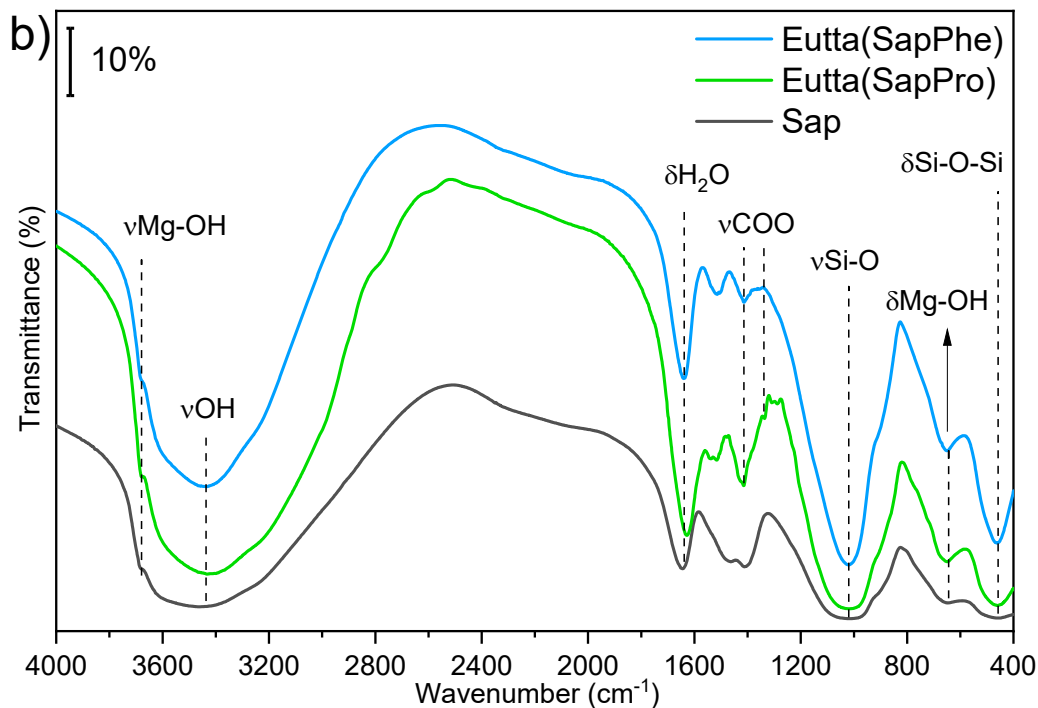


Figure 35 - Infrared vibrational spectra for samples with LAPONITE® (a) and saponite (b) and their main attributions.

Through vibrational spectra in the infrared region, it is possible to observe the characteristic bands of LAPONITE®, the first being at approximately 3687 cm^{-1} attributed to stretching vibrations of the hydroxyls of the Mg-OH octahedron. The second band is observed near the vibrations of these hydroxyls, close to 3640 cm^{-1} referring to the stretch vibrations of Si-OH tetrahedral hydroxyls, the remainder of the hydroxyls referring to adsorbed water molecules appear between 3600 to 3200 cm^{-1} , with angular vibration of adsorbed and intercalated water molecules in 1630 cm^{-1} (XIONG et al., 2019). In the region between 800 and 1200 cm^{-1} the Si-O and Si-O-Si stretching vibrations are located. The width of the bands and their displacement after the intercalation of the complexes shows their interaction in these regions through hydrogen bonds between the carboxylated or amine group of these amino acids with the oxygen of the Si-O group (GHADIRI et al., 2014). After the intercalation

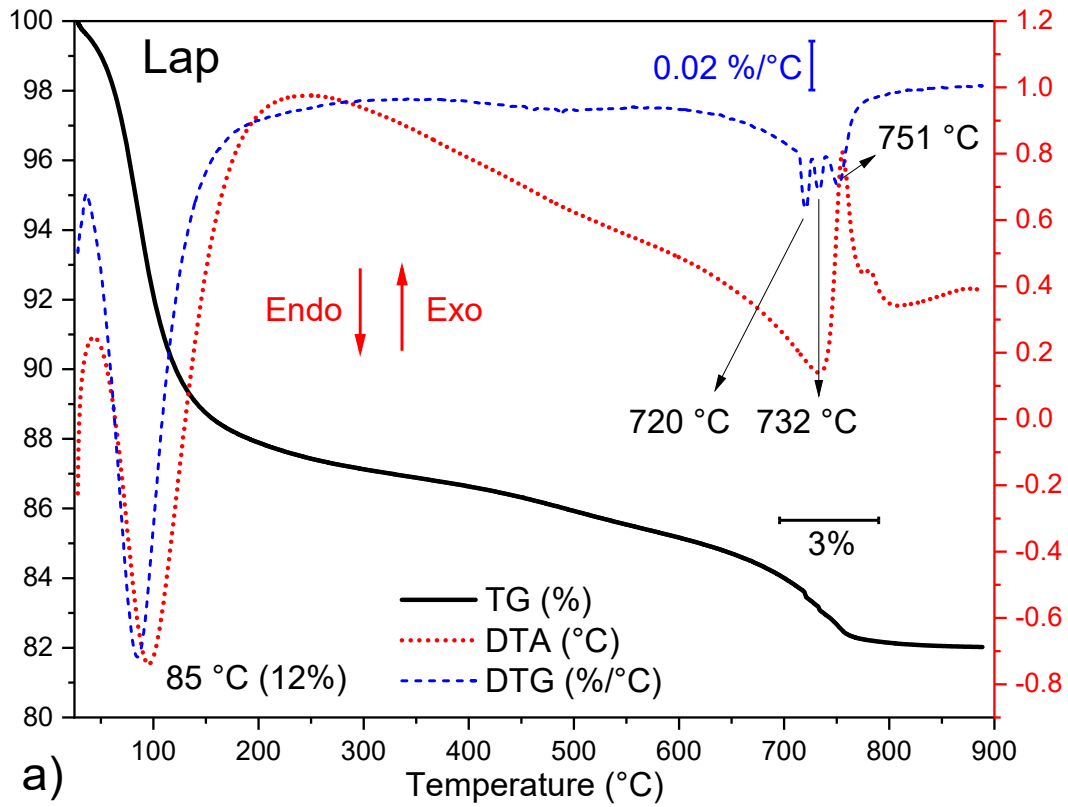
of the complexes, the vibrations of the carboxylate group for the two amino acids in LAPONITE® were observed, in the region of 1410 and 1340 cm^{-1} for antisymmetric and symmetric stretch vibrations respectively. In addition, it is possible to observe the amine stretch vibration at 1497 cm^{-1} in the Eutta(LapPhe) sample, which in general, the identification bands of the organic groups were more defined in relation to the Eutta(LapPro) sample.

As for the saponite samples, the structural vibrations of Mg-OH hydroxyls are found at 3674 cm^{-1} , while the stretch vibrations of free hydroxyls and adsorbed water appear between 3200 to 3600 cm^{-1} , with the angular vibrations of water in 1640 cm^{-1} (TRUJILLANO et al., 2010, 2011). In the region between 800 to 1200 cm^{-1} , Si-O stretch vibrations are found, which, as in LAPONITE®, are also sensitive to the chemical environment and the intercalated material, where changes in the intensity and width of this band were observed, indicating interactions between the Si-O group and the complexes intercalated through hydrogen bonds or weaker forces such as Van der Waals interactions. At 650 cm^{-1} bands of angular vibrations of Mg-OH are observed and angular vibrations of Si-O-Si are observed at 458 cm^{-1} (AVILA et al., 2010). Amino acid vibrations in saponite are observed at 1416 and 1336 cm^{-1} , attributed to antisymmetric and symmetric stretch vibrations of the COO^- grouping respectively, in addition to amine stretch vibrations close to 1520 cm^{-1} .

4.1.3.3. Thermal analysis

Both saponite and LAPONITE® have three stages of mass loss in heat treatment, the first with mass loss peak between 80 and 85 °C relative to water adsorbed on the clay mineral surface, while the second is the gradual loss of interlamellar water and exchangeable sodium hydration phase, and finally,

around 800 °C, dehydroxylation and collapse of the lamellar structure occur (GHADIRI et al., 2014; RYU et al., 2014). Thermal analyzes of LAPONITE® materials are shown in figures 36.



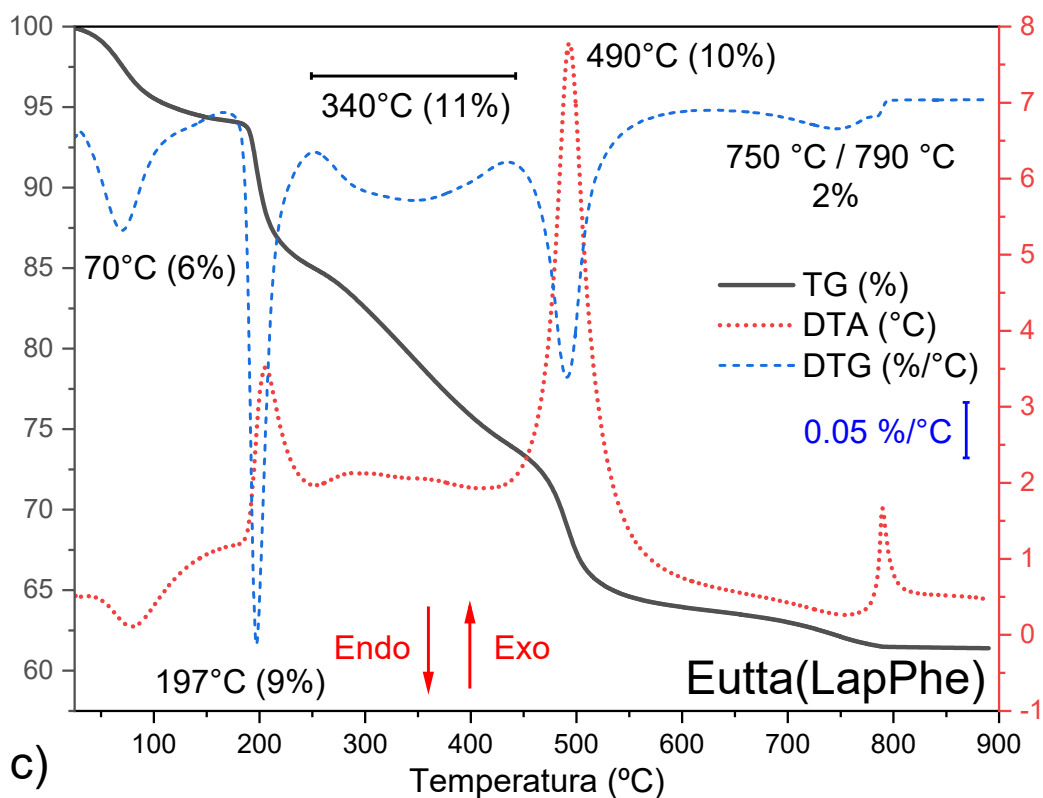
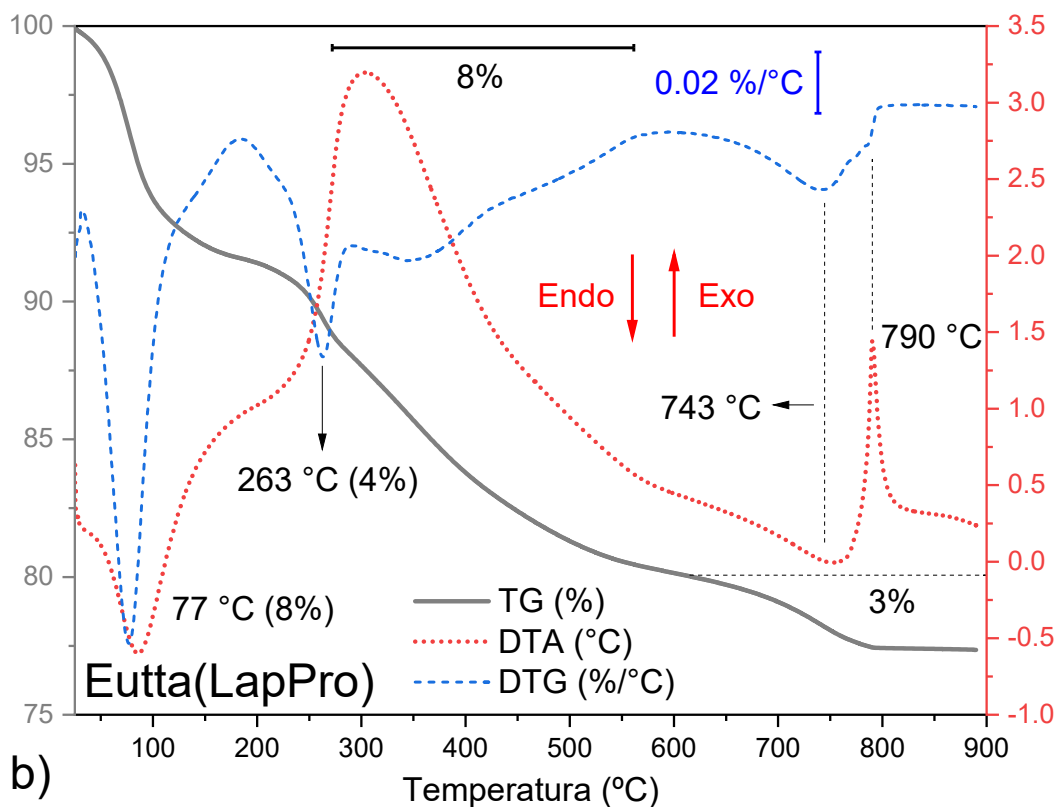
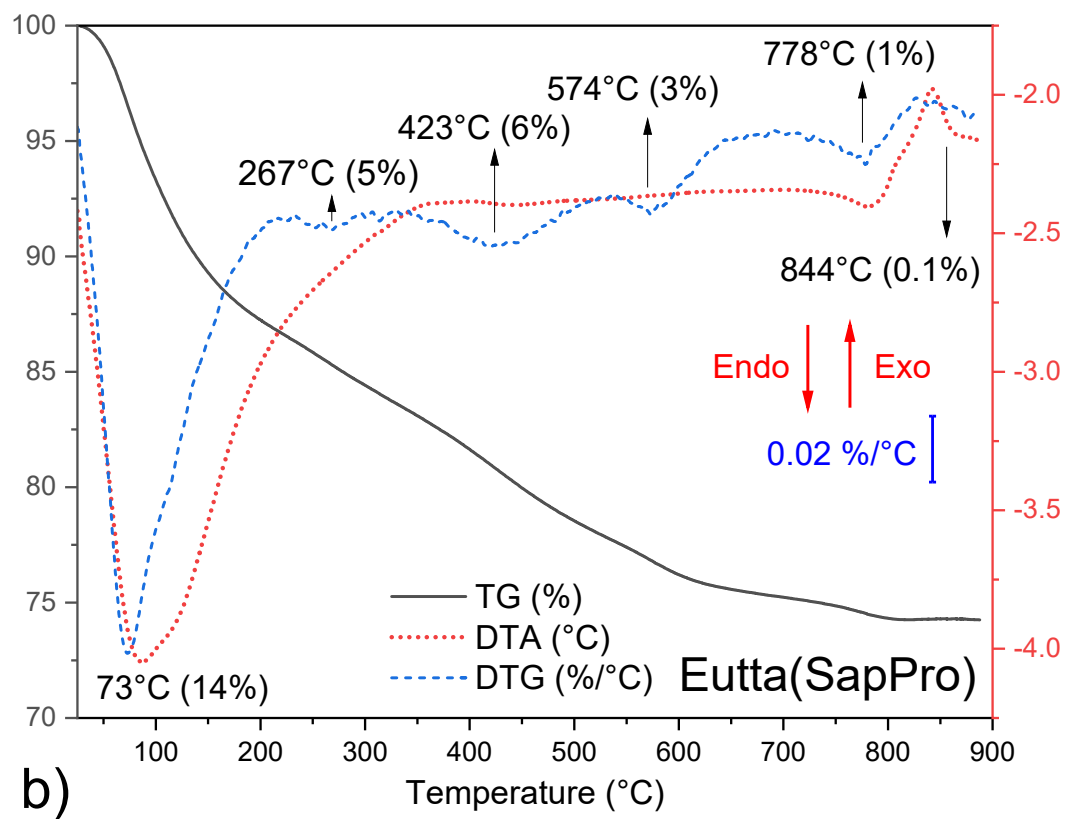
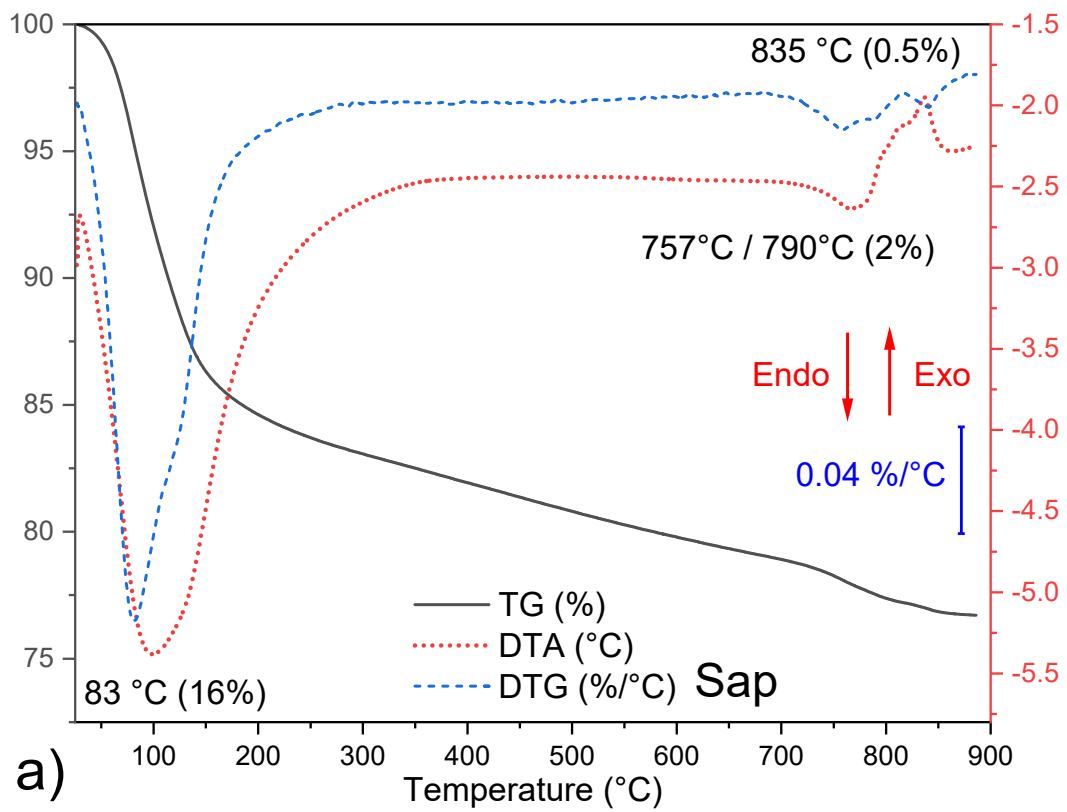


Figure 36 - Thermal analysis (TG, DTA and DTG) of pure LAPONITE® and intercalated with amino acid complexes. With ramp from 25 to 900 °C in oxidizing atmosphere.

In the LAPONITE® dehydroxylation stage between 700 and 750 °C, a loss of 3% of mass is observed with 3 peaks of mass loss, where the first two (720 and 732 °C) are attributed to dehydroxylation presenting an endothermic behavior while the last peak of mass loss (751 °C) of exothermic character is attributed to recrystallization of the amorphous meta-phase (PÁLKOVÁ et al., 2010). After the addition of complexes with amino acids in LAPONITE®, the dehydroxylation temperature undergoes a slight increase, with broader peaks of mass loss, showing the interaction of interlamellar hydroxides with the luminescent complex.

In the Eutta(LapPro) sample, the exothermic mass loss stage relative to the complex is located between 200 to 600 °C representing approximately 12% of the mass loss, the main peak (260 °C) being related to the breakage of the rings of the tta and the cyclic structure of proline while the last rather broad peak close to 500 °C is attributed to the final stages of organic matter decomposition, together with the complete decomposition of the Eu(III) complex into EuClO (RYU et al., 2014). In the Eutta(LapPhe) sample these peaks are thinner and more defined in relation to proline, the first loss with a peak at 197 °C being attributed to the breakage of the aromatic rings of phenylalanine and tta, while at 490 °C the peak is observed of loss of mass of the last stage of decomposition of the organic matter of the complex.

Like LAPONITE®, saponite also has three defined stages of mass loss with dehydroxylation occurring around 800 °C, with two endothermic mass loss peaks at 757 and 790 °C and an exothermic peak at 835° C for saponite meta-phase recrystallization and lamellar structure collapse. The thermal analyzes of the saponite samples are shown in Figure 37.



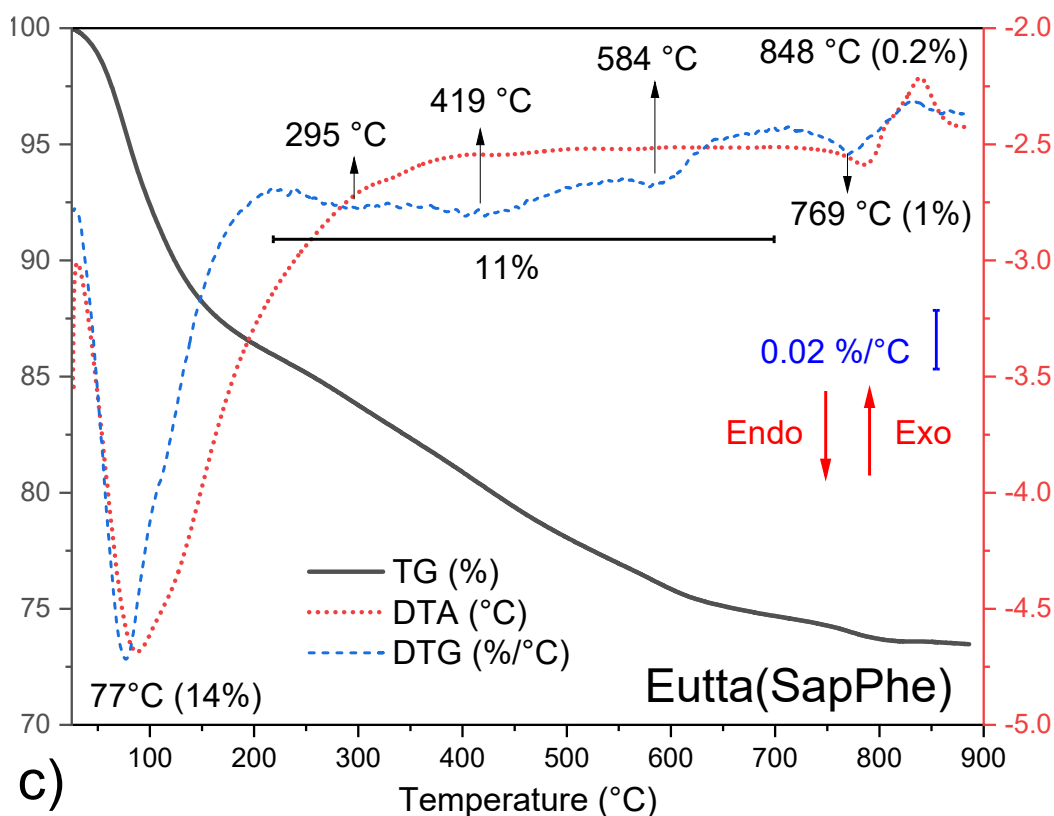


Figure 37 - Thermal analysis (TG, DTA and DTG) of pure saponite and intercalated with amino acid complexes. With ramp from 25 to 900 °C in oxidizing atmosphere.

After the addition of the complexes, only a broad and endothermic peak is observed between 770 and 780 °C, showing the interaction of the complexes with the interlamellar hydroxyls. For the Eutta(SapPro) sample, the complex decomposition occurs in three steps between 200 to 600 °C and approximately 14% mass loss, while in the Eutta(SapPhe) sample the complex decomposition presents 11% of the mass loss. material. On the other hand, the sample with phenylalanine showed greater thermal stability compared to the sample with proline with higher temperature of dehydroxylation and the final stage of decomposition of the Eu(III) complex.

4.1.3.4. Scanning Electron Microscopy (SEM)

Scanning electron microscopy images are shown in Figures 38 and 39:

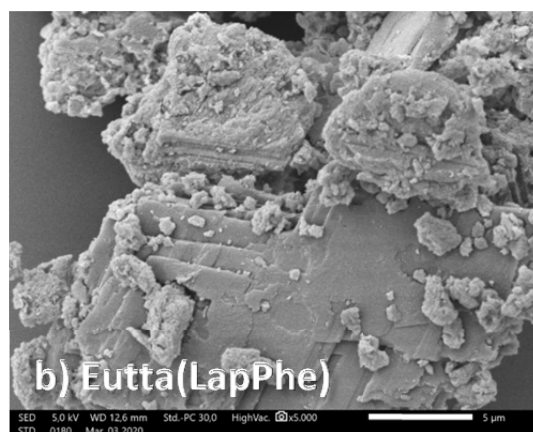
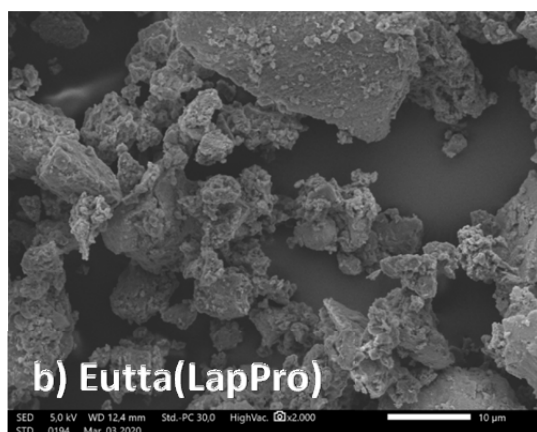
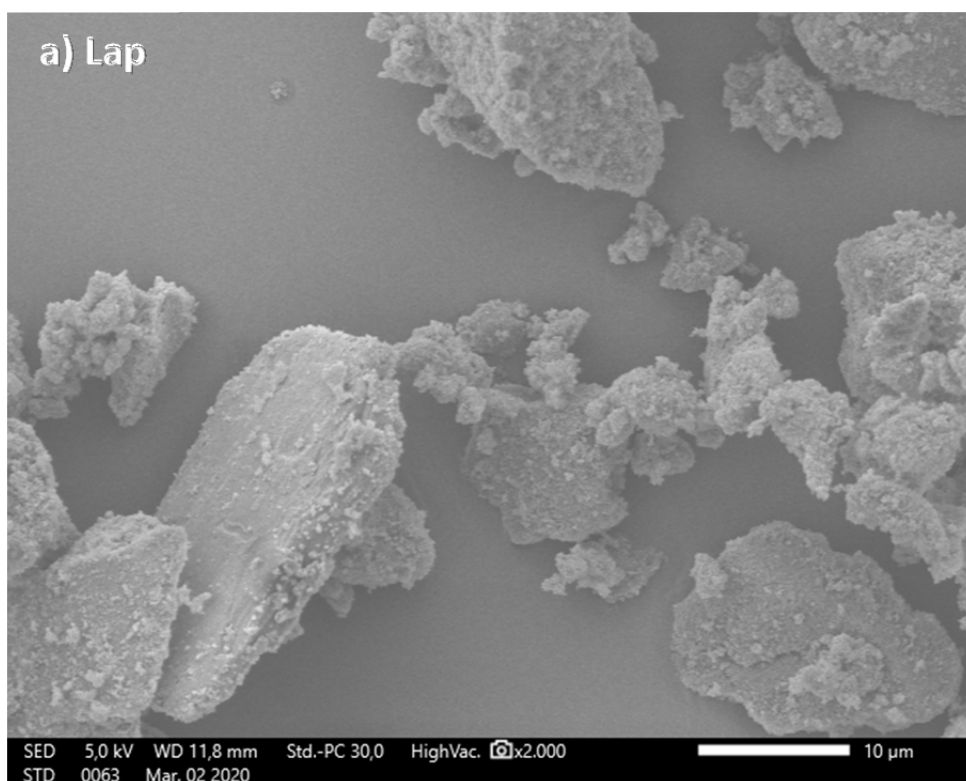


Figure 38 - SEM images of pure LAPONITE® and intercalated with Eu(III) complexes.

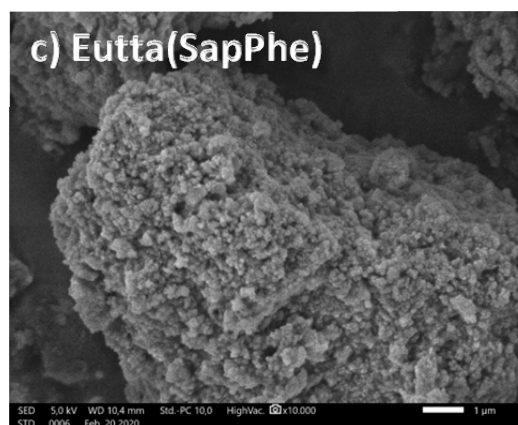
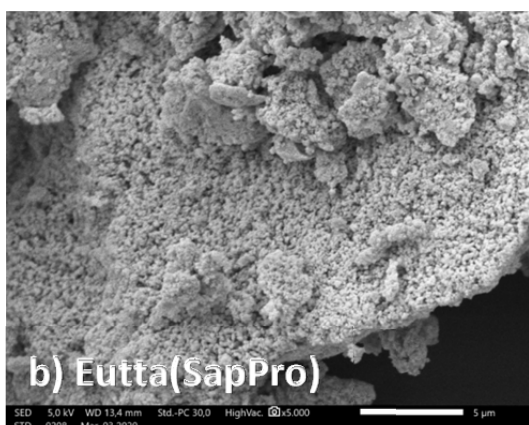
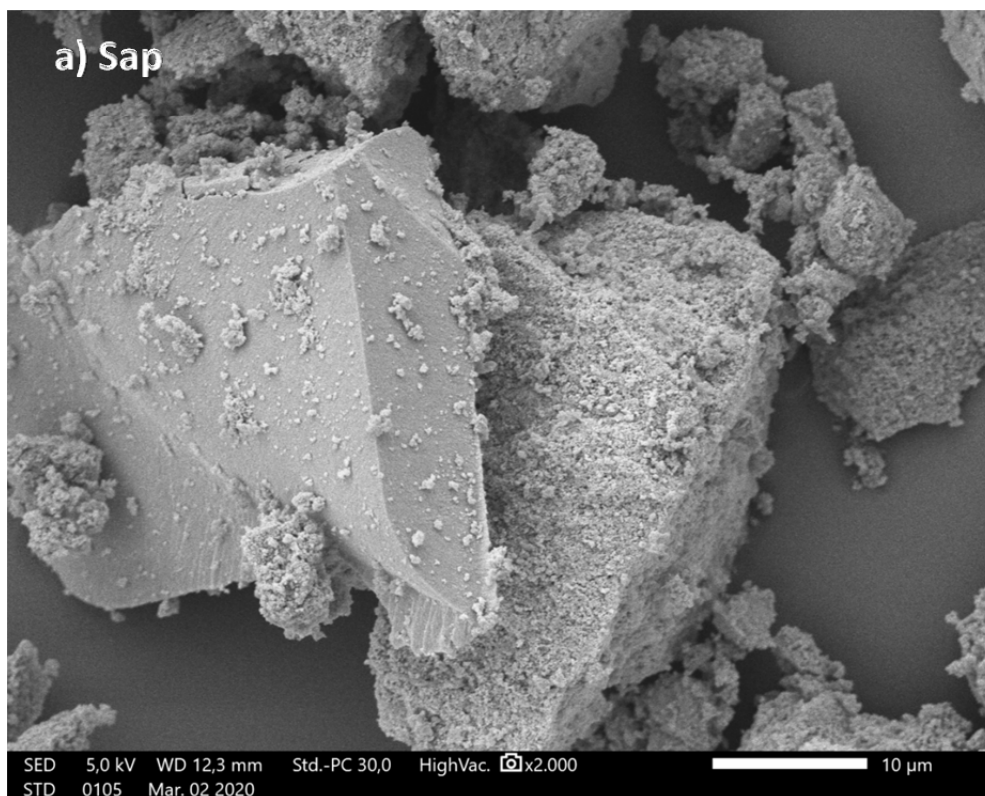


Figure 39 - SEM images of pure saponite intercalated with Eu(III) complexes.

In the images with LAPONITE® it is possible to observe that the crystallite has a structure with a size ranging from 15 to 25 nm in diameter and morphology in the form of platelets with lamellar structure. After the clay mineral complexes, the structure remains with a higher incidence of smaller crystallites and a spongier surface morphology compared to pure LAPONITE®, resulting from the interaction of the complex with the matrix. It was also possible to observe a parallel stacking of the tactoids compatible with similar works in the

literature (GHADIRI et al., 2014; GUIMARÃES; CIMINELLI; VASCONCELOS, 2007; PÁLKOVÁ et al., 2010). In saponite, the morphology is more irregular and with larger crystallites than in LAPONITE®. After the complexation of the Eu^{3+} ion, the spongy surface is more evident in samples with saponite, despite maintaining the size and general characteristics of the crystallites.

4.2. Luminescent properties of the materials obtained

In luminescence spectroscopy, the detection limits as well as the analytical sensitivity promote an advantage over other characterization spectroscopic methods such as UV-Visible, increasing the selectivity of the analysis, being ideal for obtaining optical information of materials.

In a common spectrophotometer, the sample absorbs photons by a source that covers a wide range of the electromagnetic spectrum, promoting a high energy state (excited state), which when relaxing to the ground state, emits photons that are propagated to all dimensions. These photons are directed by monochromators and converted into electrical signals forming the spectrum record, as seen in figure 40.

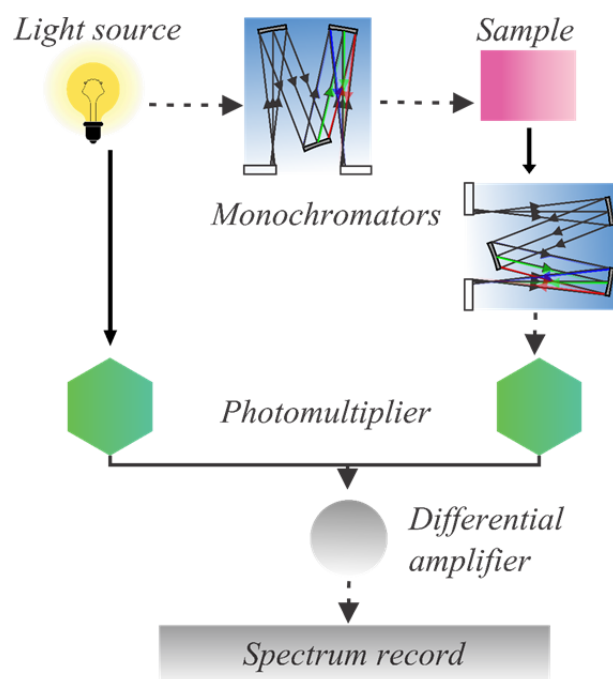


Figure 40 - Schematic representation of a common fluorimeter (font = author).

The Eu(III) ion emits mainly in the red region, generally relaxing from the excited state 5D_0 to the ground states 7F_J ($J= 0-6$), the last two being observed in the infrared region and generally with the most intense transition at approximately 610 nm ($^5D_0 \rightarrow ^7F_2$). Due to the low molar absorption, lanthanide ions are usually complexed with organic ligands of high molar absorptivity to transfer the absorbed energy to the central ion transitions. Ligands absorb energy from the ground state (S_0) to the singlet excited state (S_1), and can return to the ground state releasing this energy through radiative or non-radiative emission such as molecular vibrations for example (HAGAN; ZUCHNER, 2011), as shown in figure 41. Once excited, the ligand can also transfer this energy to the triplet state (T_1), which in turn can transfer to the excited state of the europium ion, releasing this energy radiatively when decaying to the ground state 7F_J .

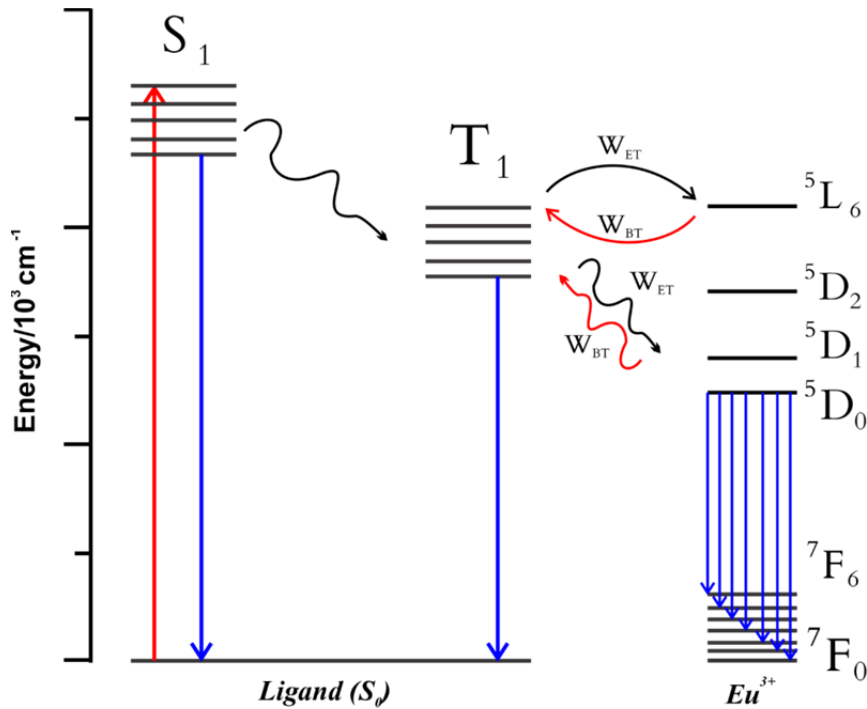


Figure 41 - Representation of energy levels in the process of energy transfer from the ligand to the Eu(III) ion. W_{ET} and W_{BT} are energy transfer rates and back energy transfer rates respectively. (font: author)

To interpret the emission spectra, it is necessary to integrate the intensity of the transitions in the spectrum to obtain the area (A_{0-J}) and transform the wavelength (nm) of the barycenter of the transitions to frequency (cm^{-1}) through the formula: $\nu (\text{cm}^{-1}) = 1/(\lambda \times 10^{-7})$. After this procedure, it is possible to find the Einstein's spontaneous emission coefficient by equation 12:

$$A_{0J} = \frac{A_{0-J} \cdot \nu_{01}}{I_{01} \cdot \nu_{0J}} \times 50 \text{s}^{-1} \quad \text{Equation 12}$$

Where A_{0J} is the spontaneous emission coefficient of the transition ${}^5D_0 \rightarrow {}^7F_J$; A_{0-J} is the integrated area of transition ${}^5D_0 \rightarrow {}^7F_J$; 50 s^{-1} is the spontaneous emission coefficient of the transition ${}^5D_0 \rightarrow {}^7F_1$ which is independent of the chemical environment (BALA et al., 2018; DE ARAUJO et al., 2017; MATOS et al., 2014). The sum of these coefficients results in the radiative emission rate (A_{rad}).

The emission lifetime can also be obtained in a fluorimeter by fixing the excitation and emission wavelengths and analyzing the decay in the detection time. The result can be analyzed by an exponential decay function ($y = y_0 + A_1 \times 10^{[-(x-x_0/\tau_{obs})]}$) (FARAT et al., 2019) to find the observed lifetime (τ_{obs}). The radiative emission lifetime can be obtained by equation 13:

$$\frac{1}{\tau_{rad}} = A_{MD} \times n^3 \left(\frac{I_{tot}}{I_{0-1}} \right) \quad \text{Equation 13}$$

Where A_{MD} is the probability of spontaneous emission of the magnetic dipole transition ${}^5D_0 \rightarrow {}^7F_1$, calculated as 14.65 s^{-1} ; n is the refraction index and is assigned as 1.33 for H_2O , 1.328 for D_2O , 1.3288 for methanol and 1.55 to solid state metal-organic complex. The value of 1.55 was assumed because it is accepted for Eu^{3+} -organic complexes and because it is close to the refractive indices of clay minerals (LDH = 1.510, Saponite = 1.559, Laponite = 1.540 and Kaolinite = 1.559) (ARAKAWA et al., 1997; BINNEMANS, 2015; DAS et al., 2019; HOXHA et al., 2020; ISHII; HASEGAWA, 2015); I_{tot} is the sum of the integrated area of luminescence intensity and I_{1-0} is the integrated area of transition intensity ${}^5D_0 \rightarrow {}^7F_1$ (FARAT et al., 2019; UTOCHNIKOVA et al., 2016). With the lifetimes, it is possible to obtain the quantum yield of emission of the ion Eu(III) through the equation:

$$Q_{Ln}^{Ln} = \frac{\tau_{obs}}{\tau_{rad}} \quad \text{Equação 14}$$

Where Q_{Ln}^{Ln} is the quantum yield of emission of the Eu(III) ion, also called the intrinsic or internal quantum yield. To find the emission quantum yield of the complex ($Q = \frac{\text{n}^\circ \text{ of photons absorbed}}{\text{n}^\circ \text{ of emitted photons}}$), that is, the general quantum yield, it is necessary to calculate the quantum yield of the ligand (Q_{Ln}^L), also known as

external quantum yield and the sensitization efficiency (η_{sens}), through the formula $\eta_{sens} = Q_{Ln}^L / Q_{Ln}^{Ln}$ (BÜNZLI, 2015). However, to define the external quantum yield, more advanced techniques such as an integration sphere are needed (UTOCHNIKOVA et al., 2016) or using a reference with known quantum yield (BOSSHARD et al., 2016).

In addition to the quantum yield, the lifetimes τ_{obs} and τ_{rad} can also be used to calculate the amount of water molecules coordinated in the first coordination sphere of the Eu(III) ion, as proposed by Horrocks (SUPKOWSKI; HORROCKS, 1999, 2002), equation 15.

$$q = A \left(\frac{1}{\tau_{H_2O}} - \frac{1}{\tau_{D_2O}} - \alpha \right) \quad \text{Equation 15}$$

Where q is the amount of water molecules in the first coordination sphere of the complex; $A = 1.1$; $\tau_{H_2O} = \tau_{obs}$; $\tau_{D_2O} = \tau_{rad}$ for the ion Eu(III) and $\alpha = 0.31$.

The europium(III) ion has a unique property involving the transition ${}^5D_0 \rightarrow {}^7F_1$, as it is a magnetic dipole (MD) transition, the dipole strength is independent of the chemical environment and can be calculated and used as a reference for transitions caused by the excited state 5D_0 , being calculated as: $D_{MD} = 9.6 \times 10^{-42} \text{ esu}^2\text{cm}^2$ (ĆIRIĆ et al., 2019). Another property that can be calculated is the reduced matrix elements, $|\langle J | U^\lambda | J' \rangle|^2$, where the magnetic dipole transitions caused by the excited state 5D_0 are calculated as zero, with the exception of transitions 7F_J ($J = 2, 4$ and 6), that have the value of $U^2 = 0.0032$, $U^4 = 0.0023$ and $U^6 = 0.0002$ (ĆIRIĆ et al., 2019; ĐAČANIN et al., 2011), however, as the transition ${}^5D_0 \rightarrow {}^7F_6$ is not observed in the visible region, it is not considered. From this information it is possible to calculate the Judd-Ofelt

parameters for europium (III) ion emissions (BALA et al., 2018; DE SÁ et al., 2000; PARRA et al., 2002), according to equation 16.

$$\Omega_{\lambda} = \frac{D_{MD}v_1^3}{e^2v_{\lambda}^3| \langle J|U^{\lambda}|J' \rangle |^2} \times \frac{9n^3}{n(n^2+2)^2} \times \frac{I_{0-J}}{I_{0-1}} \quad \text{Equation 16}$$

Where e is the elementary charge of the electron (4.803×10^{-10} esu); v is the frequency at the barycenter of the transition ${}^5D_0 \rightarrow {}^7F_J$; I_{0-J} is the integrated area of transition ${}^5D_0 \rightarrow {}^7F_1$ and the expression $\frac{9n^3}{n(n^2+2)^2}$ is the local Lorentz field correction with n being the refractive index with a standardized value of $n = 1.55$ (PARRA et al., 2002). The Judd-Ofelt parameters include the contribution of electrical dipoles and the dynamic coupling mechanism, providing information about structural changes in the complex, allowing to compare the contributions of covalence between Ln-Ligand interactions. The parameter Ω_2 it is very sensitive to micro symmetry and the ligand's electric field, where the higher the value, the lower the local symmetry (BOSSHARD et al., 2016). While the parameter Ω_4 is related to the structural rigidity of the complexes, where higher values are related to greater sensitivity to the distance between the Eu(III) ion and the ligand (DE ARAÚJO et al., 2020; MATOS et al., 2018; PARRA et al., 2002).

Another factor that can be used to assess the symmetry of the complex is the ratio of the barycenter intensities of the transitions $I({}^5D_0 \rightarrow {}^7F_0) / I({}^5D_0 \rightarrow {}^7F_1)(R_0)$ e $I({}^5D_0 \rightarrow {}^7F_2) / I({}^5D_0 \rightarrow {}^7F_1)(R_2)$, serving as a parameter to assess the symmetry of the chemical environment and the degree of covalence in the Eu(III)-Ligand interactions (DE ARAÚJO et al., 2020; RYU et al., 2014), where the greater this ratio, the smaller the symmetry of the complex and the greater the covalent character. However, depending on the matrix where the complex is

immobilized or even on the organic molecule used as a ligand, the intensities of europium (III) emissions may be interfered with by the emission of the ligand, mainly due to the properties of organic ligands that present wide band emissions. To work around this problem, a mathematical correction to remove the emission of the ligand or matrix by modifying the baseline was proposed in this work, analyzing the position at the barycenter of the emission band (I_N) and relation to the intensity in the base linear pseudoline that intersects the peak of the transition band (I_P) to get the corrected intensity of the transition (I_C), as shown in figure 42.

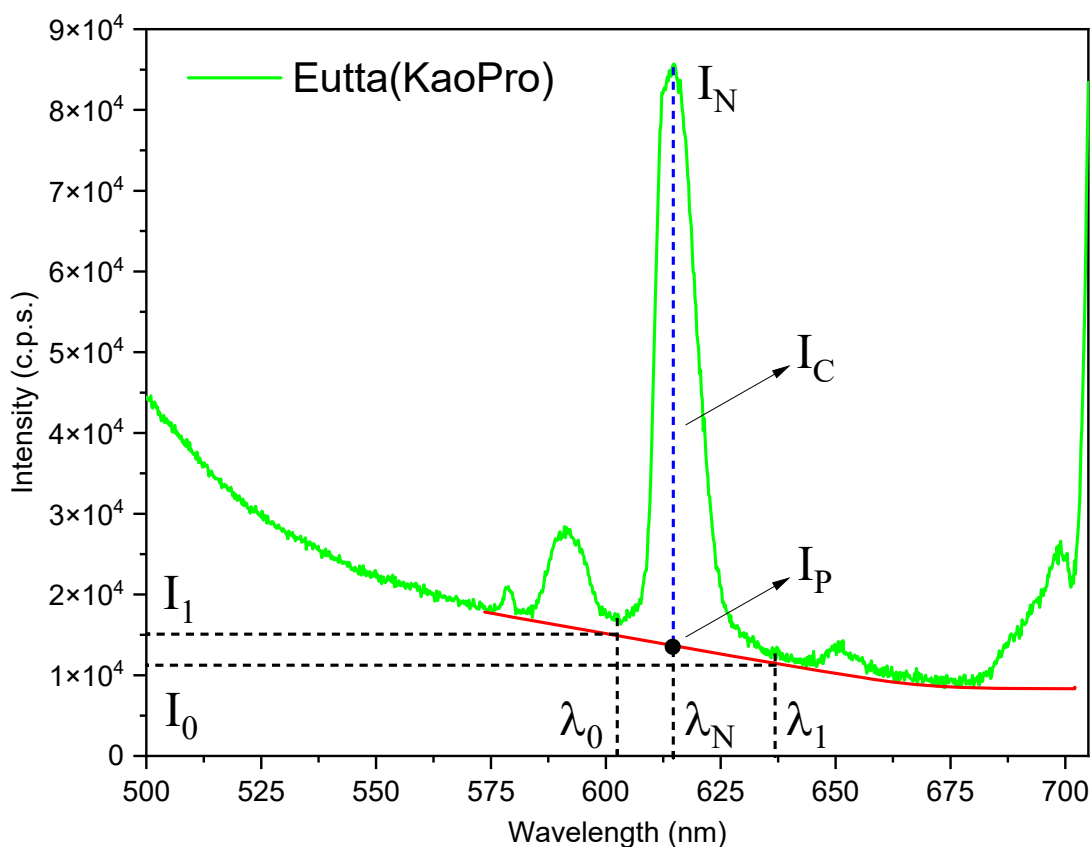


Figure 42 - Representation of the pseudo baseline emission of the Eutta(KaoPro) sample to find the calculated intensities ratio (R_{CJ}), being $J = 0$ and 2 .

It is possible to obtain the intensity with baseline correction through the equation $I_{CJ} = I_N - I_P$ (with $J = 0, 1$ and 2) and the intensity at the baseline that

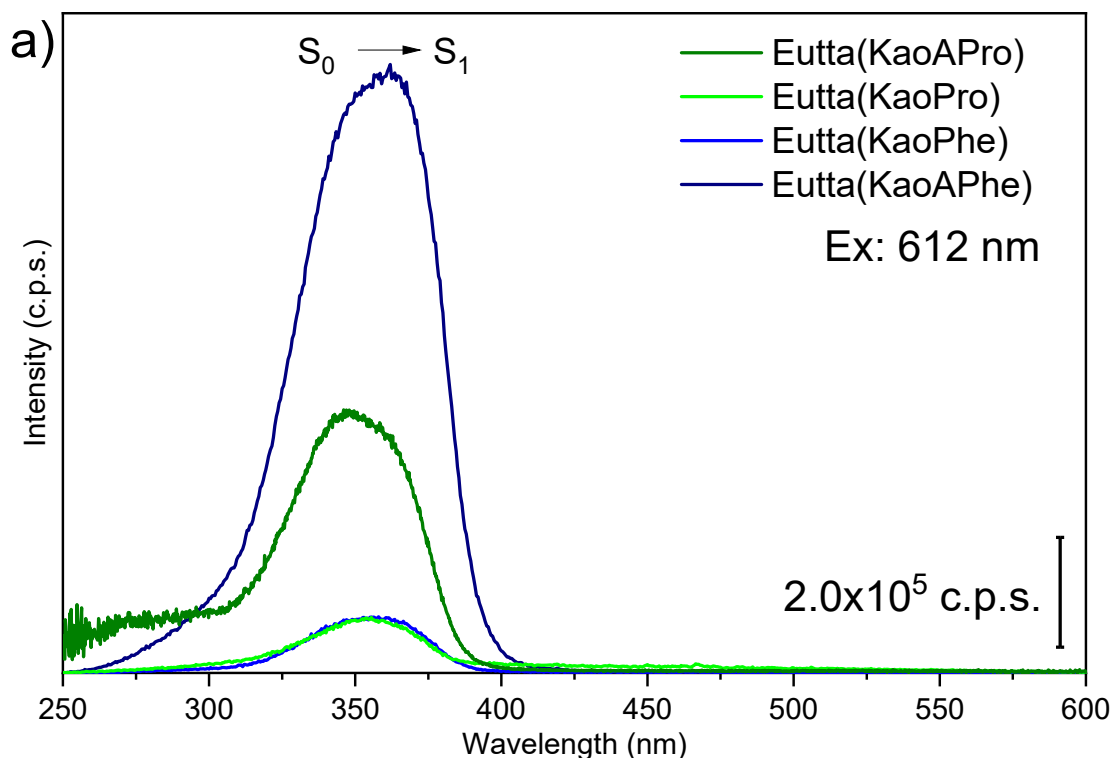
intersects the transition through the equation $I_p = \Delta I \times S_p + I_0$, where ΔI is the variation in the intensities of the transition ($\Delta I = I_1 - I_0$) and S_p is the wavelength that intersects the intensity of the transition, represented by equation 17.

$$S_p = \frac{\lambda_N - \lambda_0}{\lambda_1 - \lambda_0} \quad \text{Equation 17}$$

And finally it is possible to find the ratio between the intensities with the baseline correction (R_{CJ}), removing the matrix or ligand emission through the equation: $R_{CJ} = I_{CJ}/I_{C1}$. All spectroscopic information and parameters obtained from the resulting luminescent materials are discussed according to the matrix where they were immobilized.

4.2.1. Optical properties of materials immobilized in kaolinite

The excitation and emission spectra of luminescent materials with kaolinite are shown in Figure 43.



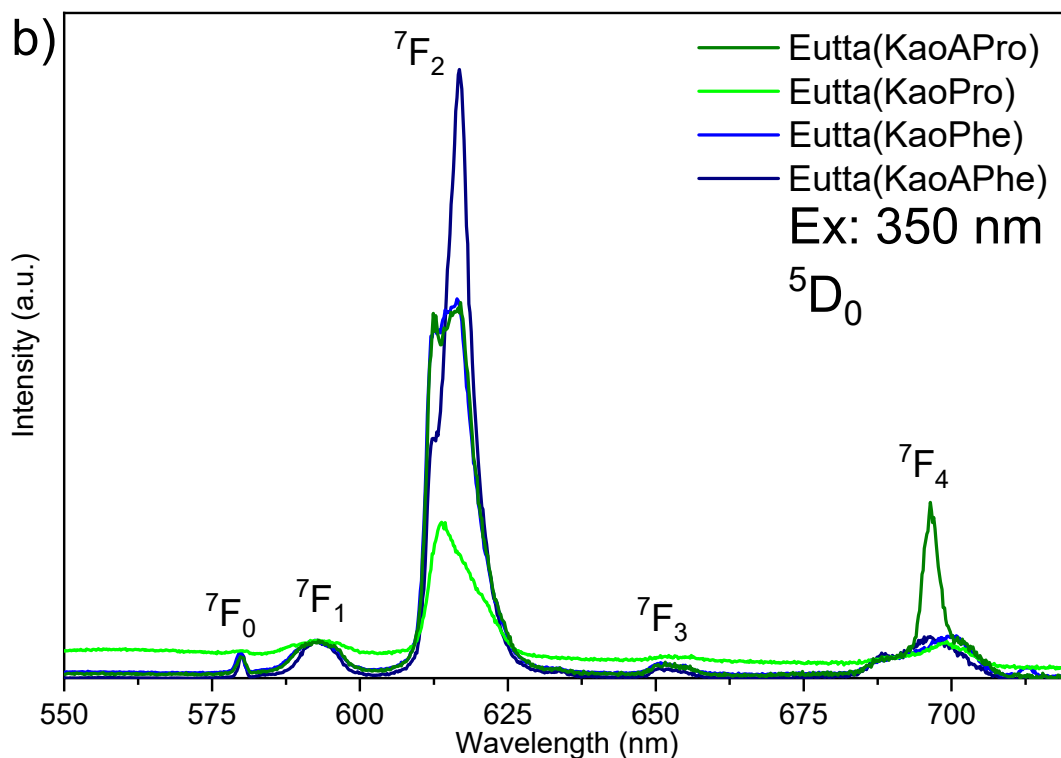


Figure 43 - Luminescence spectra of europium transitions for the kaolinite materials a) excitation and b) Emission with normalized intensity from the transition ${}^5D_0 \rightarrow {}^7F_1$.

The proline sample obtained by conventional synthesis (Eutta(KaoPro)) showed the lowest emission intensity of the europium ion and a great interference of emission from the matrix or ligands. The size of the proline molecule results in a smaller distance between the carboxylate and amine groups, making it difficult for the Eu(III) ion to complex, which explains the presence of 6 water molecules in the first coordination sphere of the complex. The increase in the radiative emission intensity of the ligand also means less energy transfer to the central ion and, consequently, lower sensitization efficiency of the complex, justifying the low internal quantum emission yield of the samples. The optical properties and parameters of luminescent materials are shown in table 15.

Table 15 - Optical properties of materials complexed with Eu(III) ion. Total radiation (A_{rad}) and non-radiation (A_{nrad}) emission rate; obtained lifetime ratio (τ_{obs}) and lifetime of radiative emission (τ_{rad}); number of water molecules in the first coordination sphere (q) and internal quantum yield of radiative emission (Q_{Ln}^{Ln}).

Sample	A_{rad} (s^{-1})	A_{nrad} (s^{-1})	τ_{obs} (ms)	τ_{rad} (ms)	q	Q_{Ln}^{Ln} (%)
Eutta(KaoPro)	3398	67539	0.16	3.30	6	5
Eutta(KaoAPro)	1362	4280	0.36	1.54	2	24
Eutta(KaoPhe)	4477	24939	0.38	2.51	2	15
Eutta(KaoAPhe)	6097	8239	0.49	1,15	1	42.5

The samples obtained by modifying the alkoxide APTES with amino acids by catalyzed amidation reaction showed better optical properties, with longer lifetimes, higher internal quantum yields and lower presence of water molecules in the first coordination sphere. This is due to the greater mobility offered by the molecule, facilitating complexation with the central ion. Another factor is related to the greater dispersion in the matrix of amino acids compared to the conventional route, which reduces the steric hindrance caused by the chemical environment.

Samples with the amino acid phenylalanine also showed better optical properties compared to proline, due to the aromatic ring present in phenylalanine, which increases its conjugation and consequently improves energy transfer and sensitization yield. The structure of phenylalanine also facilitates the chelation between the central ion and oxygen of the carboxylate and the amino acid amine, making it difficult for oscillators such as water molecules to be present in the complexes. Thus, the sample with phenylalanine obtained by the catalyzed route had the best internal quantum yield, as well as the longest lifetime and radiative emission rate among all samples with kaolinite.

In the samples obtained by synthesis of amidation reaction in a catalytic environment, no significant interferences from the radiative emission of the ligands or the matrix were observed, so it was not necessary to correct the ratios of the intensities of the transition ${}^5D_0 \rightarrow {}^7F_0$ and ${}^5D_0 \rightarrow {}^7F_2$. Information on symmetry and covalence parameters is shown in table 16.

Table 16 - Ratio between the areas of the bands corresponding to (R_0) and (R_2); ratio between areas corrected of the bands corresponding to (Rc_0) and (Rc_2) and Judd-Ofelt parameters Ω_2 and Ω_4 .

Sample	R_0	Rc_0	R_2	Rc_2	Ω_2 (10^{-20} cm^2)	Ω_4 (10^{-20} cm^2)
Eutta(KaoPro)	0.74	0.28	3.01	6.19	5.02	2.95
Eutta(KaoAPro)	0.57	-	9.90	-	15.62	2.91
Eutta(KaoPhe)	0.85	0.68	7.20	11.34	8.30	2.20
Eutta(KaoAPhe)	0.72	-	14.85	-	21.01	5.71

As seen in table 16, the samples obtained by modifying the alkoxide with the amino acids had lower symmetries in the complexes and consequently a greater sensitivity to disturbances of the Eu(III) ion with the ligands, while the samples obtained by the conventional route had less than half of the values in the Ω_2 parameter, with greater symmetry. In the Eutta(KaoPro) sample where there was a greater amount of complexed water, with 6 water molecules in the first coordination sphere, the complex tends to have greater symmetry in complexes with a higher degree of hydration. On the other hand, in the Eutta(KaoAPhe) sample, the complex presented smaller symmetries in relation to the others, due to the size of the ligand in relation to the others, as well as a greater degree of covalence between phenylalanine and the ion Eu(III) in relation to the amino acid proline.

4.2.2. Optical properties of materials immobilized in LDH

The excitation and emission spectra of luminescent materials with hydrotaalcite are shown in Figure 44.

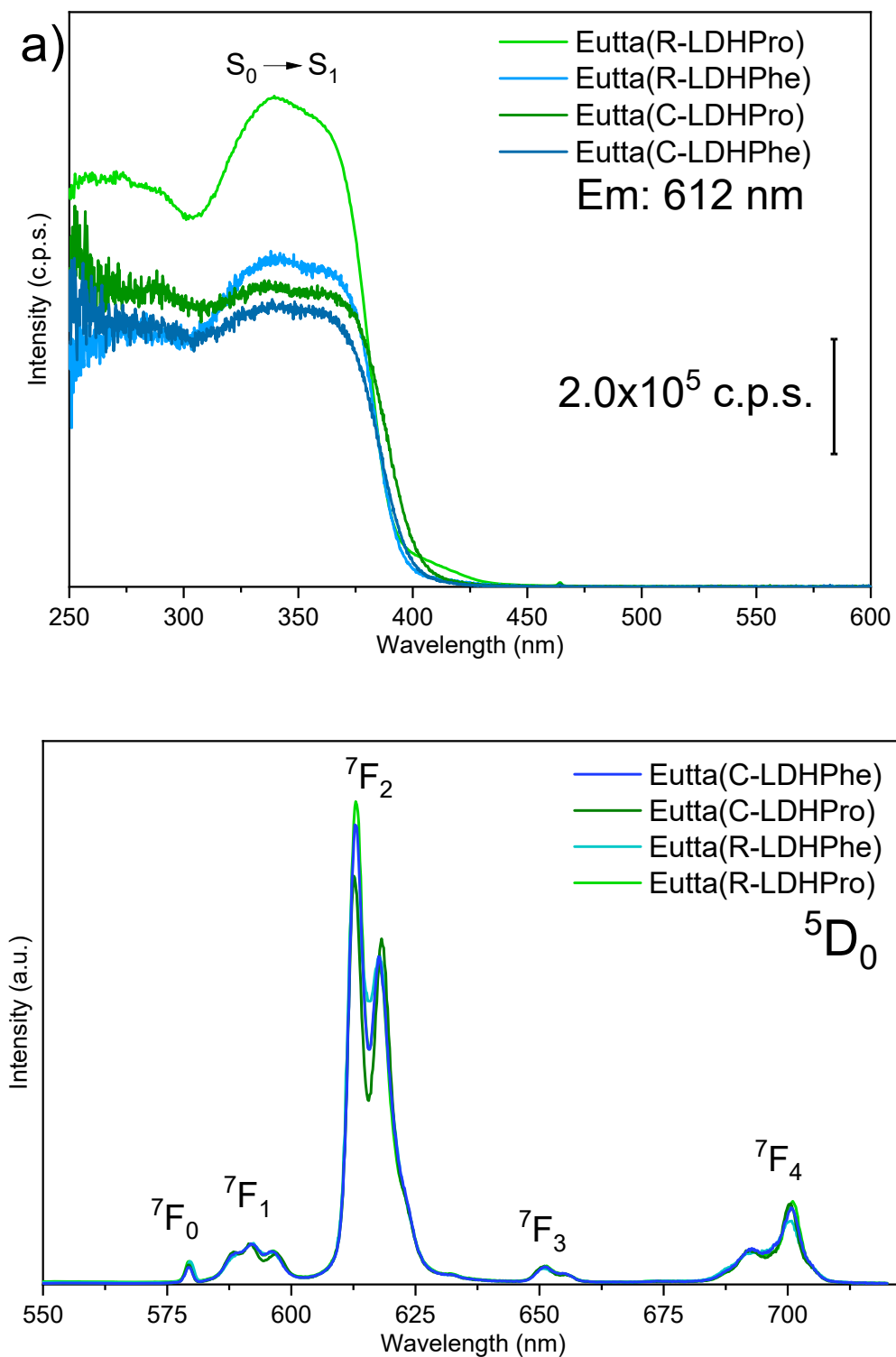


Figure 44 - Luminescence spectra of kaolinite materials a) excitation and b) Emission with normalized intensity from the transition ${}^5D_0 \rightarrow {}^7F_1$.

The transition ${}^5D_0 \rightarrow {}^7F_0$ is seen in all spectra with hydrotalcite. By the Judd-Ofelt theory the transition ${}^5D_0 \rightarrow {}^7F_0$ is prohibited by the selection rules, however, this emission band can occur by J-mixing effect caused by disturbances in the crystalline field (BINNEMANS, 2015). The observation of this transition in the spectrum indicates sites with symmetry C_{nv} , C_n or C_s . All samples had the same emission pattern, with 3 observed bands in the transition ${}^5D_0 \rightarrow {}^7F_1$, 2 bands in ${}^5D_0 \rightarrow {}^7F_2$, which can indicate the presence of several symmetry sites, however, the presence of two emission bands in the transitions ${}^5D_0 \rightarrow {}^7F_2$, ${}^5D_0 \rightarrow {}^7F_3$ and ${}^5D_0 \rightarrow {}^7F_4$ indicates the hexagonal C_6 symmetry as predominant in the chemical environment (TANNER, 2013). The symmetry parameters are shown in table 17.

Table 17 - Ratio between the areas of the bands corresponding to (R_0) and (R_2) and Judd-Ofelt parameters Ω_2 and Ω_4 .

Sample	R_0	R_2	Ω_2 (10^{-20} cm^2)	Ω_4 (10^{-20} cm^2)
Eutta(R-LDHPro)	0.56	11.99	13.05	5.23
Eutta(R-LDHPhe)	0.55	10.00	14.03	5.41
Eutta(C-LDHPro)	0.47	10.12	13.21	5.39
Eutta(C-LDHPhe)	0.41	11.40	13.66	5.51

Regardless of the amino acid and the intercalation route, the samples did not show major differences in symmetry properties. The Eu(III) emission spectra of the samples with hydrotalcites remained without interference from the matrix emission, and it was not necessary to correct the emission baseline. The complexes showed low symmetry, but with relatively high covalence between metal and ligand, being sensitive to the distance between metal-ligand.

The lifetimes of these materials showed an unusual characteristic for trivalent europium emissions, with a rise in low lifetimes before decay, showing a non-exponential or multi-exponential characteristic. This indicates that the complex has a high energy absorption rate, evidenced by the high lifetimes. The optical properties of the hydrotalcite complexes and the emission lifetimes are shown in table 18 and figure 45.

Table 18 - Optical properties of materials complexed with Eu(III) ion. Total radiation (A_{rad}) and non-radiation (A_{nrad}) emission rate; obtained lifetime ratio (τ_{obs}) and lifetime of radiative emission (τ_{rad}); number of water molecules in the first coordination sphere (q) and internal quantum yield of radiative emission (Q_{Ln}^{Ln}).

Sample	A_{rad} (s^{-1})	A_{nrad} (s^{-1})	τ_{obs} (ms)	τ_{rad} (ms)	q	Q_{Ln}^{Ln} (%)
Eutta(R-LDHPro)	6032	10590	0.52	1.65	1	31
Eutta(R-LDHPhe)	6164	9086	0.52	1.56	2	33
Eutta(C-LDHPro)	5721	13117	0.43	1.64	1	26
Eutta(C-LDHPhe)	6040	13610	0.50	1.59	1	31

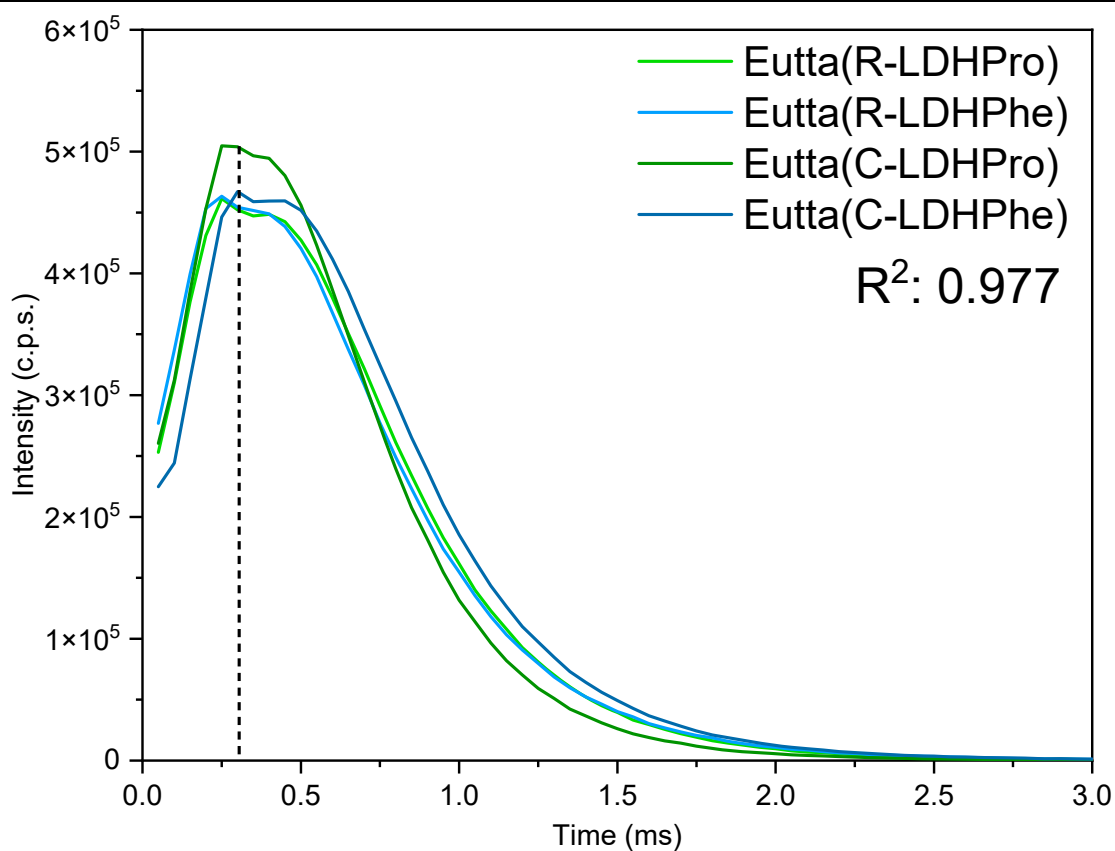


Figure 45 - Emission lifetimes of samples with hydrotalcite. With emission set at 612 nm and excitation set at 365 nm.

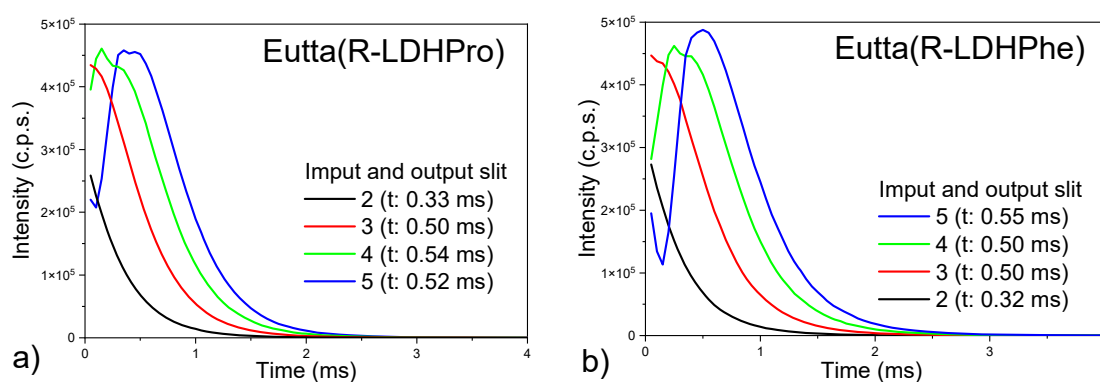
The rise in intensity at low lifetimes in photoluminescence is due to the reabsorption of photons emitted at different absorption sites independently. This effect is more commonly observed in semiconductors, when the disorder potential is greater than the binding energy of excitons, resulting in higher energy photons at low lifetimes (which are reabsorbed), while lower energy photons are emitted with long lifetimes (WANG et al., 2006). Photon reabsorption consequently increases the emission time of the process, and when the emission lifetime is greater than the excitation pulse width, there is a time lag between absorption and emission, resulting in a rise in the decay curve (SAKAI et al., 1989).

In this case, high energy photons are usually emitted with short lifetimes and only high energy photons are strongly reabsorbed in the system (DIAB et al., 2017), that is why the rise in intensity on the decay curve always occurs at low lifetimes. The interpretation of this type of decay curve (with low lifetime rise) depends on the luminophore and the chemical environment. In organic luminophores such as rhodamine B, photon reabsorption occurs at the same site and is concentration dependent, that is, a rhodamine B molecule emits a photon that is reabsorbed by another rhodamine B molecule and this reabsorption decreases proportionally with the concentration dye, where diluted systems have low reabsorption rates. In this case, the multi-exponential analysis of the non-exponential curve does not provide useful information, it is necessary to deconvolute the curve using the lifetime of a diluted solution of the material as a standard (SAKAI et al., 1989).

In materials doped with lanthanide ions such as Eu^{3+} and Tb^{3+} , there is a long pathway of energy in the transfer process to the ion Eu^{3+} , like for example,

in the compound $K_5GdLi_2F_{10}$ doped with Tb and Eu, where Solarz (2021) observed a pathway of excitation energy [$^5D_4 (Tb^{3+}) \rightarrow ^5D_1 (Eu^{3+}) \rightarrow ^5D_0 (Eu^{3+})$] which resulted in an increase in the intensity of decays, and therefore, photoluminescence was analyzed using an equation that involves the lifetime of the donor and acceptor (SOLARZ, 2021).

In the case of the materials used in this work with LDH, there is a reabsorption of high energy photons by the matrix, which in turn transfers this energy to the amino acids, due to the proximity of the hydroxalcite band gap (≈ 4.43 eV) (NASEEM et al., 2020) with the band gap of amino acids proline (≈ 4.28 eV) (CAETANO et al., 2018) and phenylalanine (≈ 4.83 eV) (BORAH; DEVI, 2017) resulting in this rise in low lifetimes. On the other hand, the radiative emission lifetime is not affected by energy transfer between molecules of the same type (SAKAI et al., 1989). To prove this behavior, an analysis of the lifetime decay was performed, adjusting the photon input and output slit in the fluorimeter, ranging from 2 nm to 5 nm, as shown in figure 46.



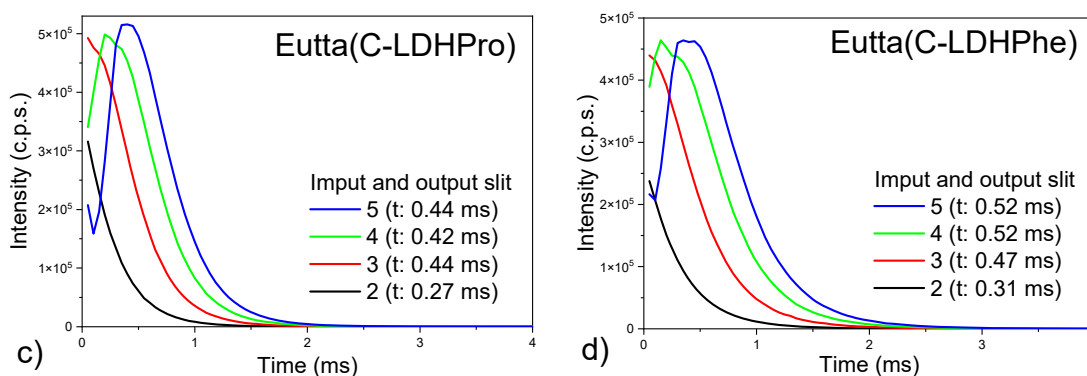


Figure 46 - Sample emission lifetime decay curves a) Eutta(R-LDHPro); b) Eutta(R-LDHPhe); c) Eutta(C-LDHPro) and d) Eutta(C-LDHPhe), varying the photon input and output slits from 2 to 5 nm.

By changing the photon input and output slit in the fluorimeter, the amount of energy that reaches the sample and the amount of energy that reaches the detector is also changed. Thus, when smaller amounts of photons affect the sample, smaller amounts of high energy photons are reabsorbed by the system shifting the decay curve and the rise in intensity, however, depending on how much the input and output slit is suppressed, even photons low energy start to be prevented from being detected, which happens in the 2nm slits. On the other hand, regardless of how many photons are reabsorbed, the mono-exponential decay curve has very close lifetime values, indicating that regardless of the photons reabsorbed by the system, the radiative emission lifetime of the complex has no significant changes.

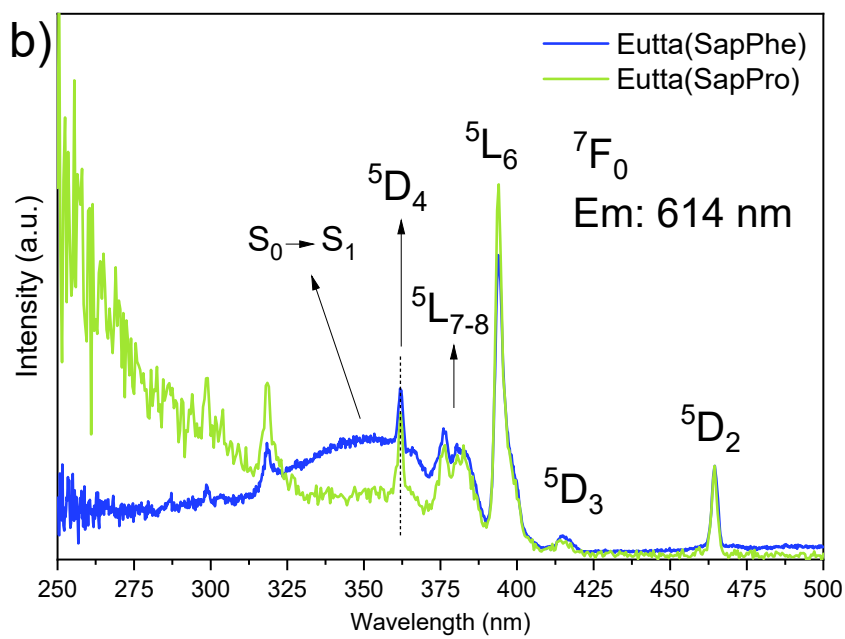
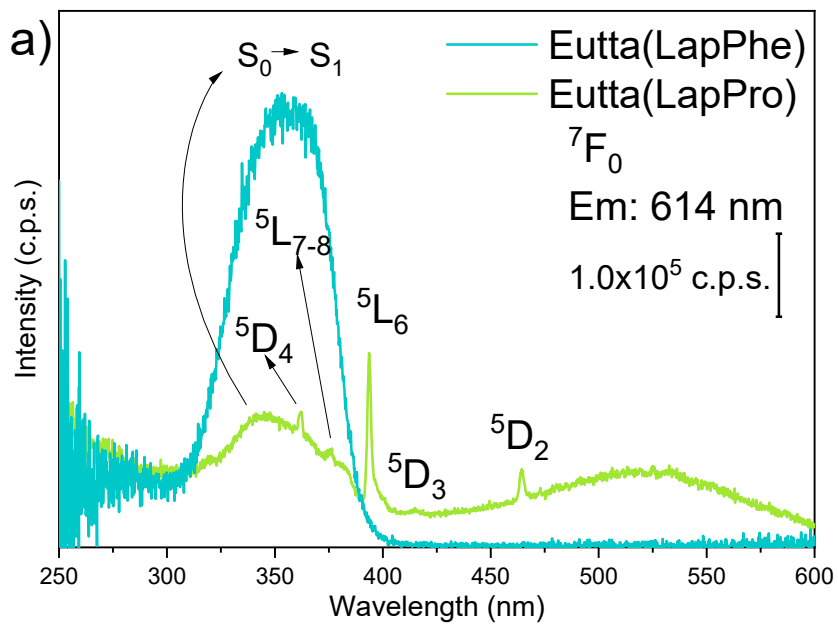
In all samples with hydrotalcite, the emission lifetime of the complex was above the average for complexes immobilized in clay minerals with lifetimes above 0.40 ms. This behavior is related to the matrix providing the complex with structural rigidity and stabilizing the charge transfer energy close to the triplet energy level of the complex, resulting in long emission lifetimes (XIE et al., 2021). This type of interaction between the matrix and the complex is a result of the contribution of hydrotalcite in the energy transfer process for the Eu^{3+} ion.

This behavior is not presented either by the isolated complex, or with the $\text{Eu}(\text{tta})_3 \cdot n\text{H}_2\text{O}$ complex, without the presence of the amino acid (with lifetimes close to 0.21 ms) (LIN et al., 2016) and is above mean for Eu^{3+} complexes immobilized in LDH (between 20 to 40 ms) (CHU et al., 2012; GAO et al., 2014; ZHANG et al., 2017).

The samples with the amino acid phenylalanine showed quantum yields with approximately 30%, due to the aromatic radical of the amino acid increasing the conjugation of the complex and consequently the radiative emission. All samples showed high lifetimes and low amounts of water molecules in the first coordination sphere, which shows the contribution of the secondary ligand in the energy transfer and removal of water molecules from the complex.

4.2.3. Optical properties of materials immobilized on LAPONITE® and saponite

The excitation and emission spectra of the samples with LAPONITE® and saponite are shown in figure 47.



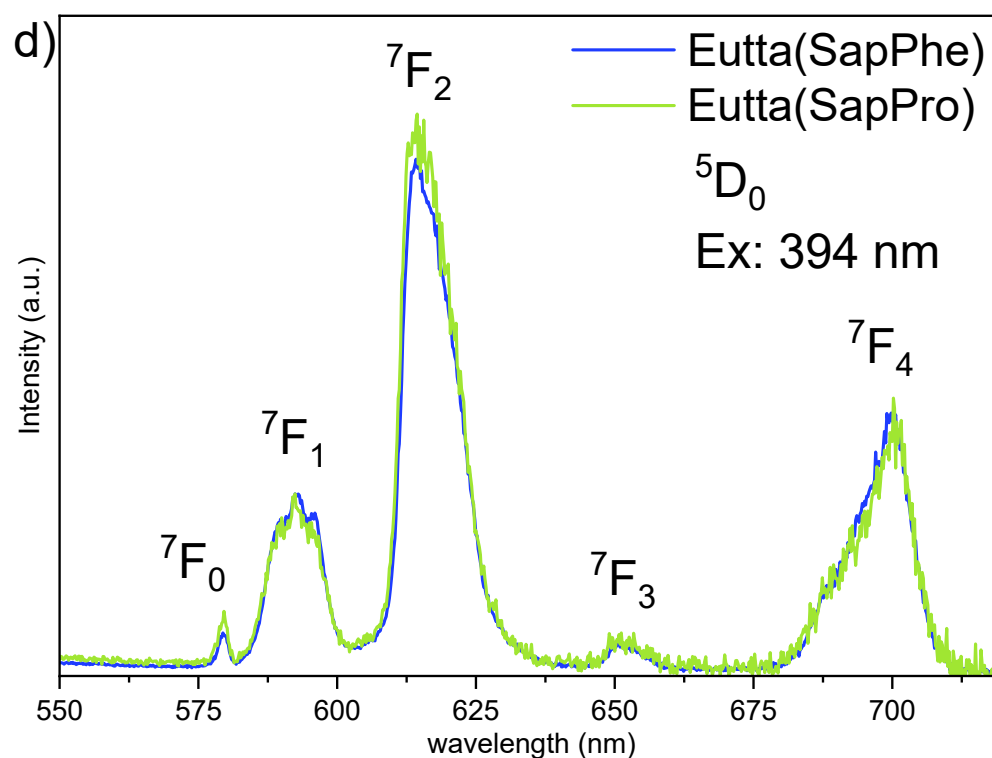
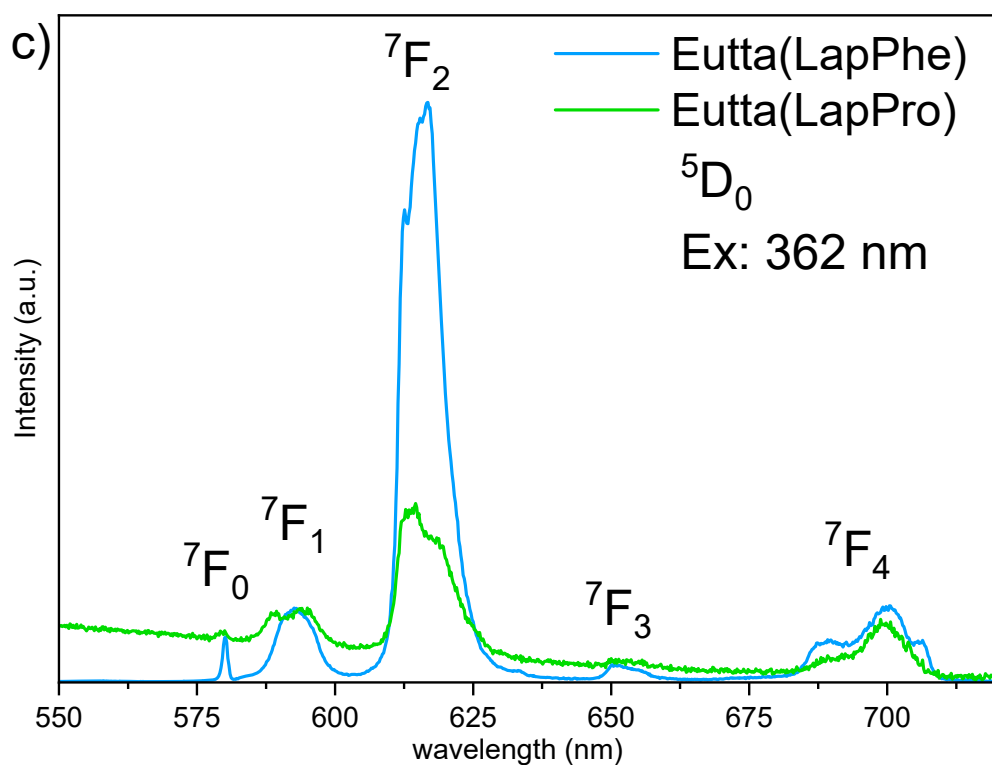


Figure 47 - Luminescence spectra of excitation (a and b) and emission (c and d) LAPONITE® and saponite materials. The excitation intensities of samples with saponite were normalized by the ${}^5D_2 \leftarrow {}^7F_0$ transition, and in the emission, all analyzed samples had the intensity normalized by the ${}^5D_0 \rightarrow {}^7F_1$ transition.

In the Eutta(SapPro) sample, the charge transfer bands were not evidently observed, where the highest intensity transition was observed at 394 nm relative to the excited state transition ${}^5L_6 \leftarrow {}^7F_0$ of the Eu(III) ion, indicating low efficiency of sensitization of the complex, affecting the quantum yield consequently. In the Eutta(LapPro) sample, the broadband transition relative to charge transfer appears close to 350 nm, however with less intensity than the transition ${}^5L_6 \leftarrow {}^7F_2$, also showing the low efficiency of sensitization of the complex. This low energy transfer efficiency from the ligand to the Eu^{3+} ion may be related to the large amount of water molecules in the first coordination sphere and/or the low complexation of the secondary ligand tta, reducing the molar absorptivity of the complex. The optical properties of the complexes are shown in table 19.

Table 19 - Optical properties of materials complexed with Eu(III) ion. Total radiation (A_{rad}) and non-radiation (A_{nrad}) emission rate; obtained lifetime ratio (τ_{obs}) and lifetime of radiative emission (τ_{rad}); number of water molecules in the first coordination sphere (q) and internal quantum yield of radiative emission (Q_{Ln}^{Ln}).

Sample	A_{rad} (s^{-1})	A_{nrad} (s^{-1})	τ_{obs} (ms)	τ_{rad} (ms)	q	Q_{Ln}^{Ln} (%)
Eutta(LapPro)	2645	23506	0.42	4.18	2	10
Eutta(LapPhe)	4880	4483	0.85	1.62	0	52
Eutta(SapPro)	3045	62258	0.14	3.10	7	4.7
Eutta(SapPhe)	3269	55859	0.15	2.81	6	5.5

As shown in table 19, samples with saponite had lower quantum yields of Eu (III) ion emission and higher amounts of water molecules in the first coordination sphere. The high non-radiative emission rate (A_{nrad}) explains this low yield being this decay by molecular vibrations caused by oscillators such as H_2O and various organic groups (MARCHESI et al., 2021b; SUPKOWSKI; HORROCKS, 2002). The structural rigidity of the complex also contributes to

the radiative emission rate, where the complex with greater rigidity tends to decrease molecular vibrations increasing the radiative emission efficiency. According to the results obtained by the thermal analysis, the samples with saponite had lower concentrations of intercalated amino acids, allowing the greater presence of intercalated water molecules, together with the ease of expansion of the clay mineral basal space, favoring the leaching of the complex in the process of adding the ligand secondary tta. As a result, the complexes that remained intercalated in the saponite had low complexation of the tta ligand and large amounts of water molecules, increasing energy dispersion by molecular vibrations, decreasing the radiative emission efficiency.

The samples with LAPONITE® presented the charge transfer bands, however in the Eutta(LapPro) sample it is still possible to observe that the transition of greater intensity is the ${}^5L_6 \leftarrow {}^7F_0$ of the Eu(III) ion, as in saponite, resulting in low sensitization efficiency and consequently internal quantum yields. However, this sample presented only 2 molecules of water in the first coordination sphere, indicating that the low yield is in the capacity of energy transfer from the ligand to the central ion. This large non-radiative emission (A_{nrad}) may be related to the amount of water in the second coordination sphere, dissipating energy through vibration between H₂O molecules and in the low conjugation of the complex in general.

On the other hand, the Eutta(LapPhe) sample showed the best optical properties among the materials, with longer lifetimes (0.85 ms), higher radiative emission rate, higher internal quantum yield with 50% and no water molecule in the first sphere of coordination. The lifetime of this sample showed a different behavior from the others with three stages of emission, the first being a slight

decay up to 0.2 ms, a second stage of increased intensity that extends to 0.55 ms and only after this time the decay starts, as shown in figure 48.

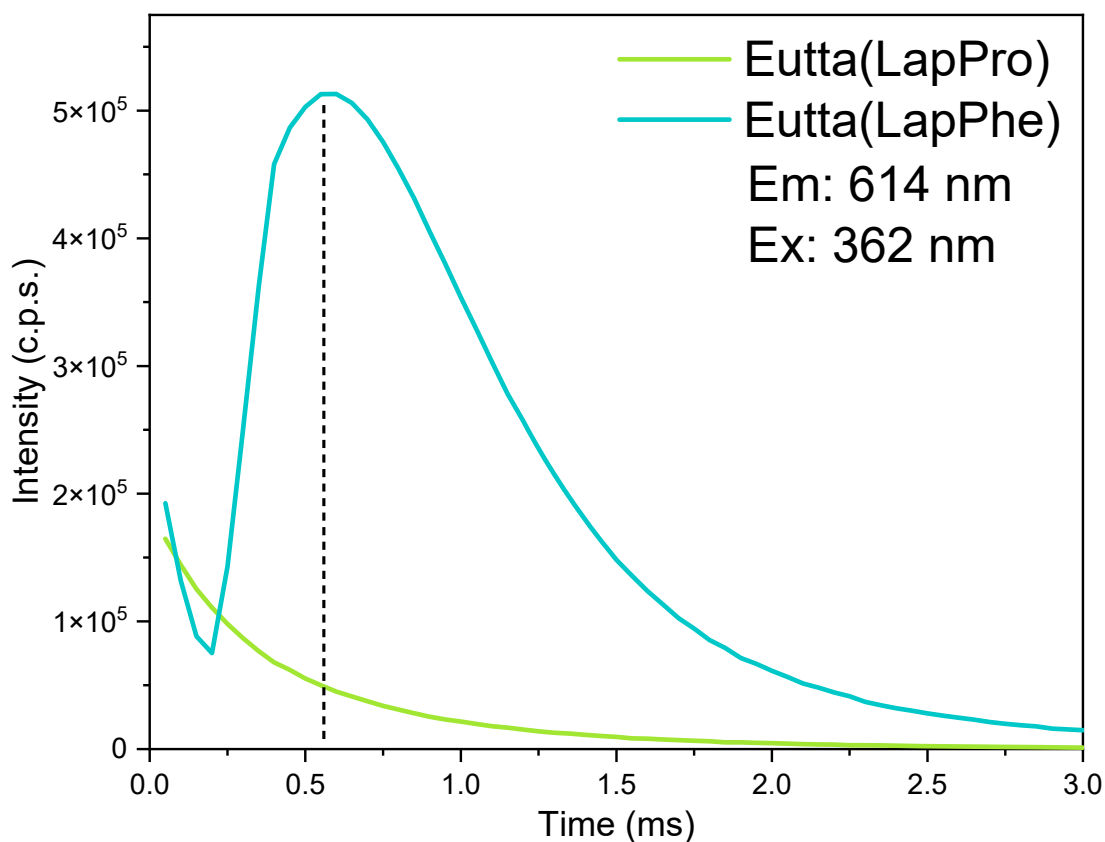


Figure 48 - Radioactive decay of samples with LAPONITE® with emission fixed at 614 nm and excitation fixed at 362 nm.

As in the samples with hydrotalcite, this high lifetime of the Eutta (LapPhe) sample is related to the contribution of LAPONITE® in the energy transfer process, providing greater structural rigidity to the complex and stabilizing the charge transfer energy for close to the triplet excited state, favoring the phosphorescent emission of the complex (XIE et al., 2021). This contribution of LAPONITE® is attributed to the proximity between the band gap energy of LAPONITE® in relation to the band gap of phenylalanine (≈ 4.83 eV) (ASLAN, 2020; BORAH; DEVI, 2017), facilitating energy transfer between

LAPONITE® and amino acid transitions, favoring complex sensitization efficiency and triplet state stability, resulting in long radiative emission lifetimes.

Isolated complexes of Eu^{3+} with phenylalanine present approximately 0.13 ms (HELLER et al., 2010), as isolated complexes of tta ($\text{Eu}(\text{tta})_3 \cdot n\text{H}_2\text{O}$) have lifetimes of approximately 0.20 ms (LIN et al., 2016). Furthermore, Eu^{3+} complexes immobilized in LAPONITE® have lifetimes ranging from 0.10 to 0.40 ms (WANG et al., 2019; YANG; WANG; LI, 2015). Long lifetimes (> 0.50 ms) in LAPONITE® are generally only observed in heat treatment above 100 °C (TRONTO et al., 2009). Therefore, this long radiative emission lifetime of the complex with phenylalanine immobilized in LAPONITE® is a novel property specific to the complex of Eu^{3+} with the amino acid and the ligand tta intercalated in LAPONITE®.

Similarly to the samples with hydrotalcite, the Eutta(LapPhe) sample showed a rise in low lifetimes, resulting from the reabsorption of high energy photons by the matrix, which in turn transfers this energy back to the complex by the amino acid phenylalanine. However, the radiative emission lifetime is not affected by energy transfer between the same system (SAKAI et al., 1989). To confirm this statement, the radiative decay was performed by changing the fluorimeter's input and output slit between 2 and 5 nm, as shown in figure 49. It was observed that even changing the amount of high energy photons reabsorbed in the system, decreasing the input and output slits, the lifetimes remain at approximately 0.85 ms, with the exception of the 2 nm slit, where the lower energy photons that were not reabsorbed began to be prevented from reaching the detector, changing the emission lifetime.

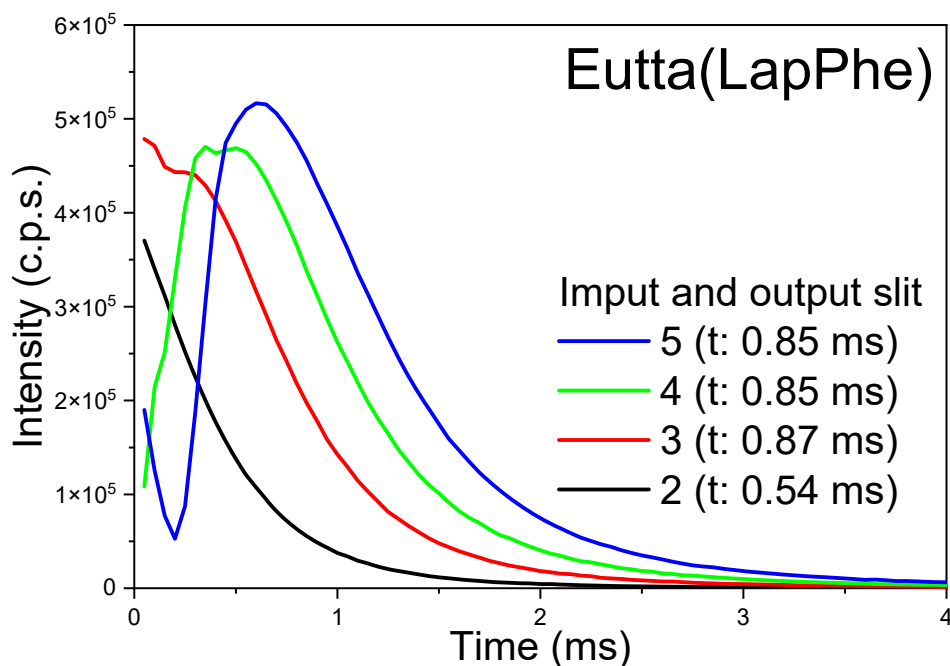


Figure 49 - Sample emission lifetime decay curves of Eutta(LapPhe), varying the photon input and output slits from 2 to 5 nm.

Analyzing the emission ${}^5D_0 \rightarrow {}^7F_2$ it is possible to obtain symmetry information when compared to the magnetic dipole (MD) transition ${}^5D_0 \rightarrow {}^7F_1$ and through the parameter Ω_2 where it is possible to obtain information about the hypersensitive behavior of the transition ${}^5D_0 \rightarrow {}^7F_2$ which indicates the polarizability of the material and the strength of the metal-binder interaction, that is, whether the complex is in a chemical environment of high polarizability (PARRA et al., 2002). Judd-Ofelt parameters and the ratio of intensities of transition ${}^5D_0 \rightarrow {}^7F_2 / {}^5D_0 \rightarrow {}^7F_1$ (R_2) and ${}^5D_0 \rightarrow {}^7F_0 / {}^5D_0 \rightarrow {}^7F_1$ (R_0) are in table 20.

Table 20 - Ratio between the areas of the bands corresponding to (R_0) and (R_2); ratio between areas corrected of the bands corresponding to (Rc_0) and (Rc_2) and Judd-Ofelt parameters Ω_2 and Ω_4 .

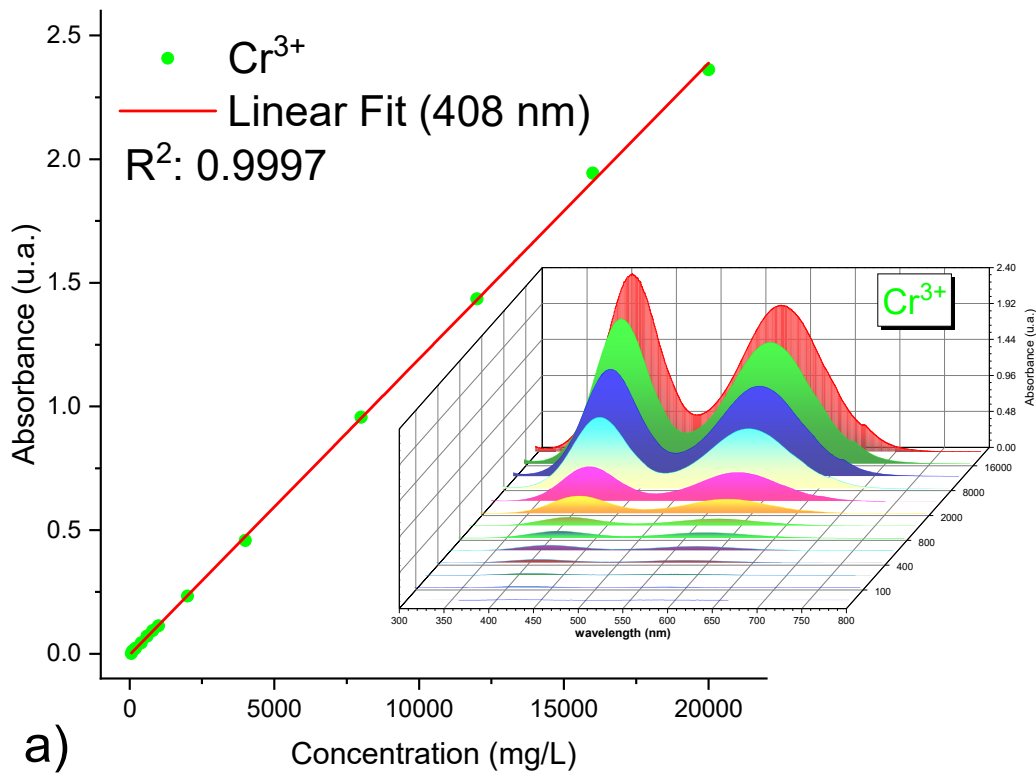
Sample	R_0	Rc_0	R_2	Rc_2	Ω_2 (10^{-20} cm^2)	Ω_4 (10^{-20} cm^2)
Eutta(LapPro)	0.69	0.28	2.41	3.87	3.52	2.45
Eutta(LapPhe)	0.61	-	7.82	-	13.55	5.72
Eutta(SapPro)	0.35	-	3.08	-	6.42	6.57
Eutta(SapPhe)	0.24	-	2.85	-	4.87	3.81

The large amount of water molecules in the first coordination sphere results in less disturbance of the crystalline field and greater symmetries, as seen in table 20. Saponite materials had low ratio values between areas, with high local symmetries and a lower degree of covalence in relation to materials with LAPONITE®, a factor also evidenced by parameters Ω_2 and Ω_4 . Relatively high values of Ω_4 indicate complexes with high sensitivity between the distance of the Eu(III) ion and the ligand. The intensity of emissions of transition $^5D_0 \rightarrow ^7F_4$ are relatively tall and wide in relation to the transition $^5D_0 \rightarrow ^7F_2$ in samples with saponite, which is an unusual characteristic for these complexes, a factor evidenced by the low ratio between the parameters Ω_2 and Ω_4 . Studies indicate that this characteristic is related to a local symmetry of a slightly distorted polyhedron of D_{4d} , with square antiprism coordination geometry, where this distortion is related to a chemical environment of high polarizability (CHAN et al., 2015; SÁ FERREIRA et al., 2006).

4.3. Applications of luminescent materials

4.3.1. Adsorption Tests

After studying and determining the luminescent properties of materials intercalated in clay minerals, the samples were subjected to adsorption treatment of Cr^{3+} , caffeine and estrogen contaminants to evaluate the adsorption efficiency of these contaminants and their impact on the optical properties of the materials obtained. Through UV/Vis spectroscopy, a calibration curve is initially made to determine the concentration of the contaminant in the sample. In all samples, curves with high linear correlation values (R^2) were obtained, as shown in figure 50.



a)

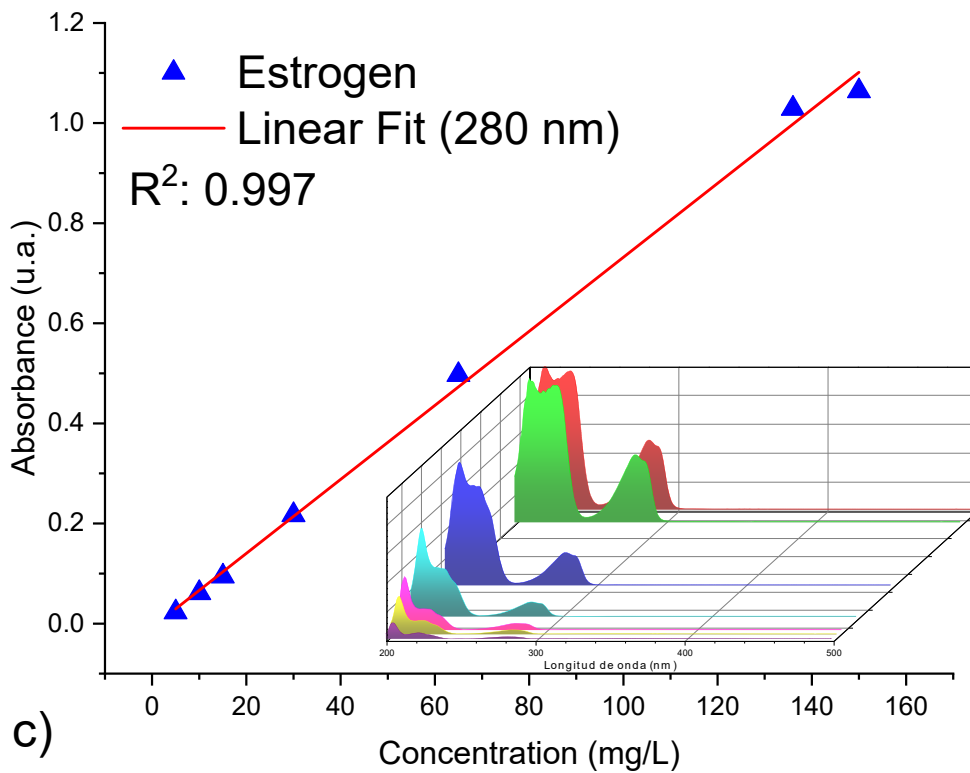
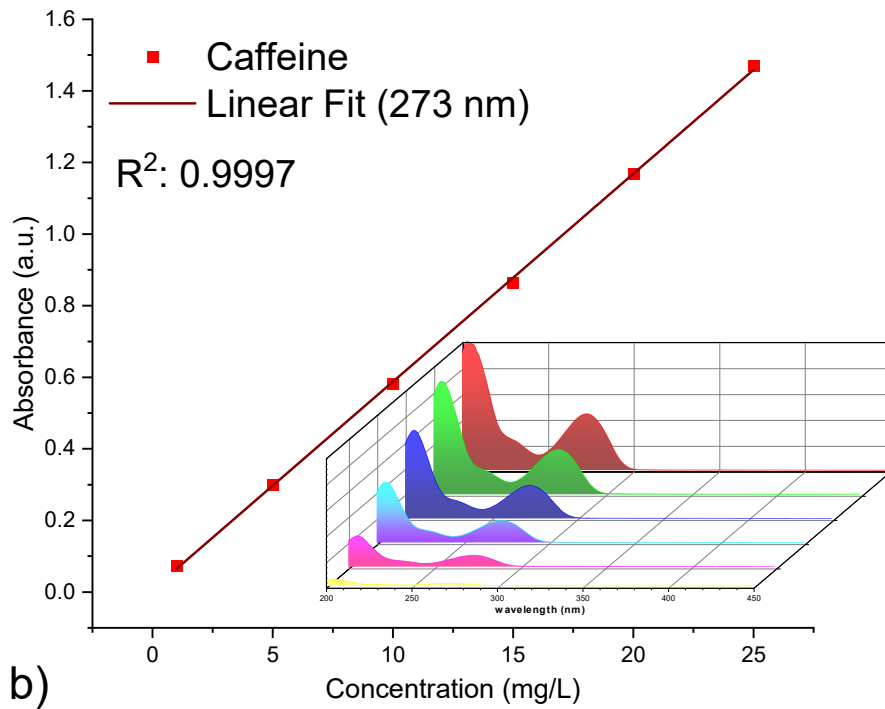


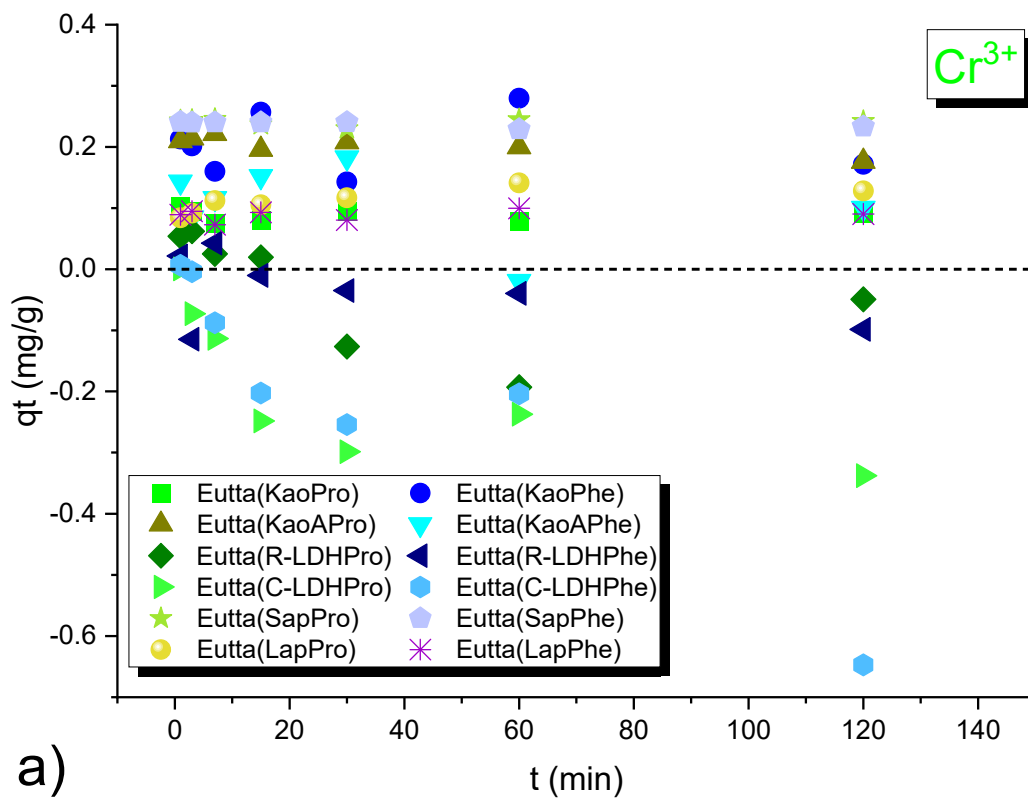
Figure 50 - Calibration curves for a) Cr^{3+} ; b) caffeine and c) estrogen.

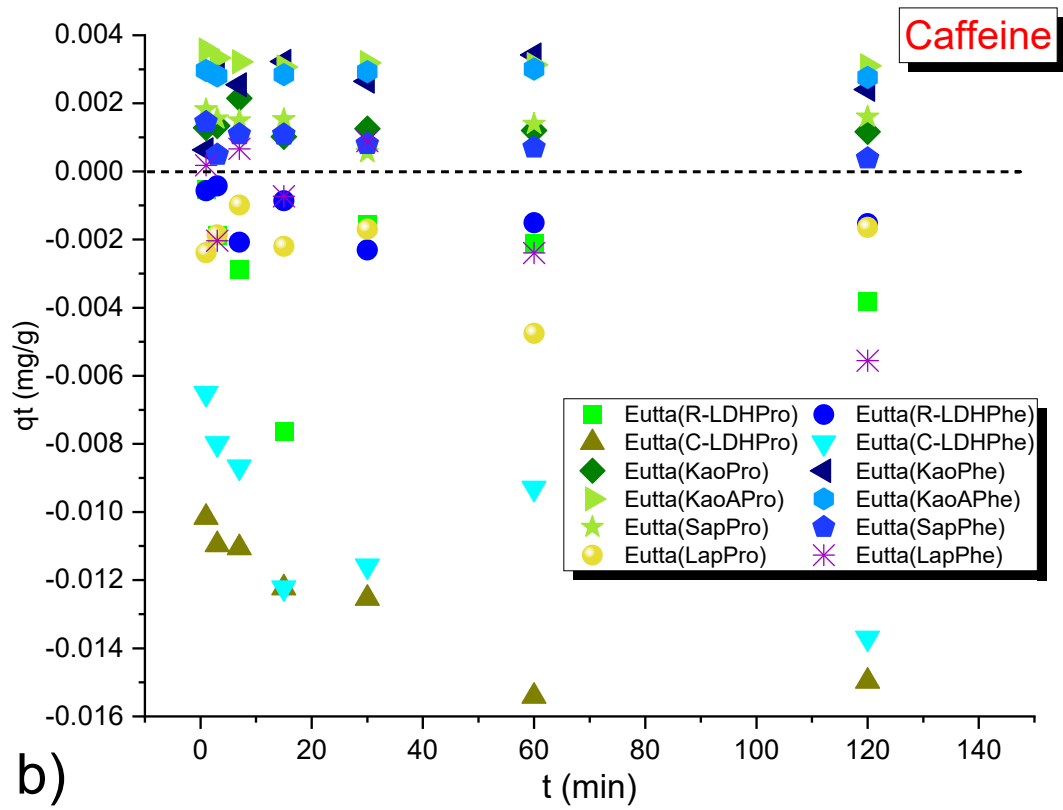
After obtaining the calibration curve, it is possible to analyze the adsorption kinetics to find the adsorption capacity of the materials for each

contaminant. To determine the adsorption capacity, it is necessary to evaluate the initial and final concentration of the contaminant in relation to the mass of the adsorbent through equation 18 (ALMEIDA NETO; VIEIRA; SILVA, 2012; TRAN; LIN; CHAO, 2018):

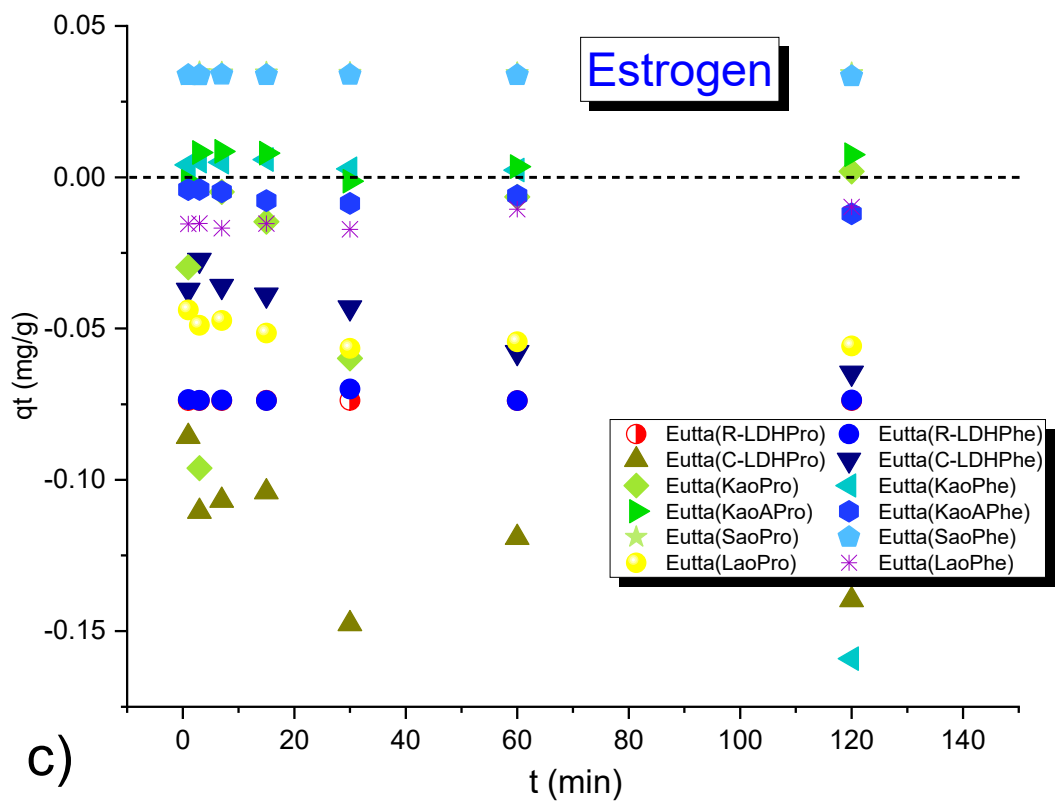
$$q_t = \frac{(C_0 - C_t) \times v}{m} \quad \text{Equation 18}$$

Where q_t is the adsorption capacity on time t ; C_0 is the initial concentration (mg/L); C_t is the concentration on time t (mg/L); v is the volume used that has been standardized at 0.005 L and m as the mass of the adsorbent (mg). The adsorption kinetics of the materials for the contaminants used are shown in Figure 51.





b)



c)

Figure 51 - Adsorption kinetics where qt is the adsorption capacity of the material at time t , for materials with adsorption of a) Cr^{3+} , b) Caffeine and c) Estrogen.

Values of q_t below zero are related to material leaching, indicating that the material is not applicable for adsorption. Among the contaminants, the Cr^{3+} ion showed the best applicability for sensing, with greater affinity with the materials without leaching, except for samples with hydrotalcite, which showed leaching in all contaminants.

The organophilicity of the Eu^{3+} complex results in a greater affinity with organic molecules in relation to the matrix, facilitating the leaching of the complex during interaction with the contaminant. The greater the covalence between the matrix and the complex, the lesser the leaching. Due to this factor, the materials immobilized in kaolinite were the ones with the greatest applicability as a luminescent sensor due to the interaction strength (covalent bond) between the complex and the matrix. On the other hand, LDH samples cannot be applied for sensing due to the low interaction between the complex and the matrix during adsorption kinetics. Only the Eutta(R-LDHPro) sample among the materials with LDH showed low leaching in Cr^{3+} and was therefore applied. Thus, the samples where it was possible to evaluate the adsorption capacity as well as analyze their isotherms are shown in table 21.

Table 21 - Adsorption capacity (qt) in the longest time (t) for Cr^{3+} , caffeine and estrogen contaminants.

Samples	Cr^{3+}		Caffeine		Estrogen	
	qt (mg/g)	t (min)	qt (mg/g)	t (min)	qt (mg/g)	t (min)
Eutta(KaoPro)	0.104	1	0.002	7	-	-
Eutta(KaoPhe)	0.280	60	0.003	60	0.006	15
Eutta(KaoAPro)	0.222	7	0.004	1	0.008	7
Eutta(KaoAPhe)	0.182	30	0.003	60	-	-
Eutta(R-LDHPPro)	0.062	3	-	-	-	-
Eutta(R-LDHPhe)	-	-	-	-	-	-
Eutta(C-LDHPPro)	-	-	-	-	-	-
Eutta(C-LDHPhe)	-	-	-	-	-	-
Eutta(SapPro)	0.245	3	0.002	1	0.346	3
Eutta(SapPhe)	0.241	1	0.001	1	0.339	7
Eutta(LapPro)	0.100	60	-	-	-	-
Eutta(LapPhe)	0.141	60	-	-	-	-

Cr^{3+} was the contaminant where it was possible to obtain the highest adsorption capacities, obtaining a high adsorption already in the initial times in all samples observed, with the Eutta(KaoPhe) sample having the highest adsorption capacity with 0.280 mg/g of Cr^{3+} adsorbed on 60 min. For caffeine, only half of the samples showed adsorption capacity without leaching of the material, with the Eutta(KaoAPro) sample having the highest capacity with 0.004 mg/g in 1 minute. It was possible to identify the estrogen adsorption capacity in only 4 samples, two in kaolinite samples and in the two saponite samples with higher adsorption capacity in saponite samples, with the

Eutta(SapPro) sample having the highest capacity with 0.346 mg/g in 3 minutes.

After obtaining the adsorption capacity of each applicable material, kinetic adsorption models were proposed to understand the kinetic behavior of the samples obtained for adsorption of contaminants. Lagergren's pseudo-first order kinetic models were used (LAGERGREN, 1907)(Equation 19), and pseudo-second order (HO; OFOMAJA, 2006) using the linear equation of Ho and McKay (Equation 20), as shown in equations 19 and 20.

$$\frac{1}{q_t} = \frac{k_1}{q_1 \times t} + \frac{1}{q_1} \quad \text{Equation 19}$$

Where k_1 is the first order adsorbate/adsorbent interaction constant (L/mg) and q_1 is the pseudo-first order adsorption capacity. These parameters can be obtained through a linear graph of $1/q_t$ over $1/t$.

$$\frac{t}{q_t} = \frac{1}{(k_2 \times q_2^2)} + \frac{t}{q_2} \quad \text{Equation 20}$$

Where k_2 is the second order adsorbate/adsorbent interaction constant (L/mg) and q_2 is the pseudo-second order adsorption capacity. These parameters can be obtained from a linear graph of t/q_t over t . The pseudo-first order model is described for materials where adsorption occurs by physisorption, that is, by weak interactions such as Van der Waals forces or hydrogen bonds, while the pseudo-second order model is applied to materials where adsorption occurs by chemisorption, that is, through stronger interactions such as covalent bonds or where adsorption occurs in more than one site. The error is calculated through the difference between the experimental and the

calculated qt ($E = \frac{q_{t_{exp}} - q_{t_{cal}}}{q_{t_{exp}}} \times 100$). The adsorption kinetic properties of the materials are shown in table 22-24.

Table 22 - Properties obtained from pseudo first order and pseudo second order kinetic models for Cr³⁺ adsorbents.

Sample	q _t (exp)	pseudo first order				pseudo second order			
		q ₁ (mg/g)	k ₁ (L/mg)	E (%)	R ²	q ₂ (mg/g)	k ₂ (L/mg)	E (%)	R ²
Eutta(KaoPro)	0.104	0.083	-0.196	19.78	0.241	0.089	10.377	13.76	0.992
Eutta(KaoPhe)	0.280	0.094	-0.107	32.54	-0.168	0.180	-13.312	35.62	0.943
Eutta(KaoAPro)	0.222	0.199	-0.078	10.21	-0.039	0.177	-2.855	20.00	0.995
Eutta(KaoAPhe)	0.182	0.129	0.068	29.22	-0.323	0.195	1.648	7.06	0.968
Eutta(R-LDHPro)	0.062	0.023	-0.673	62.12	0.267	0.018	-37.313	71.17	0.982
Eutta(SapPro)	0.245	0.245	-0.018	2.28	-0.111	-58.072	1.95E10 ⁻⁴	-	0.106
Eutta(SapPhe)	0.241	0.236	-0.025	10.73	0.041	0.232	-19.23	3.45	0.999
Eutta(LapPro)	0.100	0.120	0.483	14.87	0.67	0.131	5.477	7.22	0.995
Eutta(LapPhe)	0.141	0.087	-0.021	12.33	-0.195	0.092	23.624	7.85	0.995

Table 23 - Properties obtained from pseudo first order and pseudo second order kinetic models for caffeine adsorbents.

Sample	q_t (exp)	pseudo first order				pseudo second order			
		q_1 (mg/g)	k_1 (L/mg)	E (%)	R^2	q_2 (mg/g)	k_2 (L/mg)	E (%)	R^2
Eutta(KaoPro)	0.002	1.262E-3	-0.067	41.22	-0.182	1.165E-3	-1064.416	45.71	0.998
Eutta(KaoPhe)	0.003	4.011E-3	4.888	17.26	0.860	2.506E-3	-204.102	26.74	0.971
Eutta(KaoAPro)	0.004	3.127E-3	-0.128	12.16	0.861	3.099E-3	-1144.120	12.94	0.999
Eutta(KaoAPhe)	0.003	2.862E-3	-0.025	4.64	-0.145	2.778E-3	-389.401	7.45	0.998
Eutta(SapPro)	0.002	1.111E-3	-0.448	38.85	-0.067	1.600E-3	66.460	12.00	0.777
Eutta(SapPhe)	0.001	6.298E-4	-0.493	56.44	-0.004	3.927E-3	-331.651	72.84	0.934

Table 24 - Properties obtained from pseudo first order and pseudo second order kinetic models for estrogen adsorbents.

Sample	q_t (exp)	pseudo first order				pseudo second order			
		q_1 (mg/g)	k_1 (L/mg)	E (%)	R^2	q_2 (mg/g)	k_2 (L/mg)	E (%)	R^2
Eutta(KaoPhe)	0.006	3.522E-3	-0.264	39.84	-0.153	2.319E-3	-119.845	60.38	0.976
Eutta(KaoAPro)	0.008	0.019	-12.538	118.68	0.155	5.985E-3	-7.316	29.88	0.157
Eutta(SapPro)	0.346	0.033	0.022	3.64	0.579	0.034	-442.176	1.01	1.000
Eutta(SapPhe)	0.339	0.034	0.002	0.62	-0.179	0.033	-164.705	1.59	0.999

After performing the adsorption kinetic models, it was observed that the pseudo second order model came closer to the results indicating the presence of more than one adsorption site and/or interaction between the contaminant and the material through chemisorption, with the exception of samples Eutta(SapPro) in Cr^{3+} adsorption and in the Eutta(KaoAPro) sample for estrogen adsorption where neither of the two models showed high linear correlation values.

The infrared spectra of the samples after adsorption of contaminants ($q_{t_{\text{exp}}}$) provide information on the behavior of these pollutants in the adsorption process (Figure S1 in the supplementary material). The Eutta(KaoPro) sample showed a new band at 1725 cm^{-1} after the adsorption of Cr^{3+} and caffeine, referring to stretch vibrations of $\text{C}=\text{O}$, indicating the interaction of the amino acid hydroxyl in the aquocomplex of Cr^{3+} , preventing the electronic resonance of the carboxylate and favoring carbonyl vibrations in addition to the carbonyl vibrations of the caffeine molecule. The vibrations of the aquocomplex appear at 3657 cm^{-1} , while the vibrations of the hydroxyls OH2 and OH3 of kaolinite returned after the addition of the contaminants, indicating a decrease in the interaction between the complex and the matrix in the adsorption process of the Cr^{3+} and caffeine contaminants. In the presence of caffeine, the amino acid vibration bands in relation to the complex do not change, indicating that the interaction does not occur in the first coordination sphere of the complex.

In the Eutta (KaoAPro) sample, the bands of the carboxylate group shifted from 1534 and 1412 cm^{-1} to approximately 1557 and 1460 cm^{-1} for the contaminant Cr^{3+} and 1555 and 1456 cm^{-1} for caffeine. This small displacement for higher vibration energies indicates the interaction between the complex and

the contaminants by weak interactions such as Van der Waals forces in the complexes not functionalized by covalent bonds in the matrix, that is, with greater electronic affinity of the complex with the contaminants in relation to kaolinite. The presence of COO^- bands without displacement in the sample indicates that the complexes functionalized by covalent bonding in the matrix remained functionalized and interacting with the Eu^{3+} ion. In the sample in the presence of estrogen, however, there is a decrease in the intensity of the carboxylate bands, and it is only possible to identify the antisymmetric stretch vibration at 1543 cm^{-1} , which may indicate an amidation reaction between the amino acid and the hydroxyl of estrogen, reducing the covalent interaction between the complex and kaolinite, justifying the high leaching of the complex in matrices in contact with this contaminant.

For kaolinite samples with the amino acid phenylalanine, the stretch bands of the tertiary amines of caffeine, the bonds of C-H and hydroxyls to estrogen and the hydroxyls of the aquocomplex of Cr^{3+} are observed in the regions between 2800 and 3200 cm^{-1} . The amino acid carboxylate bands did not show position shifts indicating that the interaction of contaminants occurs in the second coordination sphere, without significantly altering the interactions between the complex and the matrix.

In the Eutta(R-LDHPPro) sample in the presence of Cr^{3+} , the carboxylate bands shift to smaller wavenumbers (from 1600 and 1423 cm^{-1} to 1580 and 1406 cm^{-1}), indicating a greater structural rigidity of the complex in the presence of aquocomplex, due to the interaction of Cr^{3+} in the first coordination sphere of the Eu^{3+} complex. For the samples with LAPONITE® there was a decrease in the intensities of the amino acid bands, without showing band shifts, indicating a

weaker interaction between the electronic clouds of the complex and the contaminants. Finally, in samples with saponite, there was a decrease in the intensity of the carboxylate bands and a slight displacement of the antisymmetric stretch band in the region from 1415 cm⁻¹ to 1390 cm⁻¹, indicating the interaction of the complex in the first coordination sphere, providing a more rigid structure in the complex, causing a decrease in vibration energy.

For all materials where it was possible to obtain the kinetic models, equilibrium tests were performed to know the maximum adsorption capacity of the materials up to the equilibrium point, varying the concentrations up to the detection limit of the calibration curve for each contaminant. Two models of adsorption isotherms were used for the results obtained, the first being the Langmuir isotherm, where it is possible to verify the adsorption in monolayers, that is, where each site contains an adsorbed molecule. It is possible to obtain the Langmuir adsorption isotherm through equation 21 and 22 (MALIK, 2004; TRAN; LIN; CHAO, 2018):

$$q_e = \frac{q_{max}k_L C_e}{1 + k_L C_e} \quad \text{Equation 21}$$

Where q_e is the amount of solute adsorbed per gram of adsorbent at equilibrium (mg/g); q_{max} is the maximum adsorption capacity (mg/g); K_L is the adsorbent/adsorbent interaction constant (L/mg) and C_e the concentration of the adsorbate in equilibrium. To get the value of q_{max} and K_L it is necessary to perform linear regression using equation 22:

$$\frac{1}{q_e} = \frac{1}{q_{max}} + \frac{1}{k_L q_{max} C_e} \quad \text{Equation 22}$$

Where a $1/q_e$ by $1/C_e$ graph is plotted to find the values through the intercept and slope of the line. The Langmuir isotherm can also be used to calculate the affinity between the adsorbent and adsorbent by calculating the separation factor or equilibrium parameter (R_L) through equation 23 (MALIK, 2004).

$$R_L = \frac{1}{1 + k_L C_0} \quad \text{Equation 23}$$

Where C_0 is the initial concentration of the adsorbate. The results indicate whether the Langmuir isotherm is irreversible ($R_L = 0$); if it is linear ($R_L = 1$); if the solute prefers the liquid phase, that is, unfavorable ($R_L > 1$) or if the adsorbate prefers the solid phase, the result where the adsorption is favorable ($0 < R_L < 1$) (AJENIFUJA; AJAO; AJAYI, 2017).

The second isotherm used was the Freundlich model, which is applied to non-ideal systems, such as heterogeneous or multilayer surfaces, where the adsorption occurs at several adsorption sites with different energies involved, which is obtained through equation 24 (AJENIFUJA; AJAO; AJAYI, 2017; BELTRAME et al., 2018).

$$q_e = K_F C_e^{1/n} \quad \text{Equation 24}$$

Where K_F is the Freundlich adsorption capacity constant; C_e is the concentration in equilibrium of the solution and $1/n$ is a constant related to surface heterogeneity. To obtain the values of the constants it was necessary to perform the linear regression of this equation, obtaining equation 25.

$$\log q_e = \log k_F + \frac{1}{n} \log C_e \quad \text{Equation 25}$$

Where a graph of $\log q_e$ by $\log C_e$ is plotted to obtain the constants by the slope and intersection of the line.

The information obtained by the linear isotherms were used in the nonlinear equations of Langmuir and Freundlich. The parameters obtained by the Langmuir adsorption isotherms are shown in table 25, while the parameters obtained by the Freundlich isotherms are shown in table 26.

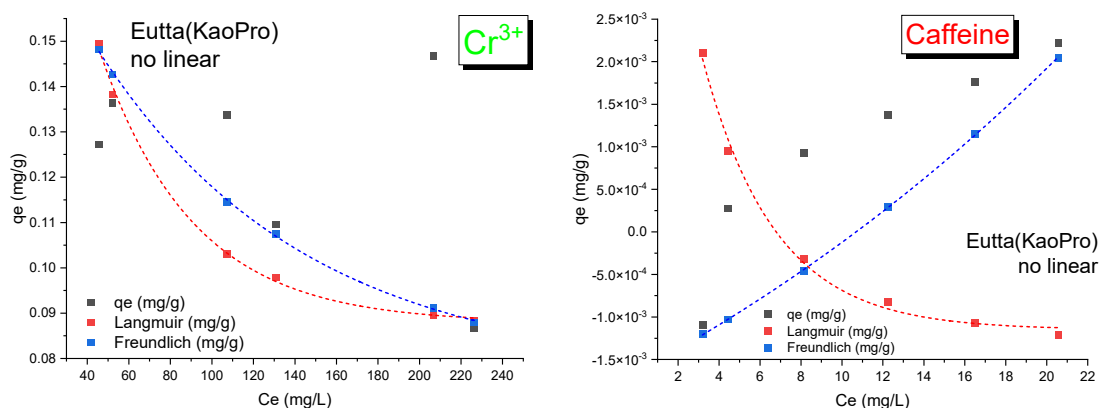
Table 25 - Parameters obtained by the Langmuir isotherm and its linear regression for Cr³⁺, caffeine and estrogen contaminants.

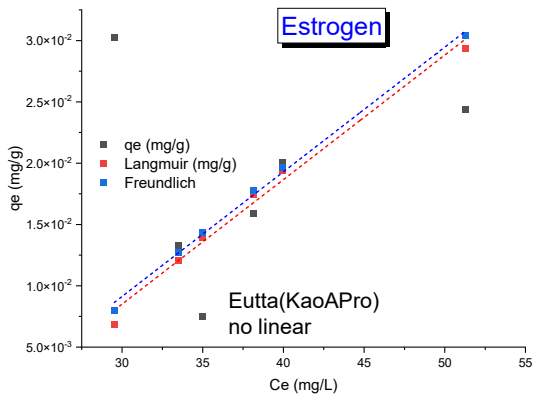
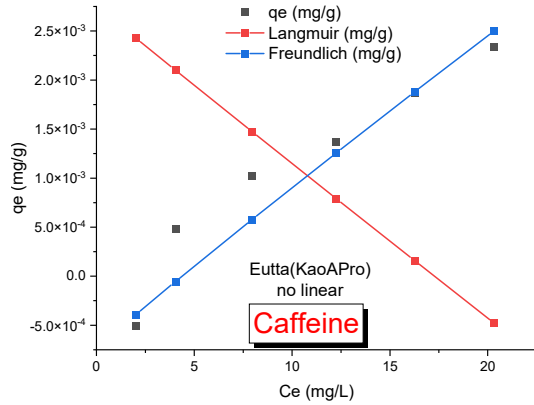
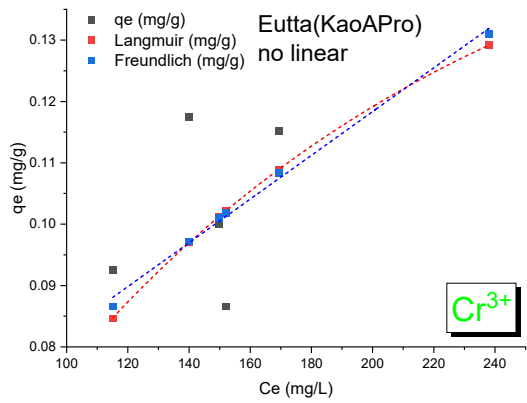
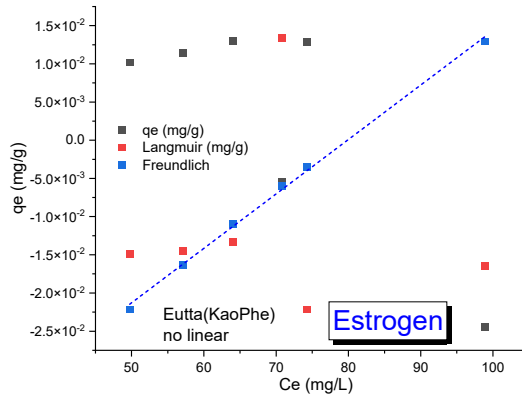
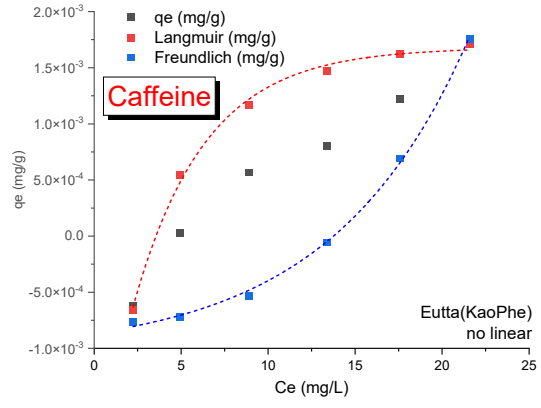
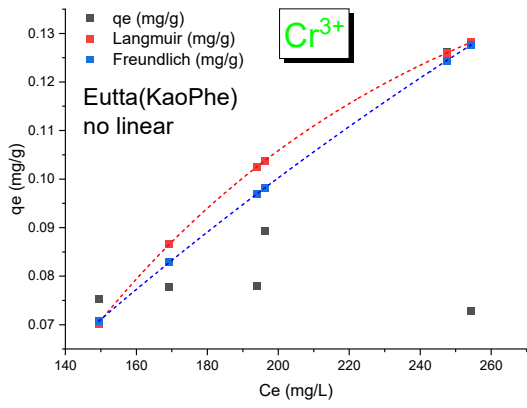
Sample	Pollutant	Linear				Not linear		
		q _{max} (mg/g)	K _L (L/mg)	R _L	R ²	q _{max} (mg/g)	K _L (L/mg)	R ²
Eutta(KaoPro)	Cr ³⁺	0.106	-0.101	$(-3.07 \times 10^{-6}) - (-1.84 \times 10^{-6})$	-0.047	7.353	-1084.87	0.780
	Caffeine	1.06x10 ⁻³	-5.191	$(-0.0027) - (-1.07 \times 10^{-4})$	-0.249	892.86	-372.69	0.744
Eutta(KaoPhe)	Cr ³⁺	0.136	0.443	$1.90 \times 10^{-7} - 1.14 \times 10^{-7}$	-0.0053	7.575	17487.51	0.970
	Caffeine	1.84x10 ⁻⁴	0.722	$0.021 - 8.64 \times 10^{-4}$	-0.242	8074.28	45.25	0.723
	Estrogen	-671.14	-10.340	$3.33 - (-2.50)$	0.079	9.233	-194.96	-0.247
Eutta(KaoAPro)	Cr ³⁺	0.194	0.008	$1.44 \times 10^{-5} - 8.64 \times 10^{-6}$	0.289	15.992	231.51	0.977
	Caffeine	7.59x10 ⁻⁴	-0.273	$0.944 - 0.402$	0.238	82250.37	0.059	0.999
	Estrogen	0.027	0.033	$3.75 \times 10^{-4} - 1.88 \times 10^{-4}$	-0.224	113.12	53.19	0.986
Eutta(KaoAPhe)	Cr ³⁺	0.583	7.56x10 ⁻⁴	$1.93 \times 10^{-5} - 1.16 \times 10^{-5}$	0.289	27.655	172.38	0.987
	Caffeine	5.38x10 ⁻⁴	-0.070	$1.07 - (-1.33)$	0.001	-531.915	-11.56	-0.061
Eutta(R-LDHPro)	Cr ³⁺	-0.013	-0.003	$(-8.10 \times 10^{-6}) - (-4.86 \times 10^{-6})$	0.111	10.803	-411.04	0.135
	Cr ³⁺	5.67x10 ⁻³	-5.84x10 ⁻³	$(-1.33) - (-0.52)$	0.245	5.143	-255.14	0.856
Eutta(SapPro)	Caffeine	1.77x10 ⁻³	5.137	$0.004 - 1.4 \times 10^{-4}$	-0.249	598.80	273.76	0.837
	Estrogen	0.024	0.027	$1.7 \times 10^{-4} - 8.5 \times 10^{-5}$	-0.153	98.52	117.03	0.793
Eutta(SapPhe)	Cr ³⁺	0.032	0.108	$0.041 - 0.040$	-0.249	33.990	58.84	0.998
	Caffeine	2.99x10 ⁻⁴	-0.106	$1.12 - (-0.61)$	0.231	-671.14	-10.34	0.114
	Estrogen	0.020	4.81x10 ⁻³	$0.91 - 1.33$	-0.224	1301.11	12.15	0.998
Eutta(LapPro)	Cr ³⁺	-0.019	-4.257x10 ⁻³	$(-5.75 \times 10^{-6}) - (-3.45 \times 10^{-6})$	0.131	24.814	-579.27	0.134
Eutta(LapPhe)	Cr ³⁺	0.078	-5.97x10 ⁻³	$4.69 \times 10^{-6} - 2.81 \times 10^{-6}$	-0.216	31.046	711.19	0.923

Table 26 - Parameters obtained by the Freundlich isotherm and its linear regression for Cr³⁺, caffeine and estrogen contaminants.

Sample	Pollutant	Linear			Not linear		
		1/n	K _F (mg/g)	R ²	1/n	K _F (mg/g)	R ²
Eutta(KaoPro)	Cr ³⁺	0.119	0.212	-0.032	-1.26x10 ⁻⁴	1.374	0.933
	Caffeine	1.323	4.55x10 ⁻⁵	0.947	0.037	0.836	0.994
Eutta(KaoPhe)	Cr ³⁺	0.457	7.59x10 ⁻³	0.015	1.94x10 ⁻⁴	1.112	0.998
	Caffeine	2.659	6.90x10 ⁻⁷	0.840	1.213	1.38x10 ⁻⁶	0.869
	Estrogen	0.627	8.995x10 ⁻⁴	0.771	1.136x10 ⁻⁴	1.011	0.997
Eutta(KaoAPro)	Cr ³⁺	0.461	0.010	0.369	2.84x10 ⁻⁴	1.142	0.995
	Caffeine	0.954	1.31x10 ⁻⁴	0.993	1.13x10 ⁻⁴	13520.72	0.999
	Estrogen	0.387	4.178x10 ⁻³	-0.223	1.68x10 ⁻⁴	1.025	0.997
Eutta(KaoAPhe)	Cr ³⁺	-0.193	0.205	0.107	-2.37x10 ⁻⁵	1.197	0.906
	Caffeine	1.703	7.69x10 ⁻³	0.981	1.30x10 ⁻⁴	0.999	0.975
Eutta(R-LDHPro)	Cr ³⁺	-1.535	89.743	0.559	-5.63x10 ⁻⁵	1.083	0.713
Eutta(SapPro)	Cr ³⁺	7.949	2.38x10 ⁻²⁰	0.926	2.86x10 ⁻³	0.300	0.964
	Caffeine	0.844	2291	0.937	1391.67	-	0.999
Eutta(SapPhe)	Cr ³⁺	-0.829	3.001	-0.234	-1.16x10 ⁻⁴	1.148	0.998
	Caffeine	1.840	9.12x10 ⁻⁶	0.968	1.27x10 ⁻⁴	0.999	0.981
	Estrogen	1.020	1.03x10 ⁻⁴	-0.153	1.14x10 ⁻⁴	0.999	1.000
Eutta(LapPhe)	Cr ³⁺	-2.478	68.103	0.674	-4.4x10 ⁻⁷	1.000	0.361

In general, the nonlinear isotherms presented more concise results and with higher values of linear correlation (R^2), being the Freundlich isotherm applicable in most materials. For the kaolinite samples, the Langmuir isotherms showed high linear correlation values in all cases, however, with K_L with negative values and q_{max} with high values as in the Eutta(KaoAPro) sample ($q_{max}= 82250.37$ mg/g). The only hydrotalcite sample, Eutta(R-LDHPPro) showed low linear correlation values in both cases. Only the Eutta(KaoAPro) sample showed a favorable separation factor (R_L) range for adsorption among the samples synthesized with the amino acid proline for the Cr^{3+} contaminant. As for caffeine, only the Eutta(KaoPro), Eutta(KaoAPhe) and Eutta(SapPhe) samples showed negative R_L values, not being applied for the Langmuir isotherm, while only the Eutta(KaoPhe) sample obtained a negative R_L value for the estrogen. The isotherms of the materials are shown in figure 52 to 55.





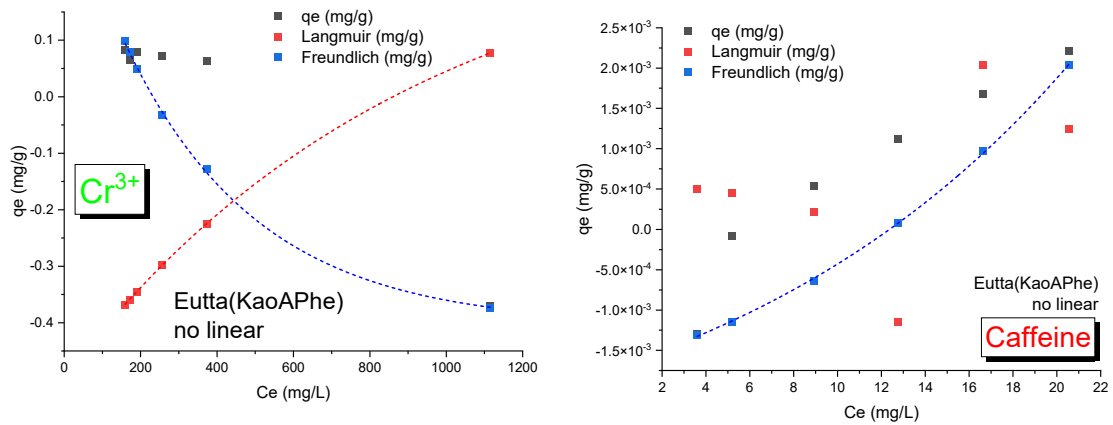


Figure 52 - Adsorption isotherms for kaolinite samples for Cr^{3+} , caffeine and estrogen contaminants.

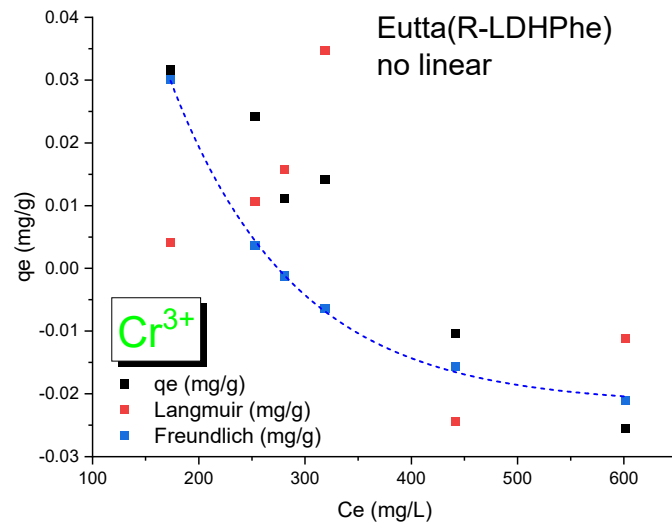


Figure 53 - Adsorption isotherms for samples with hydrotalcite for Cr^{3+} , caffeine and estrogen contaminants.

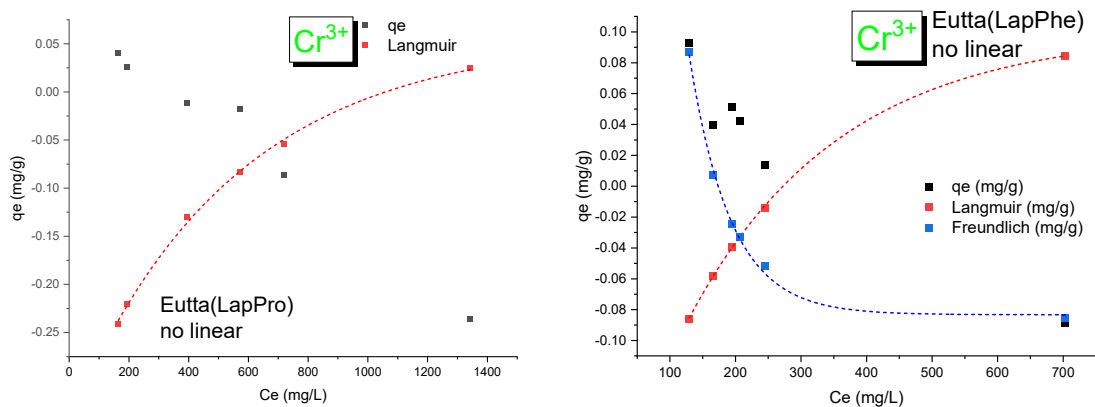
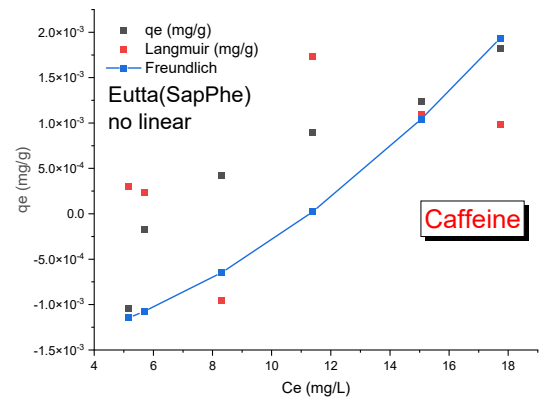
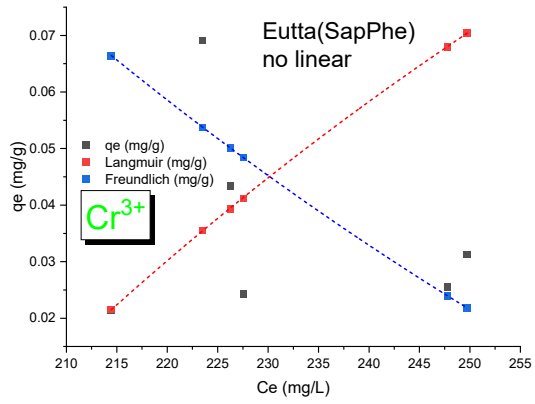
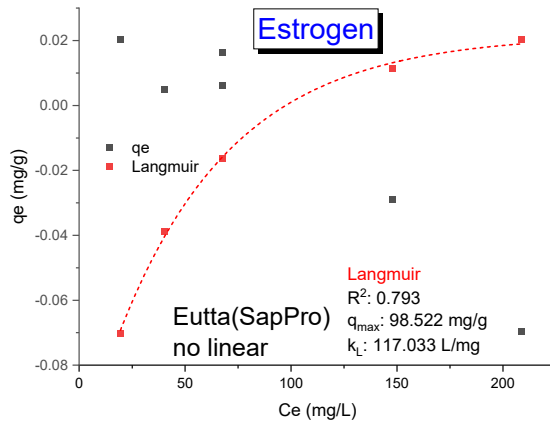
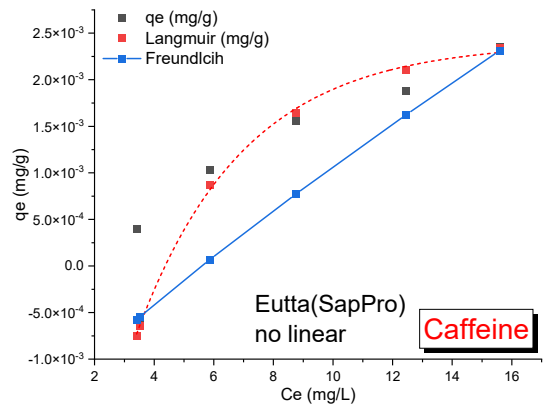
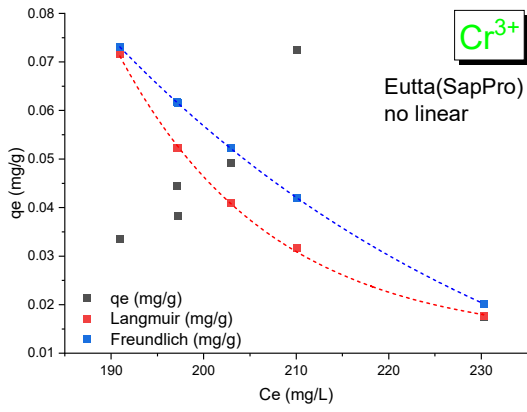


Figure 54 - Adsorption isotherms for samples with LAPONITE® for Cr^{3+} contaminants.



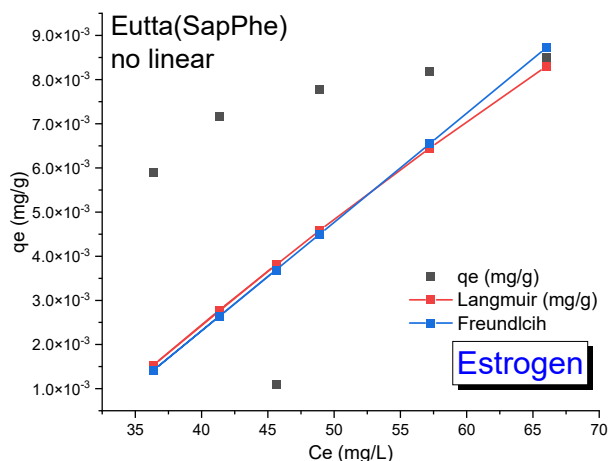


Figure 55 - Adsorption isotherms for samples with saponite for Cr³⁺, caffeine and estrogen contaminants.

The Eutta(LapPro) sample was not applicable to the Freundlich isotherm for Cr³⁺ adsorption, as well as the Eutta(KaoPhe) and Eutta(SapPro) samples were not applicable to the Freundlich model for estrogen adsorption. On the other hand, with the exception of the Eutta(LapPhe) sample, all samples that were applicable to the Freundlich isotherm showed high correlation values for the application of the nonlinear equation, which classifies these samples for application as luminescent sensors. The samples showed characteristics of several adsorption sites with different energies, in agreement with the other characterization techniques, showing adsorption capacity both in the matrix and in the different chemical environments of the complex, as evidenced by luminescence spectroscopy.

The non-linear isotherms as shown in figures 50 to 53 showed distinct characteristics in the adsorption behavior for each isotherm. For non-linear isotherms that presented a straight line, as in the Eutta(SapPhe) sample in estrogen adsorption, the adsorption is proportional, that is, the adsorption rate increases or decreases proportionally with the concentration. When an ascending curve is observed (such as in the Langmuir isotherm in the

adsorption of estrogen in the Eutta(SapPro) sample), it indicates that the adsorption is favorable and when descending (in the adsorption of Cr^{3+} in the Eutta(SapPro) sample), unfavorable, that is, when the adsorption is low regardless of the concentration.

The Langmuir isotherm has the characteristic of a rectangular hyperbola, while the Freundlich isotherm has an allometric exponential characteristic. Therefore, the non-linear fits of q_e by C_e that present a higher correlation with any of these properties apply better to the material and consequently present more precise parameters. Therefore, the non-linear fit presents more accurate results compared to those obtained by linear regression. On the other hand, to obtain the nonlinear isotherms, the fit must converge with the experimental results. In the samples tested with the Cr^{3+} contaminant, only the samples Eutta(KaoAPro), Eutta(LapPhe) and Eutta(R-LDHPhe) showed convergence between the nonlinear Freundlich isotherm and the experimental data. In the samples tested with caffeine, in all samples in the equilibrium tests it was possible to obtain the nonlinear Freundlich isotherms and in the samples tested with estrogen, none of the experimental data converged with the nonlinear Freundlich isotherm. Data from nonlinear Freundlich isotherms are shown in table 27.

Table 27 - Parameters obtained by the nonlinear Freundlich isotherm.

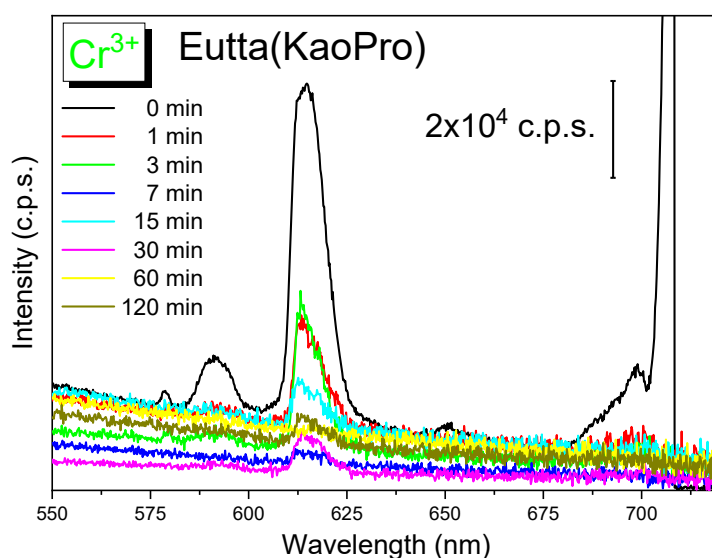
Sample	Pollutant	1/n	K _F (mg/g)	R ²
Eutta(KaoPro)	Cr ³⁺	0.469	9.95x10 ⁻³	0.431
	Caffeine	1.472	2.77x10 ⁻³	0.690
Eutta(KaoPhe)	Caffeine	1.718	8.94x10 ⁻⁶	0.829
Eutta(KaoAPro)	Caffeine	1.161	7.28x10 ⁻⁵	0.874
Eutta(KaoAPhe)	Caffeine	2.071	4.52x10 ⁻⁶	0.685
Eutta(R-LDHPhe)	Cr ³⁺	-2.555	18496.27	0.418
Eutta(LapPhe)	Cr ³⁺	-2.499	17907.16	0.422
Eutta(SapPro)	Caffeine	1.307	6.92x10 ⁻⁵	0.734
Eutta(SapPhe)	Caffeine	2.702	8.02x10 ⁻⁷	0.659

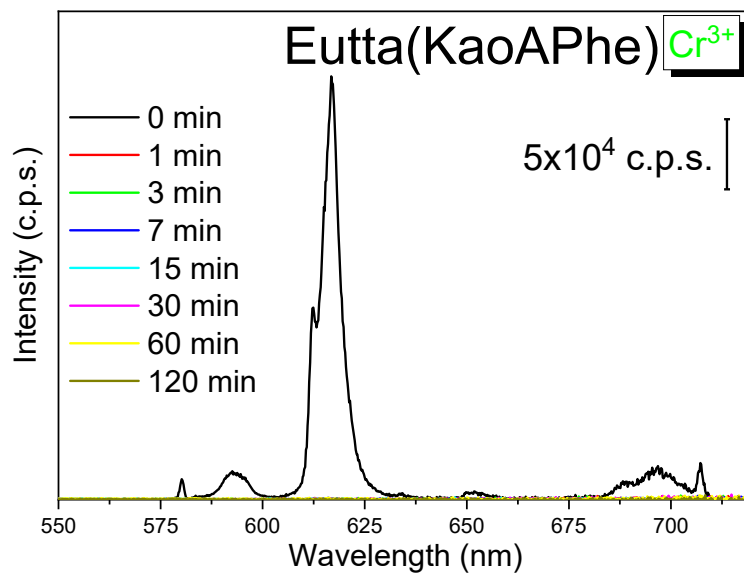
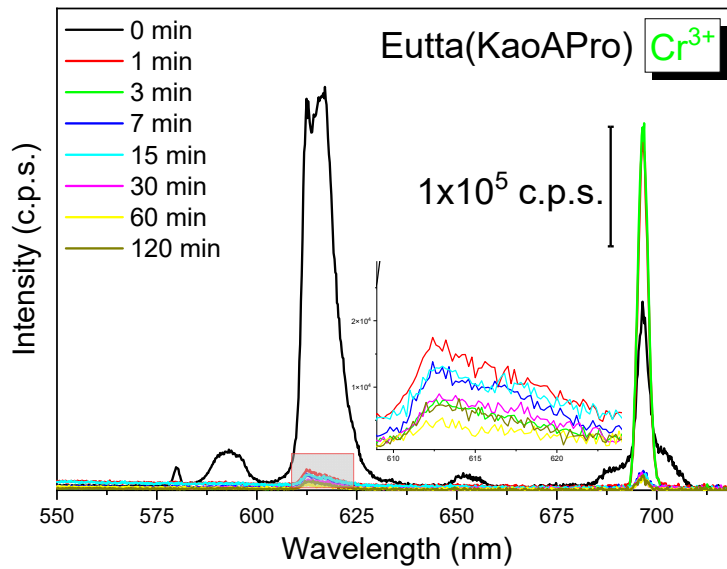
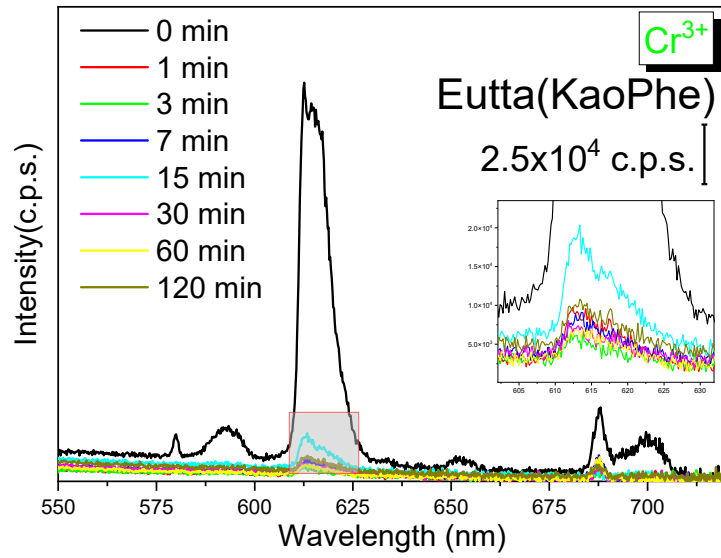
4.3.2. Quenching measurements for luminescent sensors

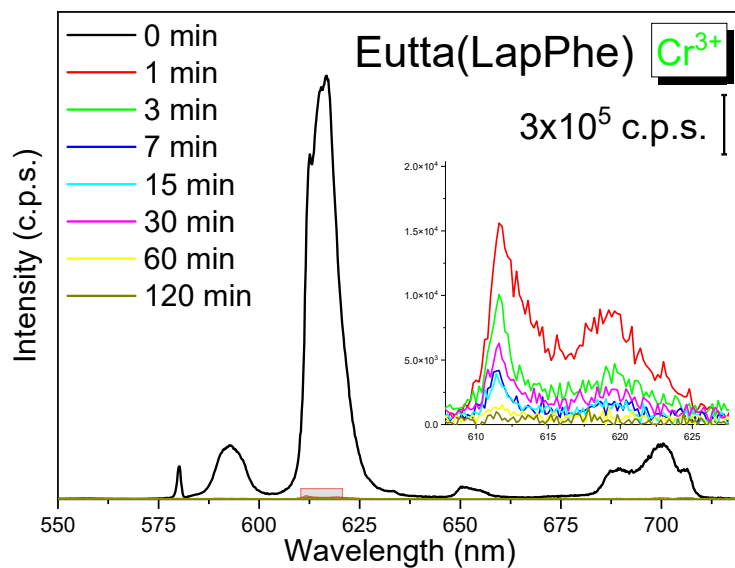
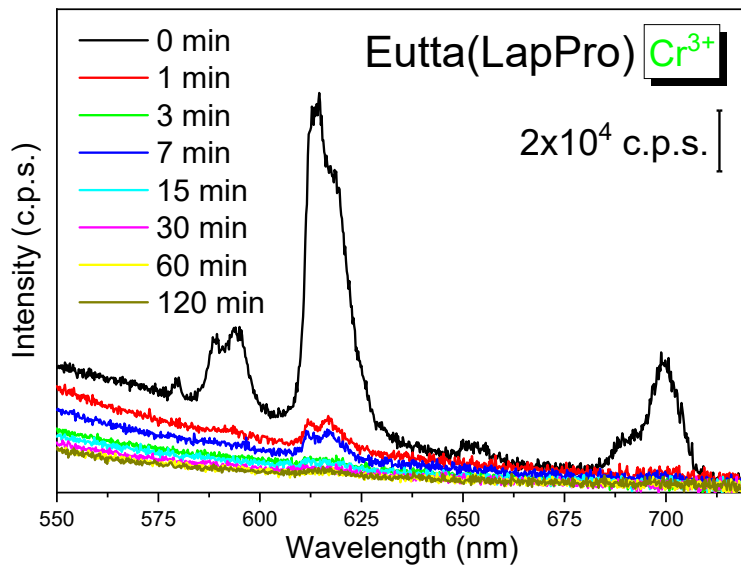
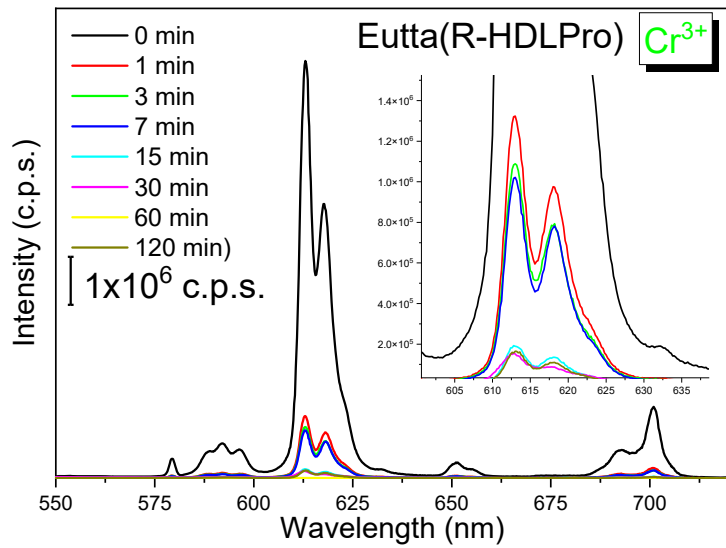
In determining the contaminants, the radiative emission intensity presents changes, which involve an increase in luminescence, obtaining a stimulating response or a decrease in radioactive emission (quenching) in the recognition of analytes (ZHAO et al., 2018). The transition band $^5D_0 \rightarrow ^7F_2$ was used for presenting greater intensity of radiative emission. In the case of the organic contaminants caffeine and β -estradiol (estrogen), in most cases a stimulating response evidenced by increased emission in initial times was observed, while suppression of luminescence was observed for the detection of Cr³⁺.

The interaction of Cr³⁺ with the complex occurs in the form of an aquocomplex ($[Cr(H_2O)_6]^{3+}$) increasing the number of oscillators, dispersing energy in the form of vibration and consequently decreasing the radiative emission of the complex. The interaction of Cr³⁺ with the cyclic grouping of

proline or with the aromatic rings of phenylalanine or the secondary ligand tta can decrease the conjugation of the complex, resulting in a lower external quantum yield (Q_{Ln}^L) and consequently in the suppression of luminescence. As for organic contaminants, both caffeine and estrogen have cyclic groups with relative conjugation, which can contribute to the transfer of energy to the central ion by antenna effect, resulting in a stimulating effect for the emission, depending on where the interaction starts. However, with the increase in the concentration of these pollutants, oscillating groups such as OH^- and CH_3 for example, can bypass the conjugation and disperse the energy by vibrations, resulting in quenching. Therefore, these contaminants may have two detection bands, a detection band with stimulating emission (at low concentrations) and another band with quenching (at higher concentrations), but only quenching was analyzed for sensor application. The photoluminescence spectra were obtained for the kinetic adsorption study samples that did not show leaching of the material intercalated in the clay minerals (Tables 22-24) and are displayed in Figures 56-58.







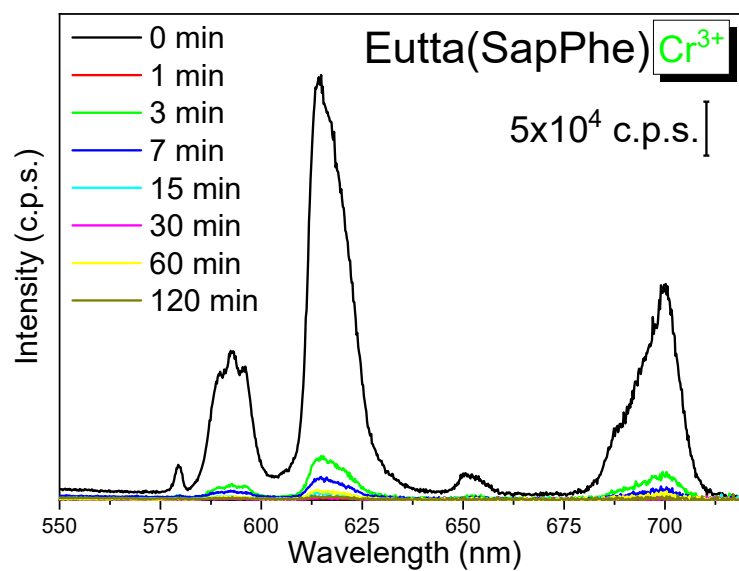
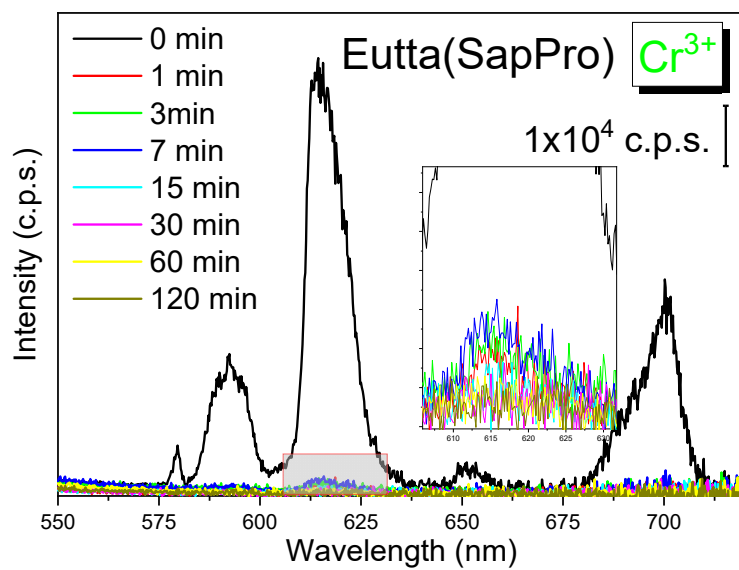
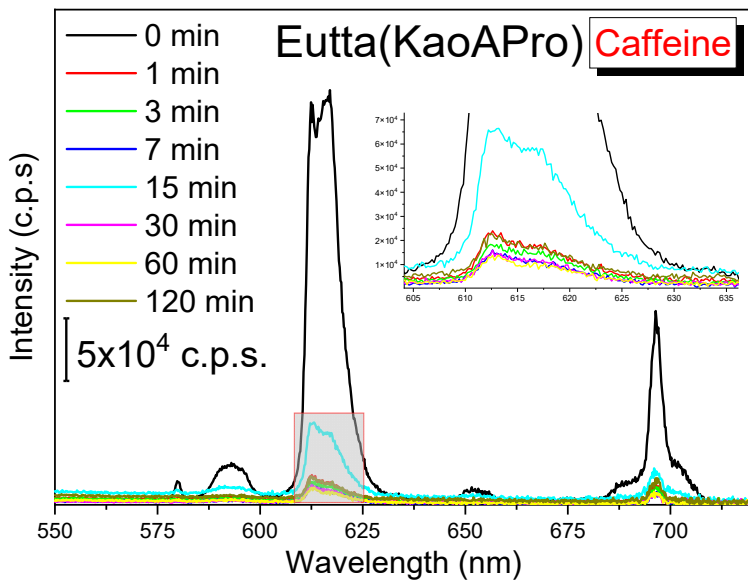
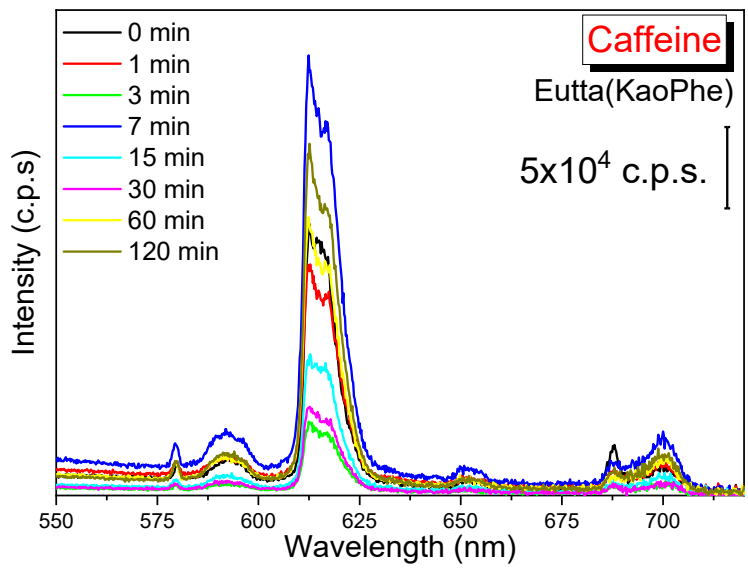
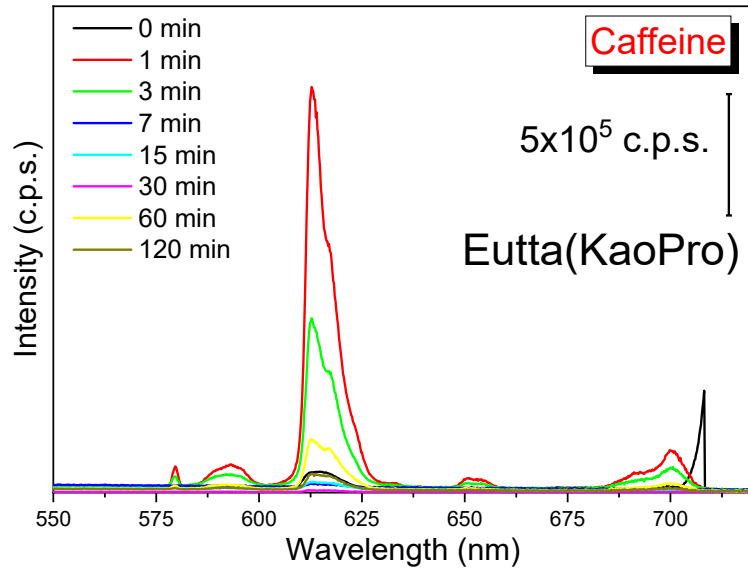
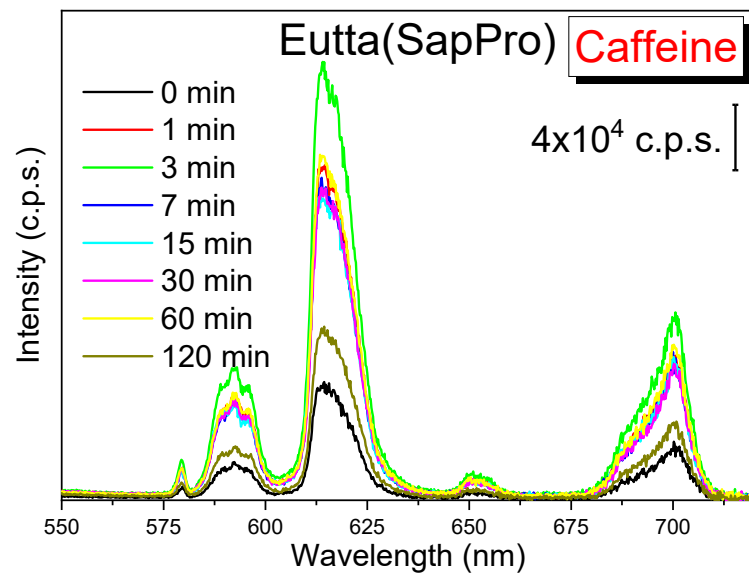
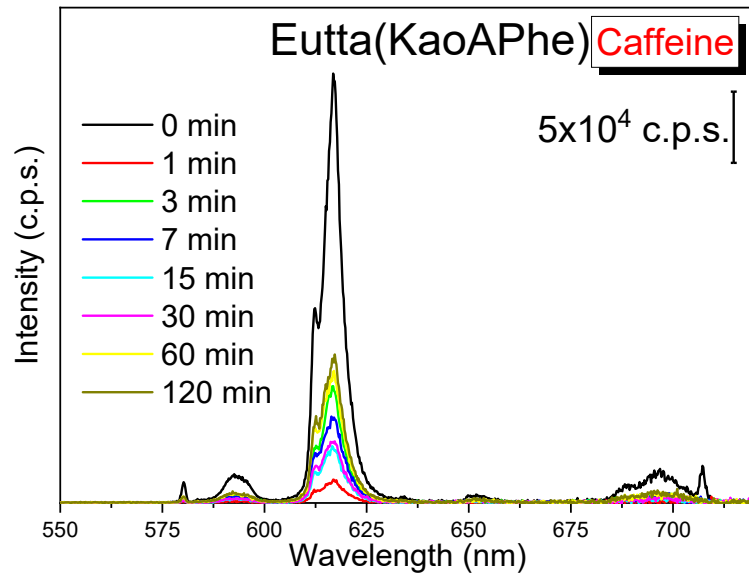


Figure 56 - Photoluminescence spectra of samples complexed with Eu^{3+} ion obtained after adsorption tests with Cr^{3+} in times from 1 to 120 min.





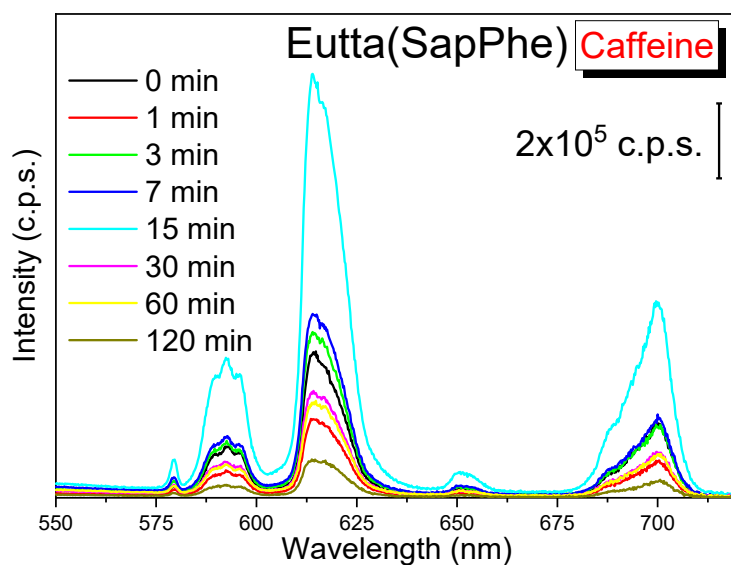
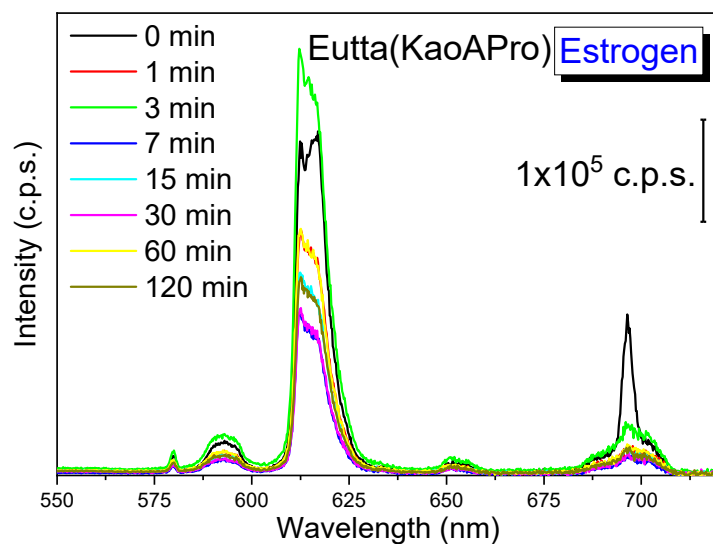
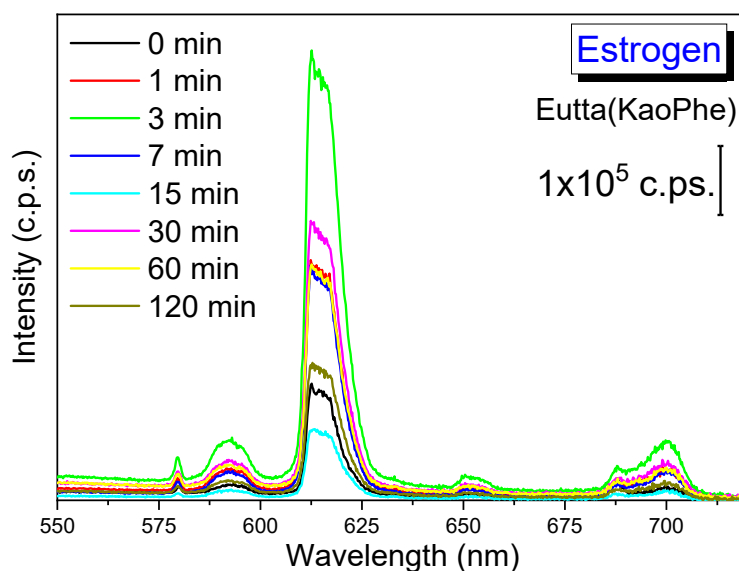


Figure 57 - Photoluminescence spectra of samples complexed with Eu^{3+} ion obtained after adsorption tests with caffeine in times from 1 to 120 min.



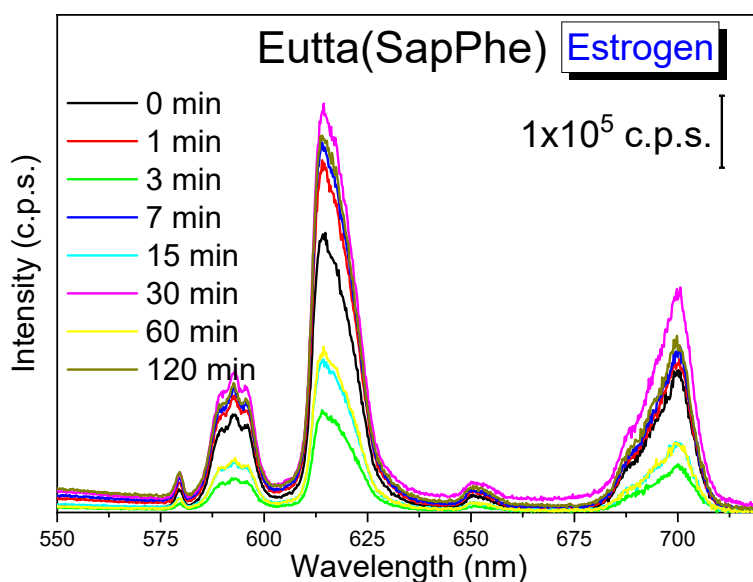
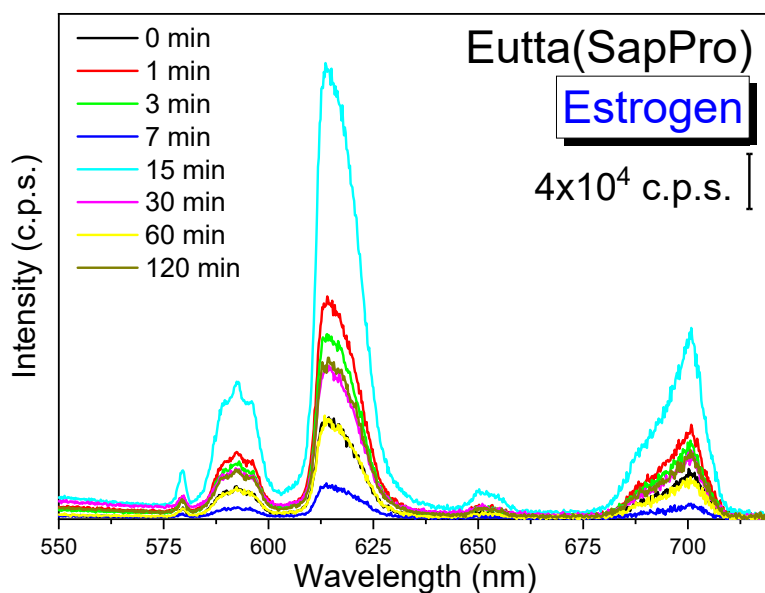


Figure 58 - Photoluminescence spectra of samples complexed with Eu^{3+} ion obtained after adsorption tests with estrogen in times from 1 to 120 min.

In the Cr^{3+} adsorption process, the luminescence suppression is observed in all tested samples, with adsorption greater than 50% of the adsorbate concentration already in the initial times. For materials with kaolinite, regular suppression of luminescence is observed in samples obtained by the conventional route (Eutta(KaoPro) and Eutta(KaoPhe)), while in samples obtained by modification of the alkoxide APTES there is almost total suppression of luminescence for the sample Eutta(KaoAPro) and total for the

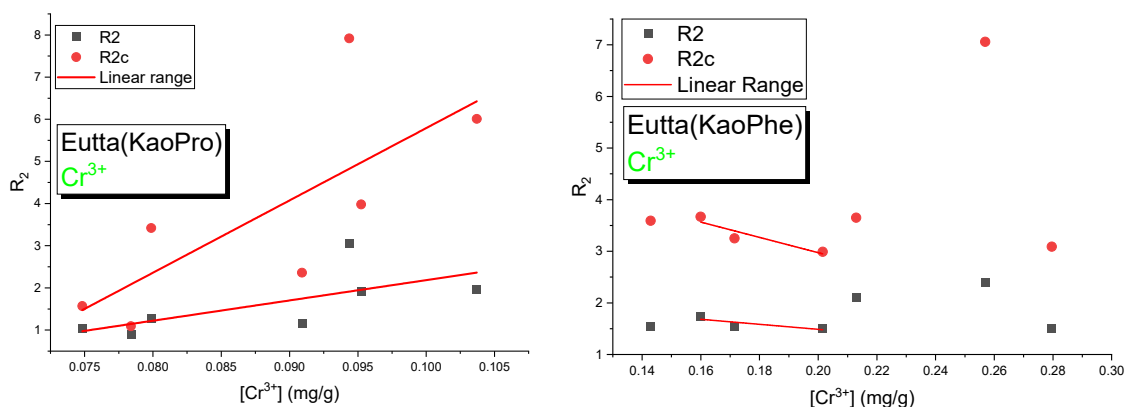
Eutta(KaoAPhe) sample, where Eu^{3+} emission bands are no longer observed. For the only sample where there was no leaching of the material intercalated in hydrotalcite (Eutta(R-LDHPro)), the quenching increases as a function of time. The same occurs for materials obtained from LAPONITE®, while for materials obtained from saponite they reduced almost entirely the emission of the Eu^{3+} bands.

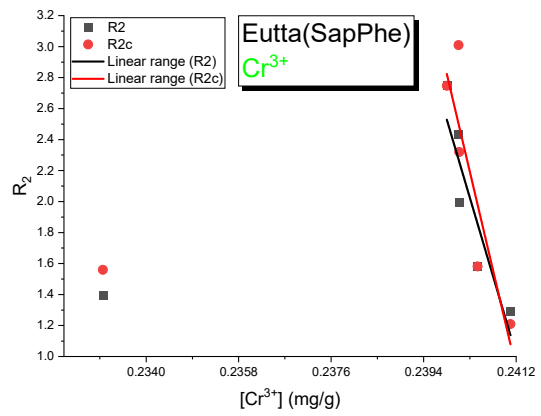
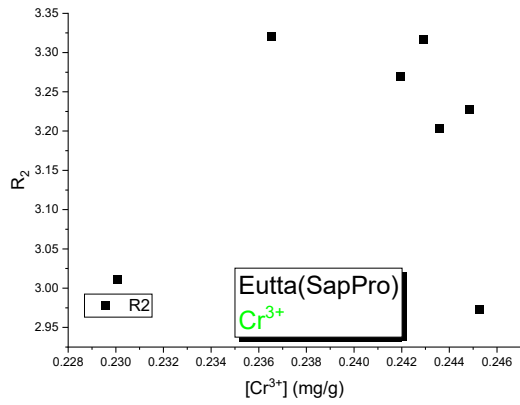
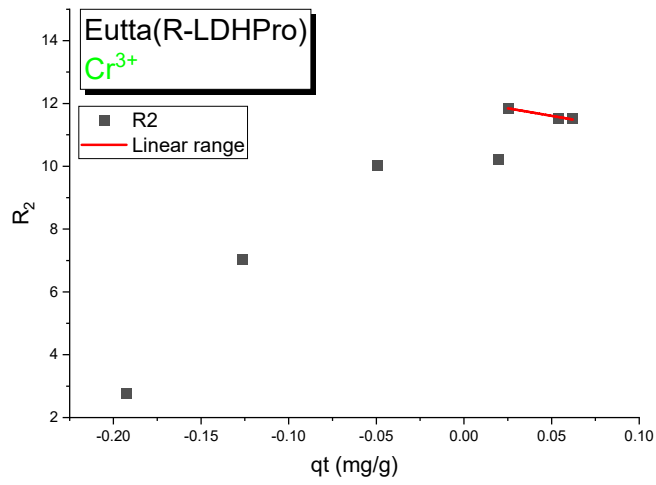
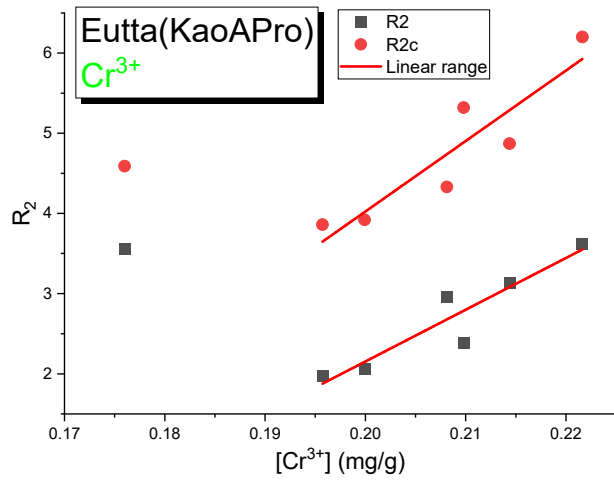
In the caffeine adsorption kinetics, there was an increase in radioactive emission in the initial times and a suppression in longer times for the Eutta (KaoPro) sample, indicating a type of interaction in lower concentrations of the adsorbate and another type in higher concentrations. At lower concentrations, caffeine can complex in the first coordination sphere, replacing water molecules in the complex and contributing to energy transfer. However, at high concentrations there may also be an interaction between the amino acid and caffeine, increasing the number of oscillators and/or decreasing the conjugation of the complex, resulting in the suppression of luminescence. The same happens for the Eutta (KaoPhe) sample, however with greater difficulty, because the complex has only 2 water molecules in the first coordination sphere. As for the samples obtained by catalyzed synthesis (Eutta(KaoAPro) and Eutta(KaoAPhe)), the complex presented greater dispersion in the matrix and greater structural rigidity compared to the conventional route, which hinders the interaction of caffeine in the first coordination sphere, resulting in the suppression of luminescence, caused by the increase of oscillators in the second coordination sphere.

The complex intercalated in saponite presented 7 water molecules for the sample Eutta(SapPro) and 6 for Eutta(SapPhe), facilitating the replacement with

organic contaminants, both caffeine and estrogen, resulting in an increase in the external quantum yield, caused by greater energy transfer between the contaminant and the Eu^{3+} ion and consequently an increase in the radiative emission of the complex after the adsorption process.

It is possible to obtain a detection range for contaminants and verify its applicability as a luminescent sensor, analyzing the transition ${}^5\text{D}_0 \rightarrow {}^7\text{F}_2$ in relation to the transition ${}^5\text{D}_0 \rightarrow {}^7\text{F}_1$ (R_2), where the detection range comprises the points of R_2 as a function of the contaminant concentration (q_t), it is possible to obtain a high linear correlation (R^2). For samples where the emission bands of the matrix and/or the organic part of the complex interfere with the emission intensity of the Eu^{3+} ion, the correction of the intensities ratio (R_{2c}) was performed, as shown in figure 46. The relationships between the intensities and concentration of contaminants are shown in Figure 59-61.





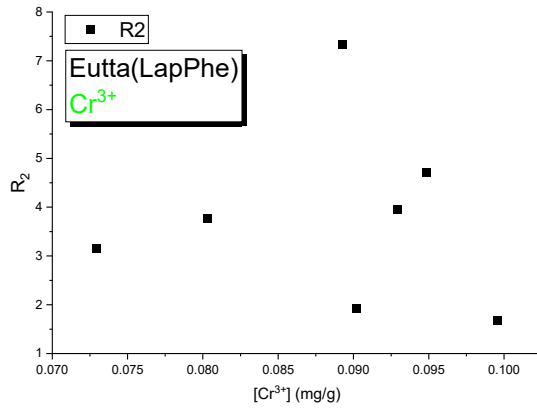
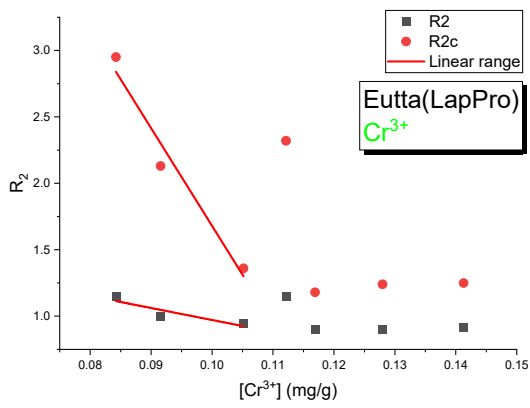
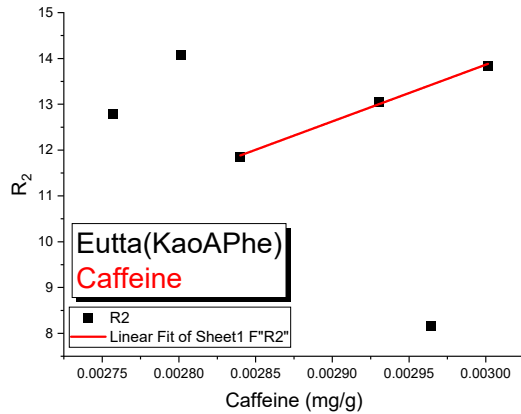
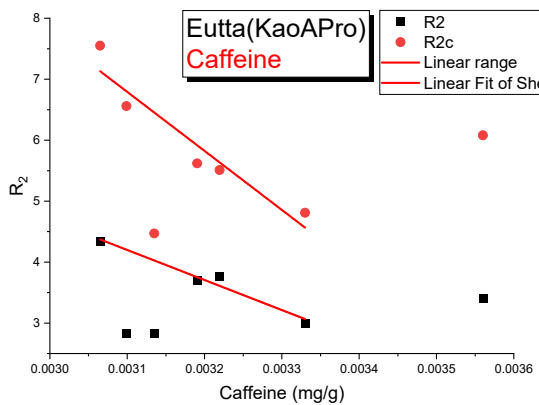
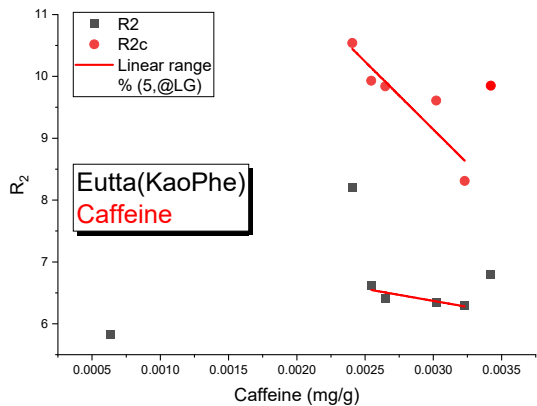
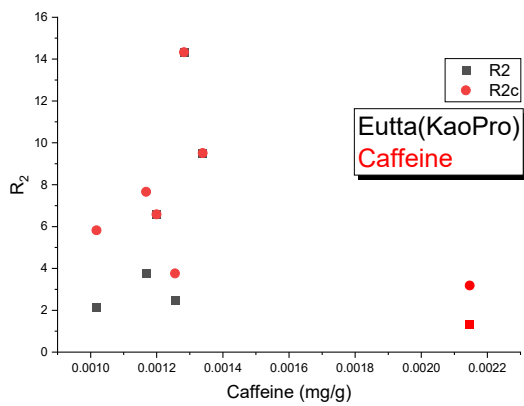


Figure 59 – Variation in the relationship between intensities R_2 ($^5D_0 \rightarrow ^7F_2 / ^5D_0 \rightarrow ^7F_1$) of the samples in relation to the concentration of Cr^{3+} .



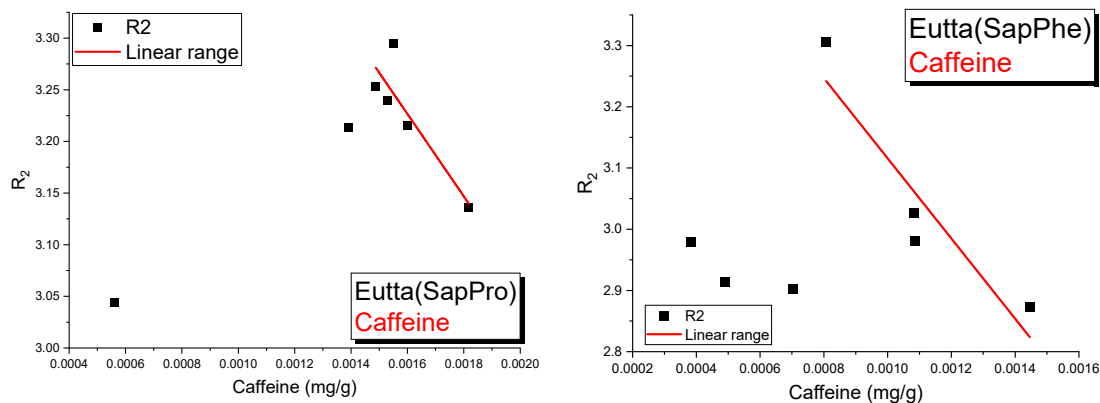


Figure 60 - Variation in the relationship between intensities R_2 (${}^5D_0 \rightarrow {}^7F_2 / {}^5D_0 \rightarrow {}^7F_1$) of the samples in relation to the concentration of caffeine.

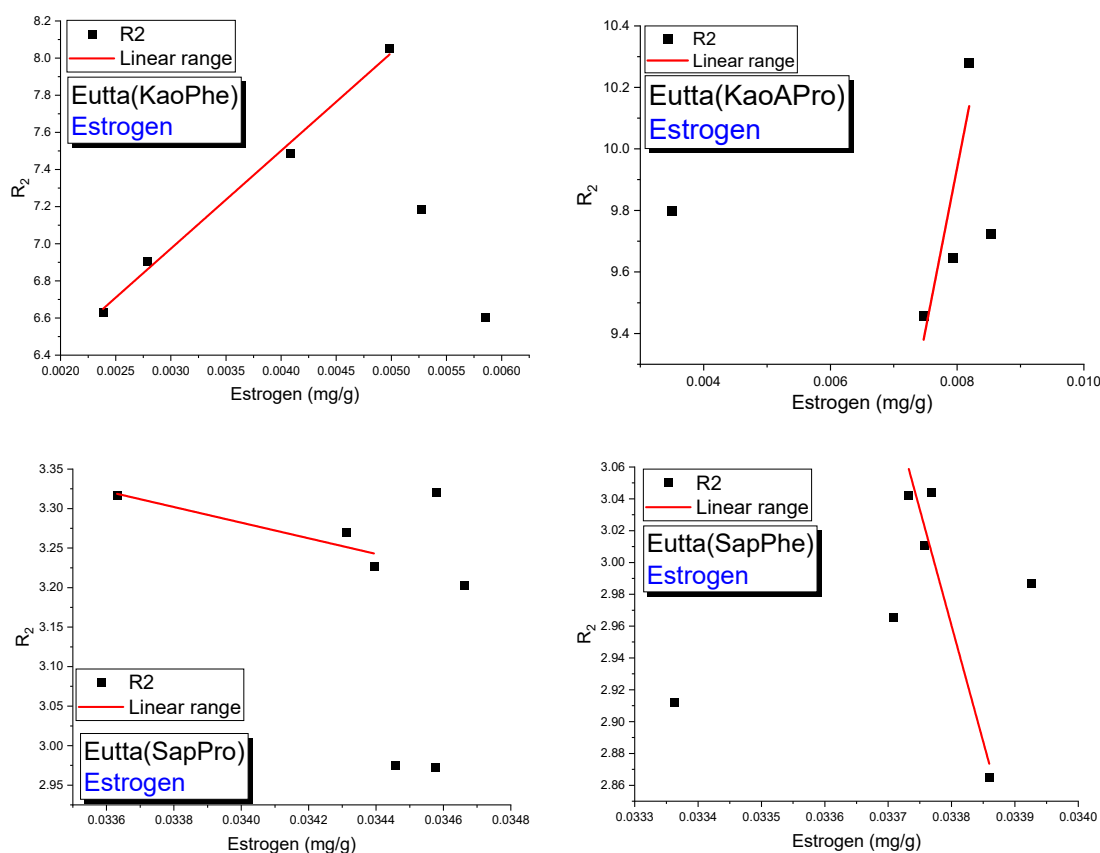


Figure 61 - Variation in the relationship between intensities R_2 (${}^5D_0 \rightarrow {}^7F_2 / {}^5D_0 \rightarrow {}^7F_1$) of the samples in relation to the concentration of estrogen.

In almost all samples it was possible to obtain a detection range of contaminants. For the Cr^{3+} ion, only the Eutta(SapPro) and Eutta(LapPhe) sample did not present a detection range with linear correction. As for caffeine, it was necessary to disregard the adsorption at 1 min and 120 min in samples with kaolinite to obtain a straight line with linear correlation. As for the estrogen

contaminant, although few samples were tested due to the leaching effect, all 4 tested samples showed a detection range with linear correlation. Sample detection ranges for contaminants and their respective linear correlation indicators are shown in table 28.

Table 28 - Linear correlation data between the luminescence intensity of the synthesized hybrid materials and the adsorbed amounts of Cr³⁺, caffeine and estrogen.

Sample	Pollutant	Points	R ₂			R _{2c}		
			Operation range (mg/g)	R ²	a	Operation range (mg/g)	R ²	a
Eutta(KaoPro)	Cr ³⁺	7	0.075 – 0.140	0.344	48.131	0.075 – 0.14	0.459	171.552
	Cr ³⁺	3	0.160 – 0.201	0.466	-4.859	0.160 – 0.201	0.716	-14.808
Eutta(KaoPhe)	Caffeine	5	2.54x10 ⁻³ – 3.23x10 ⁻³	0.628	-387.258	2.41x10 ⁻³ – 3.23x10 ⁻³	0.788	-2194.793
	Estrogen	4	2.38x10 ⁻³ – 4.98x10 ⁻³	0.992	527.294	-	-	-
Eutta(KaoAPro)	Cr ³⁺	6	0.196 – 0.222	0.844	64.551	0.196 – 0.222	0.799	87.905
	Caffeine	5	3.07x10 ⁻³ – 3.33x10 ⁻³	0.946	-4928.297	3.07x10 ⁻³ – 3.33x10 ⁻³	0.883	-9680.616
	Estrogen	5	7.47x10 ⁻³ – 8.20x10 ⁻³	0.603	1054.967	-	-	-
Eutta(KaoAPhe)	Caffeine	3	2.84x10 ⁻³ – 3.00x10 ⁻³	0.995	12381.241	-	-	-
Eutta(R-LDHPro)	Cr ³⁺	3	0.025 – 0.062	0.928	-9.614	-	-	-
Eutta(LapPro)	Cr ³⁺	3	0.084 – 0.105	0.637	-9.026	0.084 – 0.105	0.929	-73.533
Eutta(SapPro)	Caffeine	4	1.48x10 ⁻³ – 1.82x10 ⁻³	0.716	-398.916	-	-	-
	Estrogen	3	3.36x10 ⁻³ – 3.44x10 ⁻³	0.707	-98.933	-	-	-
Eutta(SapPhe)	Cr ³⁺	5	0.239 – 0.241	0.774	-1122.712	0.239 – 0.241	0.732	-1408.546
	Caffeine	4	8.07x10 ⁻⁴ – 1.45x10 ⁻³	0.796	-654.958	-	-	-
	Estrogen	6	3.37x10 ⁻³ – 3.39x10 ⁻³	0.862	-1458.619	-	-	-

After obtaining the detection ranges for the contaminants through the kinetic study and determining which samples were applicable as a luminescent sensor, it is possible to assess the reliability of the sensor through the equilibrium study, using the most convergent isotherm with the experimental results and applying the Stern-Volmer equation (LIN et al., 2021; ZHAI et al., 2012).

The Stern-Volmer equation allows you to dynamically evaluate the luminescence suppression mechanism, applying the equation on the intensity of the material without the contaminant (I_0) on the concentration of the contaminant in the sample (I). The Stern-Volmer equation can be described by equation 26.

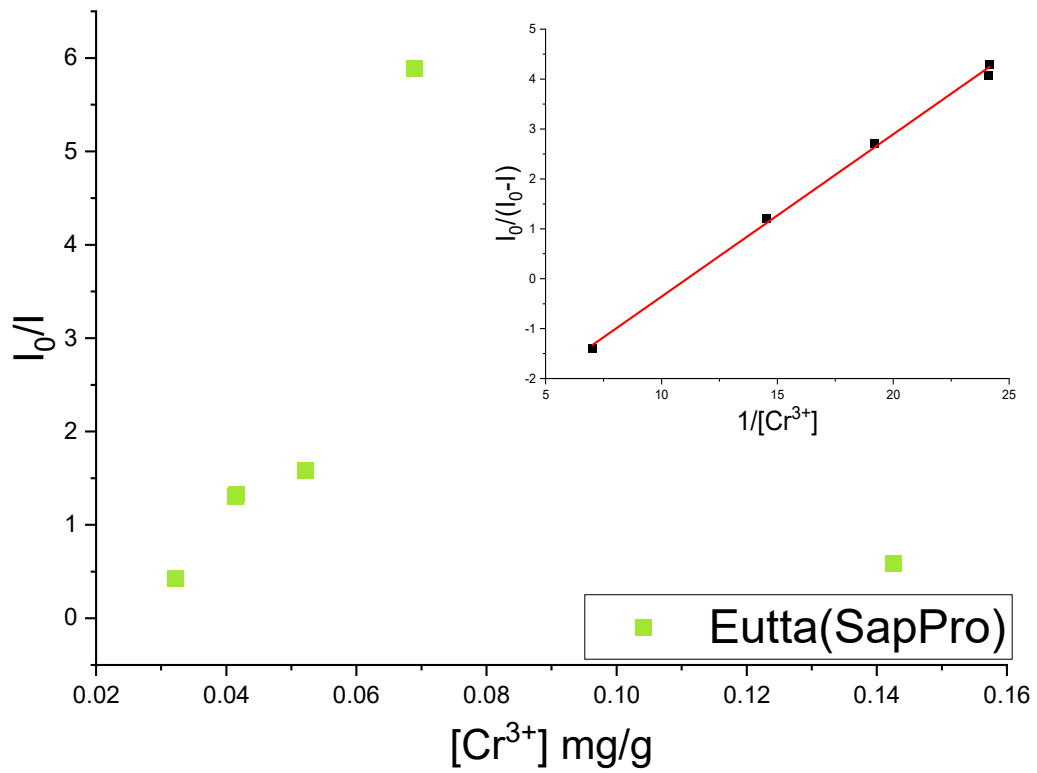
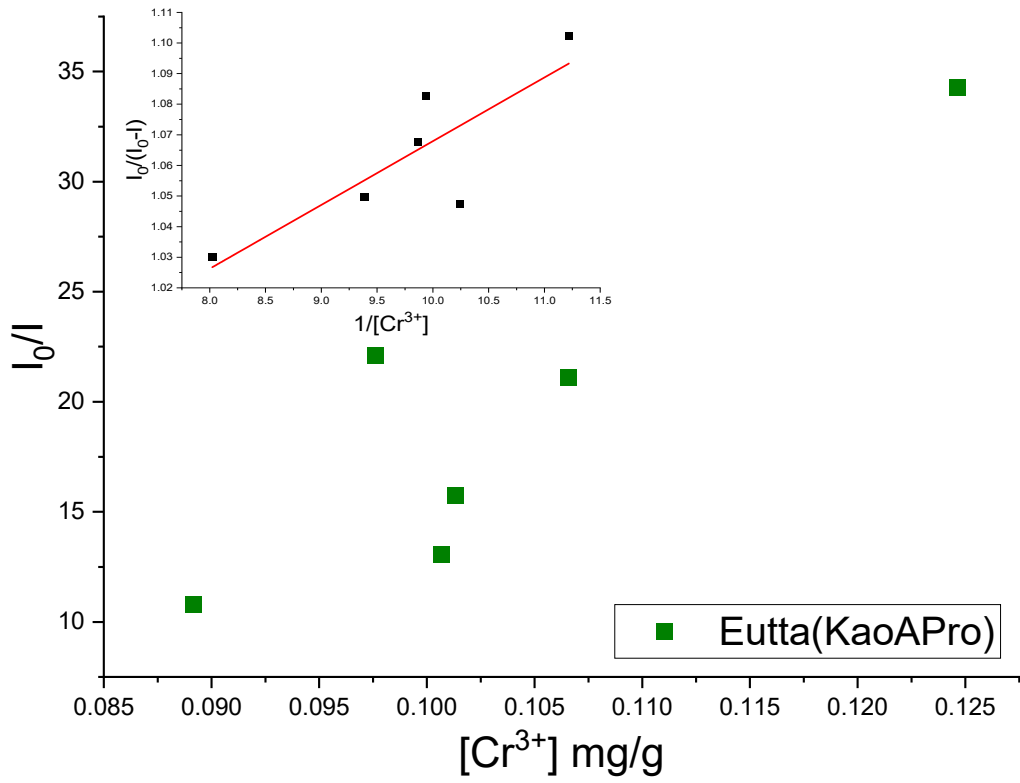
$$\frac{I_0}{I} = 1 + k_{SV}[A] \quad \text{Equation 26}$$

Where $[A]$ is the concentration of the contaminant in the sample and k_{SV} is the luminescence suppression constant and is unique for each material in contact with the specific contaminant, within a detection limit where a high linear correlation line can be obtained (AZAB; KHAIRY; KAMEL, 2015). When a non-linear plot is observed for the Stern-Volmer equation, it is likely that the different emission sites have three distinct characteristics being (i) the sites where suppression is evaluated by the Stern-Volmer constant (k_{SV}), (ii) the sites where the emission is not affected by the concentration of the contaminant (BARJA; ARAMENDÍA, 2008), (iii) and the sites where the presence of the contaminant increases the quantum yield of emission, opposing the suppression. In this case, it is necessary to perform linear regression of the Stern-Volmer equation to obtain the detection limits and the suppression constant, as shown in

equation 27 (AZAB; KHAIRY; KAMEL, 2015; BARJA et al., 2011; BARJA; ARAMENDÍA, 2008).

$$\frac{I_0}{\Delta I} = \frac{1}{f_a} + \frac{1}{f_a \cdot k_{SV}} \cdot \frac{1}{[A]} \quad \text{Equation 27}$$

Where ΔI is the variation of intensities (I_0 and I) of transition ${}^5D_0 \rightarrow {}^7F_2$ and f_a is the fraction of suppressor sites. The concentration of contaminants in the samples $[A]$ were obtained by the Freundlich isotherm where the values of q_e had a higher linear correlation with the experimental data. Among the samples that did not leach and showed good linear correlation with the Freundlich isotherm, only the materials Eutta(KaoAPro), Eutta(SapPro) and Eutta(SapPhe) presented detection limits obtained in a linear straight line for the contaminant Cr^{3+} . For caffeine, the materials where it was possible to obtain the detection limits by the Stern-Volmer equation were the samples Eutta(KaoPhe), Eutta(KaoAPro), Eutta(KaoAPhe) and Eutta(SapPro) and for estrogen, only the sample Eutta(SaoPhe) presented detection limit for the Stern-Volmer equation. Stern-Volmer luminescence suppression graphs for materials are shown in figures 62-64



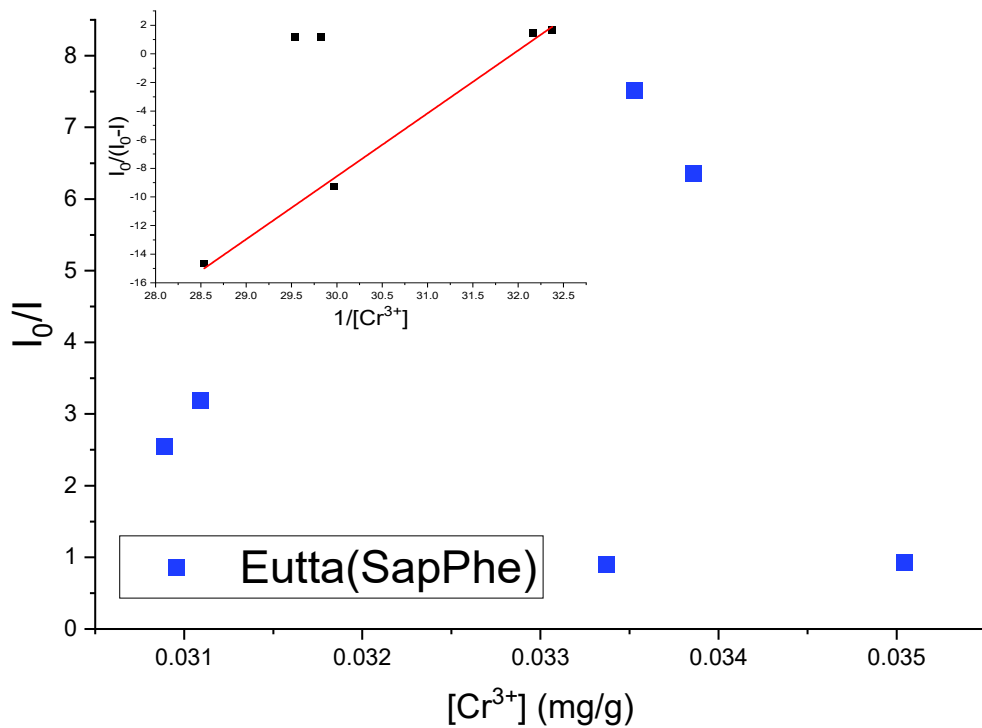
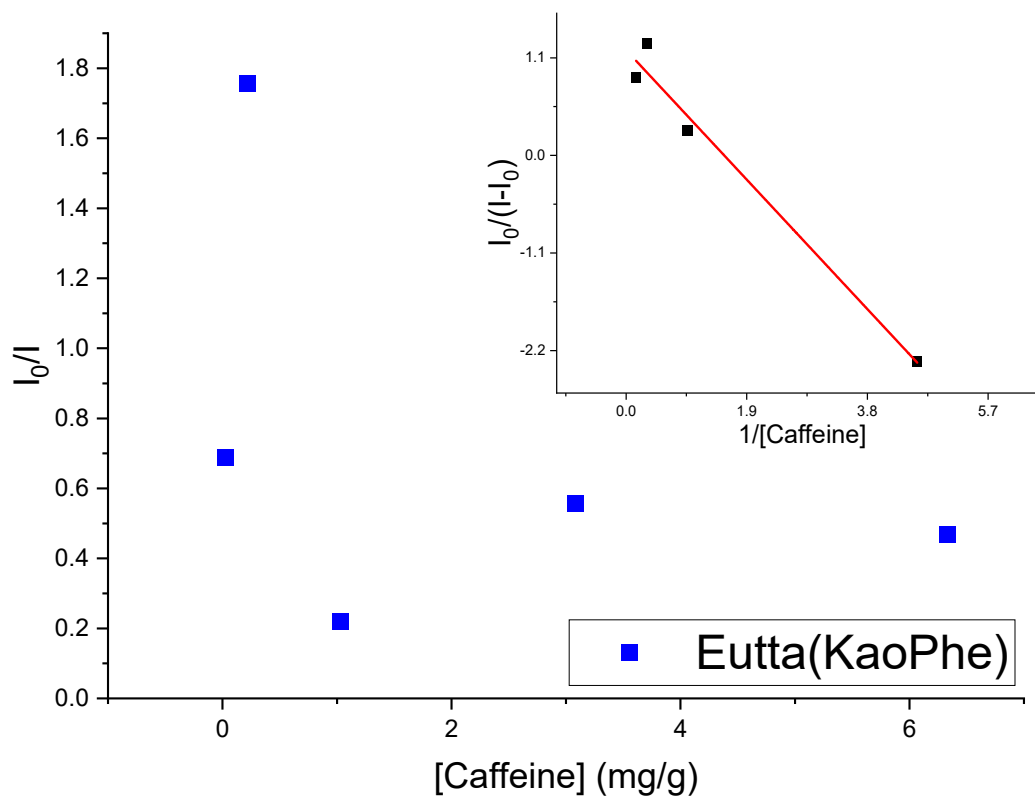
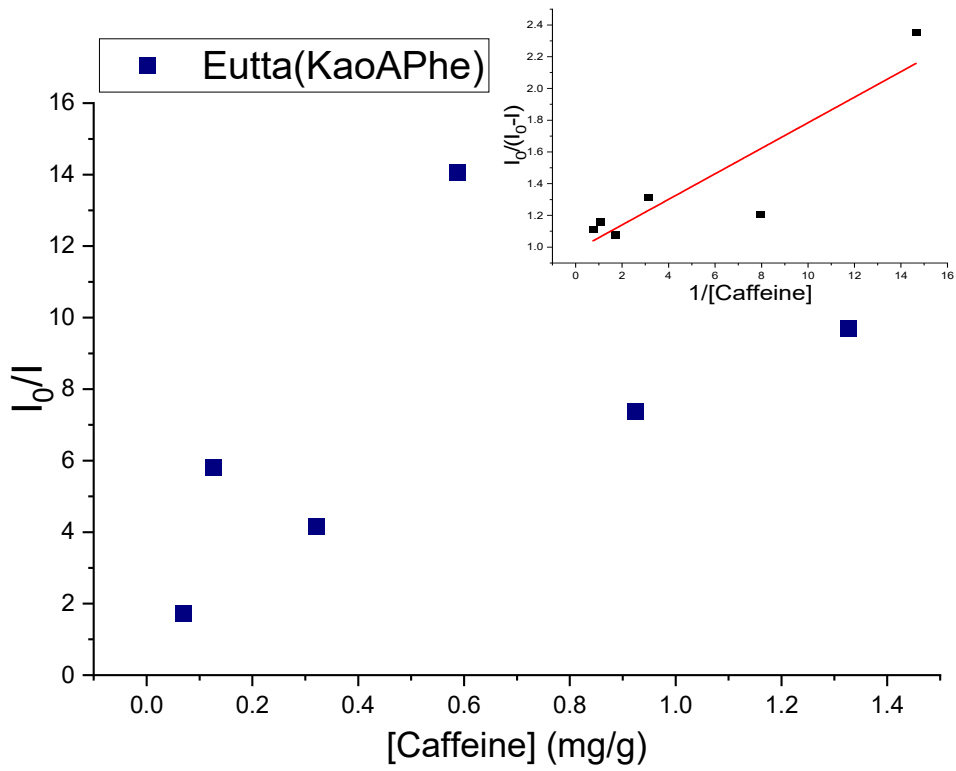
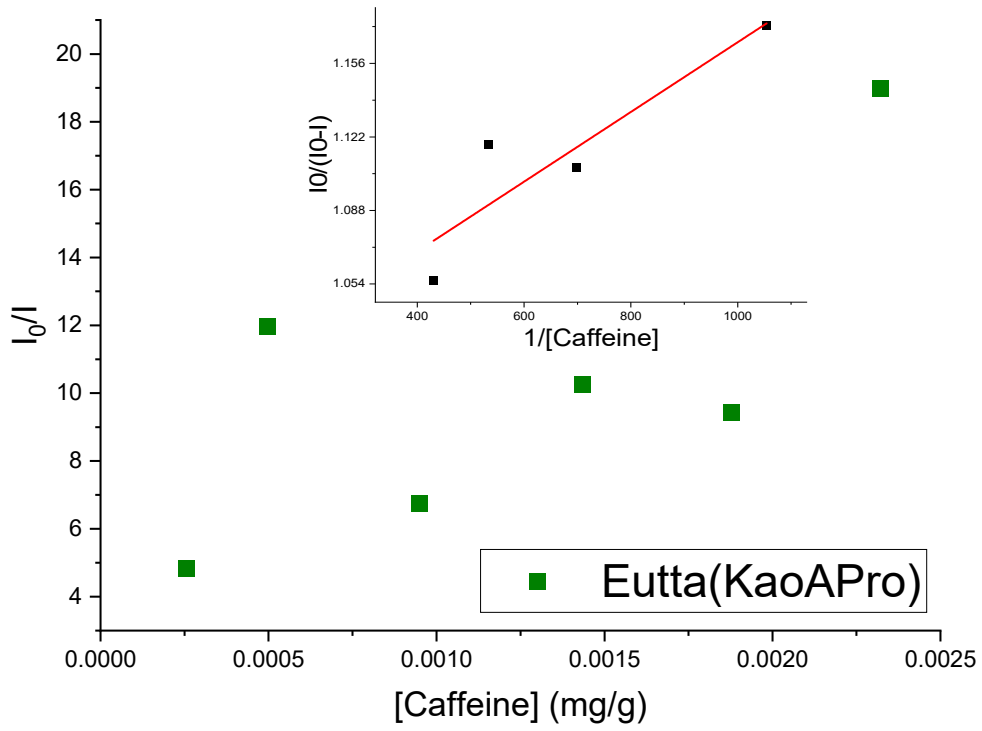


Figure 62 - Stern-Volmer plot and modified Stern-Volmer equation (inset) for the detection of Cr^{3+} for the samples where it was possible to draw a linear line for the detection limits.





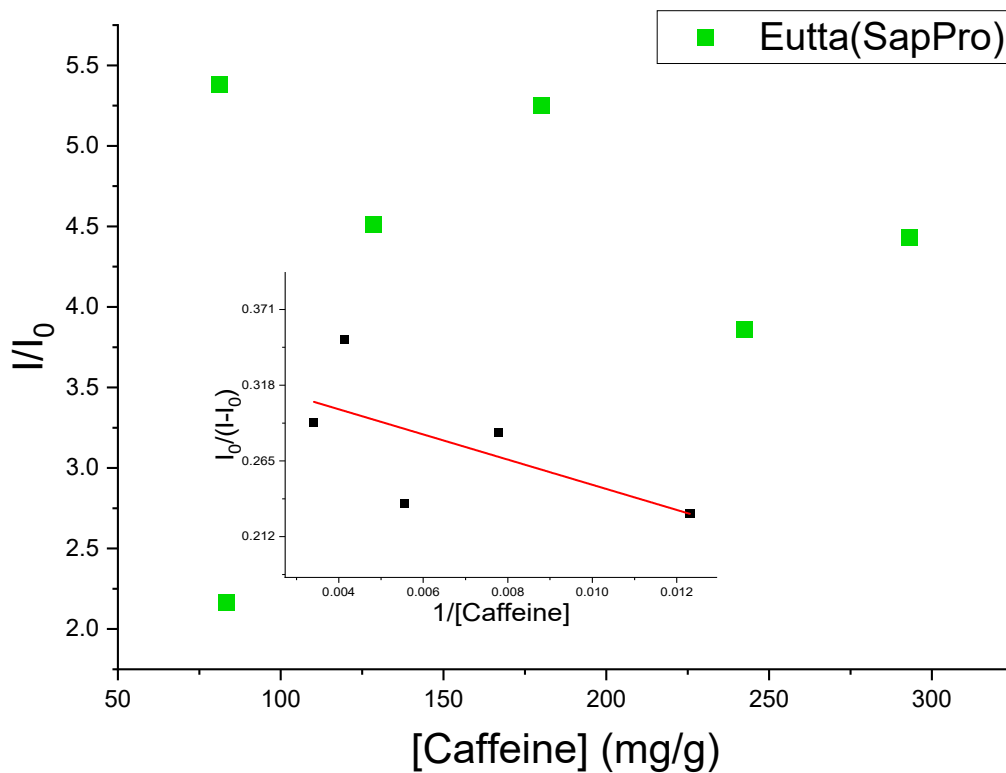


Figure 63 - Stern-Volmer plot and modified Stern-Volmer equation (inset) for the detection of caffeine for the samples where it was possible to draw a linear line for the detection limits.

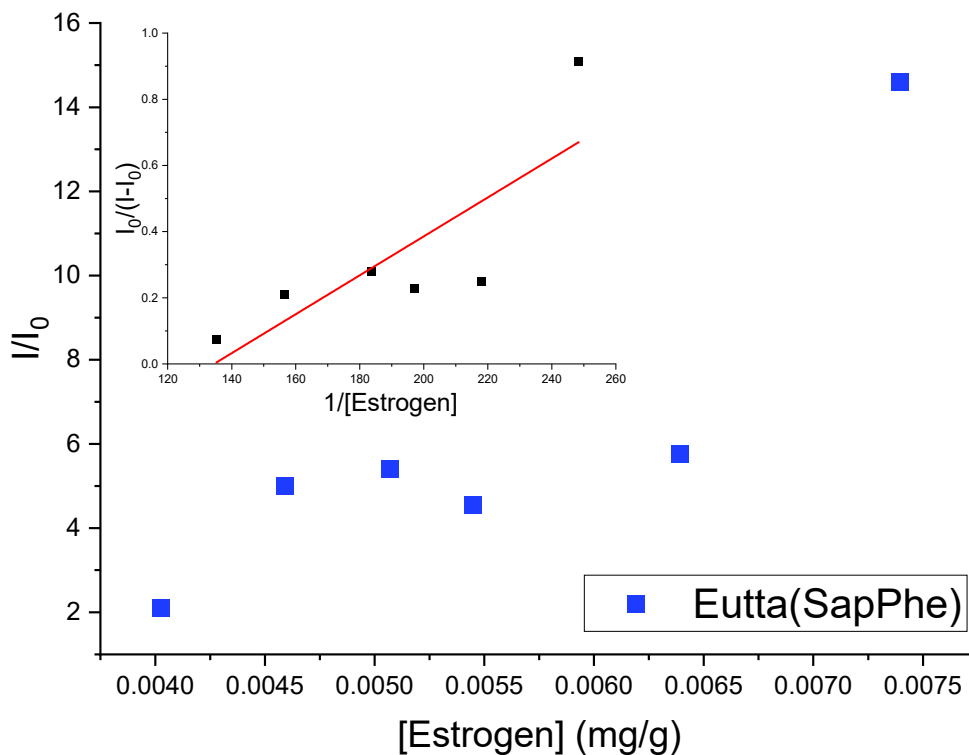


Figure 64 - Stern-Volmer plot and modified Stern-Volmer equation (inset) for estrogen detection for the Eutta(SapPhe) sample, where it was possible to draw a linear line for the detection limits.

The properties obtained by the Stern-Volmer graphs for the sensors are shown in table 29.

Table 29 - Properties of luminescent sensors obtained by the Stern-Volmer equation.

Sample	Pollutant	Operation range (mg/g)	f_a	k_{SV} (M^{-1})	R^2
Eutta(KaoPhe)	Caffeine	0.218 – 6.330	0.84	1.54	0.97
Eutta(KaoAPro)	Cr ³⁺	0.089 – 0.125	1.16	41.27	0.62
	Caffeine	9.48×10^{-4} – 2.32×10^{-3}	0.99	6.23×10^3	0.74
Eutta(KaoAPhe)	Caffeine	0.068 – 1.327	1.02	12.17	0.76
Eutta(SapPro)	Cr ³⁺	4.15×10^{-2} – 6.88×10^{-2}	0.28	11.10	0.99
	Caffeine	81.250 – 292.992	2.97	3.82×10^{-2}	0.21
Eutta(SapPhe)	Cr ³⁺	0.031 – 0.035	7.11×10^{-3}	31.94	0.99
	Estrogen	4.02×10^{-3} – 7.39×10^{-3}	1.26	134.46	0.58

The samples where it was possible to apply the Stern-Volmer equation showed higher detection limits, especially for the pollutant caffeine. The samples that showed better properties as a luminescent sensor of Cr³⁺ were the materials with saponite, both with 0.99 linear correlation. The amount of water molecules in the first coordination sphere and the ease of cation exchange in the saponite's interlamellar space facilitated the interaction between the contaminant and the sensors.

Interaction mechanism

The interaction mechanism in the complex and the contaminants can be diagrammed as shown in figure 65.

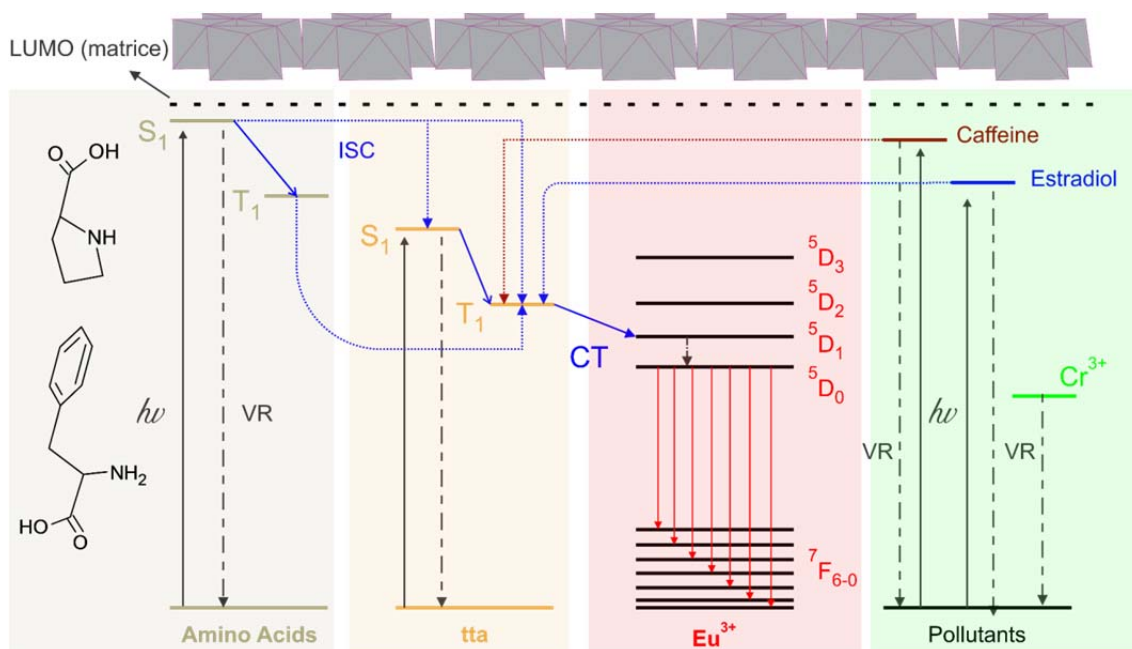


Figure 65 - Schematic representation of the energy diagram between ligands, contaminants and europium III ion.

Organic compounds such as amino acids, tta and the contaminants caffeine and estradiol absorb energy and move from the ground state to the singlet state (S_1) that decay by vibronic relaxation or transfer this energy to the triplet state (T_1). In amino acids, the energy contained in the triplet state can follow three possible routes: 1) return to ground state through vibronic relaxation (VT), 2) transfer this energy to europium III ion via charge transfer (CT), mainly for the state 5D_1 , that decays to the state 5D_0 and finally emits photons or returns to the ground state and 3) transfer this energy to the triplet state of tta, through the Intersystem crossing (ISC), due to its proximity to the 5D_1 excited state of the europium III ion, this third route being the most probable (ABBAS et al., 2019).

The same process occurs with organic contaminants, however at low concentrations, where the contaminants interact in the complex in the first coordination sphere. Due to the higher energy levels in relation to tta, it is

possible to increase the energy transfer between the systems, so the radiative emission increases instead of suffering quenching (GEORGES, 1993; GUO et al., 2021). Only when the concentration of the contaminant increases or when it interacts in the second coordination sphere, the vibronic relaxation of the organic groups of the contaminants is favored, resulting in quenching. In the case of Cr^{3+} , both transitions E_g and T_{2g} of the layer $3d^3$ have values below the transition from the excited state of the europium ion III, making the transfer of charge impossible, resulting only in the quenching of the emission (NISTORA; ANDREICI; AVRAM, 2009).

In some cases, as in the Eutta(LapPhe) sample, some energy levels in the matrix are close to the S_1 state of the amino acids, which can transfer absorbed energy, increasing the lifetime and radiative emission yield of the europium III ion.

Caffeine had better interactions as luminescent sensors applied by the Stern-Volmer equation among contaminants, especially with kaolinite samples. The covalent interactions between the complex and the matrix and the formation of well-structured complexes, with few water molecules in the first coordination sphere of the complexes and high optical properties, favored the quenching process, through the interaction between caffeine and organic part of the complex, preventing its interaction in the first sphere of coordination. Due to the low optical property of the Eutta(KaoPro) sample compared to other kaolinite samples, the quenching process was hampered for the application of the Stern-Volmer equation.

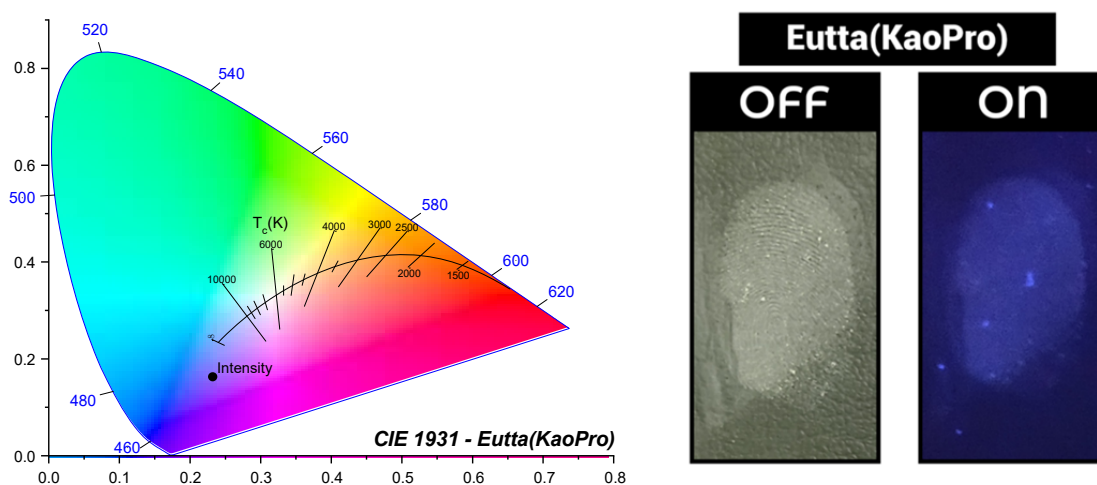
Despite the good applicability of saponite materials for the detection of Cr^{3+} , materials with kaolinite showed more promising results for the detection of contaminants, among all materials, considering the application of luminescent sensors using the ratio of intensities (R_2) and the equation by Stern-Volmer. This is due to the interaction strength between the complex and the matrix and the optical properties that favor the quenching of contaminants, especially for materials obtained by the APTES alkoxide modification route by amidation reaction, catalyzed by boric acid. As for the detection of estrogen, the hydrophobic characteristic of the contaminant under the conditions tested made it difficult to interact with the sensors, and the property of easy expansion of the basal space of smectites and hydrotalcite facilitated the leaching of complexes in contact with the contaminants. A decisive factor that places Eu^{3+} complexes functionalized in kaolinite as the most promising for application in luminescent sensors of contaminants in effluents in the form of solid powder materials, as they were applied.

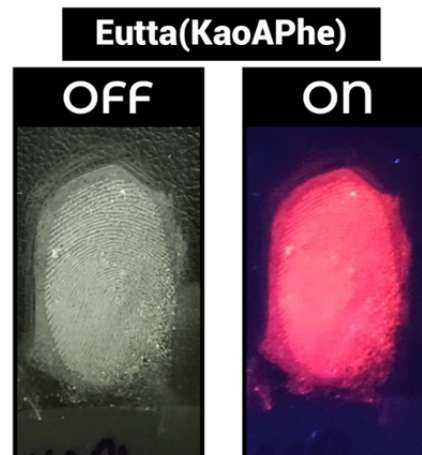
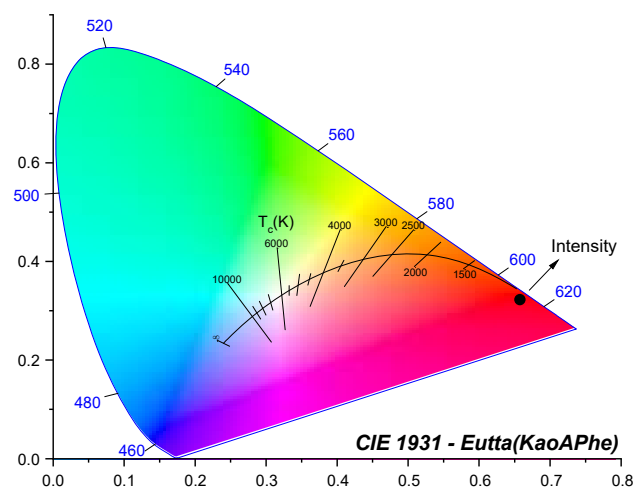
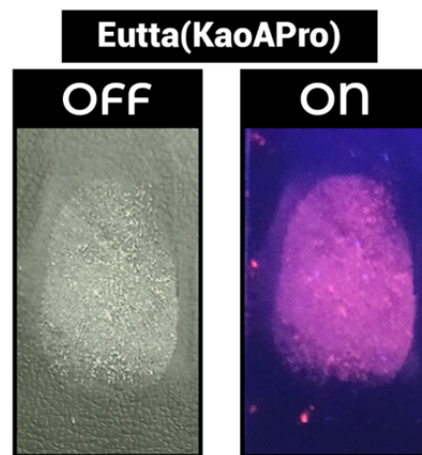
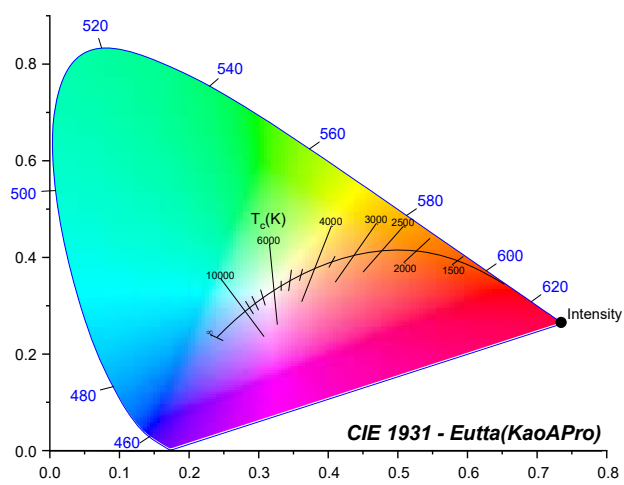
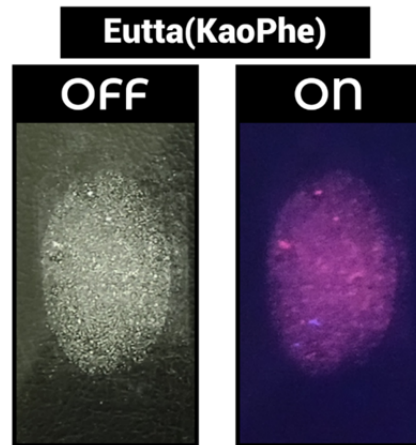
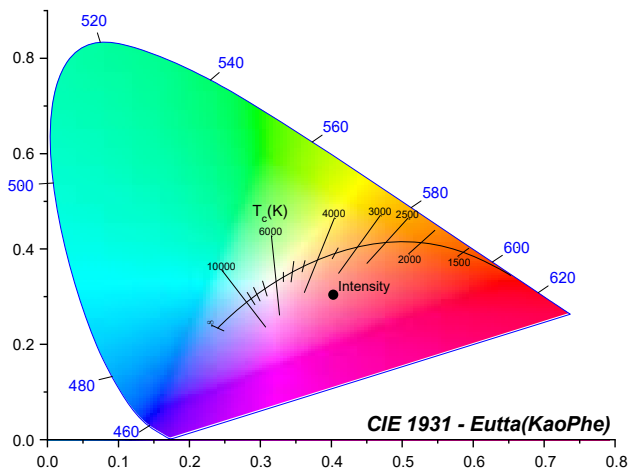
4.3.3. Application in enhanced latent fingerprint detection

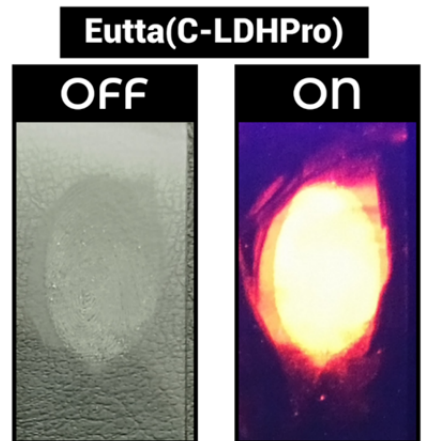
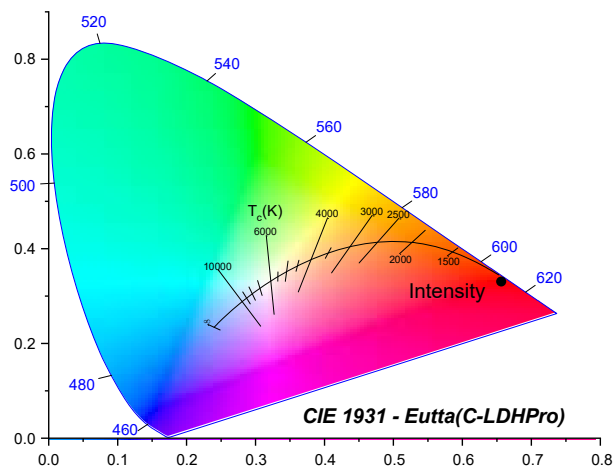
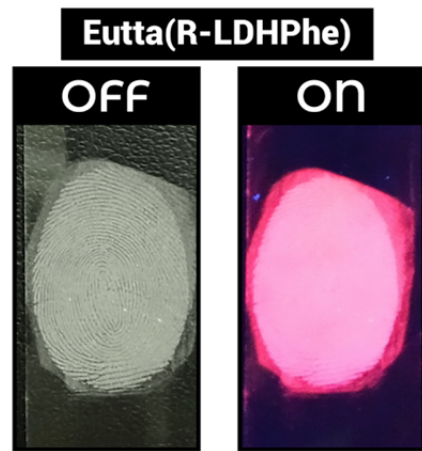
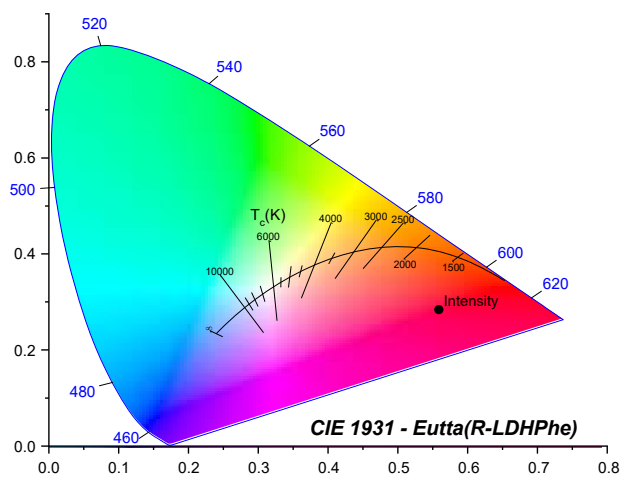
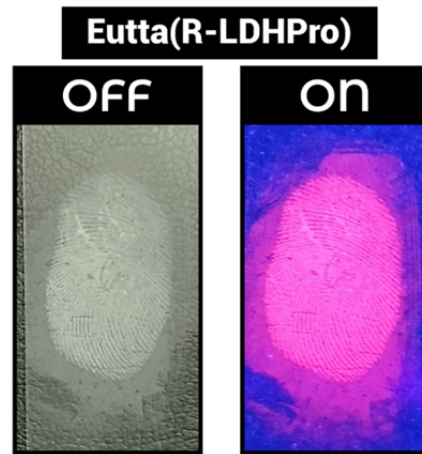
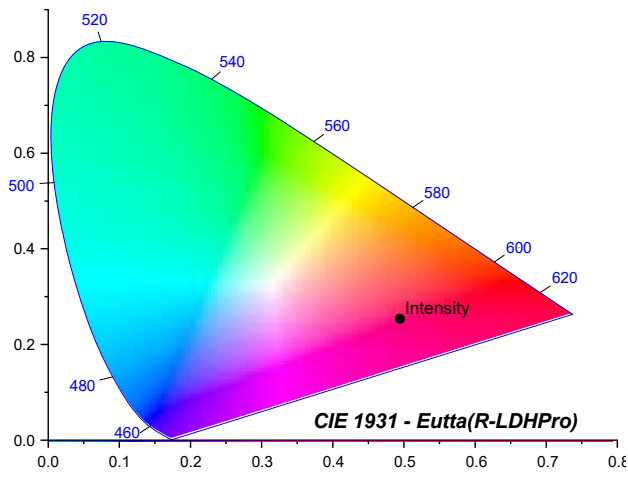
When touching an object with your hands, a fingerprint is left on the surface, composed of water-soluble components such as amino acids, amines, monosaccharides, urea, lactic acid, among others (BINNEMANS, 2005). These prints are essential in crime identification and forensic research, however, they are hardly visible and easily damaged. Therefore, the development of a material that does not damage and make visible is vital for fingerprint identification. In this case, the optical materials in this work have an emission characteristic based on downshifted, where the emission occurs in the visible region and the

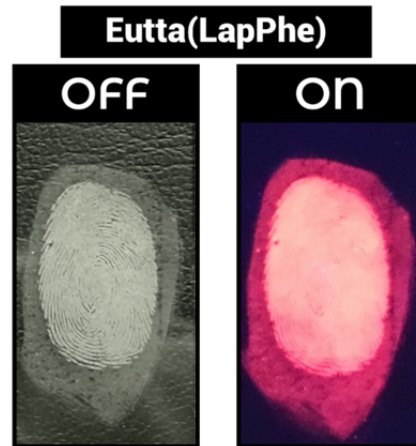
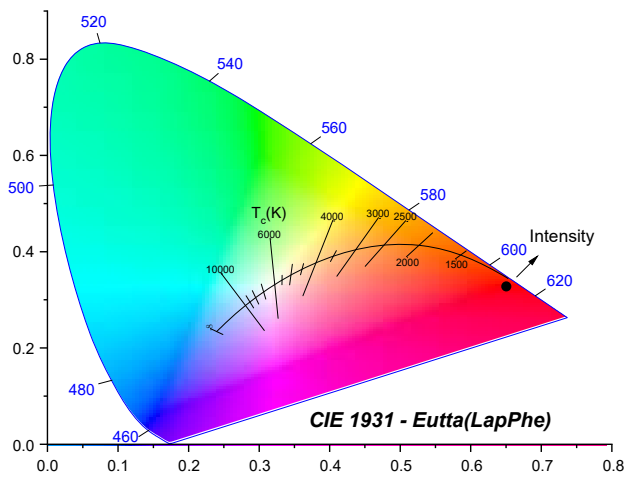
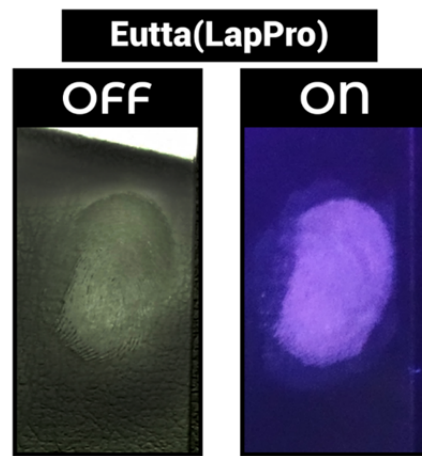
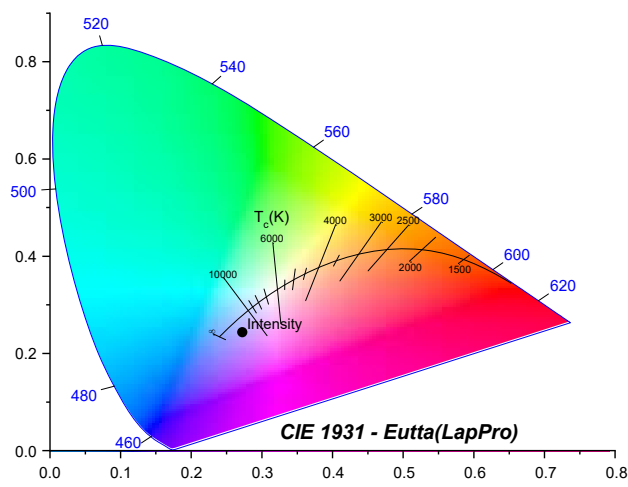
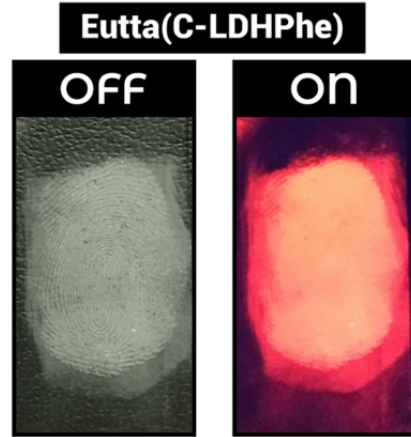
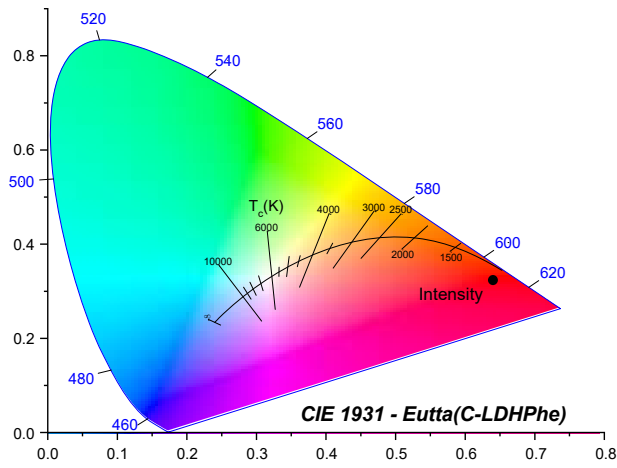
excitation is easily achieved with a lamp in the Ultraviolet region (BÜNZLI, 2016).

Eu^{3+} organocomplexes immobilized in clay minerals are promising materials for application in fingerprint detection, due to their optical characteristics and dispersion in the matrix, which results in a lower concentration of the lanthanide ion, maintaining and even improving its optical properties. The materials synthesized in this work showed a characteristic of clear and fine powder, not aggressive to the environment and of low toxicity, being easily handled and applied in-situ. The samples showed a red color in the presence of ultraviolet light (Em : 360 nm) as shown in the chromaticity diagrams, shown in figure 66.









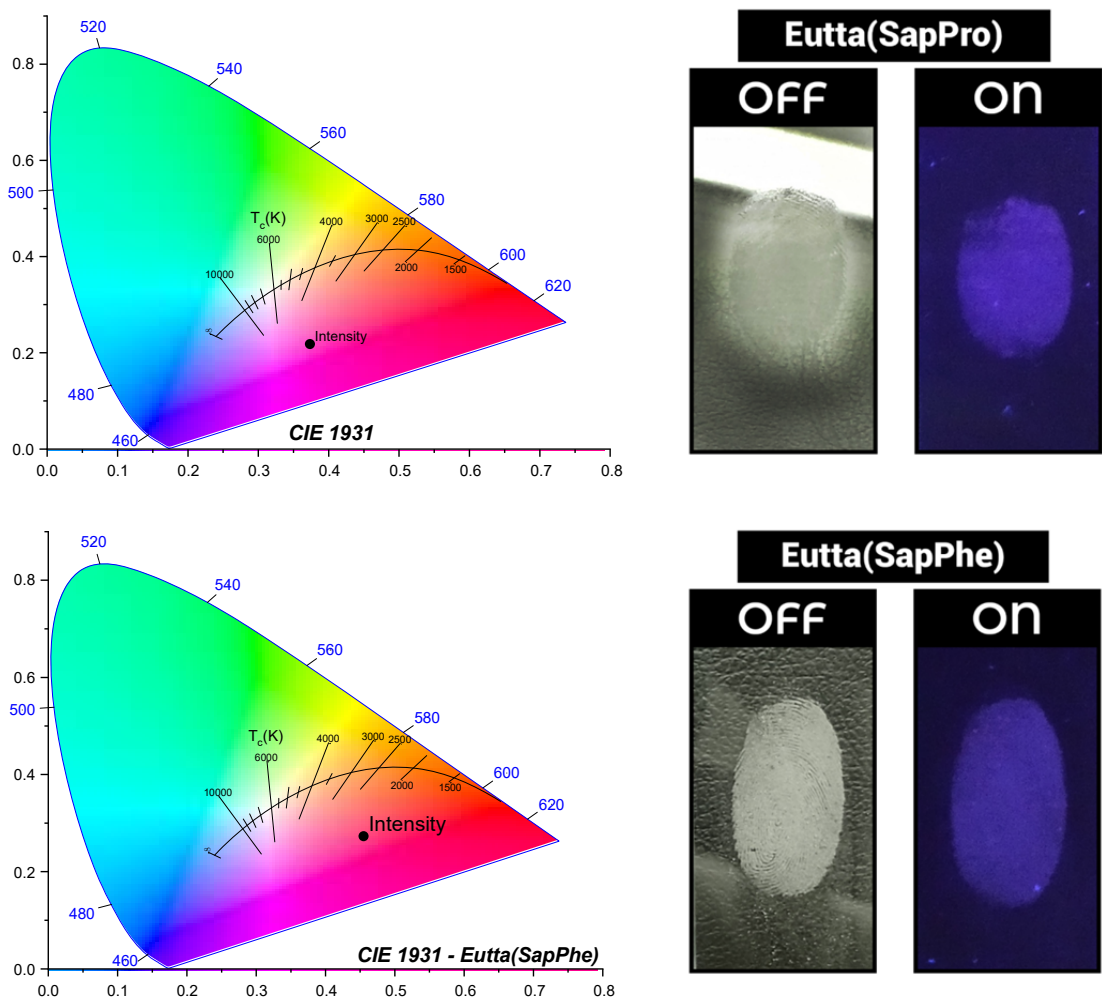


Figure 66 - CIE chromaticity coordinates of samples complexed with Eu^{3+} ion and images before and after the incidence of ultraviolet light (360 nm) on the samples.

The samples Eutta(KaoPro), Eutta(LapPro), Eutta(SapPro) and Eutta(SapPhe), did not show high intensity visible luminescence in the red. On the other hand, Eutta(KaoAPro), Eutta(KaoAPhe), Eutta(LapPhe), Eutta(C-LDHPPro) and Eutta(C-LDHHe) samples showed intense emission in the red region, being the most suitable for detecting prints digital, as it can generate a good light response with a small amount of sample and covering a larger area.

Conclusions

The luminescent complexes were efficiently immobilized in clay minerals. For kaolinite, the conventional functionalization synthesis resulted in amino acids intercalated within the interlamellar space while in the APTES alkoxide modification route by amidation reaction the amino acids interact with kaolinite through the sides of the coverslips. These materials also showed greater dispersion in the matrix, which favored the complexation with Eu^{3+} ion, offering greater mobility in the complexation process, resulting in higher chelation complexes and fewer amounts of water molecules in the first coordination sphere, which increased the internal quantum yield for radiative emission. The samples with phenylalanine had better optical properties compared to those with proline.

After a kinetic and equilibrium study with the contaminants, the samples with kaolinite leached the least, due to the strength of interaction between the complex and the matrix. Cr^{3+} interacts with the complex through the second coordination sphere, however, in the samples obtained by the catalytic route they presented higher quenching, due to the complex interaction occurring on the sides of the lamellae facilitating the access of the contaminant and consequently increasing the suppression of luminescence. With the exception of the Eutta(KaoPro) sample, the samples showed efficacy for caffeine detection while the Eutta(KaoAPro) sample showed detection efficiency for Cr^{3+} .

The samples obtained with LAPONITE® and hydrotalcite showed high leaching of the material in contact with contaminants and low efficiency as a luminescent sensor for contaminants applied as solid powder material. On the

other hand, among all samples, they were the ones that presented the best optical radiative emission properties, with the highest internal quantum yields (>30% for the samples with LDH and 52% for the Eutta(LapPhe) sample, and longer times of emission life, showing the compatibility of the amino acid complex with these clay matrices to increase luminescent properties. The complexes interact in the interlamellar space with the contaminants and three types of interaction between these materials and the contaminants were observed: (i) the contaminants interact directly with the matrix; (ii) interact in the first coordination sphere, resulting in increased emission intensity for organic contaminants and (iii) interacting in the second coordination sphere. Finally, samples with saponite had low optical properties, however, greater compatibility as a luminescent sensor for the contaminants tested, with high linear correlations and large detection range, evaluating both kinetics and equilibrium.

References

ABBAS, Z. et al. Luminescent europium(III) and terbium(III) complexes of β -diketonate and substituted terpyridine ligands: synthesis, crystal structures and elucidation of energy transfer pathways. **New Journal of Chemistry**, v. 43, n. 38, p. 15139–15152, 2019.

AISAWA, S. et al. Direct Intercalation of Amino Acids into Layered Double Hydroxides by Coprecipitation. **Journal of Solid State Chemistry**, v. 162, n. 1, p. 52–62, nov. 2001.

AJENIFUJA, E.; AJAO, J. A.; AJAYI, E. O. B. Equilibrium adsorption isotherm studies of Cu (II) and Co (II) in high concentration aqueous solutions on Ag-TiO₂-modified kaolinite ceramic adsorbents. **Applied Water Science**, v. 7, n. 5, p. 2279–2286, 2017.

ALABA, P. A. et al. Kaolinite properties and advances for solid acid and basic catalyst synthesis. **RSC Advances**, v. 5, p. 101127–101147, 2015.

ALMEIDA NETO, A. F. DE; VIEIRA, M. G. A.; SILVA, M. G. C. DA. Cu(II) adsorption on modified bentonitic clays: different isotherm behaviors in static and dynamic systems. **Materials Research**, v. 15, n. 1, p. 114–124, 2012.

ARAKAWA, E. T. et al. Measurement of optical properties of small particles. **Scientific Conference on Obscuration and Aerosol Research**, v. Aberdeen Proving Ground, Jun, p. 23–26, 1997.

ASLAN, E. Co-catalyst-free photocatalytic hydrogen evolution by Laponite D clay. **Journal of Photochemistry and Photobiology A: Chemistry**, v. 390, n. December 2019, p. 112335, mar. 2020.

AVILA, L. R. et al. New synthesis strategies for effective functionalization of kaolinite and saponite with silylating agents. **Journal of Colloid and Interface Science**, v. 341, n. 1, p. 186–193, jan. 2010.

AZAB, H. A.; KHAIRY, G. M.; KAMEL, R. M. Time-resolved fluorescence sensing of pesticides chlorpyrifos, crotoxyphos and endosulfan by the luminescent Eu(III)-8-allyl-3-carboxycoumarin probe. **Spectrochimica Acta - Part A: Molecular and Biomolecular Spectroscopy**, v. 148, p. 114–124, 2015.

BALA, M. et al. Synthesis and photoluminescence properties of europium(III) complexes sensitized with β -diketonato and N, N-donors ancillary ligands. **Spectrochimica Acta Part A: Molecular and Biomolecular Spectroscopy**, v. 196, p. 67–75, maio 2018.

BARJA, B. C. et al. Luminescent Eu(III) hybrid sensors for in situ copper

detection. **Sensors and Actuators, B: Chemical**, v. 158, n. 1, p. 214–222, 2011.

BARJA, B. C.; ARAMENDÍA, P. F. Luminescent Eu(III) hybrid materials for sensor applications. **Photochemical & photobiological sciences**, v. 7, n. 11, p. 1391–1399, 2008.

BELTRAME, K. K. et al. Adsorption of caffeine on mesoporous activated carbon fibers prepared from pineapple plant leaves. **Ecotoxicology and Environmental Safety**, v. 147, n. April 2017, p. 64–71, 2018.

BERNAL, C. et al. Influência de alguns parâmetros experimentais nos resultados de análises calorimétricas diferenciais - DSC. **Química Nova**, v. 25, n. 5, p. 849–855, 2002.

BINNEMANS, K. Rare-earth beta-diketonates. **Handbook on the Physics and Chemistry of Rare Earths**, v. 35, n. 05, p. 107–272, 2005.

BINNEMANS, K. Interpretation of europium(III) spectra. **Coordination Chemistry Reviews**, v. 295, p. 1–45, jul. 2015.

BORAH, M. M.; DEVI, T. G. The vibrational spectroscopic studies and molecular property analysis of L-Phenylalanine using quantum chemical method. **Journal of Molecular Structure**, v. 1136, p. 182–195, maio 2017.

BOSSHARD, G. Z. et al. Photophysical properties of asymmetric and water-soluble dinuclear lanthanide complexes of poly glycol chain functionalized-benzoic acid derivative: Experimental and theoretical approaches. **RSC Advances**, v. 6, n. 103, p. 101133–101141, 2016.

BÜNZLI, J.-C. G. On the design of highly luminescent lanthanide complexes. **Coordination Chemistry Reviews**, v. 293–294, p. 19–47, 2015.

BÜNZLI, J.-C. G. Lanthanide Luminescence: From a Mystery to Rationalization, Understanding, and Applications. In: JEAN-CLAUDE G. BÜNZLI; VITALIJ K. PECHARSKY (Eds.). **Handbook on the Physics and Chemistry of Rare Earths**. [s.l.] Elsevier Ltd, 2016. v. 50p. 141–176.

CAETANO, E. W. S. et al. Anhydrous proline crystals: Structural optimization, optoelectronic properties, effective masses and Frenkel exciton energy. **Journal of Physics and Chemistry of Solids**, v. 121, n. October 2017, p. 36–48, out. 2018.

CAMACHO CÓRDOVA, D. I. et al. Immobilization of laccase on hybrid layered double hydroxide. **Química Nova**, v. 32, n. 6, p. 1495–1499, 2009.

CAVANI, F.; TRIFIRÒ, F.; VACCARI, A. Hydrotalcite-type anionic clays: Preparation, properties and applications. **Catalysis Today**, v. 11, n. 2, p. 173–301, dez. 1991.

CHAN, W.-L. et al. The reported anomalous emission intensity of the $^5D_0 \rightarrow ^7F_4$ transition of Eu^{3+} in a molybdate double perovskite. **Journal of Materials Chemistry C**, v. 3, n. 5, p. 960–963, 2015.

CHOI, G. et al. Intercalative Ion-Exchange Route to Amino Acid Layered Double Hydroxide Nanohybrids and Their Sorption Properties. **European Journal of Inorganic Chemistry**, v. 2015, n. 6, p. 925–930, fev. 2015.

CHU, N. et al. Intercalation of organic sensitizers into layered europium hydroxide and enhanced luminescence property. **Dalton Transactions**, v. 41, n. 24, p. 7409, 2012.

ĆIRIĆ, A. et al. JOES: An application software for Judd-Ofelt analysis from Eu^{3+} emission spectra. **Journal of Luminescence**, v. 205, n. September 2018, p. 351–356, jan. 2019.

DA SILVA, A. C. et al. Influence of physical/chemical treatments to delamination of nanohybrid kaolinite-dipicolinate. **Applied Clay Science**, v. 126, p. 251–258, 2016.

DA SILVA, T. H. et al. Immobilization of metallophthalocyanines on hybrid materials and in-situ synthesis of pseudo-tubular structures from an aminofunctionalized kaolinite. **Dyes and Pigments**, v. 100, n. 1, p. 17–23, 2014.

ĐAČANIN, L. et al. Judd-Ofelt analysis of luminescence emission from $\text{Zn}_2\text{SiO}_4:\text{Eu}^{3+}$ nanoparticles obtained by a polymer-assisted sol-gel method. **Physica B: Condensed Matter**, v. 406, n. 11, p. 2319–2322, maio 2011.

DAS, S. S. et al. Laponite-based Nanomaterials for Biomedical Applications: A Review. **Current Pharmaceutical Design**, v. 25, n. 4, p. 424–443, 3 jun. 2019.

DE ARAÚJO, D. T. et al. Eu^{3+} - and Tb^{3+} -Dipicolinate Complexes Covalently Grafted into Kaolinite as Luminescence-Functionalized Clay Hybrid Materials. **The Journal of Physical Chemistry C**, v. 121, n. 9, p. 5081–5088, 9 mar. 2017.

DE ARAÚJO, D. T. et al. Luminescent properties of biohybrid (kaolinite-proline) materials synthesized by a new boric acid catalyzed route and complexed to Eu^{3+} . **Applied Clay Science**, v. 192, n. April, p. 105634, jul. 2020.

DE FARIA, E. H. et al. Hybrid materials prepared by interlayer functionalization of kaolinite with pyridine-carboxylic acids. **Journal of Colloid and Interface Science**, v. 335, n. 2, p. 210–215, jul. 2009.

DE FARIA, E. H. et al. Novel reactive amino-compound:

Tris(hydroxymethyl)aminomethane covalently grafted on kaolinite. **Applied Clay Science**, v. 48, n. 3, p. 516–521, abr. 2010.

DE FARIA, E. H. et al. Green and selective oxidation reactions catalyzed by kaolinite covalently grafted with Fe(III) pyridine-carboxylate complexes. **Catalysis Today**, v. 187, n. 1, p. 135–149, jun. 2012.

DE SÁ, G. et al. Spectroscopic properties and design of highly luminescent lanthanide coordination complexes. **Coordination Chemistry Reviews**, v. 196, n. 1, p. 165–195, jan. 2000.

DEDAVID, B. A.; GOMES, C. I.; MACHADO, G. **Microscopia eletrônica de varredura - Aplicações e preparação de amostras: materiais poliméricos, metálicos e semicondutores [recurso eletrônico]**. CEMM-Cen ed. Porto Alegre: EDIPUCRS, 2007.

DEDZO, G. K.; DETELLIER, C. Functional nanohybrid materials derived from kaolinite. **Applied Clay Science**, v. 130, p. 33–39, set. 2016.

DIAB, H. et al. Impact of Reabsorption on the Emission Spectra and Recombination Dynamics of Hybrid Perovskite Single Crystals. **Journal of Physical Chemistry Letters**, v. 8, n. 13, p. 2977–2983, 6 jul. 2017.

DRITS, V. A. et al. Determination of the phase composition of partially dehydroxylated kaolinites by modelling their X-ray diffraction patterns. **Clay Minerals**, v. 54, n. 3, p. 309–322, 1 set. 2019.

FARAT, O. K. et al. Europium complex of 2,2'-bipyridine-6,6'-dicarboxylic acid bis[di(phosphonomethyl)amide] as a new efficient water-soluble luminescent dye. **Mendeleev Communications**, v. 29, n. 3, p. 282–284, 2019.

FROST, R. L. The Dehydroxylation of the Kaolinite Clay Minerals using Infrared Emission Spectroscopy. **Clays and Clay Minerals**, v. 44, n. 5, p. 635–651, 1996.

FROST, R. L. et al. Molecular Structure of Dimethyl Sulfoxide in DMSO-Intercalated Kaolinites at 298 and 77 K. **The Journal of Physical Chemistry A**, v. 103, n. 48, p. 9654–9660, 1999.

GAO, X. et al. Synthesis, characterization and optical properties of a red organic–inorganic phosphor based on terephthalate intercalated Zn/Al/Eu layered double hydroxide. **Journal of Alloys and Compounds**, v. 585, p. 703–707, fev. 2014.

GEORGES, J. Lanthanide-sensitized luminescence and applications to the determination of organic analytes. A review. **The Analyst**, v. 118, n. 12, p. 1481, 1993.

GHADIRI, M. et al. Layered silicate clay functionalized with amino acids:

wound healing application. **RSC Advances**, v. 4, n. 67, p. 35332–35343, 2014.

GUIMARÃES, A. DE M. F.; CIMINELLI, V. S. T.; VASCONCELOS, W. L. Surface modification of synthetic clay aimed at biomolecule adsorption: synthesis and characterization. **Materials Research**, v. 10, n. 1, p. 37–41, mar. 2007.

GUO, Y. et al. Lanthanide Metal–Organic Frameworks for Instant Detection of 17 β -Estradiol, a Vital Physiological Index. **Small Structures**, v. 2100113, p. 2100113, 4 out. 2021.

HAGAN, A. K.; ZUCHNER, T. Lanthanide-based time-resolved luminescence immunoassays. **Analytical and Bioanalytical Chemistry**, v. 400, n. 9, p. 2847–2864, 2011.

HELLER, A. et al. Complexation of Europium(III) with the Zwitterionic Form of Amino Acids Studied with Ultraviolet–Visible and Time-Resolved Laser-Induced Fluorescence Spectroscopy. **Applied Spectroscopy**, v. 64, n. 8, p. 930–935, 1 ago. 2010.

HERALDY, E.; NUGRAHANINGTYAS, K. D.; HERIYANTO. X-ray Diffraction Analysis on Post Treatment of Ca-Mg-Al-Layered Double Hydroxide Slurry. **IOP Conference Series: Materials Science and Engineering**, v. 176, n. 1, p. 012020, fev. 2017.

HO, Y. S.; OFOMAJA, A. E. Pseudo-second-order model for lead ion sorption from aqueous solutions onto palm kernel fiber. **Journal of Hazardous Materials**, v. 129, n. 1–3, p. 137–142, 2006.

HOXHA, A. et al. Novel fluoride rechargeable dental composites containing MgAl and CaAl layered double hydroxide (LDH). **Dental Materials**, v. 36, n. 8, p. 973–986, ago. 2020.

INKSON, B. J. Scanning electron microscopy (SEM) and transmission electron microscopy (TEM) for materials characterization. In: **Materials Characterization Using Nondestructive Evaluation (NDE) Methods**. [s.l.] Elsevier, 2016. p. 17–43.

ISHII, A.; HASEGAWA, M. An Interfacial Europium Complex on SiO₂ Nanoparticles: Reduction-Induced Blue Emission System. **Scientific Reports**, v. 5, n. 1, p. 11714, 30 dez. 2015.

JACOBS, A. D. et al. Cooperative Formation of Icosahedral Proline Clusters from Dimers. **Journal of the American Society for Mass Spectrometry**, v. 29, n. 1, p. 95–102, 2018.

KACZOR, A. et al. Importance of Entropy in the Conformational Equilibrium of Phenylalanine: A Matrix-Isolation Infrared Spectroscopy and

Density Functional Theory Study. **The Journal of Physical Chemistry A**, v. 110, n. 7, p. 2360–2370, 1 fev. 2006.

KAMEDA, J.; YAMAGISHI, A.; KOGURE, T. Morphological characteristics of ordered kaolinite: Investigation using electron back-scattered diffraction. **American Mineralogist**, v. 90, n. 8–9, p. 1462–1465, 2005.

KANEZAKI, E. Effect of Temperature on the Layered Structure of Hydrotalcite-like Mg and Al Layered Double Hydroxides by Means of in situ High Temperature Powder X-ray Diffraction. **Hyomen Kagaku**, v. 19, n. 5, p. 288–293, 1998.

KREMLEVA, A.; KRÜGER, S.; RÖSCH, N. Uranyl adsorption at (010) edge surfaces of kaolinite: A density functional study. **Geochimica et Cosmochimica Acta**, v. 75, n. 3, p. 706–718, 2011.

LAGERGREN. Zur Theorie der sogenannten Adsorption gelöster Stoffe. **Zeitschrift für Chemie und Industrie der Kolloide**, v. 2, n. 1, p. 15–15, jul. 1907.

LI, H.-Q. et al. Electrochemical and FTIR studies of L-phenylalanine adsorption at the Au(111) electrode. **Journal of Electroanalytical Chemistry**, v. 500, n. 1–2, p. 299–310, mar. 2001.

LI, X. et al. Mechanism of kaolinite sheets curling via the intercalation and delamination process. **Journal of Colloid and Interface Science**, v. 444, p. 74–80, abr. 2015.

LIN, C.-H. et al. Synthesis and optical properties of Mg-Al layered double hydroxides precursor powders. **AIP Advances**, v. 7, n. 12, p. 125005, dez. 2017.

LIN, J. et al. Europium (III) Organic Complexes in Porous Boron Nitride Microfibers: Efficient Hybrid Luminescent Material. **Scientific Reports**, v. 6, n. 1, p. 34576, 30 out. 2016.

LIN, Z.-G. et al. The construction of a novel luminescent lanthanide framework for the selective sensing of Cu²⁺ and 4-nitrophenol in water. **Dalton Transactions**, v. 50, n. 5, p. 1874–1886, 2021.

MA, X.; ZHENG, J.; PANG, H. Intercalation of Mg-Al layered double hydroxides by L-proline: Synthesis and characterization. **Research on Chemical Intermediates**, v. 38, n. 2, p. 629–638, 2012.

MAHALAKSHMI, R.; JESURAJA, S. X.; DAS, S. J. Growth and characterization of L-phenylalanine. **Crystal Research and Technology**, v. 41, n. 8, p. 780–783, ago. 2006.

MALIK, P. K. Dye removal from wastewater using activated carbon

developed from sawdust: Adsorption equilibrium and kinetics. **Journal of Hazardous Materials**, v. 113, n. 1–3, p. 81–88, 2004.

MARCHESI, S. et al. Bifunctional Paramagnetic and Luminescent Clays Obtained by Incorporation of Gd^{3+} and Eu^{3+} Ions in the Saponite Framework. **Inorganic Chemistry**, v. 60, n. 14, p. 10749–10756, 19 jul. 2021.

MATOS, M. et al. Efeito da concentração dos íons Eu^{3+} e Bi^{3+} nas propriedades fotoluminescente da matriz de YVO_4 . **Química Nova**, v. 41, n. 8, p. 849–856, 2018.

MATOS, M. G. et al. Synthesis and photoluminescent properties of yttrium vanadate phosphor prepared by the non-hydrolytic sol-gel process. **Journal of Luminescence**, v. 147, p. 190–195, 2014.

MBEY, J. A. et al. An insight on the weakening of the interlayer bonds in a Cameroonian kaolinite through DMSO intercalation. **Applied Clay Science**, v. 83–84, p. 327–335, out. 2013.

NAKAYAMA, H.; WADA, N.; TSUHAKO, M. Intercalation of amino acids and peptides into Mg-Al layered double hydroxide by reconstruction method. **International Journal of Pharmaceutics**, v. 269, n. 2, p. 469–478, 2004.

NASEEM, S. et al. Preparation of Photoactive Transition-Metal Layered Double Hydroxides (LDH) to Replace Dye-Sensitized Materials in Solar Cells. **Materials**, v. 13, n. 19, p. 4384, 1 out. 2020.

NEACSU, A. et al. The effect of gamma rays upon L-proline and 4-hydroxy-L-proline. A thermochemical study. **Radiation Physics and Chemistry**, v. 156, n. November 2018, p. 115–127, mar. 2019.

NISTORA, R.; ANDREICI, L.; AVRAM, N. M. Comparative Study between Energy Levels of Cr^{3+} and Co^{2+} Ions Doped in MgF 2 Crystal. **Acta Physica Polonica A**, v. 116, n. 4, p. 538–540, out. 2009.

PÁLKOVÁ, H. et al. Laponite-derived porous clay heterostructures: I. Synthesis and physicochemical characterization. **Microporous and Mesoporous Materials**, v. 127, n. 3, p. 228–236, fev. 2010.

PARRA, D. F. et al. Enhancement of the luminescent intensity of the novel system containing Eu^{3+} - β -diketonate complex doped in the epoxy resin. **Journal of Applied Polymer Science**, v. 83, n. 12, p. 2716–2726, 2002.

POLFER, N. C. et al. Infrared spectroscopy of phenylalanine Ag(I) and Zn(II) complexes in the gas phase. **Journal of the American Chemical Society**, v. 128, n. 2, p. 517–525, 2006.

RAVIKUMAR, B.; RAJARAM, R. K.; RAMAKRISHNAN, V. Raman and IR spectral studies of L-phenylalanine-L-phenylalaninium dihydrogenphosphate

andDL-phenylalaninium dihydrogenphosphate. **Journal of Raman Spectroscopy**, v. 37, n. 5, p. 597–605, maio 2006.

RYU, S. J. et al. Photoluminescent europium(III) complex intercalated in natural and synthetic clay minerals for enhanced latent fingerprint detection. **Applied Clay Science**, v. 101, p. 52–59, 2014.

SÁ FERREIRA, R. A. et al. A theoretical interpretation of the abnormal ${}^5D_0 \rightarrow {}^7F_4$ intensity based on the Eu^{3+} local coordination in the $\text{Na}_9[\text{EuW}_{10}\text{O}_{36}] \cdot 14\text{H}_2\text{O}$ polyoxometalate. **Journal of Luminescence**, v. 121, n. 2, p. 561–567, dez. 2006.

SAHNOUNE, F. et al. Thermal analysis of dehydroxylation of Algerian kaolinite. **Journal of Thermal Analysis and Calorimetry**, v. 107, n. 3, p. 1067–1072, 2012.

SAKAI, Y. et al. Deconvolution of non-exponential emission decays arising from reabsorption of emitted light. **Journal of Luminescence**, v. 42, n. 6, p. 317–324, jan. 1989.

SILVA, A. F. DA; DUARTE, J. L. DA S.; MEILI, L. Different routes for MgFe/LDH synthesis and application to remove pollutants of emerging concern. **Separation and Purification Technology**, v. 264, n. January, p. 118353, jun. 2021.

SILVA, J. M. et al. New organic-inorganic hybrid composites based on cellulose nanofibers and modified Laponite. **Advanced Optical Technologies**, v. 7, n. 5, p. 327–334, 2018.

SILVERSTEIN, R. M.; WEBSTER, F. X.; KIEMLE, D. J. **Spectrometric identification of organic compounds**. 7th. ed. Hoboken: John Wiley & Sons, Ltd, 2005.

SMRČOK, L. et al. The combined inelastic neutron scattering (INS) and solid-state DFT study of hydrogen-atoms dynamics in kaolinite-dimethylsulfoxide intercalate. **Clays and Clay Minerals**, v. 58, n. 1, p. 52–61, 2010.

SOLARZ, P. VIS-VUV spectroscopy of $\text{K}_5\text{GdLi}_2\text{F}_{10}:\text{Tb}$, Eu and temperature activated energy transfer from terbium to europium. **Journal of Alloys and Compounds**, v. 855, p. 157459, fev. 2021.

SUPKOWSKI, R. M.; HORROCKS, W. D. Displacement of Inner-Sphere Water Molecules from Eu^{3+} Analogues of Gd^{3+} MRI Contrast Agents by Carbonate and Phosphate Anions: Dissociation Constants from Luminescence Data in the Rapid-Exchange Limit. **Inorganic Chemistry**, v. 38, n. 24, p. 5616–5619, nov. 1999.

SUPKOWSKI, R. M.; HORROCKS, W. D. On the determination of the number of water molecules, q , coordinated to europium(III) ions in solution from luminescence decay lifetimes. **Inorganica Chimica Acta**, v. 340, p. 44–48, nov. 2002.

TANNER, P. A. Some misconceptions concerning the electronic spectra of tri-positive europium and cerium. **Chemical Society Reviews**, v. 42, n. 12, p. 5090, 2013.

TONLÉ, I. K. et al. Nanohybrid kaolinite-based materials obtained from the interlayer grafting of 3-aminopropyltriethoxysilane and their potential use as electrochemical sensors. **Chemistry of Materials**, v. 19, n. 26, p. 6629–6636, 2007.

TOSONI, S.; DOLL, K.; UGLIENGO, P. Hydrogen bond in layered materials: Structural and vibrational properties of kaolinite by aperiodic B3LYP approach. **Chemistry of Materials**, v. 18, n. 8, p. 2135–2143, 2006.

TRAN, H. N.; LIN, C.-C.; CHAO, H.-P. Amino acids-intercalated Mg/Al layered double hydroxides as dual-electronic adsorbent for effective removal of cationic and oxyanionic metal ions. **Separation and Purification Technology**, v. 192, p. 36–45, fev. 2018.

TRONTO, J. et al. Visible and near-infrared luminescent Eu^{3+} or Er^{3+} doped laponite-derived xerogels and thick films: Structural and spectroscopic properties. **Materials Chemistry and Physics**, v. 113, n. 1, p. 71–77, jan. 2009.

TRUJILLANO, R. et al. Microwave radiation and mechanical grinding as new ways for preparation of saponite-like materials. **Applied Clay Science**, v. 48, n. 1–2, p. 32–38, mar. 2010.

TRUJILLANO, R. et al. Rapid microwave-assisted synthesis of saponites and their use as oxidation catalysts. **Applied Clay Science**, v. 53, n. 2, p. 326–330, 2011.

UTOCHNIKOVA, V. V. et al. Luminescence enhancement of nanosized ytterbium and europium fluorides by surface complex formation with aromatic carboxylates. **Journal of Luminescence**, v. 170, p. 633–640, 2016.

VOGELS, R. J. M. J.; KLOPROGGE, J. T.; GEUS, J. W. Synthesis and characterization of saponite clays. **American Mineralogist**, v. 90, n. 5–6, p. 931–944, 2005.

WAGNER, C. C.; TORRE, M. H.; BARAN, E. J. Vibrational spectra of copper(II) complexes of L-proline. **Latin American Journal of Pharmacy**, v. 27, n. 2, p. 197–202, 2008.

WANG, Y. et al. Recent progress in luminescent materials based on lanthanide complexes intercalated synthetic clays. **Journal of Rare Earths**, v. 37, n. 5, p. 451–467, 2019.

WANG, Y. J. et al. Non-exponential photoluminescence decay dynamics of localized carriers in disordered InGaN/GaN quantum wells: the role of localization length. **Optics Express**, v. 14, n. 26, p. 13151, 2006.

XIE, Z. et al. Wide-range lifetime-tunable and responsive ultralong organic phosphorescent multi-host/guest system. **Nature Communications**, v. 12, n. 1, p. 3522, 10 dez. 2021.

XIONG, Z.-Q. et al. Performance evaluation of laponite as a mud-making material for drilling fluids. **Petroleum Science**, v. 16, n. 4, p. 890–900, 14 ago. 2019.

YANG, D.; WANG, J.; LI, H. Photo- and thermo-stable luminescent nanocomposite resulting from hybridization of Eu(III)- β -diketonate complexes with laponite. **Dyes and Pigments**, v. 118, p. 53–57, jul. 2015.

YANG, S. QIN et al. Effect of reaction temperature on grafting of γ -aminopropyl triethoxysilane (APTES) onto kaolinite. **Applied Clay Science**, v. 62–63, p. 8–14, 2012.

ZHAI, D. et al. Mesoporous silica equipped with europium-based chemosensor for mercury ion detection: Synthesis, characterization, and sensing performance. **Inorganica Chimica Acta**, v. 387, p. 396–400, 2012.

ZHANG, S. et al. Combined experimental and theoretical investigation of interactions between kaolinite inner surface and intercalated dimethyl sulfoxide. **Applied Surface Science**, v. 331, p. 234–240, 2015.

ZHANG, S. et al. Mechanism responsible for intercalation of dimethyl sulfoxide in kaolinite: Molecular dynamics simulations. **Applied Clay Science**, v. 151, n. June 2017, p. 46–53, 2018.

ZHANG, W. et al. Intercalation of Europium Inclusion Complex of β -Cyclodextrin into Layered Double Hydroxides Through Layer-By-Layer Assembly and Its Luminescent Properties. **Nanomaterials**, v. 12, n. 10, p. 1750126, 30 out. 2017.

ZHAO, S.-N. et al. Luminescent Lanthanide MOFs: A Unique Platform for Chemical Sensing. **Materials**, v. 11, n. 4, p. 572, 7 abr. 2018.

ZHAO, S. et al. Preparation and Fluorescent Property of Eu(TTA)₃Phen Incorporated in Polycarbonate Resin. **Polymer Journal**, v. 38, n. 6, p. 523–526, 15 jun. 2006.

ZHITOVA, E. S. et al. Thermal Evolution of Natural Layered Double

Hydroxides: Insight from Quintinite, Hydrotalcite, Stichtite, and Iowaite as Reference Samples for CO_3^- and Cl-Members of the Hydrotalcite Supergroup. **Minerals**, v. 10, n. 11, p. 961, 28 out. 2020.

Final considerations and perspectives

In this thesis, the development of new hybrid materials formed by the complexation of the europium (III) ion with the amino acids proline and phenylalanine and immobilized in natural and synthetic clay minerals was presented. These materials were applied (i) as adsorbent materials for Cr³⁺ contaminants, caffeine and estrogen; (ii) as luminescent sensors of these same contaminants and as (iii) materials applied in improved fingerprint detection.

The materials immobilized in kaolinite were functionalized by two distinct routes, one by the conventional synthesis and the other by the modification of the alkoxide APTES with the amino acids through an amidation reaction catalyzed by boric acid. In this new catalyzed route, the materials showed greater dispersion in the matrix, greater thermal resistance and better luminescent properties compared to those synthesized by conventional synthesis. The interaction between the complex and the matrix was fundamental for application in the adsorption of contaminants, presenting pseudo second order kinetic behavior and convergence to the Freundlich isotherm. Based on the results obtained, luminophores immobilized in kaolinite have properties that make their research attractive and commercially viable, with high quantum yield, especially for materials obtained with the amino acid phenylalanine, maintaining the lamellar structure of kaolinite even after several treatments, in adsorption, equilibrium and leaching processes, bringing high added value.

The samples immobilized in hydrotalcite were synthesized in two routes, being them by the reconstruction method and by the co-precipitation method.

The co-precipitation method showed better optical properties and high lifetimes, being qualified as phosphorescent materials, and can be applied as a fingerprint detector, security materials, LEDs and OLEDs, in addition to being easily synthesized and with low concentrations of lanthanide ion, which makes it commercially viable in the widest variety of related areas.

As for the smectites (LAPONITE® and saponite) the finished complex was intercalated in the interlamellar space by ion exchange. The Eutta(LapPhe) sample showed unique optical properties for materials immobilized in clay minerals that could not be achieved in the isolated complex or in the direct addition of europium (III) ion in the matrix, with high lifetimes, being classified as phosphorescent material, and high internal quantum yield of radiative emission, which makes it ideal to be applied in several luminescent areas on a commercial scale, since the dispersion of the complex in the matrix attributes low concentration of the complex, with low production cost, non-toxic, non-polluting, expanding the perspectives for application where you need high emission yield.

Samples with saponite showed high affinity for the detection of contaminants, bypassing the low quantum emission yield, and can be used as a sensor for emerging contaminants and potentially toxic metals, expanding its application area, and can be used in polymeric films and others matrices to further improve their optical properties in identifying polluting compounds. The ease of synthesizing this material, together with its low toxicity and low cost, makes its application on a commercial scale viable, in addition to justifying research involving these matrices for ecological purposes.

Considerações finais e perspectivas

Nesta tese foi apresentado o desenvolvimento de novos materiais híbridos formados pela complexação do íon európio (III) com os aminoácidos prolina e fenilalanina e imobilizados em argilominerais naturais e sintéticos. Estes materiais foram aplicados (i) como materiais adsorventes dos contaminantes Cr^{3+} , cafeína e estrogênio; (ii) como sensores luminescentes destes mesmos contaminantes e como (iii) materiais aplicados na detecção aprimorada de impressões digitais.

Os materiais imobilizados em caulinita foram funcionalizados por duas rotas distintas, sendo uma pela síntese convencional e a outra pela modificação do alcóxido APTES com os aminoácidos através de reação de amidação catalisada por ácido bórico. Nesta nova rota catalisada, os materiais apresentaram maior dispersão na matriz, maiores resistências térmicas e melhores propriedades luminescentes em relação aos sintetizados pela síntese convencional. A força de interação entre o complexo e a matriz foi fundamental para aplicação na adsorção dos contaminantes, apresentado comportamento cinético de pseudo segunda ordem e convergência para a isoterma de Freundlich. Baseado nos resultados obtidos, os luminóforos imobilizados em caulinita apresentam propriedades que tornam sua pesquisa atraente e de grande viabilidade comercial, com alta eficiência quântica, principalmente para os materiais obtidos com o aminoácido fenilalanina, mantendo a estrutura lamelar da caulinita mesmo após vários tratamentos, nos processos de adsorção, equilíbrio e lixiviação, trazendo alto valor agregado.

Já as amostras imobilizadas em hidrotalcita foram sintetizadas em duas rotas, sendo elas pelo método de reconstrução e pelo método de

coprecipitação. O método de coprecipitação apresentou melhores propriedades ópticas e altos tempos de vida, sendo qualificados como materiais fosforescentes, podendo ser aplicado como detector de impressões digitais, materiais de segurança, LEDs e OLEDs, além de serem facilmente sintetizados e com baixas concentrações do íon lantanídeo, que o viabiliza comercialmente nas mais variedades de áreas afins.

Já para as esmectitas (LAPONITE® e saponita) o complexo pronto foi intercalado no espaço interlamelar por troca iônica. A amostra Eutta(LapPhe) apresentou propriedades ópticas únicas para os materiais immobilizados em argilominerais que não poderiam ser alcançados no complexo isolado ou na adição direta do íon európio (III) na matriz, com tempos de vida altos, sendo classificado como material fosforescente, e alto rendimento quântico interno de emissão radiativa, que o torna ideal para ser aplicado em várias áreas luminescentes em escala comercial, já que a dispersão do complexo na matriz atribui baixa concentração do complexo, com baixo custo de produção, não tóxico, não poluente, ampliando as perspectivas para aplicação onde necessita de alta eficiência de emissão.

As amostras com saponita apresentaram alta afinidade para a detecção de contaminantes, contornando a baixa eficiência quântica de emissão, podendo ser utilizada com sensor de contaminantes emergentes e de metais potencialmente tóxicos, ampliando sua área de aplicação, podendo ser utilizada em filmes poliméricos e em outras matrizes para melhorar ainda mais suas propriedades ópticas na identificação de compostos poluentes. A facilidade de sintetizar este material, junto com sua baixa toxicidade e baixo

custo, torna viável sua aplicação em escala comercial, além de justificar a pesquisa envolvendo estas matrizes para fins ecológicos.

Consideraciones y perspectivas finales

En esta tesis se presentó el desarrollo de nuevos materiales híbridos formados por la complejación del ion europio (III) con los aminoácidos prolina y fenilalanina e inmovilizados en minerales arcillosos naturales y sintéticos. Estos materiales se aplicaron (i) como materiales adsorbentes de contaminantes Cr^{3+} , cafeína y estrógeno; (ii) como sensores luminiscentes de estos mismos contaminantes, y como (iii) materiales aplicados en la detección mejorada de huellas dactilares.

Los materiales inmovilizados en caolinita fueron funcionalizados por dos rutas distintas, una por la síntesis convencional y la otra por la modificación del alcóxido APTES con los aminoácidos mediante una reacción de amidación catalizada por ácido bórico. En esta nueva ruta catalizada, los materiales mostraron mayor dispersión en la matriz, mayor resistencia térmica y mejores propiedades luminiscentes en comparación con los sintetizados por síntesis convencional. La fuerza de interacción entre el complejo y la matriz fue fundamental para su aplicación en la adsorción de contaminantes, presentando un comportamiento cinético de pseudo segundo orden y convergencia a la isoterma de Freundlich. Basados en los resultados obtenidos, los luminóforos inmovilizados en caolinita presentan propiedades que hacen atractiva y viable comercialmente su investigación, con alta eficiencia cuántica, especialmente para materiales obtenidos con el aminoácido fenilalanina, manteniendo la estructura laminar de la caolinita incluso después de varios tratamientos, en adsorción, procesos de equilibrio y lixiviación, aportando un alto valor añadido.

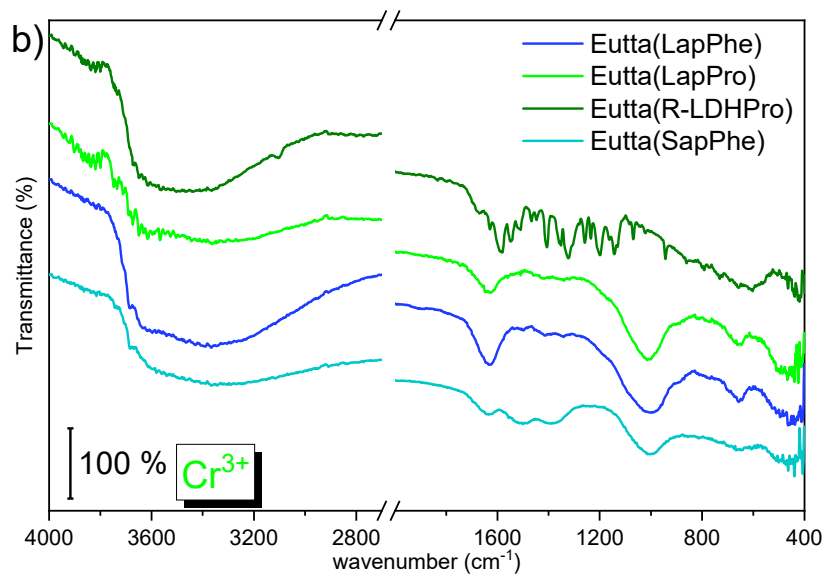
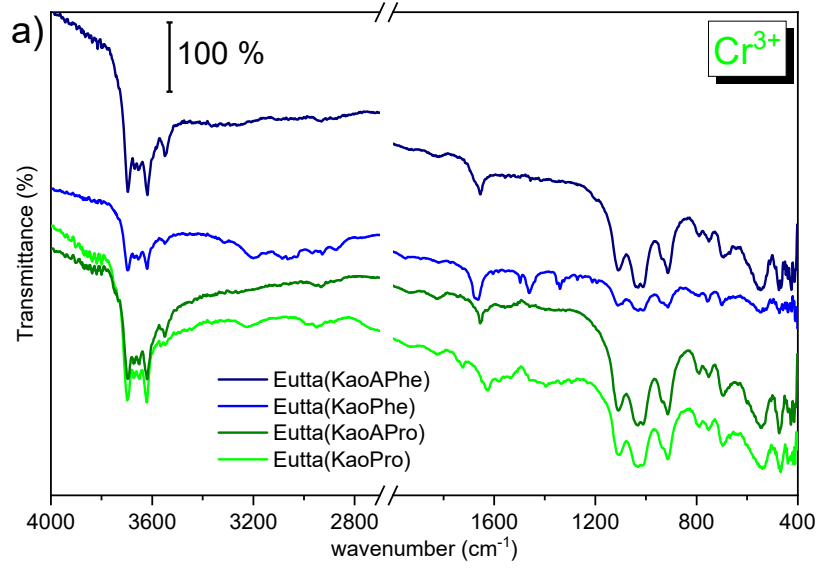
Las muestras inmovilizadas en hidrotalcita se sintetizaron en dos rutas, por el método de reconstrucción y por el método de coprecipitación. El método

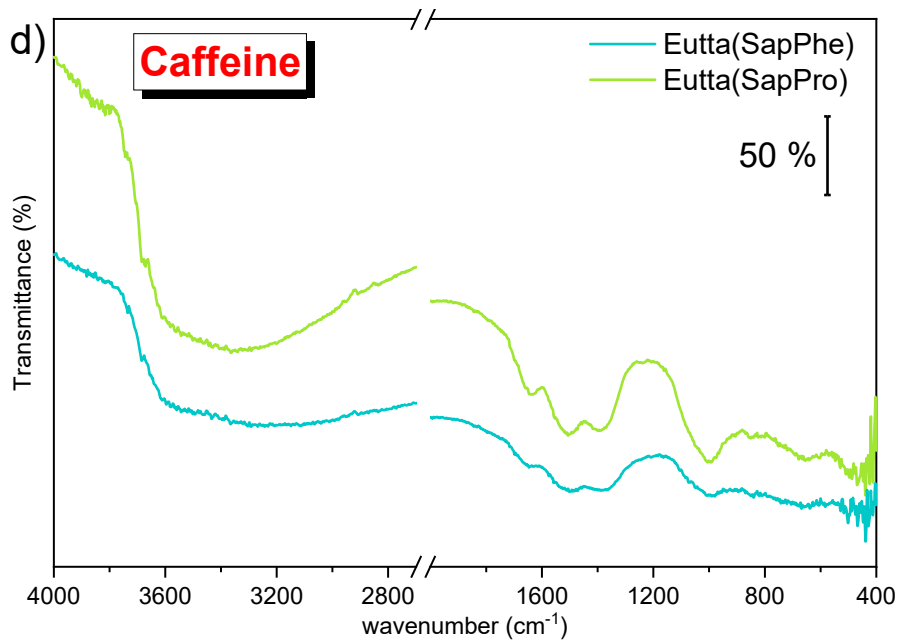
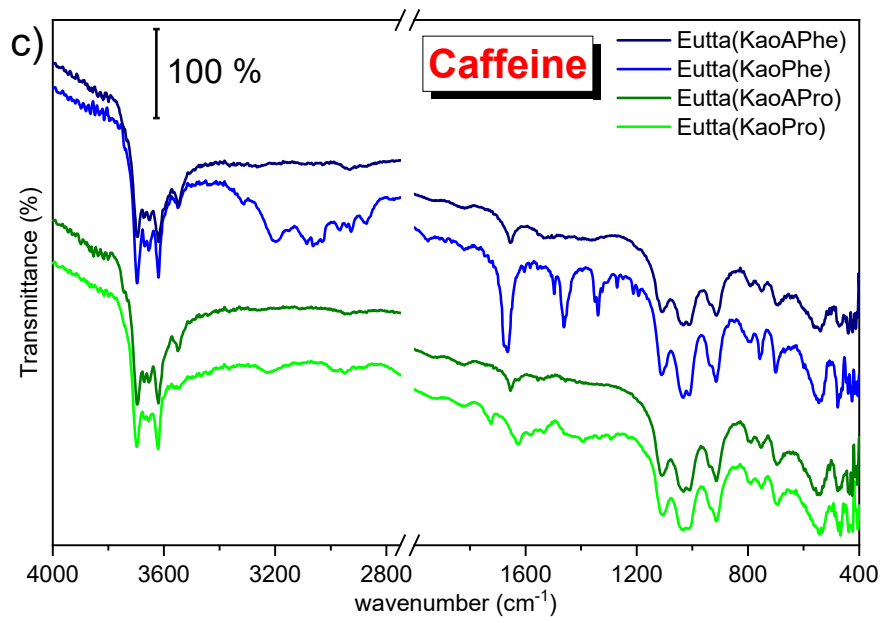
de coprecipitación mostró mejores propiedades ópticas y mayor tiempo de vida, calificándose como materiales fosforescentes, y puede ser aplicado como detector de huellas, materiales de seguridad, LED y OLED, además de ser fácilmente sintetizado y con bajas concentraciones de iones lantánidos, que lo hace comercialmente viable en la más amplia variedad de áreas relacionadas.

En cuanto a las esmectitas (LAPONITA® y saponita), el complejo se intercaló en el espacio interlaminar mediante intercambio iónico. La muestra Eutta(LapPhe) presentó propiedades ópticas únicas para materiales inmovilizados en minerales arcillosos que no se pudieron lograr en el complejo aislado o mediante la adición directa del ion europio (III) en la matriz, con altos tiempos de vida, siendo clasificado como material fosforescente, y alto rendimiento cuántico interno de emisión radiativa, lo que lo hace ideal para ser aplicado en varias áreas luminiscentes a escala comercial, ya que la dispersión del complejo en la matriz implica baja concentración del complejo, con bajo coste de producción, no tóxico, no contaminante, ampliando las perspectivas de aplicación donde se necesita una alta eficiencia de emisión.

Las muestras con saponita mostraron una alta afinidad para la detección de contaminantes, eludiendo la baja eficiencia de emisión cuántica, y pueden usarse como sensor para contaminantes emergentes y metales potencialmente tóxicos, expandiendo su área de aplicación, y pueden usarse en películas poliméricas y otras matrices para mejorar aún más sus propiedades ópticas en la identificación de compuestos contaminantes. La facilidad de síntesis de este material, junto con su baja toxicidad y bajo costo, hace viable su aplicación a escala comercial, además de justificar la investigación que involucre estas matrices con fines ecológicos.

Supplementary Material





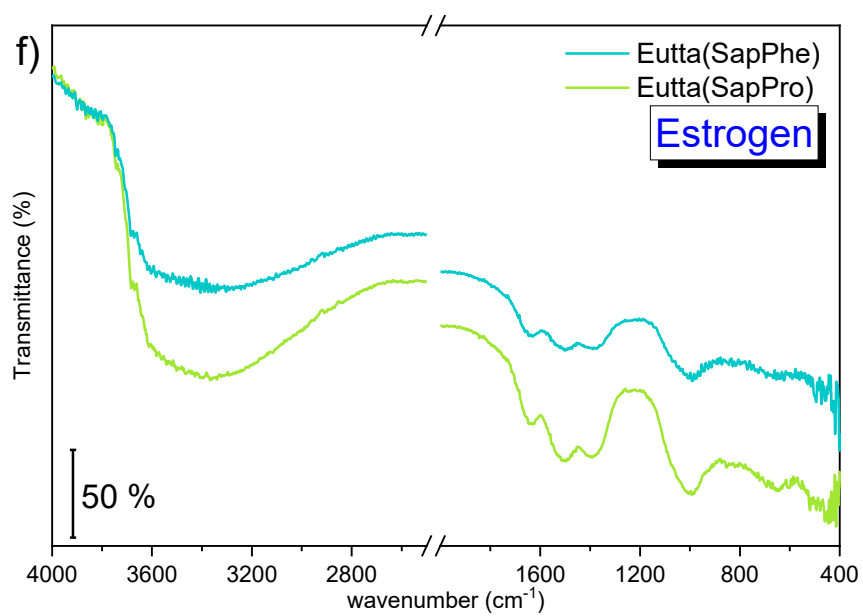
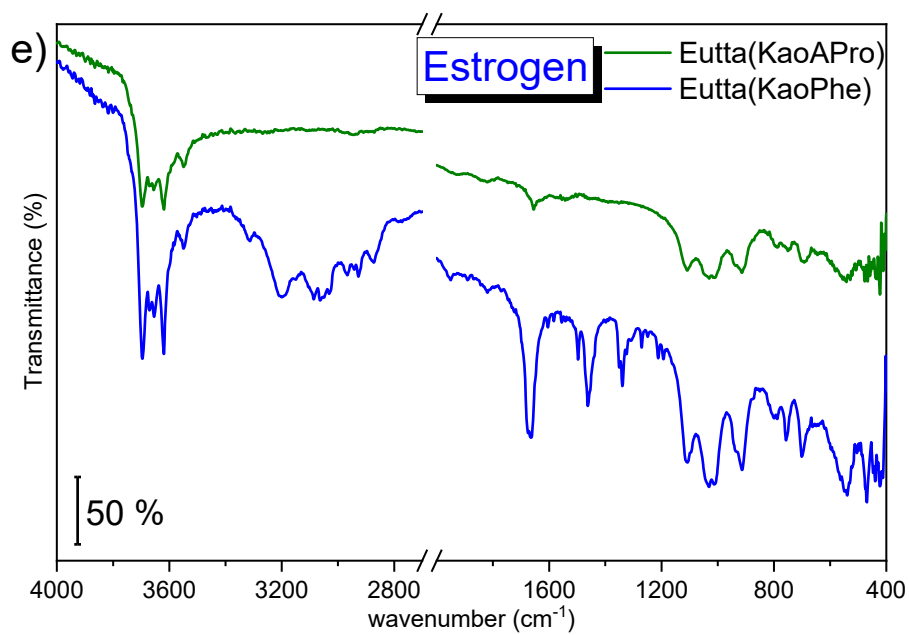


Figure S1 - Infrared spectra of samples after addition of Cr³⁺ (a and b), caffeine (c and d) and estrogen (e and f) contaminants. With break between 2700 to 2000 cm⁻¹.

APPENDIX

ARTICLES

Eu³⁺- and Tb³⁺-Dipicolinate Complexes Covalently Grafted into Kaolinite as Luminescence-Functionalized Clay Hybrid Materials

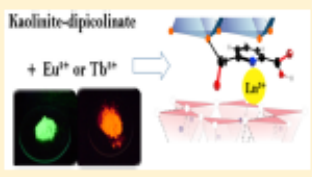
Denis Talarico de Araujo,^{*,†} Katia J. Ciuffi,[†] Eduardo J. Nassar,[†] Miguel A. Vicente,^{*,‡} Raquel Trujillano,[‡] Paulo S. Calefi,[†] Vicente Rives,[‡] and Emerson H. de Faria^{*,†}

[†]Universidade de Franca, Parque Universitário, 201, 14404-600 Franca, São Paulo, Brazil

[‡]GIR-QUESCAT, Departamento de Química Inorgánica, Universidad de Salamanca, 37008 Salamanca, Spain

Supporting Information

ABSTRACT: The luminescence properties of Eu³⁺- and Tb³⁺-dipicolinate (pyridine-dicarboxylate) complexes covalently grafted into a kaolinite matrix were studied. The stability of the grafted lanthanide complexes as a function of the thermal treatment was also investigated. Kaolinite intercalated with dimethyl sulfoxide was heated in the presence of melted dipicolinic acid to form dipicolinate-intercalated kaolinite. The luminescent hybrid solids were obtained by complexation of Eu³⁺ or Tb³⁺ cations with this intercalated solid at cation/ligand molar ratios of 1:1, 1:2, or 1:3. The resulting materials were characterized by thermal analysis, CHN element analysis, powder X-ray diffraction, infrared absorption spectroscopy, and photoluminescence. The lanthanide complexes covalently grafted into kaolinite were thermally more stable than the isolated lanthanide complexes. The hybrid materials exhibited more intense Eu³⁺ and Tb³⁺ emissions than the isolated complexes. The excitation spectra of the hybrid materials showed a broad band at 277 nm, assigned to a ligand-to-metal charge transfer, whereas the emission spectra showed bands related to the typical electronic transitions of Eu³⁺ and Tb³⁺ ions from the excited states ⁵D₀ and ⁵D₄ to the ⁷F_j fundamental states. The (4 → 5 and 4 → 4) and (0 → 2) transitions were the most intense ones and corresponded to green and red emissions, respectively.



INTRODUCTION

Lanthanide pyridinecarboxylic (picolinic) acid complexes are important to develop advanced luminescent materials with applications in photoelectronics, laser, luminescence labels, fluorescent probes, luminescence sensors, light-conversion molecular devices (LCMDs), organic light-emitting devices (OLEDs), fluorescent lamps, and cathode-ray tubes as well as plasma display panels (PDPs).^{1–10} Lanthanide-aromatic carboxylate complexes display interesting photophysical properties due to the antenna effect; that is, the organic ligand in the complex absorbs energy more intensely than the isolated organic ligand.¹¹ However, these complexes exhibit low thermal and chemical stabilities. One strategy to render more stable lanthanide-aromatic carboxylates is to immobilize them on inorganic matrixes.

Hybrid materials obtained by modification of the surface of clay minerals with luminescent organic complexes have attracted the attention of several scientists as the synthesis

of alcohols, polyalcohols, polymers, and alkoxides, among others, to yield organic–inorganic hybrids that can further accommodate luminescent ions.^{18,19}

Smectite clays belong to the tetrahedral–octahedral–tetrahedral (TOT) type clays. Weak interactions between luminescent organic species and smectite allow only a partial modification of this clay with luminescent organic complexes. Indeed, the resulting hybrid material has low chemical and thermal stability, and the luminescent organic complex is easily leached from the clay.²⁰ Another factor that limits the use of TOT clays to immobilize luminescent organic complexes is the presence of water molecules in the interlayer space of the inorganic matrix,²¹ the water molecules interact with the lanthanide ions, leading to nonradiative decays between the excited and fundamental levels and quenching the luminescence of the lanthanide complex.²²

Kaolinites with the theoretical formula Al₂Si₂O₅(OH)₄ and a basal interlayer distance of 7.1 Å are clay minerals belonging to



Contents lists available at ScienceDirect

Journal of Solid State Chemistry

journal homepage: www.elsevier.com/locate/jssc

Immobilization of L-alanine into natural kaolinite via amidation catalyzed by boric acid for the development of biohybrid materials



Alexandre Fernando da Silva, Gabriel Silva de Pádua, Denis Talarico de Araújo, Carlos Alexandre Vieira, Emerson H. de Faria^{*}

Grupo de Pesquisa em Materiais Lamelares Híbridos (GPMatLam) - Universidade de Franca, Av. Dr. Amândio Salles Oliveira, Parque Universitário, 201, 14404-600, Franca, SP, Brazil

ARTICLE INFO

Keywords:
Amino acid
Biohybrid materials
Amidation
Clay minerals

ABSTRACT

The natural amino acid L-alanine was immobilized on the interlayer space and surface of the natural Brazilian São Simão's kaolinite using two different routes. In the first 3-aminopropyltriethoxysilane was previously grafted into kaolinite interlayer space resulting into aminofunctionalized kaolinite that was further employed as reactive sites on kaolinite surfaces to bond L-alanine via amidation reaction. In the second route 3-aminopropyltriethoxysilane was first modified by L-alanine via amidation reaction catalyzed by boric acid and the modified alkoxide grafted into kaolinite using kaolinite-dimethylsulfoxide resulting on the biohybrid. In both strategies the amino acid was covalently bounded using the carboxylic acid from the amino acids and amine groups present on the kaolinite surfaces resulting in amide bonds. In both routes, the reaction was catalyzed by boric acid. Results confirms that the nature and loading of immobilized L-alanine changes depending of the route employed. X-ray diffraction confirmed the expansion of the interlayer spaces of the grafted solids resulting in 8.3 Å and 10.8 Å respectively for grafted materials routes one and two respectively. Reaction effectivity was kinetically evaluated by infrared vibrational spectroscopy that confirms the presence of amide bonds in both products due to the bands at 1560 cm^{-1} , due to carbonyl (N-C=O) stretching, and 1490 cm^{-1} , ascribed to N-H plane vibrations and C-N stretching. The typical vibration of inner surface aluminol groups at 938 cm^{-1} (for purified kaolinite) is absent for both routes employed after grafting reactions confirming the attachment of the modified alkoxide into aluminol groups via covalent bonds resulting in bonds type Al-O-Si. Thermal analysis showed the typical reduction of dehydroxylation temperature from 510 °C on pure kaolinite to 480 and 450 °C, respectively, on the biohybrid materials and confirmed the functionalization in both routes, the amount of organic content was quantified and was 0.193 and 0.298 mol of organic unit per 1 mol of kaolinite minimal formulae using route of previous grafting of kaolinite with amine groups and direct grafting of modified alkoxide into kaolinite dimethyl sulfoxide respectively. Specific surface area analysis by N_2 adsorption-desorption isotherms (BET method), cationic exchange capacity, and total specific surface area by the methylene blue method also confirmed the reduction of specific surface area from kaolinite grafted derivatives induced by amidation reaction. The solids obtained was tested as matrix to incorporate a cetyl salicylic acid and ibuprofen and reveal that grafted clays incorporate a higher amount of both drugs ($q_t = 210 \text{ mg/g}$). The model that explain the adsorption kinetic mechanism was the pseudo-second order that reveal the higher affinity between adsorbent and acetyl salicylic acid and ibuprofen using the



Contents lists available at ScienceDirect

Applied Clay Science

journal homepage: www.elsevier.com/locate/clay

Research paper

Effect of sodium bentonite content on structural-properties of ureasil poly(ethylene oxide)-PEO hybrid: A perspective for water treatment



Eduardo P. de Sousa, Denis T. de Araujo, Vinilson G. Peixoto, Breno F. Ferreira, Emerson H. de Faria, Eduardo F. Molina*

Universidade de Franca, Av. Dr. Amendo Sales Oliveira 201, Franca, SP 14404-600, Brazil

ARTICLE INFO

Keywords:
Nanocomposites
Swelling
Clay
Synchrotron X-ray tomography
Water treatment

ABSTRACT

We report here the synthesis of an ureasil poly(ethylene oxide)-PEO nanocomposite (UPEO) containing sodium bentonite (Bent) for removal of cation species. The sol-gel process allows the clay dispersion throughout the matrix. Toward the goal of understanding properties-structure relationships the present study use X-ray diffraction (XRD), differential scanning calorimetry (DSC), Fourier Transform infrared (FTIR). The influence of clay amount on morphology and submicron microstructural properties was tracked by Scanning electron microscopy (SEM) and Synchrotron X-ray tomography. Regardless of the amount of Bent incorporated into UPEO (1 from 10 wt%), homogeneous nanocomposites were obtained. The dispersion/intercalated Bent into UPEO clearly showed a decrease of water uptake by the matrix and could be used as vehicle to transport therapeutic agents and as flame retardancy systems. A partial intercalation of PEO in the interlayer space of the Bent was observed by XRD and a change of the PEO backbone environmental was evidenced by FTIR. A wider Bent distribution along the UPEO hybrid thickness, leads to a more fractured and tortuous microstructure evidenced by SEM and X-ray tomography images. These changes directly affects the thermal properties (DSC features) leading to a decrease of crystallinity degree of UPEO loaded with Bent. The adsorption selectivity of UPEO can be easily tuned from cations to anions species by the presence or not of clay in the nanocomposites due to the cation exchange capacity from Bent present in the surface of the matrix following an intraparticle diffusion mechanism.

1. Introduction

Since the Toyota group reported the montmorillonite Mt-nylon-6 nanocomposite (Kojima et al., 1993), research and development of new hybrid/nanocomposite materials have attracted both industrial and academic interest around the world. The structural characteristics and functional applications of nanostructured hybrids based on natural (or synthetic) clays allow distinct applications of these materials, including

vinyl triethoxysilane-VTES and acrylamide (AM) via radical polymerization. The authors observed both exfoliation and intercalation effect of the nanoclay into the hydrogels with increased SiO₂ particles (acting as crosslinker) that improved the mechanical properties under different water contents (Yu et al., 2018). Despite the easy intercalation of drugs (positively charged – cation) into montmorillonite (Mt), the fine control of drug release (amount and rate) still shows some difficulty using ion exchange methods. A strategy to develop new drug



Contents lists available at ScienceDirect

Applied Clay Science

journal homepage: www.elsevier.com/locate/clay

Research Paper

Luminescent properties of biohybrid (kaolinite-proline) materials synthesized by a new boric acid catalyzed route and complexed to Eu^{3+}

D.T. de Araújo^a, G.S. de Pádua^a, V.G. Peixoto^a, K.J. Ciuffi^a, E.J. Nassar^a, M.A. Vicente^{b,*},
R. Trujillano^b, V. Rives^b, M.E. Pérez-Bernal^b, E.H. de Faria^a

^a Universidade de Franca, UNIFRAN, Grupo de Pesquisas em Materiais Lamelares Híbridos (GPMatLam), Av. Dr. Armando Salles Oliveira, Parque Universitário, 201, 14404-600 Franca, São Paulo, Brazil

^b GIR-QUESCAT, Departamento de Química Inorgánica, Universidad de Salamanca, 37008 Salamanca, Spain



ARTICLE INFO

Keywords:
Kaolinite
L-Proline
Biohybrids
Amidation
Europium
Luminescence

ABSTRACT

The properties of Eu^{3+} -biohybrid (kaolinite-proline) materials were investigated by powder X-ray diffraction, vibrational spectroscopy, scanning electron microscopy, nitrogen adsorption and photoluminescence to understand how Eu^{3+} interacts with the biohybrid matrices. Biohybrids were obtained through the conventional route and by two new catalytic routes for functionalization of clay minerals, and were then complexed to Eu^{3+} ions at a constant proline: Eu^{3+} molar ratio of 3:1, while the water molecules originally existing in the first coordination sphere of Eu^{3+} ions in the kaolinite-grafted complexes were replaced by 2-thenoyltrifluoroacetone (tta). The typical Eu^{3+} emission spectra for solids containing tta revealed the characteristic Eu^{3+} transitions from fundamental $^5\text{D}_0$ state to excited $^7\text{F}_j$ ($J = 0, 1, 2, 3$ and 4) states. The lifetime measurements also confirmed that water molecules were exchanged, increasing emission efficiency. The time-resolved spectra allowed to remove the matrix and ligand emissions and thus to evaluate their influence on the emission of the lanthanide ion. After incorporation of Eu^{3+} , the thermal stability of the solids improved. The intercalated europium complexes did not show the same ligand/ Eu^{3+} molar ratio as the free complexes, due to the restricted mobility of the ligands grafted within the interlayer spaces of kaolinite. On the contrary, these complexes showed high internal quantum yields, low luminescence suppression (after tta coordination), preserved the kaolinite layered structure. They also showed a low water molecules coordination number, which made them very attractive for luminescent applications, in addition to bringing high added value, due to a low cost, non-toxicity, non-polluting and high efficiency.

1. Introduction

Lanthanide ions have been the subject of research in luminescent applications for many years due to their [Xe] $4f^n$ electronic configuration. The $4f$ shells are shielded by outer filled $5s$ and $5p$ orbitals, which

Rare earth metal compounds have low direct excitation luminescence efficiency, due to the low molar absorptivity, low ion concentration and the parity-selection rule, which prohibits these transitions that can be 10^6 times weaker than the permitted transitions (Ribeiro and Crabtree, 1994). This factor makes these ions to require a



Contents lists available at ScienceDirect

Applied Surface Science Advances

journal homepage: www.elsevier.com/locate/apsadv

Grafting of L-proline and L-phenylalanine amino acids on kaolinite through synthesis catalyzed by boric acid



Denis T. de Araújo^a, Katia J. Ciuffi^a, Eduardo J. Nassar^a, Miguel A. Vicente^b, Raquel Trujillano^b, Vicente Rives^b, Elena P. Bernal^b, Emerson H. de Faria^{a,*}

^a Grupo de Pesquisas em Materiais Lamelares Híbridos (GPMatLam), Universidade de Franca, Av. Dr. Armando Salles Oliveira, Parque Universitário, 201, 14404-600 Franca, SP, Brazil

^b GIR-QUESCAT, Departamento de Química Inorgánica, Universidad de Salamanca, 37008 Salamanca, Spain

ARTICLE INFO

Keywords:

Kaolinite
Functionalization
Phenylalanine
Organically modified kaolinite

ABSTRACT

The amidation reaction catalyzed by boric acid between the amino acids proline and phenylalanine and the alkoxide 3-aminopropyltriethoxysilane was studied. Afterwards, the modified alkoxide was used to functionalize the clay mineral kaolinite. The hybrid material was characterized by powder X-ray diffraction, molecular absorption spectroscopy in the infrared region, thermal analysis and scanning electron microscopy, to understand the influence of the reaction time on the kaolinite intercalation process, in order to improve this functionalization route for both amino acids. The reaction times evaluated varied from 0 to 24 h, keeping the reflux temperature fixed at 180 °C, being then reacted with kaolinite previously intercalated with dimethyl sulfoxide (DMSO). After 24 h of reaction the modified alkoxide interacted effectively, replacing the DMSO molecules and resulting in the formation of covalent bonds between the modified alkoxide and the clay. The material showed greater dispersion of the organic phase along the layered matrix, and significantly increased its thermal stability, with maximum loss at 320 °C. The sample containing phenylalanine was more agglomerated than that containing proline, with 2.4 times in mol number. In all cases, the crystallinity of the material decreased by the interaction of the modified alkoxide with the kaolinite matrix, the modified alkoxide being partially outside the interlayer space because of its large molecular size.

1. Introduction

Organic-inorganic hybrid materials have attracted interest among researchers due to their broad variety of properties. Consequently, hybrid materials synthesized from layered clay minerals as inorganic matrixes have been studied extensively in recent years for the most diverse applications such as catalysis [1,2], luminescent sensors [3], adsorption [4], and controlled drug release [5], among others. Among these clay

to the interlayer space, which can form covalent bonds through condensation reactions [7]. In the context of this work, the amino acids L-proline and L-phenylalanine were chosen because they are molecules with high potential for different applications, being already widely used in the pharmaceutical industry, in addition to show low toxicity, being of low cost and non-polluting.

The most common route for grafting is the displacement method [8–10], which provides a greater concentration of the functionalized ma-